Mineralogy and petrology of the Good Hope carbonatite complex, Marathon, Ontario

by

Rebecca Lynne Price

A thesis submitted to the

Faculty of Science and Environmental Studies

in partial fulfillment of the requirements

for the degree of

Master of Science

Department of Geology

Lakehead University

Thunder Bay, Ontario

January 2023

Abstract

The Good Hope carbonatite is located northwest of Marathon, Ontario (49° 02’ N, 86° 43’ W). It occurs along the northwest margin of the Prairie Lake complex. The objectives of this research are to characterize the carbonate and other minerals of the Good Hope carbonatite, use mineral compositions and textural associations to discuss the petrogenesis, and compare the mineralogy of the Good Hope and Prairie Lake carbonatites to assess potential relationships.

The major rock-forming minerals in the Good Hope carbonatite are calcite, ferroan dolomite, and apatite. The apatite occurs predominantly as elongated aggregates and clasts that define heterogeneous banding within the carbonatite. Syenite xenoliths are centimeter-scale, entrained within the carbonatite, composed of K-feldspar, biotite-phlogopite, magnesio-arfvedsonite, aegirine, quartz, and carbonate. The minor minerals within the carbonatite include dolomite, K-feldspar, quartz, chlorite, magnetite, barite, biotite – phlogopite, magnesio-arfvedsonite, aegirine, pyrochlore, albite, and fluorite. The accessory minerals include pyrite, synchysite-(Ce), rutile, siderite, strontianite, thorite, parisite-(Ce), bastnaesite-(Ce), burbankite, and zircon.

The sequence of formation began with the crystallization of the syenite from an unknown alkaline parent magma, which was followed by the first pulse of carbonatitic magma that disaggregated and entrapped the syenite xenoliths and began crystallizing the Ca-Na pyrochlore and apatite. Subsequent evolution of the initial carbonatitic magma resulted in the alteration of the pyrochlore as well as the dissolution-reprecipitation of the apatite. The second pulse of carbonatitic magma resulted in the resumption of magmatic crystallization of the Ca-Na pyrochlore and apatite together with the crystallization of the alkaline silicates, aegirine and magnesio-arfvedsonite. The apatite + pyrochlore ± magnesio-arfvedsonite accumulate and are subsequently disaggregated with the clasts being deformed by turbulent flow of the third carbonatitic magma pulse. Groundmass calcite and dolomite with increasingly Fe-rich compositions were formed as crystallization progressed. The system becomes increasingly influenced by hydrothermal and carbothermal processes with the crystallization of the late ferroan dolomite with associated late-hydrothermal apatite ± pyrochlore. The precipitation of the hydrothermal phases and Fe-overgrowths are the last stages of crystallization.

The close spatial association with the Prairie Lake carbonatite complex and the crystallization sequence consistent with other alkaline rock-carbonatite complexes may support a genetic association. However, the mineralogy of Good Hope is distinctly different from that of Prairie Lake and as yet there is insufficient mineralogical or geological evidence to permit formulation of any simple genetic relationships between the two complexes.

Acknowledgments

I would like to first extend my deepest gratitude to my co-supervisor Dr. Shannon Zurevinski for offering me this interesting and challenging learning opportunity. I would also like to thank her for her continued support and time spent throughout this project. I couldn't have completed this thesis without the guidance and expertise of my other co-supervisor Dr. Roger Mitchell. I would like to thank him for his time and patience throughout this process, especially during the editorial stage. Huge thanks to prospector Rudy Wahl for his assistance and insight in the field and Plato Gold for allowing access to the Good Hope property. This project would not have been possible without the financial assistance of the Natural Sciences and Engineering Research Council or Lakehead University. Many thanks to Dr. Guosheng Wu in the Lakehead University Instrumentation Laboratory for helping me to troubleshoot the SEM-EDS system. I would like to thank Dr. Panseok Yang at the University of Manitoba for his help training me on the CL imaging system. I would also like to thank Leandro Silva at Queen's University for assisting me in running the CL spectra and imaging system. I am very grateful to my family and friends for their support during this uniquely challenging process.

Table of Contents

List of Figures

List of Tables

Chapter 1. Introduction

The Good Hope carbonatite occurrence is located 45 km northwest of Marathon, Ontario (49° 02’ N, 86° 43’ W), adjacent to the Prairie Lake carbonatite complex (PLCC) within the Superior Province (Figure 1.1). These carbonatite occurrences are located on a splay of the Big Bay-Ashburton Fault along which the Chipman Lake dikes and fenites, Killala Lake complex, and the Coldwell complex occur. Good Hope and Prairie Lake are emplaced in the Archean gneisses of the Wawa subprovince.

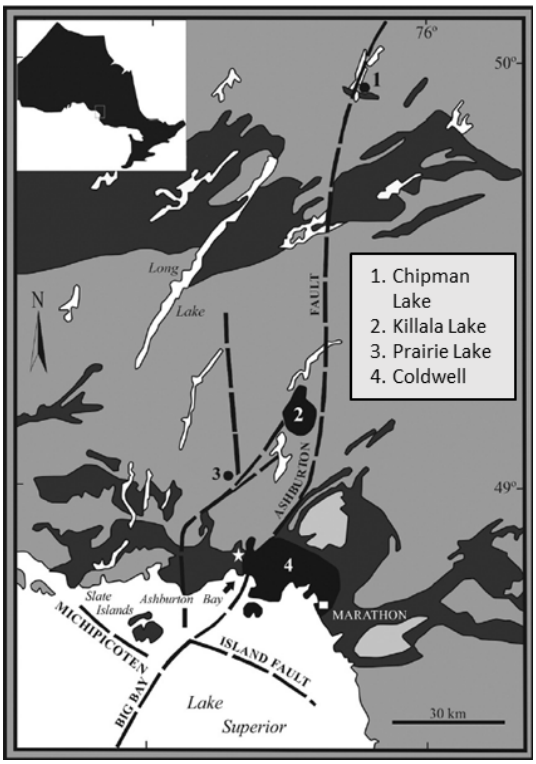

Figure 1.1: The location of Prairie Lake complex, Chipman Lake dikes and fenites, Killala Lake complex, and Coldwell complex relative to the approximately north-south trending Big Bay-Ashburton Fault. From Zurevinski and Mitchell (2015).

Although the Prairie Lake carbonatite complex is a well-studied occurrence representing over 30 years of exploration, the Good Hope carbonatite went unrecognized as a potential target, due to the absence of a magnetic signature and the significant variation in topography between

the two occurrences (Figure 1.2). The primary objectives of this research are to characterize the carbonate and silicate mineralogy of the Good Hope carbonatite, to classify the carbonatite and discuss the petrogenesis of this occurrence. The secondary objectives are to provide a general comparison with the Prairie Lake carbonatite complex, including a comparison of the orbicular occurrences from each complex, and discuss the possible implications of a genetic link. Establishing a genetic relationship between Prairie Lake and Good Hope would provide evidence for how carbonatites evolve, indicating the mineralogy and processes of emplacement can change in a single occurrence. Conversely, if they are not genetically related it would indicate that carbonatites can exploit previous conduits and suggest that spatially related carbonatites are not necessarily genetically related, which emphasizes the importance of using isotopic and age determination studies on multiple regions of a single occurrence.

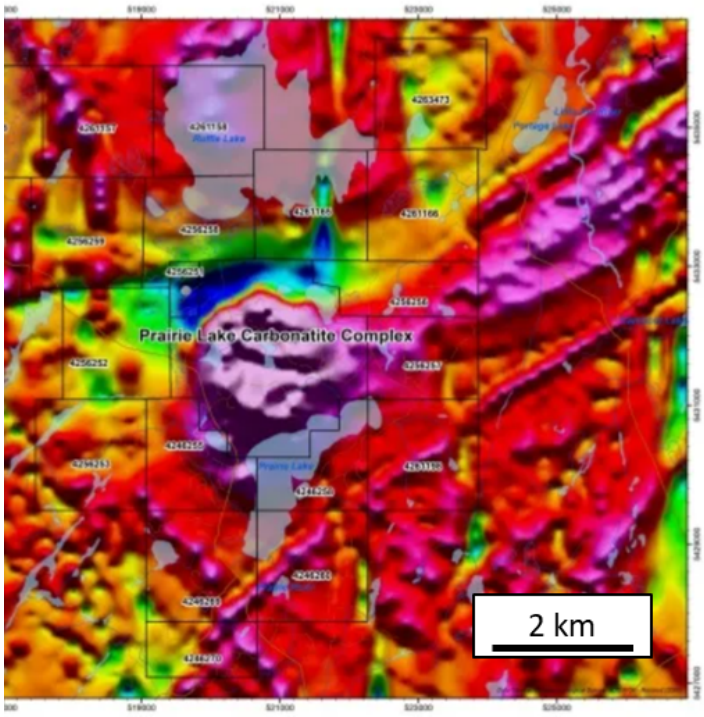

Figure 1.2: Residual magnetic intensity map of the regional area surrounding the Prairie Lake carbonatite complex. The Prairie Lake carbonatite complex is delineated by a magnetic high that likely corresponds to the ijolitic rocks present. The Good Hope carbonatite corresponds to a magnetic low to the northwest of the Prairie Lake carbonatite complex. From Plato Gold (2018).

1.1 Carbonatites

Carbonatites can be classified using the IUGS system of classification as igneous rocks with > 50 modal percent primary magmatic carbonate, and less than 20 wt. % SiO_2. This classification is not satisfactory in some respects as it results in many igneous rocks being incorrectly classified as carbonatite, as these rocks tend to have centimeter-scale compositional heterogeneity. This heterogeneity can influence the classification if some areas have more silicates or an exceptional modal percent of carbonates in a single sample. Mitchell (2005) proposed a genetic classification that defines a carbonatite as containing an arbitrary 30 vol. % magmatic carbonate, regardless of the silica content. Using this approach, Mitchell (2005) defined two general groups: primary carbonatites and carbothermal residua. Carbothermal residua are not considered as carbonatites *sensu stricto* as they are for the most part carbohydrothermal residua produced by the differentiation of a wide variety of parental magmas i.e., nepheline syenites, shonkinites, A-type granites, etc. They are classified as belonging to either a potassic suite, which are most common, or a sodic suite (Mitchell, 2005). The primary carbonatites are subdivided based on their associated silicate rocks, which include the nephelinite clan, the melilitite clan, and the aillikite association. These groups are genetically distinct, formed at different depths in the upper mantle and by varying degrees of partial melting. Carbonatites can exist without associated silicate rocks and should be evaluated individually as to whether they are carbonatites (Mitchell, 2005). Also included with the primary carbonatites are natrocarbonatites, as observed at the active Oldoinyo Lengai volcano, Tanzania, however, there are no other preserved natrocarbonatite occurrences.

Wyllie and Tuttle (1960) showed that carbonate magmas can form at moderate temperatures (minimum liquidus temperatures of 685-640°C) over a broad range of pressures (27 – 4000 bar) in the system CaO-CO_2-H_2O, undoubtedly illustrating the magmatic origin of carbonatites. The source of carbonatite melts is still speculative, although there seems to be consensus that the parental melts form in the mantle. The most common models include low degree partial melts of carbonated peridotite (e.g., Wyllie and Huang, 1975; Eggler, 1978; and Barker, 1996), separation of a carbonatite melt from a silicate parental magma by liquid immiscibility (e.g., Hamilton et al., 1989; Woolley and Kempe, 1989; Lee and Wyllie, 1998; and Veksler et al., 1998), or fractional crystallization of a carbonated silicate melt (e.g., Le Bas, 1977; Gittins, 1989; and Cooper and Reid, 1998). The latter two hypotheses are the most widely accepted owing to the small volume of carbonatites and their common association with alkaline complexes. These carbonatite-silicate rock complexes are circular to elliptical in plan view, although cone sheets and ring dykes are also common (Mitchell, 2015). The sequence of intrusion is typically: silicate rocks, calcite carbonatite, dolomite carbonatite, and ferro-carbonatite, followed by carbohydrothermal veins (Mitchell, 2015).

There are over 527 known carbonatite occurrences worldwide ranging in age from Archean to the present, distributed across every continent, with only three (Canaries, Cape Verde, and Kerguelen) occurring on oceanic islands (Woolley and Kjarsgaard, 2008). The majority form in continental crust, suggesting the thicker continental crust is important for the development of these CO_2-rich melts. They also tend to exploit extensional discontinuities such as rift valley systems (e.g., Kerimasi, Oldoinyo Lengai in the East African Rift Valley system) and major faults or large-scale domal swells (e.g., Mount Weld and Gifford Creek “carbonatites” in

Western Australia; Pirajno, 2015). Some authors (e.g., Ernst and Bell, 2010) have spatially correlated them with Large Igneous Provinces (LIPs), for example, the 66 Ma Deccan flood basalt province with the Amba Dongar, Sarnu-Dandali (Barmer), and Mundwara carbonatites, or the 2055 Ma Bushveld event of the Kaapvaal craton with the Phalaborwa and Shiel carbonatites. This temporal relationship is not conclusive however, due to the lack of precise age determinations for the carbonatites.

1.2 Economic potential

Carbonatites are a rare type of igneous rock that are exploited for their niobium, rare earth element (REE) and phosphorous content. Niobium is a strategic mineral, currently being mined at only three deposits. Two are in Brazil, producing more than 90 % of the world's niobium, and one is in Canada (Saint-Honoré, Quebec; Néron et al., 2018). Niobium is primarily used in the High Strength Low Alloy (HSLA) steel industry although it is beginning to be used in electric vehicle batteries and quantum computing chips. Pyrochlore group minerals are the dominant Nb ore mineral in carbonatite complexes (Mitchell, 2015). A working model suggests fractional crystallization within a magma chamber produces early pyrochlore-bearing cumulates at the walls and base of the chamber with subsequent rheological factors forming complex pyrochlore assemblages with the evolved carbonate-rich melts (Mitchell, 2015). This working model, as well as the current hypotheses for the generation of carbonatites considers pyrochlore as transported assemblages that do not crystallize from their current host (Mitchell, 2015). Niobium deposits can generally be divided as either primary deposits, associated with carbonatites and undersaturated silicate rocks, oversaturated alkaline to peralkaline granitoids and syenites, or secondary (supergene) deposits that form in zones of lateritic weathering

above primary deposits (Mitchell, 2015). Supergene processes, as at Araxa (Brazil), lead to significant enrichment in Nb mineralization with Nb grades well above those of the primary deposit. Although secondary deposits contain higher Nb grades, the mineral liberation and ore beneficiation may be more complex than that for the primary deposits. Secondary alteration (i.e., supergene alteration) produces laterites that are unconsolidated making extraction more cost effective than hard rock mining of fresh carbonatite, however these products are generally fine-grained and typically complexly intergrown making the beneficiation process more difficult (Mitchell, 2015).

Chapter 2. Regional Geology

The Superior Province consists of Archean subprovinces of supracrustal and plutonic rocks metamorphosed to upper amphibolite- and granulite-facies, as well as metavolcanic and metasedimentary greenstone belt sequences surrounded and intruded by granitic batholiths (Figure 2.1) (Stott et al., 2010). These subprovinces are distinguished by lithology, age, isotopic character, geochemistry, and bounding faults (Stott et al., 2010). The intervening metasedimentary terranes contain variably deformed greenstone belts separated by migmatized metasedimentary basins (Stott et al., 2010). Emplacement of plutonic rocks were associated with multiple periods of metamorphism, including the 2.89-to-2.895 Ga and 2.85-to-2.86 Ga episodes across the North Caribou terrane (Stott et al., 2010). The Wawa subprovince extends from the Vermilion district of Minnesota in the west to the Kapuskasing structural zone in the east and is bounded in the north by the Quetico basin and the Midcontinent Rift System in the south (Stott et al., 2010). The Wawa subprovince developed in a rifted oceanic basin without preserved crustal substrate, which may have influenced the emplacement of high temperature rhyolites and komatiites (Ayer et al., 2010). This sequence of sedimentary and volcanic rocks was subsequently metamorphosed and deformed, resulting in uplift and folding, and overlain unconformably by turbiditic sediments (Ayer et al., 2010). This was followed by multiple episodes of deformation under both sinistral and dextral transpressive regimes that resulted in a series of thrusts and folds (Ayer et al., 2010).

The Good Hope carbonatite is emplaced in the Archean gneisses of the Wawa subprovince in the Superior Province (Figure 2.1) (Zurevinski and Mitchell, 2015). The Prairie Lake complex, and subsequently the Good Hope carbonatite, is located at the intersection of

two lineaments, one that trends north and the other that trends northeast between Prairie Lake and Killala Lake (Sage, 1987) (Figure 1.1). The north-trending lineament is parallel and subsidiary to the Big Bay-Ashburton Fault, which is the site of several alkaline rock and carbonatite intrusions, including the Coldwell complex, Chipman Lake Dykes, and Killala Lake (Sage, 1987). The Big Bay-Ashburton Fault lies along a ridge-like structure that trends northeast across the Lake Superior Basin (Sage, 1987), termed the Trans Superior Tectonic Zone (Figure 2.2).

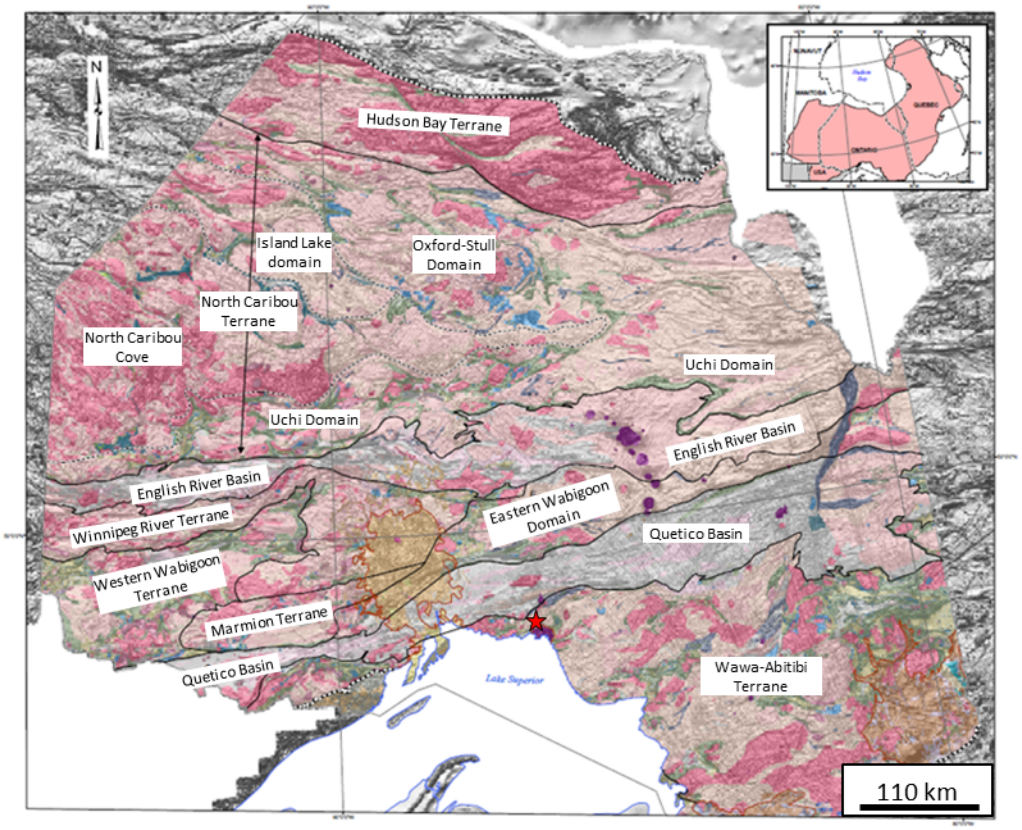

Figure 2.1: Regional geology map of the accreted terranes that define the Superior Province in Ontario, the red star is the approximate location of the Prairie Lake and Good Hope Complexes. From Stott (2011).

The alkaline and carbonatitic complexes within the Superior Province are mostly concordant with the Kapuskasing structural zone that extends from Lake Superior north to

James Bay. Some are also spatially, with few temporally, associated with the curvilinear Midcontinent Rift System that is oriented approximately east-west in the Lake Superior region (Figure 2.2). Woodruff et al. (2020) divided the igneous activity associated with the Midcontinent Rift System of the Lake Superior region into three main stages of rift development. These include the Plateau stage (1112 – 1105 Ma), the Rift stage (1102 – 1090 Ma), and the Late Rift stage (1090 – 1083 Ma), which was followed by a compressional stage (1060 – 1040 Ma), believed to be related to Grenville orogenesis reaching the Lake Superior region (Woodruff et al. 2020).

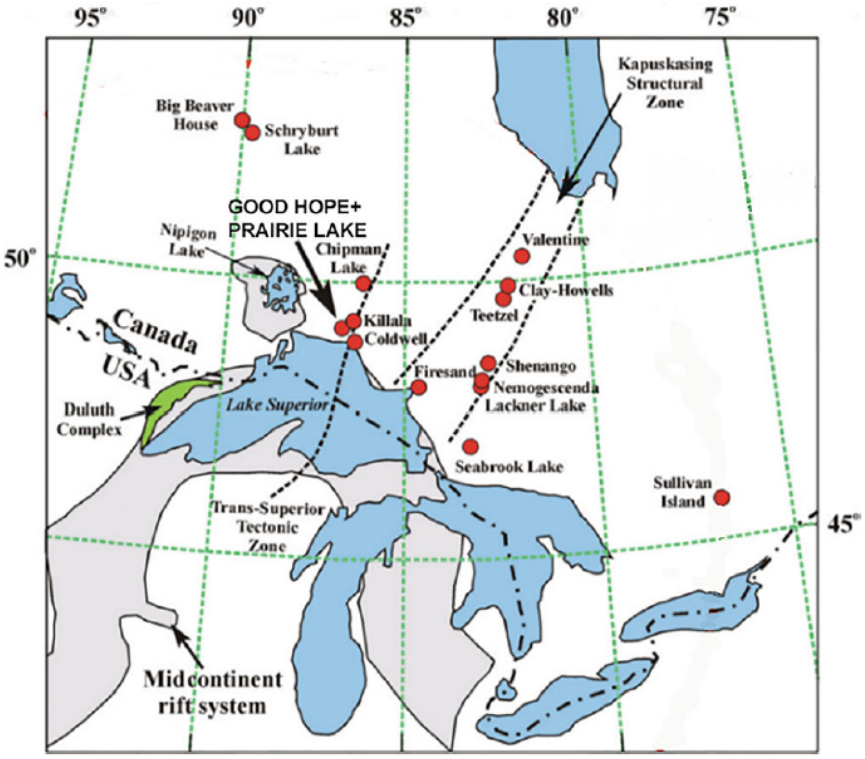

Figure 2.2: The location of the Good Hope carbonatite and Prairie Lake complex relative to the major structures and other carbonatitic and alkalic complexes in the area, from Mitchell et al. (2020).

The Plateau stage consists of extensional basin development that controlled the thickness of flood basalts with plutons and sills accompanying the volcanic eruptions. The Rift stage consists

of intermittent voluminous subaerial flood basalt eruptions with multiple sedimentary interflow conglomerate and sandstone units. The Late Rift stage sees the end of voluminous volcanism and subsidence within the central rift basin and an increase in deposition of coarse-grained conglomerates. Ernst and Bell (2010) suggest many of the carbonatites within the Superior Province are associated with either the 1880-1870 Ma Pan-Superior Large Igneous Province or the 1115 – 1085 Ma Keweenawan Large Igneous Province, which is proposed to be the driving force of the rifting of the failed Midcontinent Rift.

2.1 Prairie Lake Carbonatite Complex

The Prairie Lake carbonatite complex forms a circular topographic high to the southeast of the Good Hope carbonatite. The complex consists of a complexly interfingered sequence of arcuate to curvilinear bands of carbonatite and pyroxene-nepheline rocks of the ijolite series (melteigite – urtite) (Sage, 1987). These ijolite rocks are the dominant rock type within the core of the complex, with the carbonatite rocks prevalent towards the western periphery of the intrusion (Sage, 1987).

The approximate order of intrusion of these units is, (1) biotite pyroxenite and calcite carbonatite-(I), (2) ijolite series rocks, (3) potassic syenite rocks, (4) heterogeneous carbonatite-(II), and (5) dolomitic carbonatite (Figure 2.3). The biotite pyroxenite consists of modally diverse rocks of biotite + clinopyroxene ± calcite ± apatite, which are cut by numerous veins of coarse-grained calcite with rare apatite aggregates (calcite carbonatite-(I)) (Savard and Mitchell, 2021). The ijolite series rocks are modally heterogeneous on the meter-scale with varieties that include ijolite (nepheline + pyroxene) and mela-ijolite (pyroxene > nepheline + biotite + andradite-schlorlomitic garnet) (Savard and Mitchell, 2021). The potassic syenite rocks, also

termed malignite, consist of alkali feldspar + clinopyroxene + nepheline (Savard and Mitchell, 2021). The heterogeneous carbonatite-(II) rocks are the dominant carbonatites within the complex. They consist of four types, coarse-grained apatite-poor calcite carbonatite, olivine-apatite-magnetite calcite carbonatite with phoscorite (magnetite + apatite + olivine ± diopside ± perovskite ± pyrochlore), phlogopite-tetraferriphlogopite-magnetite-perovskite calcite carbonatite, and dolomite-calcite apatite carbonatite (Mitchell, unpub. data). These carbonatites are all re-equilibrated and represent cumulates that have been recrystallized and deformed (Mitchell, unpub. data).

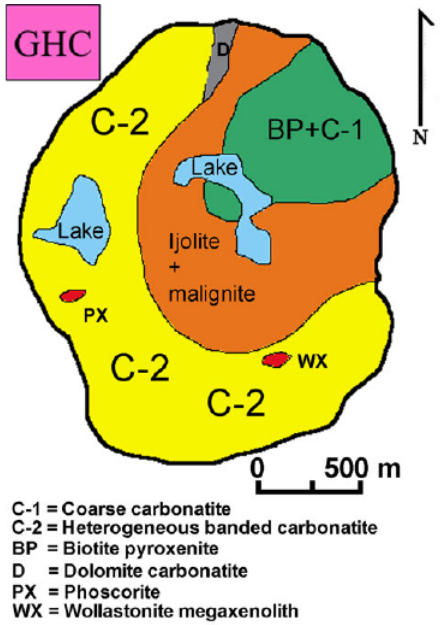

Figure 2.3: Simplified geological map of the major units in the Prairie Lake complex. From Mitchell et al. (2020).

Both the alkaline rocks and the carbonatites formed contemporaneously at ~1160 Ma (Wu et al., 2017). Initial Sr and Nd isotopic compositions indicate all the rock units are derived from the same parental magma, which is considered to have formed by partial melting of a weakly depleted ~3 Ga mantle source (Wu et al., 2017). Wu et al. (2017) suggested that the

Prairie Lake complex formed beneath a nephelinitic volcano, which Savard and Mitchell (2021) suggest involved a series of anastomosing channels that facilitated small batches of similar magma to evolve and crystallize in a different manner during emplacement. A variety of emplacement processes were considered active, including magma mixing, crystal settling and differentiation, solid-state deformation and re-equilibration, and deuteric alteration. A rare orbicular ijolite is present at Prairie Lake which consists of centimeter-scale orbicules composed of recrystallized ijolite set within a matrix of ijolite (Zurevinski and Mitchell, 2015). The formation of these orbicules is suggested to be due to a secondary pulse of ijolitic magma into partially crystallized ijolite melt (Zurevinski and Mitchell, 2015). This is consistent with the petrogenesis suggested by Wu et al. (2017) and Savard and Mitchell (2021) and is also consistent with the observations by Sage (1987), who observed at least three types of ijolite within the complex.

2.2 Good Hope carbonatite

Cleaver (2017) identified two phases of mineralization, a pyrochlore-rich and a pyrochlore-poor phase and characterized the main Nb mineralization to be Na-Ca pyrochlore. Mitchell et al. (2020) further characterized the Nb mineralization at Good Hope, indicating that much of the pyrochlore mineralization occurs within apatitite clasts rather than being disseminated throughout the carbonatite. Mitchell et al. (2020) describes the Good Hope carbonatite as a heterolithic breccia consisting of potassium feldspar ± magnesio-arfvedsonite ± phlogopite clasts, interpreted as fragments of consanguineous intrusions, and pyrochlore apatitite set in a diverse carbonatite matrix of dolomite and ferrodolomite together with calcite carbonatites and lesser hydrothermal carbonatites, including quartz fluorite carbonatites. The

apatitite clasts are texturally diverse and vary from folded clasts to elongated and boudinaged types to schlieren-like varieties that are composed of prismatic apatite that commonly exhibits undulose extinction (Mitchell et al., 2020). The pyrochlore apatitite clasts are interpreted to have formed with the pyrochlore crystallizing as the primary liquidus phase from a magma distinct from that of the apatite which crystallized rapidly as a primary liquidus phase as well. The transport of the apatite into the pyrochlore-bearing magma resulted in magma mixing and the mechanical incorporation of pyrochlore into the apatite. The lithified pyrochlore apatitite was subsequently disrupted by the intrusion of the carbonatite, which formed the clasts (Mitchell et al., 2020).

2.3 Exploration of the Good Hope Carbonatite

Prospector Rudy Wahl discovered niobium mineralization on the Good Hope property in 2010. He subsequently completed mapping and excavation of five trenches in the area in 2014. Exploration work included grab sampling, channel sampling, trenching, ground radiometric surveys, limited diamond drilling, and mineralogical studies. The first two diamond drill holes were drilled in 2016 for a total length of 280.7 m that targeted an airborne radiometric anomaly. The assay highlights from this first drill program included 0.45 % Nb_2O_5 and 6.25 % P_2O_5 over 1 m from drill hole PL-01 and 0.34 % Nb_2O_5 and 5.81 % P_2O_5 over 1 m from PL-02 (Plato Gold, 2018). Plato Gold Corp. optioned the property in 2017 and completed mapping and a due diligence program that confirmed previous results. Further work by Plato Gold Corp. completed 5016 m of drilling in 2018, with 9 holes ranging in length from 372 – 672 m. The assays for this drill program peaked at 0.950 % Nb_2O_5 and 6.20 % P_2O_5 over 1.1 m from drill hole PGH-18-06.

Chapter 3. Methods

Petrographic thin sections for this study were previously cut from drill core and surface samples selected by Dr. Roger H. Mitchell and carbon coated for optical microscopy, back-scattered electron (BSE) petrography, and energy dispersive x-ray spectrometry (EDS). The drill core samples were taken from drill holes PGH-18-01, DDH-02, DDH-03, DDH-04, PGH-18-06, PGH-18-07, PGH-18-08, DDH-07, DDH-08, and DDH-09. The locations of the 2018 drilling program are shown in Figure 3.1. Thirty of the petrographic thin sections were also selected for cathodoluminescence imaging and spectrometry on the basis of the observed optical textural variation of apatite.

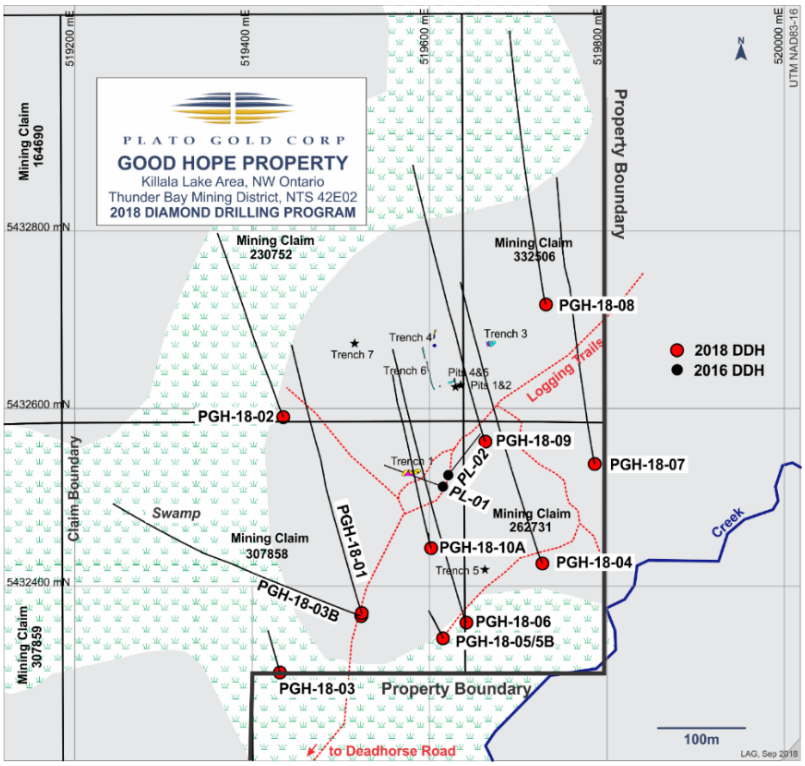

Figure 3.1: Property map of the Good Hope carbonatite that includes the location of the various drill holes and trenches where the samples were collected from for the petrographic thin sections (from Plato Gold Corp.).

3.1 Secondary Electron Microscopy - Energy Dispersive X-ray Spectrometry (SEM-EDS)

Back-scattered Secondary Electron (BSE) imaging and Energy Dispersive Spectrometry (EDS) were completed at Lakehead University using a Hitachi SU-70 scanning electron microscope. Analyses were completed using an accelerating voltage of 20 kV and a beam current of 300 pA. Compositional data were obtained using the attached Oxford AZtec 80 mm/124 eV energy dispersive x-ray spectrometer with a processing time of 60 seconds using a rastered area as opposed to a spot. The energy calibration of the system was completed using a nickel standard. The standards used were: jadeite (Na), periclase (Mg), corundum (Al), wollastonite (Ca), orthoclase (K), pyrophanite (Mn), tausonite (Sr), pyroxene (I.D. DJ35, Si), Mn-hortonolite (Fe), barite (Ba), fluorite (Ca, F), apatite (BM1926, Ca, P), thorite (Th), and synthetic REE phosphates (La, Ce, Pr, Nd, Sm, Gd, Dy, and Y).

3.2 Cathodoluminescence (CL) Imaging and Spectroscopy

Cathodoluminescence photomicrography was undertaken at the University of Manitoba, Winnipeg, Canada using a Reliotron Cathodoluminescence Instrument mounted on a Nikon Optiphot optical microscope. The imaging software used was NIS Elements F4.6. The floodgun of the cold cathode electron beam was set to a voltage of 9 kV with a current of 0.35 mA. The CL spectra for apatite was obtained at Queen's University, Kingston, Canada using a Reliotron Cathodoluminescence Instrument mounted on a Nikon Eclipse E400 POL microscope connected to an Ocean Optics Spectrometer. The electron beam was set to a voltage of 7 kV with a current of 0.6 mA.

Chapter 4. Mineralogy

4.1 Apatite

Apatite [$Ca_5(PO_4)_3(OH, F, Cl)$] at Good Hope is classified as fluorapatite, as the dominant anion is F. Apatite occurs in almost all the units in varying amounts, ranging from trace to 40 vol. % of the rock. It most commonly forms clasts composed of subhedral, randomly oriented prismatic crystals 100-to-500 μm in size, although some reach sizes longer than a millimeter in length. These crystals have a pill-like morphology as defined by Chakhmouradian et al. (2017). Bladed apatite, 50-to-200 μm in length, can form discrete clasts or occur within clasts with prismatic apatite (Figure 4.1a). These clasts are commonly elongate, forming sub-parallel bands at a millimeter-to-centimeter scale and rarely contain iron-oxide/hydroxide staining. These clasts may be disaggregated as seen in Figure 4.1b, where calcite is mantling euhedral-to-subhedral equant grains of apatite adjacent to the clasts of prismatic apatite within a ferroan dolomite groundmass. Figure 4.1c shows an apatite clast with fine-grained, bladed apatite, as well as larger, isolated grains that are subhedral-to-anhedral occurring interstitially in the calcite groundmass. The apatite shown in Figure 4.1c is also associated with acicular magnesio-arfvedsonite, which is observed in many samples. Isolated crystals of apatite, not associated with apatitite clasts are also present, occurring interstitial to the carbonate groundmass. They are commonly rounded and inconsistently associated with ferroan dolomite ± dolomite ± REE-fluorocarbonates (Figure 4.1d). The isolated, equant grains that are euhedral-to-subhedral are typically associated with quartz ± magnetite ± synchysite-(Ce), Figure 4.1 (e and f) shows this relationship, in these examples the equant apatite is mantled by magnetite and associated with synchysite-(Ce).

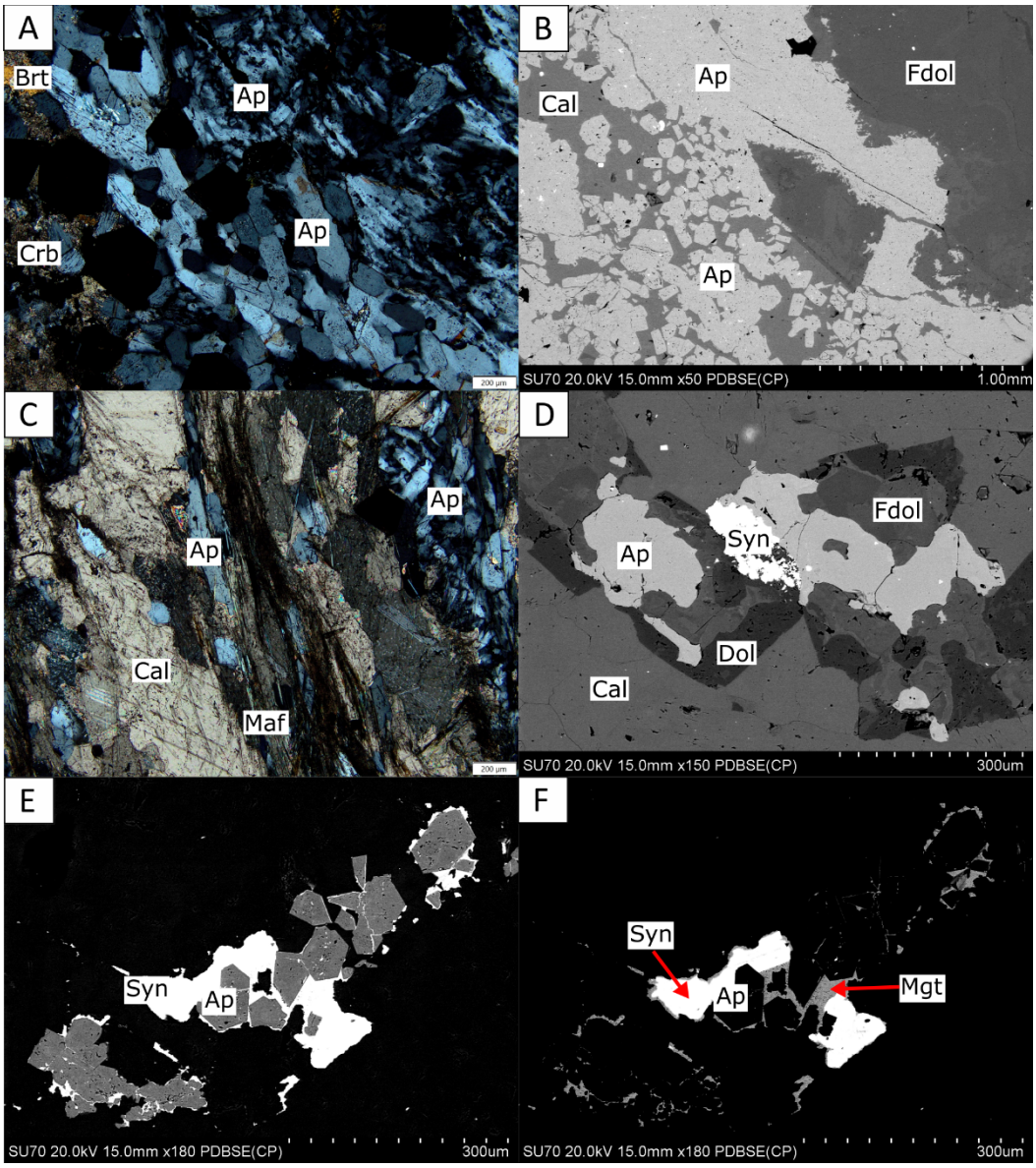

Figure 4.1: Photomicrographs of apatite in cross-polarized light (a) and (c) (scale bar in the bottom right is 200 µm) and BSE images (b), (d), (e), and (f). (a) medium-grained apatite that contains inclusions in the cores and clear rims and fine-grained apatite that is clear and more bladed (02-118). (b) an apatite clast within the ferroan dolomite groundmass, there is some interstitial calcite surrounding isolated, euhedral apatite grains (RHM-12). (c) aggregate- to- disseminated apatite within a calcite groundmass with associated needle-like magnesio-arfvedsonite (DDH-03-192). (d) associated apatite, zoned dolomite and ferroan dolomite within the calcite groundmass (02-45.78). (e) isolated, euhedral apatite surrounded by magnetite and synchysite-(Ce) (DDH-02-42). (f) the same area as Figure 4.1e with decreased brightness showing the magnetite mantling the isolated apatite and the synchysite-(Ce) grains (DDH-02-42). Abbreviations: apatite (Ap), barite (Brt), carbonate (Crb), ferroan dolomite (Fdol), calcite (Cal), magnesio-arfvedsonite (Maf), synchysite-(Ce) (Syn), dolomite (Dol), and magnetite (Mgt).

Compositional data for apatite from Good Hope was obtained from 126 EDS analyses and are presented in Appendix I. Representative compositions are presented in Table 4.1 with structural formulae calculated on the basis of twelve and a half atoms of oxygen. The compositional ranges are limited, with the major oxides varying only 4-to-7 wt. %; CaO (i.e., 49.7 – 56.6 wt. %) and P_2O_5 (i.e., 38.5 – 42.4 wt. %). These compositional variations result from the incorporation of Na, Si, Sr, and rare earth elements (REE) into the crystal structure. The apatite is poor in these elements with Na_2O ranging from below detection (b.d.)-to-1.4 wt. %, SiO_2 from b.d.-to-1.5 wt. %, SrO from b.d.-to-1.7 wt. %, and total rare earth elements including yttrium (TREY) from b.d.-to-4.1 wt. %. The apatite that contain REE are typically enriched in Nd, however Ce is the most enriched REE when La, Ce, and Nd are all present together. When Y is present it occurs in the highest concentrations relative to the other REE. La_2O_3 ranges from b.d.-to-0.4 wt. %, Ce_2O_3 from b.d.-to-1.4 wt. %, Nd_2O_3 from b.d.-to-1.2 wt. %, and Y_2O_3 from b.d.-to-2.6 wt. %. Most of the REE-bearing apatite occurs as the rims of isolated grains and as fine-grained aggregates associated with hydrothermal phases such as quartz, chlorite, and barite.

The apatite at Good Hope is rarely visibly zoned in BSE images but can contain patchy variation in composition that is typically consistent with variation in the Na ± REE. The patchy zoned apatite is commonly associated with magnetite ± chlorite ± quartz. Figure 4.2 shows an example of the rarely observed, distinctly zoned apatite. The cores of these grains are anhedral and embayed, containing ~41.0 wt. % P_2O_5, ~54.4 wt. % CaO, ~0.9 wt. % SrO, and variably exhibit replacement by magnetite. The inner rim is euhedral-to-subhedral and contains ~38.9 wt. % P_2O_5, ~50.5 wt. % CaO, ~0.8 wt. % SrO, and ~0.9 wt. % Na_2O, while the outer rim is

thinner, euhedral, containing ~40.9 wt. % P_2O_5, ~52.6 wt. % CaO, ~1.1 wt. % SrO, and ~0.3 wt. % Na_2O (Figure 4.2a).

Table 4.1: Representative compositions of apatite from Good Hope.

	DDH-07-103	DDH-04-37	DDH-04-37	DDH-08-13	DDH-04-34	02-260B	PGH-18-07-174
Wt. %							
Na_2O	-	0.31	-	0.19	-	0.24	0.55
Al_2O_3	-	-	-	-	-	-	-
SiO_2	-	-	-	0.31	1.22	-	0.10
P_2O_5	40.00	39.26	39.26	41.58	38.97	41.17	40.26
K_2O	-	-	-	-	-	-	-
CaO	56.58	55.24	55.53	55.26	53.40	54.41	52.57
FeO	-	-	0.17	-	-	-	-
SrO	0.86	0.88	-	0.40	1.59	0.91	0.59
Y_2O_3	-	-	-	0.39	-	-	-
La_2O_3	-	-	-	0.11	-	-	0.10
Ce_2O_3	-	-	-	0.26	0.53	-	0.75
Nd_2O_3	-	-	-	0.12	-	0.45	0.59
F	4.30	3.75	4.65	4.36	3.54	4.25	4.79
Total	**101.75**	**99.71**	**99.96**	**102.98**	**99.22**	**101.43**	**100.40**
-O=F	1.81	1.58	1.96	1.83	1.49	1.79	2.02
Total	**99.93**	**98.14**	**98.00**	**101.14**	**97.73**	**99.64**	**98.38**
Structural formulae calculated on the basis of 12.5 oxygen							
Na	-	0.05	-	0.03	-	0.04	0.10
Al	-	-	-	-	-	-	-
Si	-	-	-	0.03	0.11	-	0.01
P	3.05	3.03	3.07	3.10	2.99	3.12	3.14
K	-	-	-	-	-	-	-
Ca	5.45	5.39	5.49	5.21	5.19	5.22	5.18
Fe	-	-	0.01	-	-	-	-
Sr	0.04	0.05	-	0.02	0.08	0.05	0.03
Y	-	-	-	0.02	-	-	-
La	-	-	-	-	-	-	-
Ce	-	-	-	0.01	0.02	-	0.03
Nd	-	-	-	-	-	0.01	0.02
F	1.22	1.08	1.36	1.21	1.02	1.20	1.39
Cations	**8.54**	**8.52**	**8.58**	**8.43**	**8.40**	**8.44**	**8.51**

Dash (-) - indicates values are b.d. limits

The euhedral apatite, especially the distinctly zoned variety, are associated with quartz. Other euhedral apatite that lack zoning occur in calcite with associated magnetite ± synchysite-(Ce) (Figure 4.1e and f) ± barite ± calcite. The euhedral apatite that forms clasts can contain interstitial quartz, strontianite, or magnetite and are variably cut by veins of quartz, chlorite, calcite, and/or ferroan dolomite.

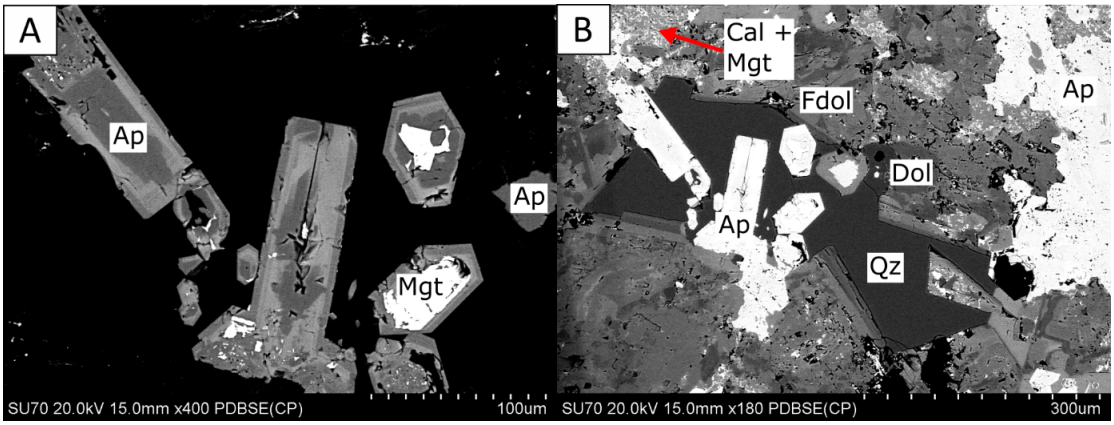

Figure 4.2: BSE images of apatite. (a) isolated, distinctly zoned, euhedral apatite with low Z compositions being Sr-rich and Na-poor and the high Z compositions being Sr-poor and Na-rich (PL-S1-P3-1). (b) the same area as figure 4.2a with increased brightness showing the relationship of the isolated, distinctly zoned, euhedral apatite with the interstitial quartz in irregularly zoned ferroan dolomite and dolomite with interstitial calcite + magnetite (PL-S1-P3-1). Abbreviations; apatite (Ap), magnetite (Mgt), quartz (Qz), ferroan dolomite (Fdol), dolomite (Dol), and calcite (Cal).

Further characterization using cathodoluminescence imaging shows that almost all apatite are zoned. Zoning not visible using BSE imagery, but distinct using CL imaging, suggests that the CL activators and thus the compositional variation in the zoning is due to variation in REE contents. Zonation is dominantly concentric with some of the cores containing patchy zonation that likely resulted from dissolution and subsequent reprecipitation of later apatite (Figure 4.3a). The concentric zonation is typically sharp with bands of variable thickness that can have several repetitions (Figure 4.3b), indicating physico-chemical conditions changed rapidly and multiple times. The sharp concentric zoned apatite are more commonly observed in

the apatitite clasts. The cores of the apatite typically exhibit green and/or orange-brown luminescence with the concentric zonation defined by alternating green and orange-pink luminescence that variably contains an outer rim that exhibits violet-blue luminescence. The CL spectrum (Figure 4.3d) contains large, complex peaks of Sm, Dy, and Pr emission (550-650 nm) that may also be influenced by minor Mn (600 nm) as well as a broad blue-green band of Dy and Eu^{2+} and/or Ce emission (400-500 nm) and Nd emission in the infrared (850-900 nm). The isolated apatite within the carbonatite typically contain a core that can show evidence for dissolution with infilled holes and embayed margins in contact with the rim composition (Figure 4.3c). The isolated apatite within the calcite groundmass typically exhibits green and orange-pink CL colours while the apatite associated with ferroan dolomite more commonly exhibits violet CL colours. The CL spectrum for the isolated crystals is strongly influenced by the Mn emission (600 nm) but exhibit similar peaks to the apatitite clast apatite (Figure 4.3d). Some of the apatite, typically fine-grained and associated with ferroan dolomite or late crystallizing phases such as quartz and/or chlorite, can contain no zonation and exhibit blue-violet CL colours (Figure 4.3e). The CL spectrum (Figure 4.3f) has strong Dy and Sm emission peaks together with Pr and Tb (550-650 nm) with little influence from Mn (600 nm). There is a strong Dy peak potentially with some Eu^{2+} and/or Ce that defines the broad blue band (400-500 nm) and a weak Nd emission peak in the infrared (850-900 nm). Mitchell (2014) defined two groups of blue luminescing apatite from carbonatites: (1) spectra lacking a broad blue band (Fen, Oka, Cargill) and (2) spectra with a distinct blue emission band (Howard Creek, Verity, Big Beaver House). Both spectra presented above, representative of the Good Hope apatite, would belong to group 2.

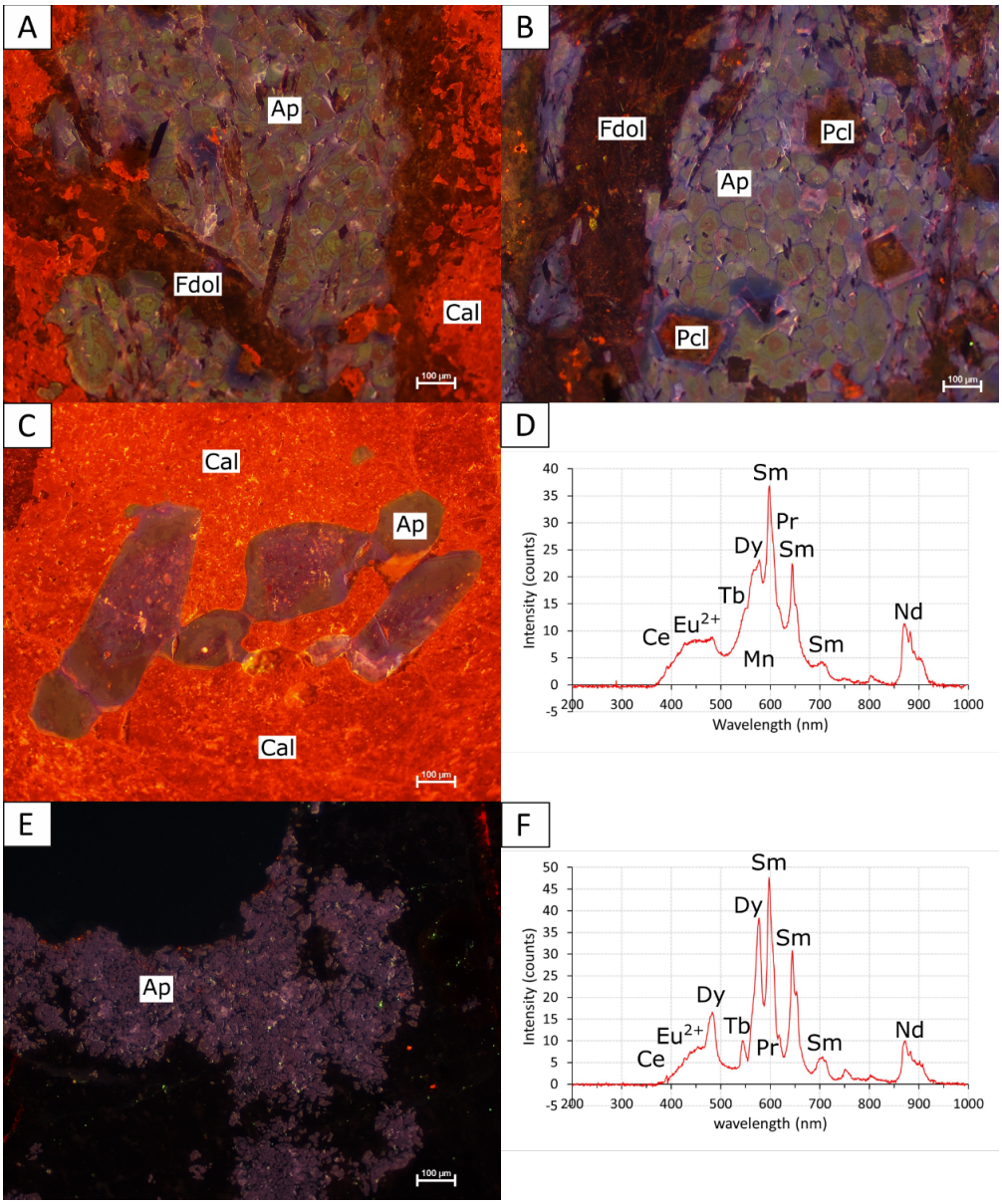

Figure 4.3: Cathodoluminescence images (a-c and e) and spectrum (d and f) of apatite from Good Hope. (a) concentric zoned apatite that contains orange-pink CL cores with holes filled by the later green CL apatite (DDH-04-608). (b) concentric zoned apatite that contains bands of variable thickness and multiple repetitions of green and orange-pink CL (DDH-09-457B). (c) isolated apatite that shows evidence of dissolution in the core with holes filled by the groundmass calcite (DDH-04-495). (d) CL spectrum from the apatitite clast that contains green and orange-pink luminescent distinctly zoned apatite (DDH-09-457B). (e) fine-grained apatite that has violet CL (DDH-08-13). (f) CL spectrum from the blue-violet indistinctly zoned apatite (DDH-08-13). Abbreviations; apatite (Ap), calcite (Cal), ferroan dolomite (Fdol), and pyrochlore (Pcl).

Mitchell (2014) also characterized the two groups by their Sm, Nd, Dy, Tb, and Mn peaks: (1) spectra with well-defined Sm and Nd peaks with minor Dy and Tb lines on a broad Mn band (Fen, Oka, Cargill), and (2) spectra with clearly defined Dy and Sm lines with insignificant Nd emission bands (Howard Creek, Verity, Big Beaver House). At Good Hope, the green and orange-pink distinctly zoned apatite would belong to group 1, while the blue-violet, indistinctly zoned apatite would belong to group 2. Some of the apatite in the apatitite clasts have pink luminescent apatite along the grain boundaries and/or within turbid cores of the apatite (Figure 4.4a). The CL spectrum (Figure 4.4b) shows stronger influence by Mn (600 nm) together with Sm and Dy emission peaks (550-650 nm) and a broad blue-green band (400-500 nm) that has emission peaks consistent with Dy and Eu^{2+} and/or Ce as well as a Nd emission peak in the infrared (850-900 nm). This spectrum is very similar to the spectrum from the apatitite clasts (Figure 4.1.3d) with the exception of the Mn band being more significant.

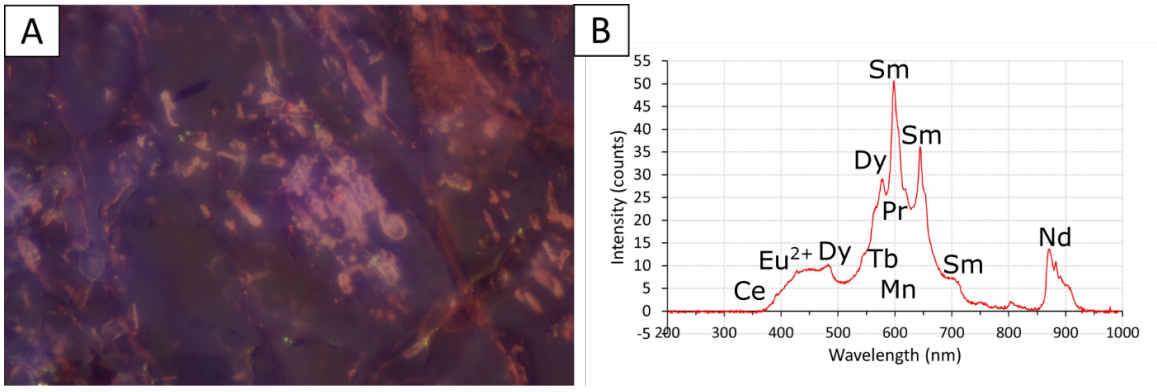

Figure 4.4: Cathodoluminescence image (a) and associated spectrum (b) from Good Hope apatite. (a) patchy green and violet luminescing apatite with turbid cores that contain pink luminescing apatite (PGH-18-07-650). (b) CL spectrum from (Figure 4.4a).

The fluorine contents range from 3.01-to-4.87 wt. %, which is greater than the theoretical amount calculated on stoichiometry that would estimate 3.77 wt. % fluorine. Excess

fluorine has been shown to be accommodated by the substitution (Binder and Troll, 1989; Yi et al., 2013):

$$(1) \quad (PO_4)^{3-} = (CO_3)^{2-} + F^-$$

that allows for at least 0.2 a.p.f.u. excess F, raising the amount of F to ~4.50 wt. % F in natural fluorapatites (Mason et al., 2009). The positive trend between P and F (Figure 4.5a) in the fluorapatites suggests this substitution is not dominant. Other substitutions suggested by Pan and Fleet (2002) include:

$$(2) \quad \square + M^+ = F^- + Ca^{2+}$$

$$(3) \quad X^{2-} + M^{3+} = F^- + Ca^{2+}$$

$$(4) \quad \square + ZO_4^{4-} = F^- + PO_4^{3-}$$

that are consistent with the positive trend between P and F as well as between Ca and F (Figure 4.5b). The excess F could also be analytical error as F can migrate under the electron beam.

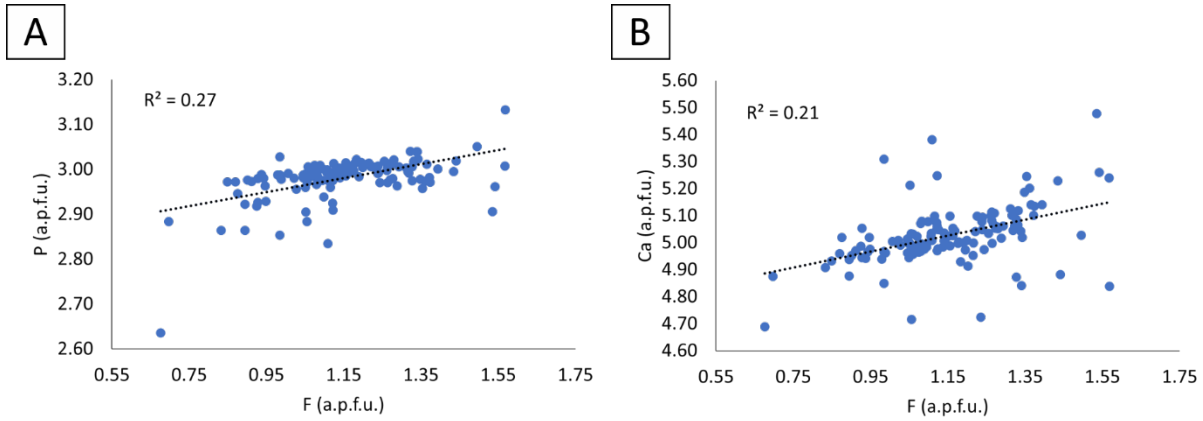

Figure 4.5: Bivariate plots of the apatite compositions from Good Hope; (a) P (a.p.f.u.) verses F (a.p.f.u.) that shows a positive trend but no correlation (R^2 = 0.27); and (b) Ca (a.p.f.u.) verses F (a.p.f.u.) that shows a positive trend but no correlation (R^2 = 0.21).

Substitution of the REE for Ca and P is shown by the negative correlation in the bivariate plot of Ca + P verses TREY (Figure 4.6a). The REE cannot substitute directly for either Ca or P

and require the addition of other elements for charge balance. Figure 4.6b shows the negative correlation of Na and Si with Ca, while there is no obvious trend between Sr and Ca. These elements substituting with the REE is confirmed by the positive correlation in the bivariate plot of Na verses TREY and Si verses TREY (Figure 4.6c). The bivariate plot against P shows only one defined negative correlation between Si and P (Figure 4.6d), which is consistent with the substitution (Roeder et al., 1987; Ronsbo, 1989; Hughes et al., 1991; and Pan and Fleet, 2002):

(5) $REE^{3+} + Si^{4+} = Ca^{2+} + P^{5+}$ (britholite component)

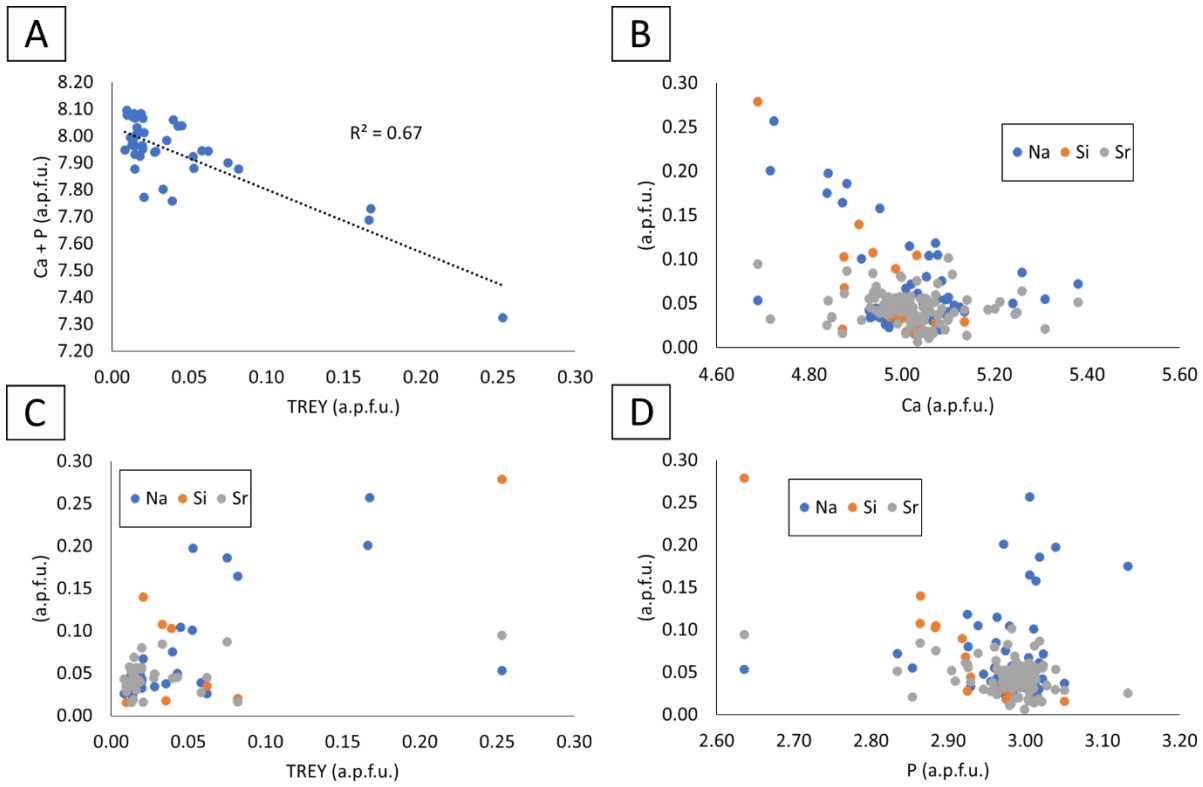

Figure 4.6: Bivariate plots of the apatite compositions from Good Hope; (a) Ca + P (a.p.f.u.) verses TREY (a.p.f.u.) that shows a negative relationship; (b) Na (a.p.f.u.) verses Ca (a.p.f.u.) (blue) that shows a negative relationship, Si (a.p.f.u.) verses Ca (a.p.f.u.) (orange) that shows a slight negative relationship, and Sr (a.p.f.u.) verses Ca (a.p.f.u.) (gray) that shows little correlation; (c) Na (a.p.f.u.) verses TREY (a.p.f.u.) (blue) that shows a positive relationship, Si (a.p.f.u.) verses TREY (a.p.f.u.) (orange) that shows a weak positive correlation, and Sr (a.p.f.u.) verses TREY (a.p.f.u.) (gray) that shows little correlation; and (d) Na (a.p.f.u.) (blue) and Sr (a.p.f.u.) (gray) verses P (a.p.f.u.) that show little to no correlation and Si (a.p.f.u.) verses P (a.p.f.u.) (orange) that shows a negative relationship.

Figure 4.7a, the bivariate plot of TREY + Si verses Ca + P, further supports the presence of this substitution in the fluorapatites. The correlation between Na and Ca (Figure 4.6b) indicates the presence of another substitution (Roeder et al., 1987; Ronsbo, 1989; Hughes et al., 1991; and Pan and Fleet, 2002):

$$(6) \qquad REE^{3+} + Na^{+} = 2Ca^{2+}$$

This substitution is supported by the negative correlation in the bivariate plot of Na + TREY verses Ca (Figure 4.7b).

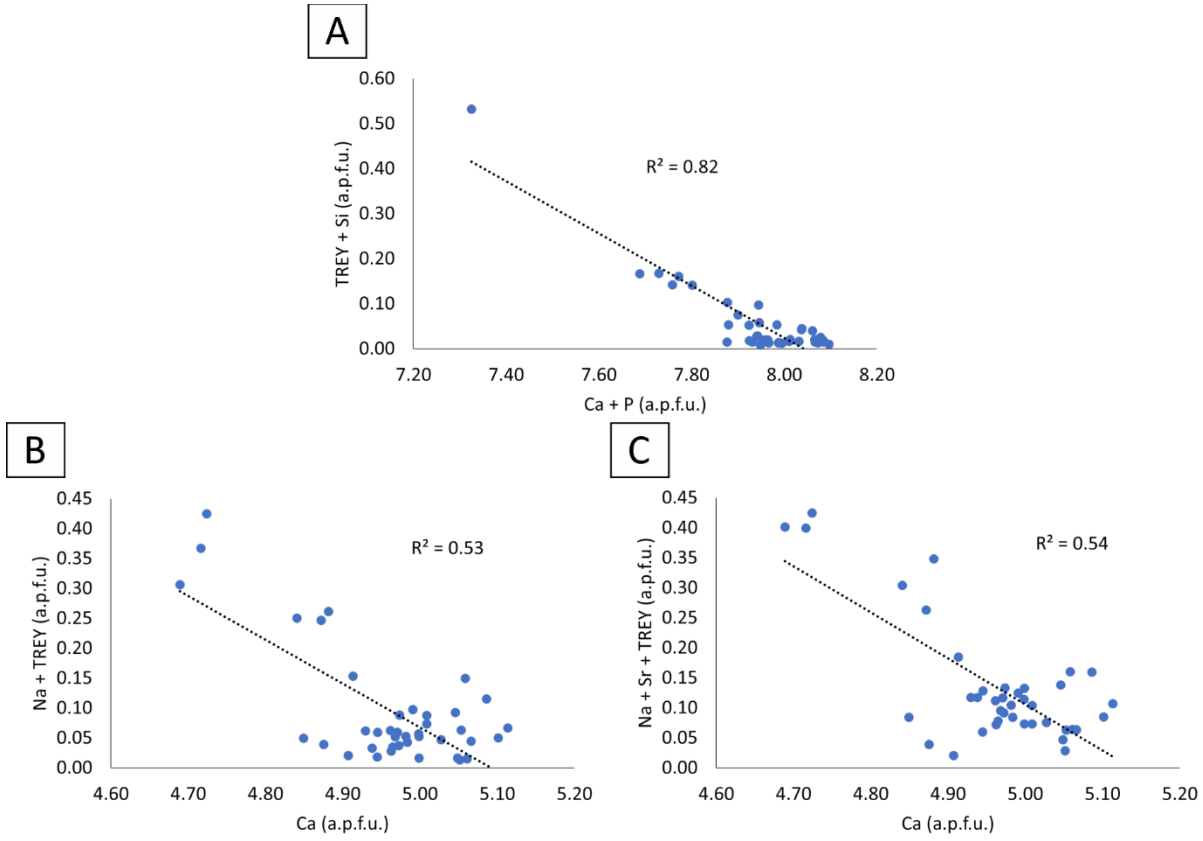

Figure 4.7: Bivariate plots of the apatite compositions that contain REY from Good Hope; (a) TREY + Si (a.p.f.u.) verses Ca + P (a.p.f.u.) that shows a negative correlation (R^2 = 0.82) with values concentrating at the high Ca + P end; (b) Na + TREY (a.p.f.u.) verses Ca (a.p.f.u.) that shows a moderate negative trend (R^2 = 0.53); and (c) Na + Sr + TREY (a.p.f.u.) verses Ca (a.p.f.u.) that shows a moderate negative trend (R^2 = 0.54).

The belovite substitution that includes Sr is also a possibility (Giebel et al., 2019):

$$(7) \qquad REE^{3+} + Na^{+} + 3Sr^{2+} = 5Ca^{2+}$$

Figure 4.7c shows the bivariate plot of TREY + Sr + Na verses Ca, which has a negative correlation, but is almost identical to the bivariate plot of Figure 4.7b, suggesting Sr does not play a major role in REE substitution in the fluorapatites.

4.2 Calcite

Calcite is the dominant carbonate within the Good Hope carbonatite complex, occurring in most samples, including the groundmass phase in the orbicular sample, ranging from trace amounts to 100 vol. %. The calcite is dominantly anhedral with embayed or serrated grain boundaries ranging in size from 100 µm-to-3 mm. The grain size can vary on a millimeter-scale with coarse-grained calcite and fine-grained calcite exhibiting well-defined contacts. Euhedral calcite is rarely observed and occurs intergrown with anhedral ferroan dolomite forming a centimeter-scale vein that cuts a silicate-rich carbonatite. Calcite can also occur with euhedral grain boundaries that extend into late phases, most commonly quartz (Figure 4.8a), but also synchysite-(Ce) and thorite. Calcite is typically a groundmass phase, which can be equant, elongated parallel to a preferred orientation, or elongate-to-skeletal in random orientation (Figure 4.8b). The calcite is inconsistently twinned, with twinned crystals adjacent to untwinned crystals (Figure 4.8c). The twins are typically thin, but thicker discontinuous twins are also observed (Figure 4.8d). The thicker twins commonly occur within the larger crystals.

Calcite also occur as isolated grains or clasts, typically within a ferroan dolomite groundmass (Figure 4.9a), but also within fluorite. Calcite occurs as clasts of: quartz +

strontianite + REE-fluorocarbonates; apatite + REE-fluorocarbonates; and quartz ± K-feldspar ± barite ± thorite ± synchysite-(Ce) (Figure 4.9b).

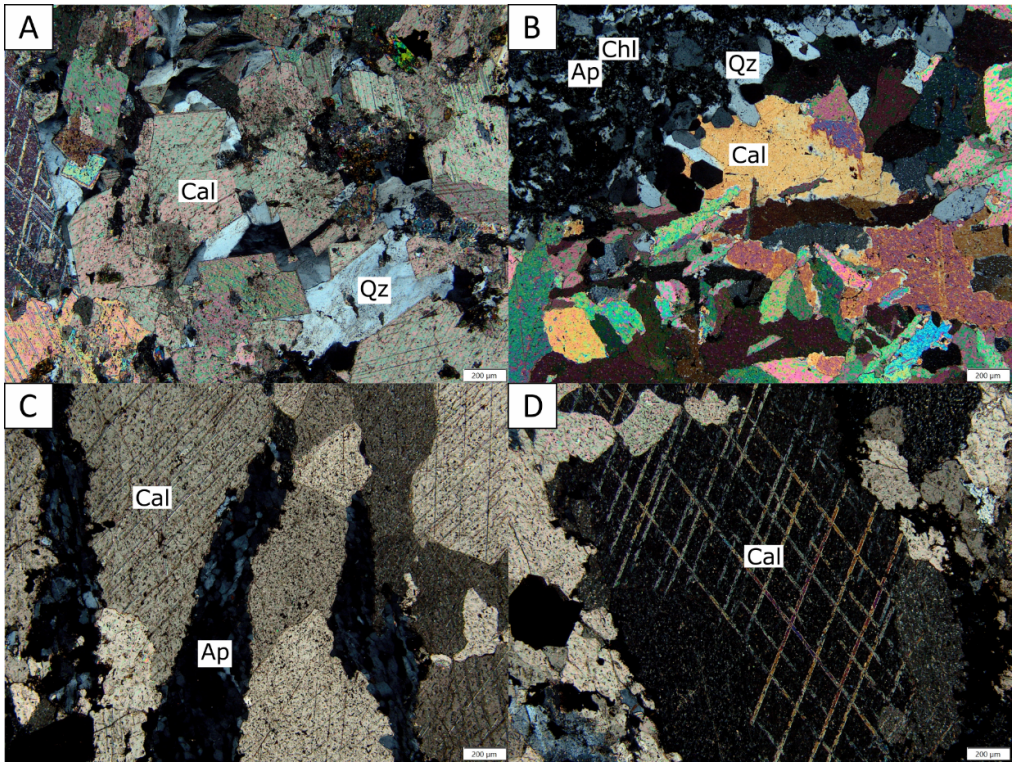

Figure 4.8: Photomicrographs in cross-polarized light of calcite from Good Hope (the scale bar in the bottom right is 200 µm). (a) Euhedral calcite associated with interstitial quartz (DDH-04-34). (b) Euhedral quartz extending into the elongate-to-skeletal calcite groundmass (RHM-07). (c) twinned calcite with thin twins adjacent to twin-free calcite (RW-PL-01). (d) thick, discontinuous twins in calcite (RW-PL-01). Abbreviations; calcite (Cal), quartz (Qz), chlorite (Chl), and apatite (Ap).

Calcite is rarely entrained in apatitite clasts, occurring as isolated grains, and associated with ferroan dolomite. Calcite variably contain microinclusions that are typically heterogeneously dispersed on a millimeter-scale (Figure 4.9c). These are typically exsolved strontianite or inclusions of magnetite, but also barite, REE-fluorocarbonates, or burbankite. The presence of anomalous Si peaks in some of the EDS analyses suggests there may also be micro inclusions of quartz. Calcite also commonly contains entrained grains of ferroan dolomite and apatite (Figure 4.9d).

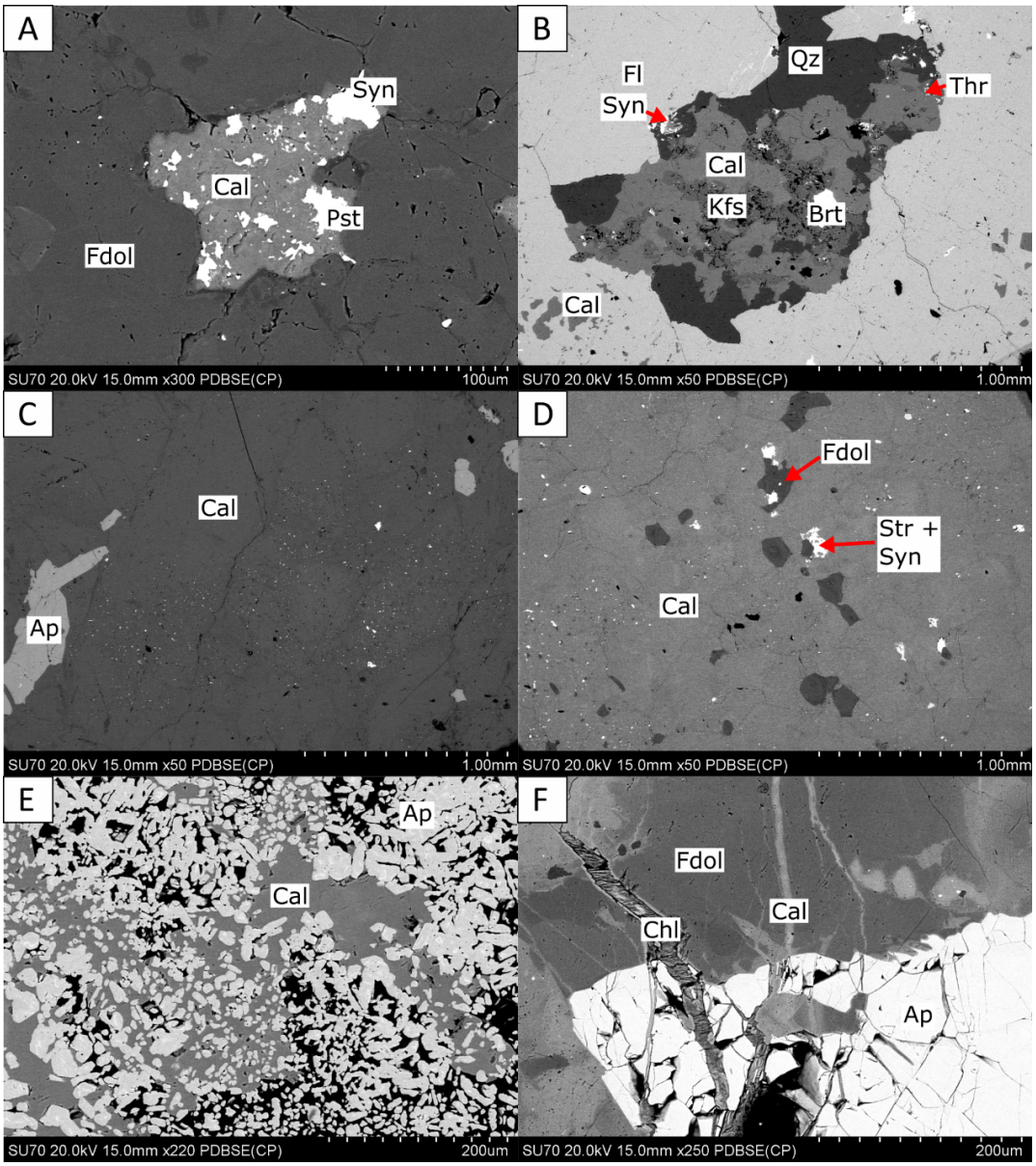

Figure 4.9: BSE images of calcite from Good Hope. (a) Intergrown calcite + synchysite-(Ce) + parisite-(Ce) forming interstitially in the ferroan dolomite groundmass (DDH-04-606). (b) Clast of calcite + orthoclase + quartz with isolated synchysite-(Ce), thorite, and barite within a fluorite clast (PL-S2-PI-1). (c) Calcite groundmass that contains isolated apatite and a variable amount and distribution of inclusions of burbankite, strontianite, and synchysite-(Ce) (DDH-03-192), (d) Groundmass calcite that contains isolated ferroan dolomite and variably dispersed inclusions of apatite, strontianite, burbankite, and synchysite-(Ce) (PGH-18-06-199). (e) Interstitial calcite surrounding subhedral-to-anhedral apatite, the black are just holes in the slide (DDH-08-13). (f) Margin of an apatite clast in a ferroan dolomite + siderite groundmass that is cut by veins of calcite and chlorite (PGH-18-06-199). Abbreviations; calcite (Cal), ferroan dolomite (Fdol), parisite-(Ce) (Pst), K-feldspar (Kfs), thorite (Thr), barite (Brt), fluorite (Fl), apatite (Ap), strontianite (Str), synchysite-(Ce) (Syn), and chlorite (Chl).

Inclusion-free calcite occurs interstitially in ferroan dolomite or within apatitite clasts and can be poikilitic with included grains of ferroan dolomite or apatite (Figure 4.9e). Calcite also forms veins that are observed crosscutting ferroan dolomite and apatite (Figure 4.9f). These veins are typically inclusion-free, but some do contain associated strontianite ± barite ± quartz.

Compositional data for calcite from Good Hope were obtained from 132 EDS analyses and are presented in Appendix I. Representative compositions are presented in Table 4.2 with structural formulae calculated on the basis of six atoms of oxygen.

Table 4.2: Representative compositions of calcite from Good Hope.

	RHM-07	**RHM-10**	**DDH-02-42**	**DDH-04-37**	**DDH-02-42**	**DDH-03-251**
Wt. %						
$MgCO_3$	-	0.88	-	-	-	0.36
$CaCO_3$	93.25	94.09	91.91	96.44	96.01	93.48
$MnCO_3$	5.63	1.30	1.04	-	-	-
$FeCO_3$	-	1.77	1.16	0.84	-	-
$SrCO_3$	-	0.91	-	0.83	-	1.48
Total	**98.89**	**98.95**	**94.11**	**98.11**	**96.01**	**95.32**
Structural formulae calculated on the basis of 6 oxygens						
Mg	-	0.06	-	-	-	0.07
Ca	5.70	5.74	5.88	5.92	6.00	5.77
Mn	0.30	0.07	0.06	-	-	0.03
Fe	-	0.09	0.06	0.04	-	0.07
Sr	-	0.04	-	0.03	-	0.06
Total	**6.00**	**6.00**	**6.00**	**6.00**	**6.00**	**6.00**

Dash (-) - indicates values are b.d. limits

The compositional ranges are limited, the major oxides vary; 49.2-to-54.3 wt. % CaO, b.d.-to-2.4 wt. % MgO, b.d.-to-3.8 wt. % MnO, b.d.-to-1.2 wt. % FeO, and b.d.-to-3.4 wt. % SrO. These

calcite by definition are Ca-rich, resulting in the compositions plotting in the 90 % a.p.f.u. Ca region of the ternary diagram Ca – Mg – Fe + Mn (Figure 4.10).

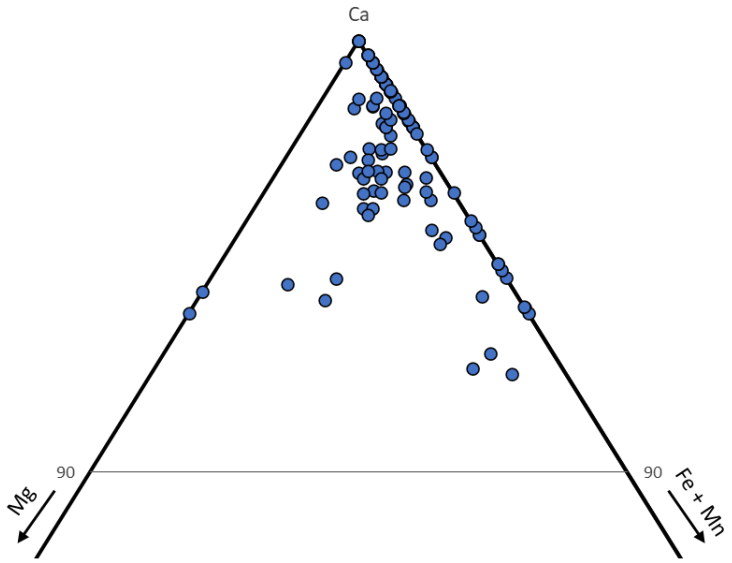

Figure 4.10: Ternary diagram Ca – Mg – Fe + Mn for the calcite compositions from Good Hope.

The variation in composition results from the substitution of Mg, Mn, Fe, or Sr for Ca. The majority of the calcite compositions contain substitution of one or more of the above oxides, however there are some that are pure $CaCO_3$. The substitution of Mg, Mn, Fe, and Sr for Ca is shown by the bivariate plot in Figure 4.11a, where calcite compositions have a strong negative correlation ($R^2 = 0.99$) indicating these are the dominant substituting cations. The trend shows a consistent rate of substitution with the variability being in the element being substituted. Figure 4.11b is the bivariate plot of Mg (a.p.f.u.), Mn (a.p.f.u.), Fe (a.p.f.u.), and Sr (a.p.f.u.) versus Ca (a.p.f.u.) that shows a shallow trend for the cation substitution for Ca as well as an increase in the substitution of Mn, Mg, and Sr for Ca at approximately 5.7 a.p.f.u. Ca.

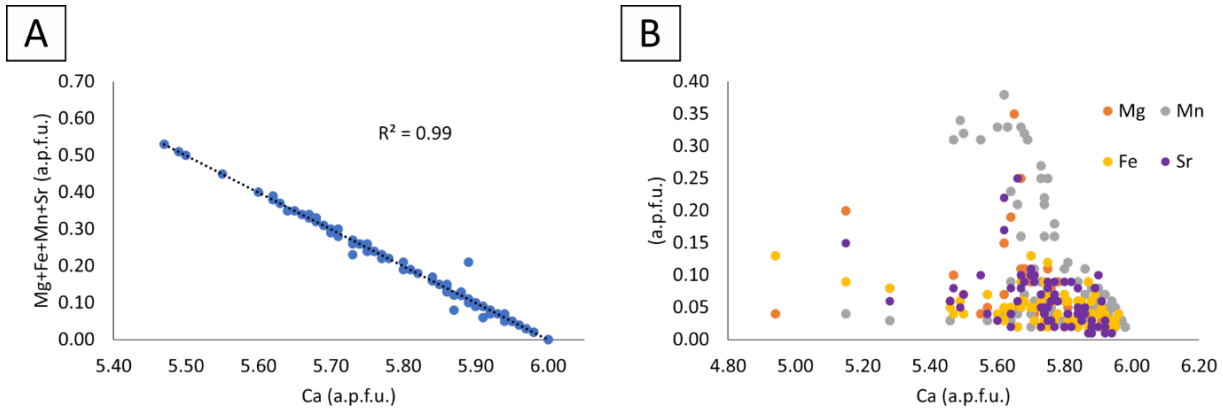

Figure 4.11: Bivariate plots of the calcite compositions from Good Hope; (a) Mg + Fe + Mn + Sr (a.p.f.u.) versus Ca (a.p.f.u.) showing a strong negative correlation (R^2 = 0.99) (b) Mg (a.p.f.u.) versus Ca (a.p.f.u.) (orange), Mn (a.p.f.u.) versus Ca (a.p.f.u.) (gray), Fe (a.p.f.u.) versus Ca (a.p.f.u.) (yellow), Sr (a.p.f.u.) versus Ca (a.p.f.u.) (purple), which shows a consistent shallow trend for the cation substitution for Ca and an increase in the substitution of Mn, Mg, and Sr at approximately 5.7 a.p.f.u. Ca.

Cathodoluminescence of calcite is dominantly bright orange due to Mn activation, indicating there is Mn present in the calcite at Good Hope, even if it is below detection in EDS analyses. Some of the calcite is not bright orange, likely due to the presence of Fe in the structure, as Fe quenches the luminescence (Figure 4.12a). The CL shows that the calcite can be patchy or concentrically zoned with variation in the brightness of the orange due to the amount of Fe and Mn substituting in the calcite structure. Concentric zoning is observed in the interstitial calcite (Figure 4.12b) whereas the patchy zonation is more commonly observed in the groundmass calcite (Figure 4.12c). The twins in the calcite tend to be brighter orange than the rest of the crystal, suggesting more Mn is present in the twins (Figure 4.12d).

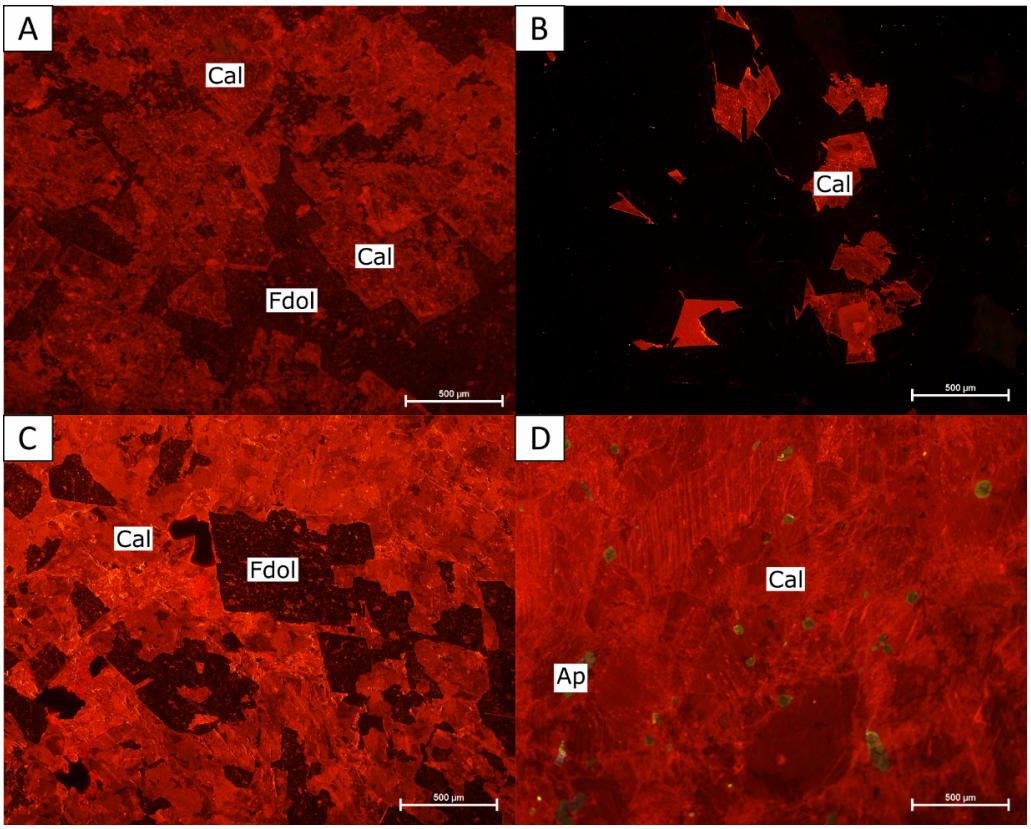

Figure 4.12: CL images of calcite from Good Hope. (a) euhedral calcite with orange CL with variable brightness (DDH-04-37). (b) concentrically zoned interstitial calcite (DDH-04-47A). (c) patchy zoned groundmass calcite (DDH-03-61). (d) twinned calcite, the twins have brighter CL than the crystals they occur in (RHM-09). Abbreviations; calcite (Cal), ferroan dolomite (Fdol), and apatite (Ap).

4.3 Ferroan Dolomite and Dolomite

The Mg-carbonate present is dominantly ferroan dolomite, and dolomite *sensu stricto* is only observed in zoned grains with variable Fe content. Calcite is the dominant carbonate, however ferroan dolomite can occur as a groundmass phase ranging from absence up to 80 vol. %. Ferroan dolomite is also observed in the calcite groundmass, in the syenite xenoliths, and in the orbicular sample. Groundmass ferroan dolomite is subhedral-to-anhedral ranging from 50 µm-to-2 mm in size and invariably contain patchy zonation. The grain size variation occurs on a millimeter-scale with the contacts commonly being well-defined (Figure 4.13a). The grain boundaries can be straight or embayed-to-bulging. The ferroan dolomite can contain twin

lamellae that commonly occur as thin twins within the granular crystals. There are also some thicker, discontinuous twin lamellae that occur within the larger grains (Figure 4.13b).

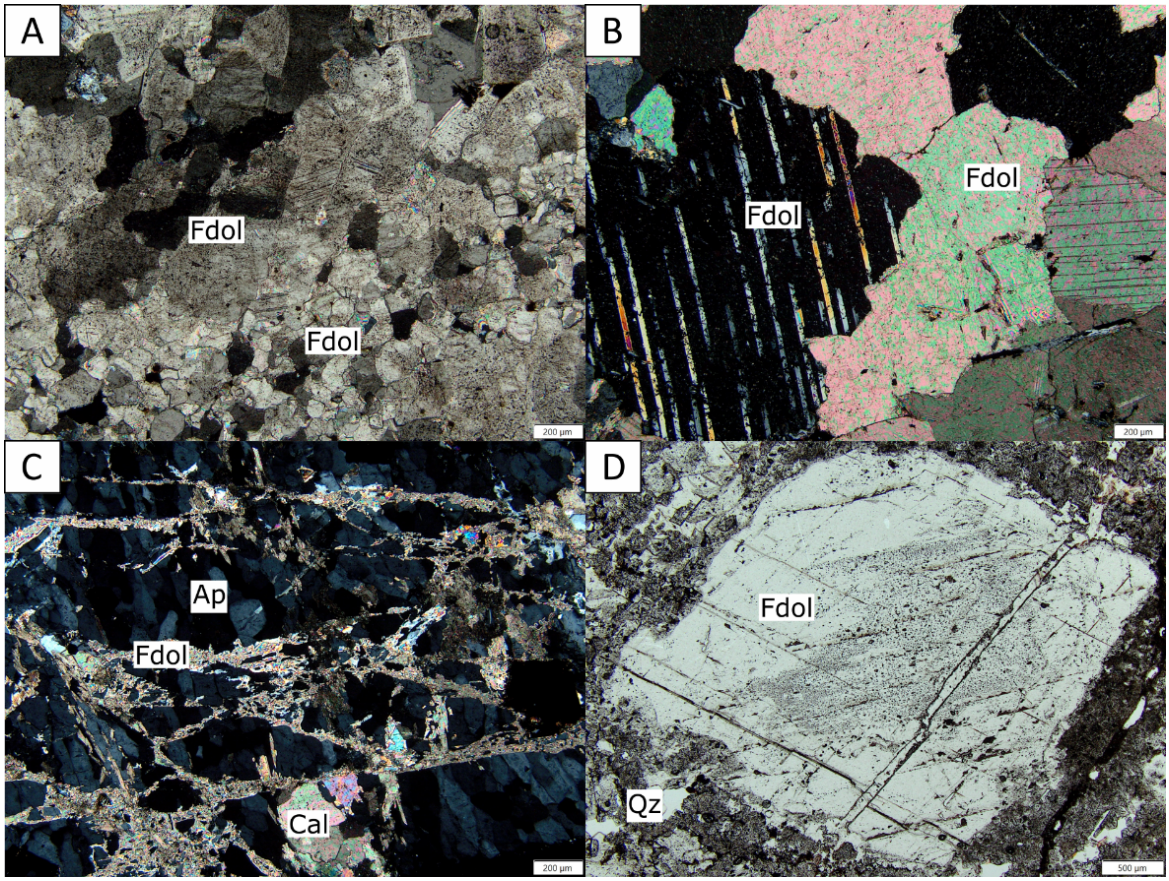

Figure 4.13: Photomicrographs in cross-polarized light (a), (b), and (c) (scale bar at the bottom right is 200 µm) and plane-polarized light (d) (scale bar at the bottom right is 500 µm) of ferroan dolomite from Good Hope. (a) shows the variation in grain size within the ferroan dolomite groundmass (DDH-04-666). (b) thick, discontinuous twin lamellae in a large ferroan dolomite crystal (RW-PL-06). (c) apatitite clast that is overgrown by dendritic ferroan dolomite (PGH-18-06-384). (d) antecryst of ferroan dolomite with heterogeneously dispersed inclusions that occurs within a groundmass of calcite + apatite + quartz (DDH-07-179). Abbreviations; ferroan dolomite (Fdol), apatite (Ap), calcite (Cal), and quartz (Qz).

There are several occurrences of ferroan dolomite intergrown with K-feldspar of similar size that form the groundmass to apatite aggregates. In feldspar-rich compositions, the ferroan dolomite can also occur intergrown with quartz and magnetite that are elongate with serrated grain boundaries. At the contact with ferroan dolomite, isolated grains of calcite can contain

spherulitic magnetite extending from the contact into the calcite. Ferroan dolomite can also occur in the calcite groundmass and in apatitite clasts as euhedral-to-anhedral crystals that are 25-to-200 µm in size. In apatitite clasts it can occur as dendritic crystals forming a web or aggregate texture that appears to be overgrowing the apatite (Figure 4.13c) and is also observed mantling apatitite clasts within the calcite groundmass. Ferroan dolomite occurs in clasts within the calcite groundmass commonly associated with apatite ± quartz ± magnetite ± strontianite ± REE-fluorocarbonates (Figure 4.14a). Ferroan dolomite can also form irregular veins that crosscut the calcite groundmass and apatitite clasts and commonly contain entrained crystals and clasts of the material it crosscuts. The ferroan dolomite contains euhedral grain boundaries more commonly than the calcite and occurs in contact with late crystallizing phases, including quartz ± apatite ± chlorite ± calcite ± REE-fluorocarbonates (Figure 4.14b). There are many occurrences of euhedral-to-subhedral ferroan dolomite that can be variably fractured and surrounded by interstitial ferroan dolomite that contains more Fe or calcite (Figure 4.14c). There are subhedral ferroan dolomite antecrysts, 3-to-6 mm in size, that contain entrained calcite and heterogeneously dispersed inclusions of burbankite, synchysite-(Ce), and magnetite that occur in a calcite + apatite + quartz groundmass (Figure 4.13d). The ferroan dolomite infrequently contain entrained calcite, barite, and siderite as well as heterogeneously dispersed inclusions, which in order of decreasing abundance are burbankite, strontianite, synchysite-(Ce), and magnetite.

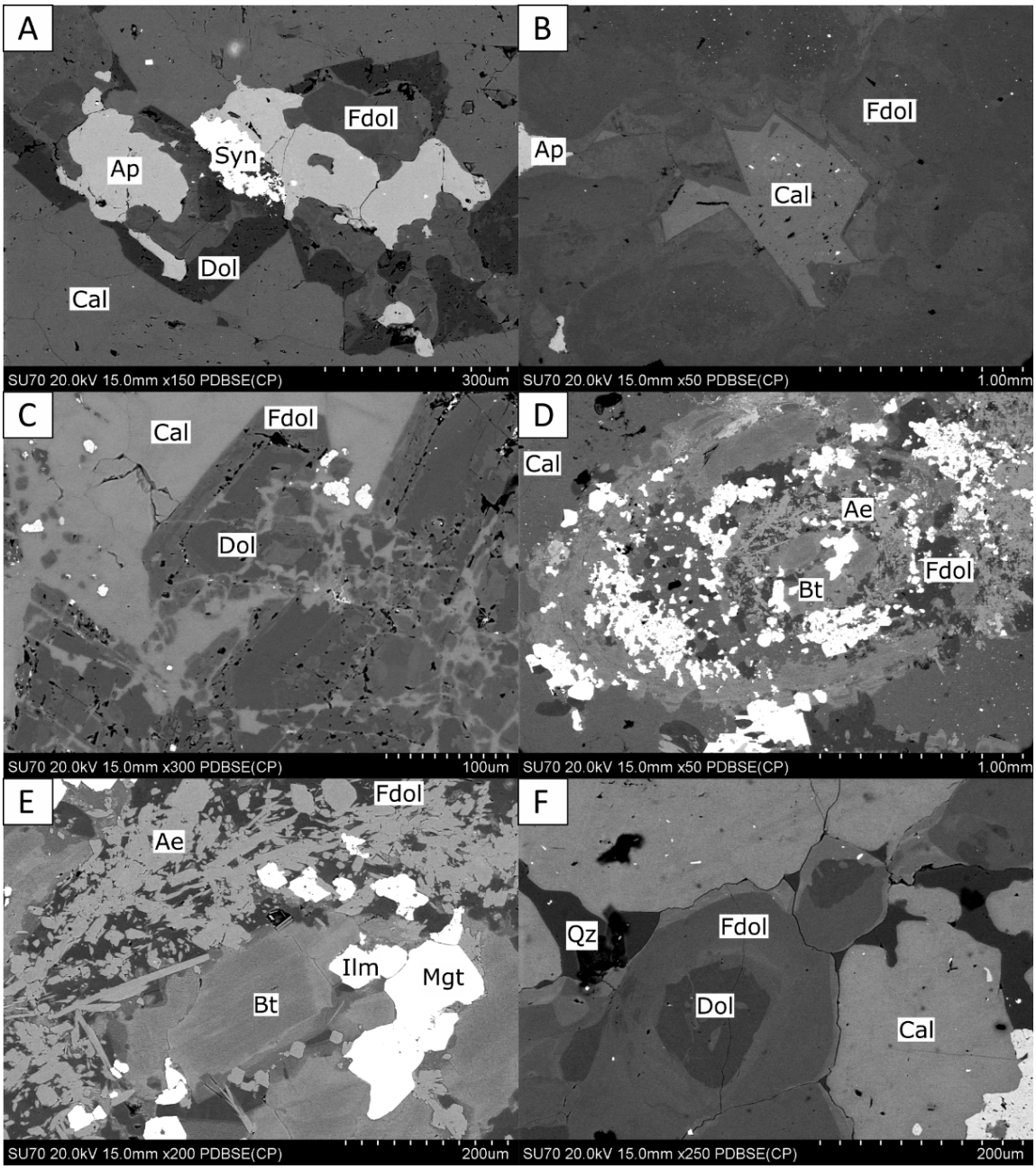

Figure 4.14: BSE images of dolomite from Good Hope. (a) zoned ferroan dolomite with associated apatite and synchysite-(Ce) within a calcite groundmass (02-45.78). (b) ferroan dolomite groundmass that contains euhedral grain boundaries extending into a clast of calcite ± apatite, the ferroan dolomite contains inclusions of burbankite and strontianite (RHM-12). (c) fractured, euhedral-to-subhedral dolomite grains with Fe-poor cores and Fe-rich rims that are entrained and infilled by interstitial calcite (PL-S2-PI-2). (d) orbicule with aegirine and ferroan dolomite intergrown in the inner rim and isolated ferroan dolomite in the calcite groundmass (PGH-18-06-416). (e) ferroan dolomite intergrown with aegirine in an orbicule (PGH-18-06-416). (f) anhedral zoned ferroan dolomite grains with an Fe-poor core and an Fe-rich rim with anhedral calcite grains and interstitial quartz showing the embayed-to-bulging grain boundaries (DDH-07-103). Abbreviations; ferroan dolomite (Fdol), dolomite (Dol), apatite (Ap), calcite (Cal), synchysite-(Ce) (Syn), aegirine (Ae), biotite (Bt), magnetite (Mgt), ilmenite (Ilm), and quartz (Qz).

Interstitial ferroan dolomite can occur in the syenite clasts associated with biotite, magnesio-arfvedsonite, and K-feldspar. Ferroan dolomite occurs along cleavage planes of some anhedral cores of biotite that form at the margin of the syenite clasts and occur intergrown with K-feldspar mantling isolated biotite. Ferroan dolomite is observed mantling calcite in contact with quartz, biotite, or magnesio-arfvedsonite and can be mantled by calcite in contact with chlorite. In the orbicular sample the ferroan dolomite typically occurs as isolated crystals within the calcite groundmass as well as forming within the orbicules (Figure 4.14d). In the orbicules the ferroan dolomite is commonly associated with aegirine in the rims of the orbicules (Figure 4.14e).

Dolomite commonly exhibits either concentric zoning or heterogeneous patchy zonation. Concentric zonation occurs in three typical ways: (1) ferroan dolomite core with a dolomite rim (Figure 4.14a); (2) dolomite core with a ferroan dolomite rim (Figure 4.14c and f); or (3) a dolomite core with a ferroan dolomite inner rim and a dolomite outer rim (Figure 4.14b). This zonation and variation in composition is not observed in the cathodoluminescence images because they all contain Fe, which quenches the luminescence causing the crystals to appear dark red-to-black (Figure 4.15a). As is observed in the calcite, the twinned ferroan dolomite contain twins that are brighter orange, indicating higher concentrations of Mn and lower concentrations of Fe in the twin lamellae (Figure 4.15b).

Compositional data for dolomite from Good Hope was obtained from 232 EDS analyses and are presented in Appendix I. Representative compositions are presented in Table 4.3 with structural formulae calculated on the basis of 6 atoms of oxygen. The compositional ranges vary with the MgO and FeO contents, and with the other major oxides having a limited range.

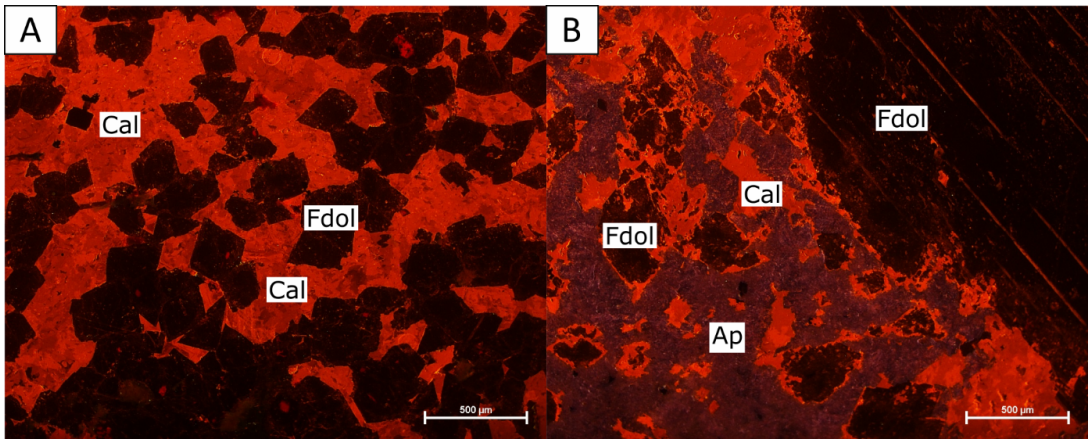

Figure 4.15: Cathodoluminescence images of ferroan dolomite from Good Hope. (a) euhedral-to-subhedral ferroan dolomite with dark red-to-black CL colours with interstitial calcite (DDH-04-171). (b) near black ferroan dolomite with orange twin lamellae adjacent to orange calcite and violet apatite (DDH-07-179). Abbreviations; ferroan dolomite (Fdol), calcite (Cal), and apatite (Ap).

MgO varies 5.3-to-19.2 wt. % and FeO varies 0.13-to-22.7 wt. %, while the other oxides vary;

27.2-to-33.9 wt. % CaO, b.d.-to-5.12 wt. % MnO, and b.d.-to-1.5 wt. % SrO.

Table 4.3: Representative compositions of ferroan dolomite and dolomite from Good Hope.

	DDH-07-103	DDH-04-177	DDH-04-37	DDH-03-251	DDH-03-192	PL-S2-PI
Wt. %						
$MgCO_3$	32.58	38.56	17.95	34.58	28.43	18.85
$CaCO_3$	53.31	54.14	52.74	53.45	57.12	49.58
$MnCO_3$	2.55	0.86	2.58	-	1.71	1.07
$FeCO_3$	12.31	2.62	27.47	10.53	14.31	29.77
$SrCO_3$	1.13	-	-	-	-	-
Total	**101.87**	**96.18**	**100.74**	**98.55**	**101.56**	**99.26**
Structural formulae calculated on the basis of 6 oxygens						
Mg	2.15	2.67	1.28	2.38	1.93	1.36
Ca	3.07	3.15	3.16	3.09	3.27	3.02
Mn	0.13	0.05	0.14	-	0.09	0.06
Fe	0.61	0.13	1.42	0.53	0.71	1.56
Sr	0.05	-	-	-	-	-
Total	**6.00**	**6.00**	**6.00**	**6.00**	**6.00**	**6.00**

Dash (-) - indicates values are b.d. limits

The restricted range in CaO for these dolomites results in them plotting in an approximately horizontal line in the ternary diagram CaO – MgO – Fe + Mn (Figure 4.16).

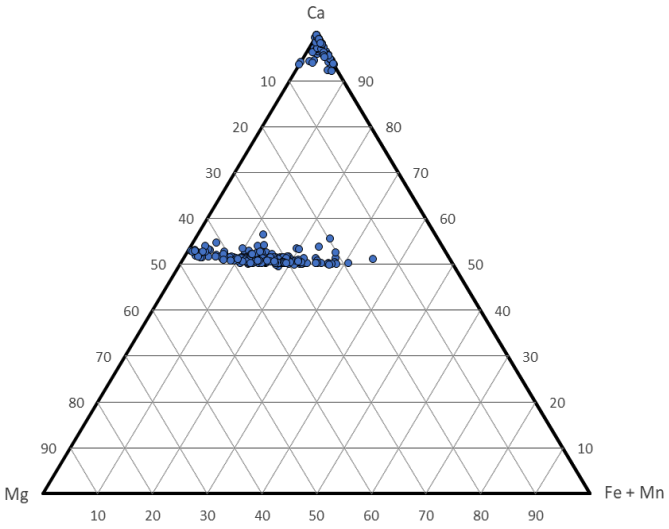

Figure 4.16: Ternary diagram Ca – Mg – (Fe + Mn) with the calcite, ferroan dolomite, and dolomite compositions from Good Hope.

Most of these compositions are ferroan dolomite and the dolomite *sensu stricto* always contains some Fe. Figure 4.17a shows a bivariate plot of Ca (a.p.f.u.) versus Mg (a.p.f.u.) in blue, Fe (a.p.f.u.) versus Mg (a.p.f.u.) in gray, Mn (a.p.f.u.) versus Mg (a.p.f.u.) in orange, and Sr (a.p.f.u.) versus Mg (a.p.f.u.) in yellow.

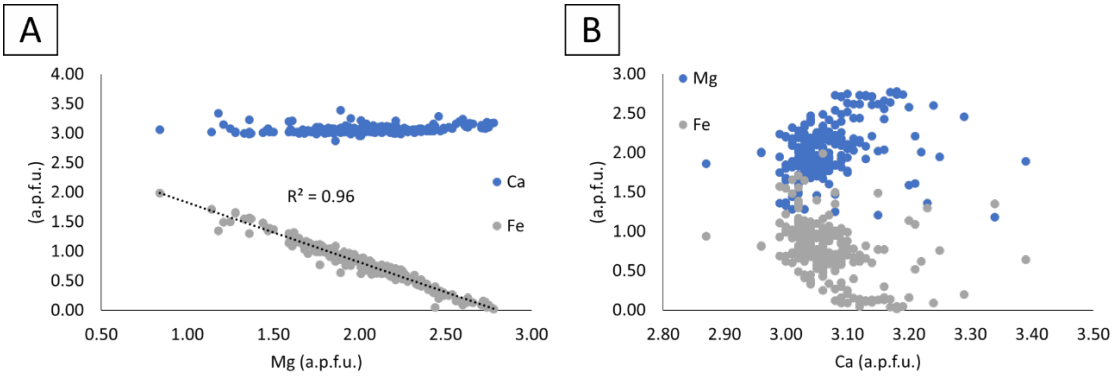

Figure 4.17: Bivariate plot of the dolomite compositions from Good Hope; (a) Ca (a.p.f.u.) (blue) versus Mg (a.p.f.u.) show little to no variation, while Fe (a.p.f.u.) versus Mg (a.p.f.u.) (Gray) shows a strong negative trend (R^2 = 0.96) ; and (b) Mg (a.p.f.u.) (blue) and Fe (a.p.f.u.) (gray) versus Ca (a.p.f.u.) that show a scatter with no obvious trends.

The consistent values for Ca suggest most of the substitution within the dolomite is for the Mg cation. The strong trend between Fe and Mg shown in Figure 4.17a indicates the dominant substitution is Fe for Mg. There is a very small amount of substitution of Mn and Sr for both Mg and Ca, however there are no distinct trends (Figure 4.17b).

4.4 Pyrochlore

Pyrochlore can comprise up to 10 vol. % of the rock, within or associated with, the apatitite clasts in addition to disaggregated clasts. The pyrochlore is subhedral-to-euhedral, ranging from 25-to-1000 µm in size. Within the apatitite clasts the pyrochlore is primarily euhedral, with subhedral pyrochlore occurring within, or adjacent to, carbonate (Figure 4.18a). Apatitite clasts with pyrochlore also commonly contain acicular magnesio-arfvedsonite (Figure 4.18b). Disseminated pyrochlore can also be associated with disaggregated apatitite within a groundmass of ferroan dolomite or calcite and tend to be variably fractured and subhedral. Although most commonly occurring with apatite, fine-grained pyrochlore is observed within the syenite xenoliths, associated with biotite and magnesio-arfvedsonite.

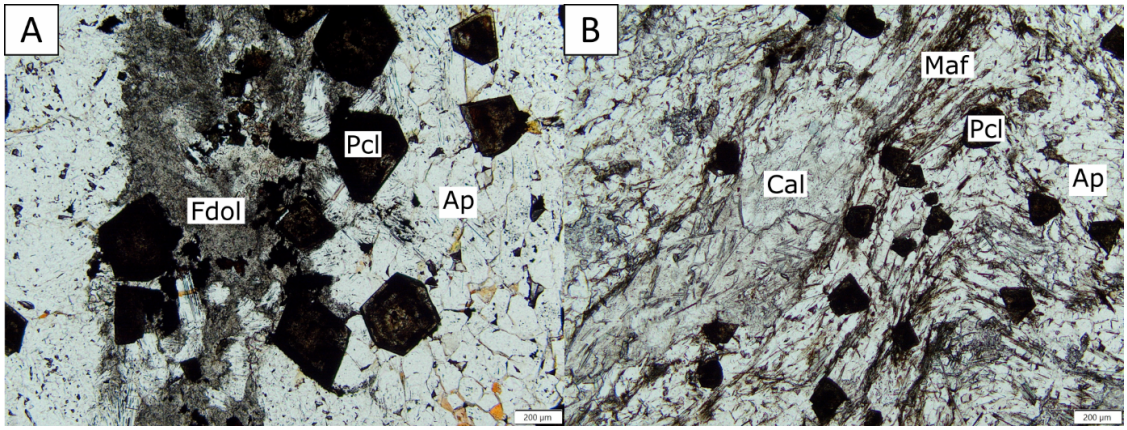

Figure 4.18: Photomicrographs in plane-polarized light of pyrochlore from Good Hope (scale bar at the bottom right is 200 µm). (a) Euhedral-to-subhedral pyrochlore within an apatitite clast that contains interstitial ferroan dolomite (02-118). (b) Euhedral pyrochlore within an apatitite clast with acicular magnesio-arfvedsonite (DDH-09-457B). Abbreviations; pyrochlore (Pcl), apatite (Ap), ferroan dolomite (Fdol), calcite (Cal), and magnesio-arfvedsonite (Maf).

Compositional data for pyrochlore from Good Hope were obtained from 55 EDS analyses and are presented in Appendix I. Representative compositions are presented in Table 4.4 with structural formulae normalized to 2 B-site cations. There is large variation within the major oxides, they vary b.d.-to-8.4 wt. % Na_2O, 3.9-to-17.4 wt. % CaO, 0.7-to-7.0 wt. % TiO_2, and 41.2-to-79.8 wt. % Nb_2O_5. Magmatic Ca-Na pyrochlore can be zoned, with only a slight variation in the Na, Ca, Ti, and Sr content within any grain. The zoning can be concentric (Figure 4.19a) but patchy zonation is more common (Figure 4.19b). The large compositional variation results from the replacement of the magmatic Ca-Na pyrochlore by fersmite or columbite-(Fe). This replacement results in the introduction of other cations, including SrO (range b.d.-to-9.9 wt. %), BaO (b.d.-to-7.0 wt. %), U (b.d.-to-7.9 wt. %), SiO_2 (b.d.-to-9.5 wt. %), FeO (b.d.-to-17.8 wt. %), and MnO (up to 11.4 wt. %). The fluorine content varies from b.d.-to-6.8 wt. % and the A-site vacancies from 0.0-to-1.2 per formula unit. Replacement to columbite-(Fe) is variably extensive and can vary within a single thin section with some fresh pyrochlore and others that are almost completely replaced (Figure 4.19c). Partial replacement by columbite-(Fe) can alter either the core (Figure 4.19d) or rim (Figure 4.19e) of pyrochlore, with the cores commonly being less pitted than rims. Pyrochlore is more prone to pitting when replaced by fersmite, which is typically patchy and variably extensive (Figure 4.19e). Figure 4.19(f) shows the fersmite alteration restricted to a thin ring within the pyrochlore that contains inclusions of magnesio-arfvedsonite and barite.

Table 4.4: Representative compositions of pyrochlore from Good Hope.

	DDH-03-192 Pcl	**RW-PL-02** Frs	**RW-PL-02** Frs	**02-260B** Clf	**02-260B** Frs	**DDH-03-251** Frs	**DDH-03-251** Clf	**PL-S1-P3-1** Pcl	**PGH-18-06-384** Frs
Wt. %									
Na_2O	7.71	5.53	4.69	-	1.28	2.32	1.55	6.51	0.55
CaO	16.08	15.27	12.88	7.74	3.96	13.77	5.41	14.24	9.74
MnO	-	1.78	4.80	-	-	-	1.27	-	0.92
SrO	1.04	1.17	0.35	-	7.69	1.97	-	2.46	-
BaO	-	-	-	1.97	7.04	-	1.47	1.17	1.40
FeO	-	0.68	2.19	15.10	2.71	-	17.53	-	6.35
Ce_2O_3	-	-	1.31	-	-	-	0.41	-	-
Nd_2O_3	-	-	0.82	-	-	-	0.76	-	1.34
UO_3	-	-	-	-	7.92	1.45	0.85	-	-
MgO	-	-	-	-	0.28	-	3.65	-	-
Al_2O_3	-	-	-	-	0.35	-	-	-	-
SiO_2	-	-	-	2.43	9.46	0.94	7.65	-	1.21
TiO_2	3.34	3.16	2.56	3.23	1.04	3.97	3.33	2.20	2.84
Nb_2O_5	70.02	70.61	66.41	55.04	41.18	68.21	52.06	69.40	69.38
Ta_2O_5	-	-	-	-	3.14	-	-	-	-
F	6.27	-	-	-	-	3.76	-	4.88	-
-O=F	2.64	-	-	-	-	1.58	-	2.05	-
Total	**101.81**	**98.20**	**96.01**	**85.51**	**86.05**	**94.81**	**95.94**	**98.81**	**93.73**

Dash (-) - indicates values are b.d. limits

	DDH-03-192 Pcl	**RW-PL-02** Frs	**RW-PL-02** Frs	**02-260B** Clf	**02-260B** Frs	**DDH-03-251** Frs	**DDH-03-251** Clf	**PL-S1-P3-1** Pcl	**PGH-18-06-384** Frs
Structural formula normalized to 2 B-site cations									
Na	0.88	0.63	0.57	-	0.16	0.26	0.15	0.76	0.06
Ca	1.01	0.95	0.86	0.56	0.28	0.85	0.30	0.92	0.60
Mn	-	0.09	0.25	-	-	-	0.05	-	0.04
Sr	0.04	0.04	0.01	-	0.29	0.07	-	0.09	-
Ba	-	-	-	0.05	0.18	-	0.03	0.03	0.03
Fe	-	0.03	0.11	0.85	0.15	-	0.74	-	0.31
Ce	-	-	0.03	-	-	-	0.01	-	-
Nd	-	-	0.02	-	-	-	0.01	-	0.03
U	-	-	-	-	0.11	0.02	0.01	-	-
A-Site Total	**1.92**	**1.74**	**1.86**	**1.46**	**1.17**	**1.19**	**1.31**	**1.80**	**1.07**
A-Site Vacancy	0.08	0.26	0.14	0.54	0.83	0.81	0.69	0.20	0.93
Mg	-	-	-	-	0.03	-	0.28	-	-
Al	-	-	-	-	0.03	-	-	-	-
Si	-	-	-	0.16	0.62	0.05	0.39	-	0.07
Ti	0.15	0.14	0.12	0.16	0.05	0.17	0.13	0.10	0.12
Nb	1.85	1.86	1.88	1.67	1.22	1.77	1.20	1.90	1.81
Ta	-	-	-	-	0.06	-	-	-	-
B-Site Total	**2.00**	**2.00**	**2.00**	**2.00**	**2.00**	**2.00**	**2.00**	**2.00**	**2.00**
F	1.16	-	-	-	-	0.68	-	0.93	-

Dash (-) - indicates values are b.d. limits

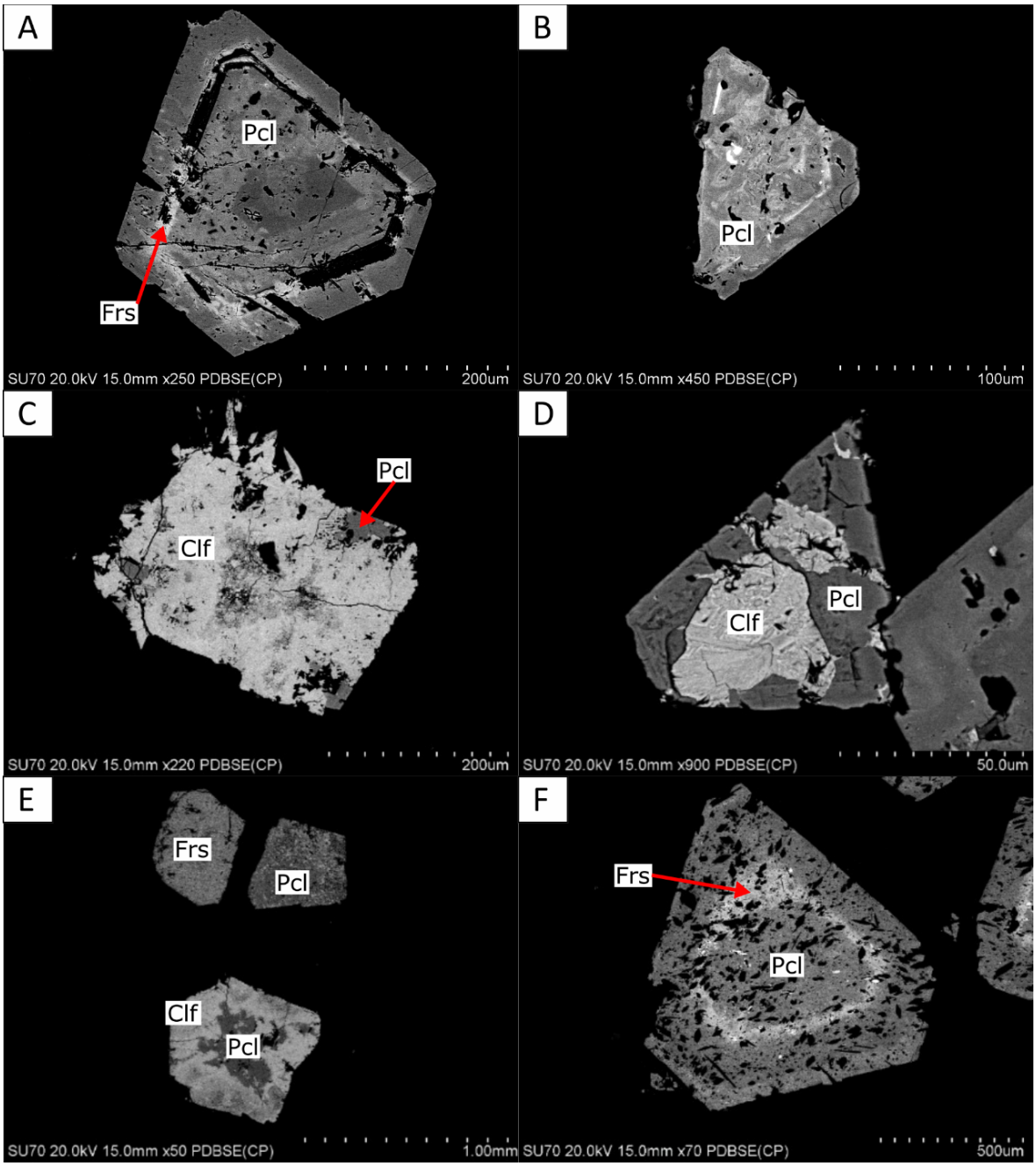

Figure 4.19: BSE images of pyrochlore from Good Hope. (a) concentric zoned pyrochlore with slightly higher Sr and Ti in the inner rim (02-118). (b) patchy zoned pyrochlore with brighter areas containing higher Sr content (DDH-04-541A). (c) pyrochlore that is almost completely replaced by the brighter columbite-(Fe) (RW-PL-06). (d) Subhedral pyrochlore with a columbite-(Fe) core (PGH-18-06-384). (e) Anhedral pyrochlore at the top of the image with patchy replacement by fersmite and the subhedral grain at the bottom of the image has a core of pyrochlore and a replacement rim of columbite-(Fe) (Pl-S1-P3-1). (f) pyrochlore with inclusions of magnesio-arfvedsonite and barite that contains a thin ring of fersmite alteration (brighter composition) (DDH-04-541A). Abbreviations; pyrochlore (Pcl), fersmite (Frs), and columbite-(Fe) (Clf).

All compositions plot in the pyrochlore field of the ternary diagram Ti – Nb – Ta (Figure 4.20) and almost all along the Nb – Ti join, with only two compositions containing Ta_2O_5 (b.d.-to-3.14 wt. %). The REE content is low with a few altered pyrochlore containing Ce_2O_3 and Nd_2O_3 in similar amounts (b.d.-to-1.9 wt. %).

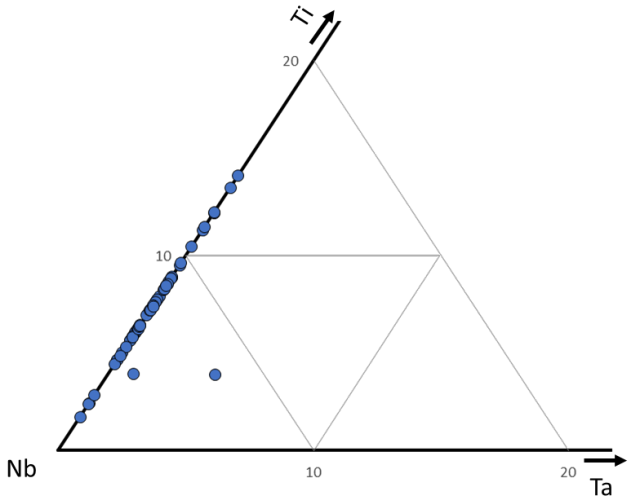

Figure 4.20: Ternary diagram with apices Ti – Nb – Ta showing the Good Hope pyrochlore compositions.

The general formula for pyrochlore is $A_2B_2X_6Y$, where A = Na, Ca, Mn, Sr, Ba, REE, and U; B = Nb, Ti, Ta, and Al; X = O and OH; and Y = O, OH, and F. Possible cation substitutions for pyrochlore in calciocarbonatite are discussed by Viladkar and Sorokhtina (2021) and include,

(1) $Na^{+} + REE^{3+} = 2Ca^{2+}$ (Ti and Nb constant)

(2) $REE^{3+} + Ti^{4+} = Ca^{2+} + Nb^{5+}$ (Na constant)

(3) $REE^{3+} + 2Ti^{4+} = Na^{+} + 2Nb^{5+}$ (Ca constant)

(4) $Ca^{2+} + Ti^{4+} = Na^{+} + Nb^{5+}$ (REE constant)

The ternary diagram REE – Ti – Na (Figure 4.21) shows the majority of the pyrochlore plot on the Ti – Na join suggesting that substitution (4) is the dominant substitution ($Ca^{2+} + Ti^{4+} = Na^{+} + Nb^{5+}$ (REE constant)).

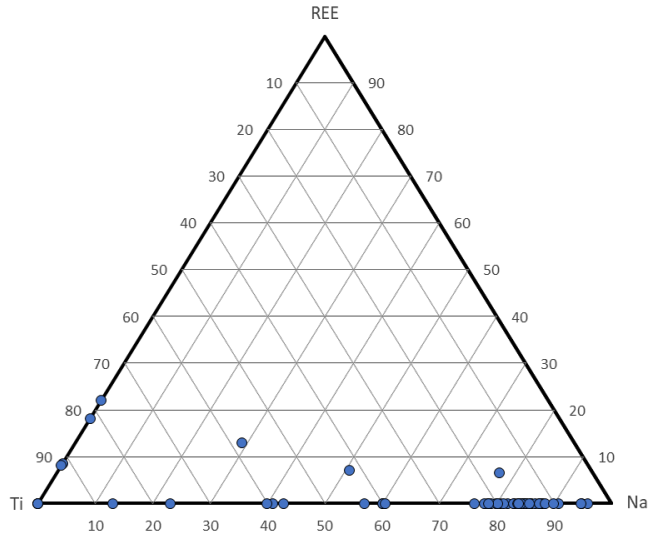

Figure 4.21: Ternary diagram REE – Ti – Na (a.p.f.u.) for the Good Hope pyrochlore.

The ternary diagram A-Vacancy – Ca – Na (Figure 4.22) shows magmatic pyrochlore that plot close to the Ca – Na join and the altered compositions plotting with increased A-vacancies. Alteration of pyrochlore trends towards a Na-poor pyrochlore, with an ideal formula of (Ca, A-vac)$_2$Nb$_2$O$_6$Y-vac (with vacancies in the A-site and Y-site).

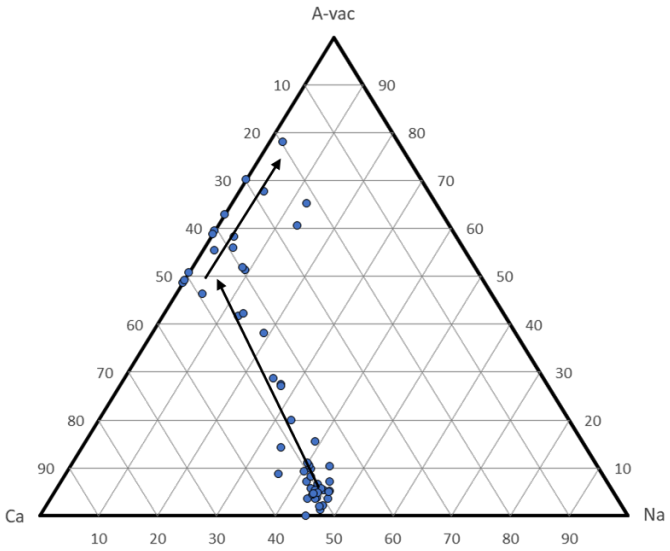

Figure 4.22: Ternary diagram A-vacancy – Ca – Na (a.p.f.u.) with the pyrochlore compositions from Good Hope that shows two trends, one where the A-vacancies are accommodated by a loss of Na and the second where the A-vacancies are accommodated by a loss of Ca.

Figure 4.23(a) shows a bivariate plot of F (a.p.f.u.) versus Na (a.p.f.u.) with a positive correlation (R^2 =0.84) consistent with the substitution (Dey et al., 2021):

(5) $Na^+ + F^- = A\text{-}Vac + Y\text{-}Vac$

Figure 4.23(b) shows a bivariate plot of A-Vacancy (a.p.f.u.) versus Na (a.p.f.u.) that shows a strong correlation (R^2 = 0.95), consistent with substitution (5). Some of the compositions contain more than just one vacancy p.f.u. suggesting another substitution involving the loss of Ca is also active:

(6) $Ca^{2+} + O^{2-} = A\text{-}Vac + Y\text{-}Vac$

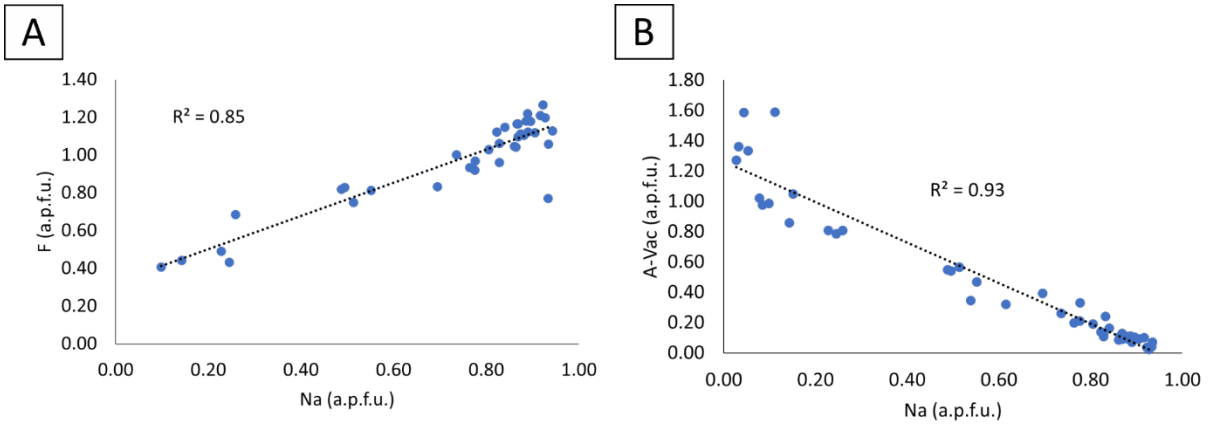

Figure 4.23: Pyrochlore compositions from Good Hope. (a) Bivariate plot of F (a.p.f.u.) versus Na (a.p.f.u.) showing a positive correlation (R^2 = 0.85). (b) Bivariate plot of A-Vacancy (a.p.f.u.) versus Na (a.p.f.u.) showing a strong negative correlation (R^2 = 0.93).

Figure 4.24 shows a bivariate plot of A-Vacancy (a.p.f.u.) versus Ca (a.p.f.u.) that displays a moderate negative correlation (R^2 = 0.57), supporting substitution (6) being active but not the dominant substitution introducing vacancies. Substitutions (5) and (6) that produce A-vacancies can be active in both hydrothermal and supergene settings. The two trends in the ternary A-vac – Na – Ca indicate that Na is preferentially lost prior to Ca with further alteration that could be either hydrothermal or supergene. Altered pyrochlore are observed in samples from drill core

and surface, suggesting they were all altered in the same type of environment, most likely hydrothermal and independent of location within the complex.

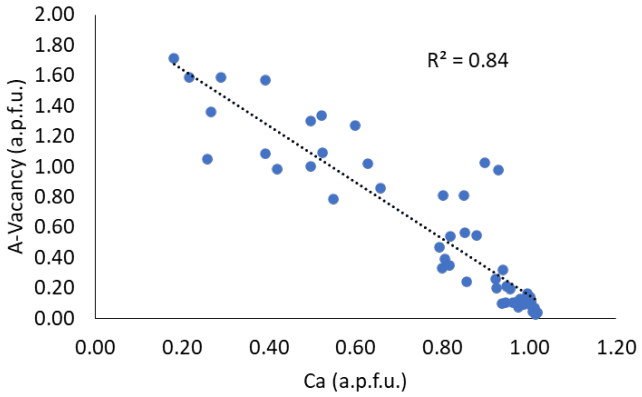

Figure 4.24: Pyrochlore compositions from Good Hope plotted in the bivariate plot of A-Vacancy (a.p.f.u.) versus Ca (a.p.f.u.) showing a negative correlation (R^2 = 0.84).

4.5 Feldspar

The feldspar within the Good Hope carbonatite is mostly K-feldspar, with lesser albite and trace hyalophane. The K-feldspar is a major component of the syenite clasts, where it is moderately-to-extensively replaced by iron oxide/hydroxide overgrowths (Figure 4.25a). It also occurs as disaggregated clasts within the carbonatite and as isolated grains that are moderately replaced by iron oxide/hydroxide overgrowths (Figure 4.25b). These grains are typically subhedral-to-anhedral and range in size from 50-to-500 µm. It is more common for the K-feldspar to occur within the ferroan dolomite carbonatite although it is also observed within the calcite carbonatite. Albite is observed in the calcite carbonatite (Figure 4.25c) and in the syenite clasts typically with inclusions of hyalophane. The feldspar are rarely twinned and do not exhibit any perthitic textures. There are a few occurrences of very coarse-grained K-feldspar (2 mm) that occur within a ferroan dolomite carbonatite that exhibit a spherulitic texture along their rims (Figure 4.25d).

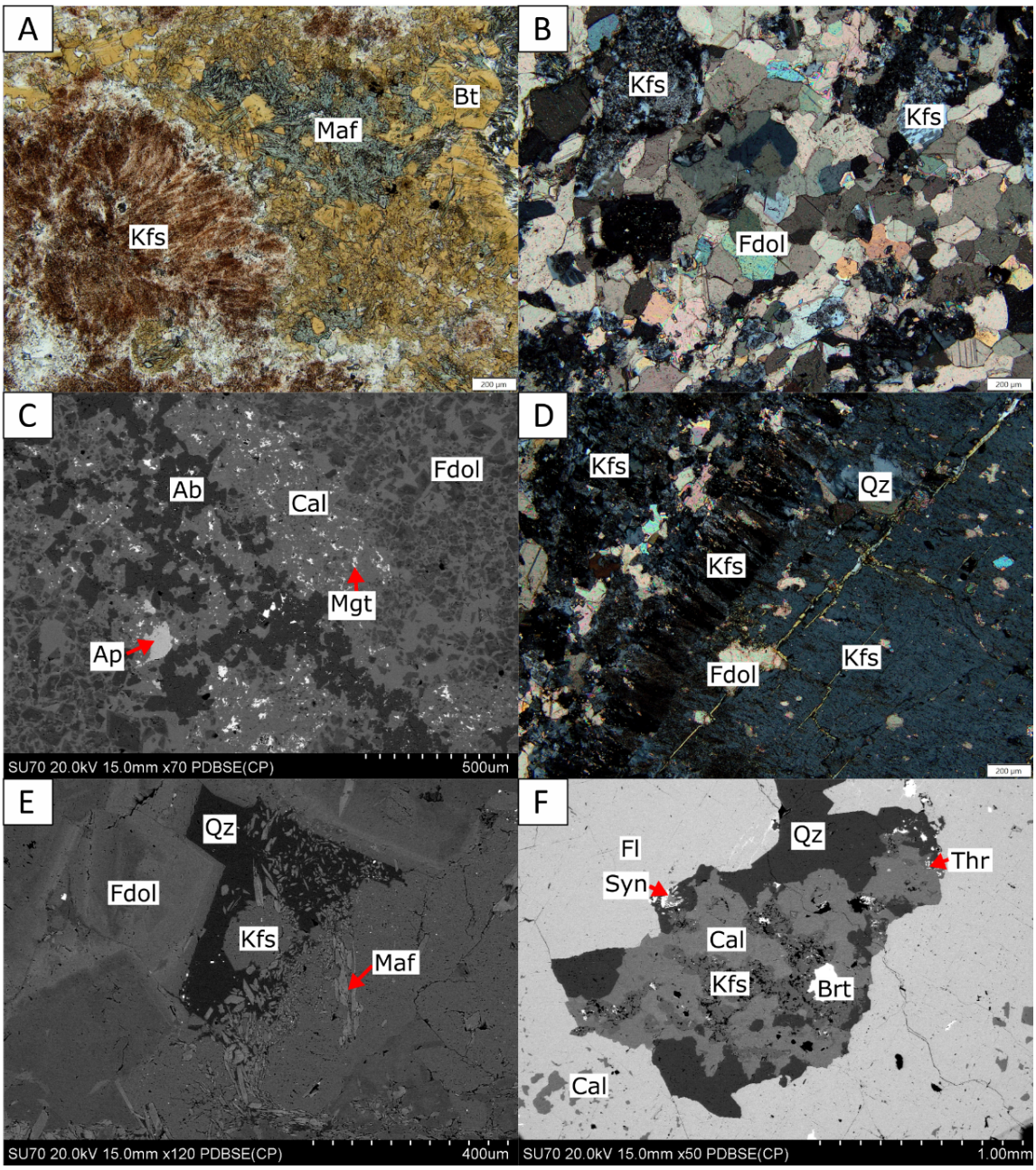

Figure 4.25: Photomicrographs of feldspar in plane-polarized light (a) and cross-polarized light (b) and (d) (scale bar in the bottom right is 200 µm) and BSE images (c), (e) and (f). (a) syenite clast that contains coarse-grained K-feldspar and intergrown biotite and magnesio-arfvedsonite (DDH-04-177). (b) isolated K-feldspar that is moderately replaced within a ferroan dolomite groundmass (DDH-04-606). (c) intergrown albite and calcite with isolated magnetite (PL-S2-PI-2). (d) coarse-grained K-feldspar with a spherulitic rim of K-feldspar (RW-PL-06). (e) complex intergrowth of K-feldspar and magnesio-arfvedsonite (DDH-04-606). (f) clast of K-feldspar + calcite + quartz within a fluorite groundmass (PL-S2-PI-1). Abbreviations; K-feldspar (Kfs), biotite (Bt), magnesio-arfvedsonite (Maf), ferroan dolomite (Fdol), albite (Ab), calcite (Cal), magnetite (Mgt), apatite (Ap), quartz (Qz), synchysite-(Ce) (Syn), thorite (Thr), barite (Brt), and fluorite (Fl).

The K-feldspar can contain inclusions of barite and the albite can contain inclusions of strontianite and REE-fluorocarbonates and are commonly associated with other silicate phases when disaggregated in the carbonatite. Figure 4.25e shows a complex intergrowth of K-feldspar with magnesio-arfvedsonite in the ferroan dolomite groundmass. K-feldspar is the predominant phase within the syenite clasts and also occurs along the cleavage planes of the biotite. Albite occurs as isolated grains within the syenite clasts adjacent and within the K-feldspar. Within a fluorite-rich sample K-feldspar forms a clast with calcite + quartz + REE-fluorocarbonates + thorite + barite (Figure 4.25f). Rutile is a common phase observed in the feldspar-rich carbonatites, including a W-bearing rutile that occurs within a K-feldspar groundmass.

Compositional data for feldspar from Good Hope was obtained from 36 EDS analyses and is presented in Appendix I. Representative compositions are presented in Table 4.5 with structural formulae calculated on the basis of eight atoms of oxygen. The compositional ranges are limited. K-feldspar has major oxides ranging from 17.3-to-18.2 wt. % (Al_2O_3), 61.8-to-64.9 wt. % (SiO_2), and 16-to-16.6 wt. % (K_2O). There are trace amounts of Na_2O, CaO, Fe_2O_3, and BaO that ranges from b.d.-to-1.39 wt. %. In the hyalophane compositions the BaO contents range up to 13.9 wt. %. Albite has major oxides that range from 8.6-to-11.9 wt. % (Na_2O), 13.6-to-19.4 wt. % (Al_2O_3), and 65.9-to-75.7 wt. % (SiO_2). There are trace amounts of K_2O, CaO, and Fe_2O_3 that range from b.d.-to-0.5 wt. %. The albite compositions plot in a tight cluster at the albite apex of the K-feldspar – albite – anorthite ternary diagram (mol %) (Figure 4.26). The K-feldspar compositions dominantly plot along the albite – K-feldspar join with up to 10 mol % albite with only a few compositions that contain up to 10 mol % anorthite (Figure 4.27).

Table 4.5: Representative compositions of feldspar from Good Hope.

	DDH-04-37 (Kfs)	**PL-S2-PI-2** (Ab)	**DDH-04-177** (Hyn)
Wt. %			
Na_2O	0.16	11.63	-
Al_2O_3	17.71	19.00	21.26
SiO_2	64.35	68.36	54.88
K_2O	16.17	-	11.06
CaO	-	0.06	-
Fe_2O_3	0.54	0.13	0.61
BaO	-	-	13.88
Total	**98.93**	**99.18**	**101.69**
Structural formulae calculated on the basis of 8 oxygens			
Na	0.01	0.99	-
Al	0.98	0.99	1.10
Si	3.01	3.01	2.41
K	0.96	-	0.62
Ca	-	-	-
Fe^{3+}	0.02	-	0.02
Ba	-	-	1.19
Total	**4.98**	**4.99**	**5.34**

Kfs (K-feldspar), Ab (albite), Hyn (hyalophane)
Dash (-) - indicates values are b.d. limits

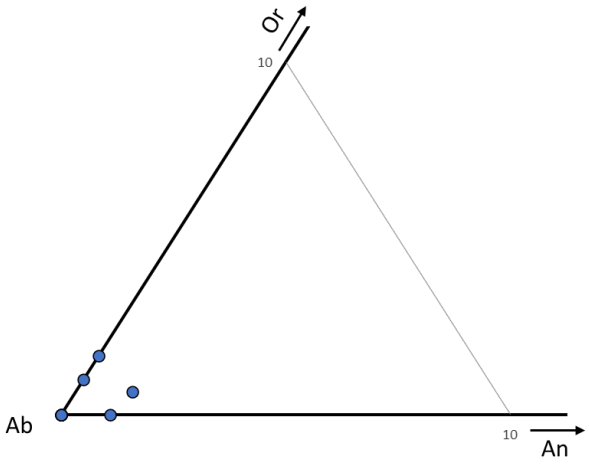

Figure 4.26: The Good Hope albite compositions plotted in the K-feldspar – albite – anorthite ternary diagram.

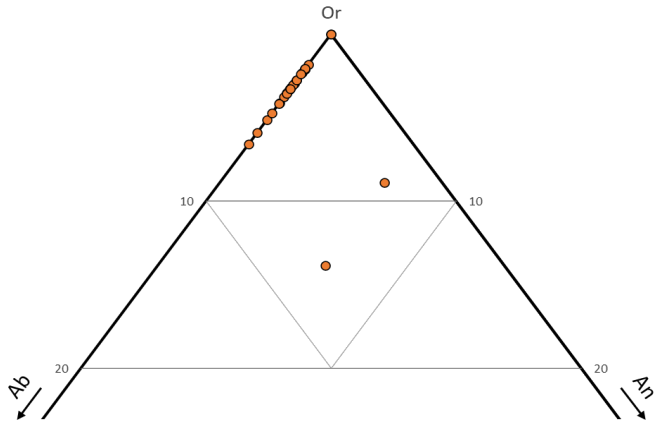

Figure 4.27: The Good Hope K-feldspar compositions plotted in the K-feldspar – albite – anorthite ternary diagram.

4.6 Magnesio-arfvedsonite

Magnesio-arfvedsonite is the only amphibole observed at Good Hope and it occurs within the syenite xenoliths and the carbonatite. Within the syenite xenoliths the magnesio-arfvedsonite is euhedral-to-subhedral and variably pitted, forming prismatic-to-acicular crystals that are 50-to-400 µm in length (Figure 4.28a). It is commonly associated with biotite and is observed replacing or overgrowing aegirine (Figure 4.28b and c). The syenite xenoliths are typically rimmed by a reaction rind of phlogopite – biotite that can contain fine magnesio-arfvedsonite that is euhedral and unaltered (Figure 4.28d). The magnesio-arfvedsonite is observed in both the calcite carbonatite and the ferroan dolomite carbonatite. It is common for the magnesio-arfvedsonite to be associated with other silicate phases, including K-feldspar and biotite, that are disaggregated within a ferroan dolomite groundmass (Figure 4.29a). These grains tend to be euhedral-to-subhedral, prismatic crystals that range in grain size from 50-to-200 µm.

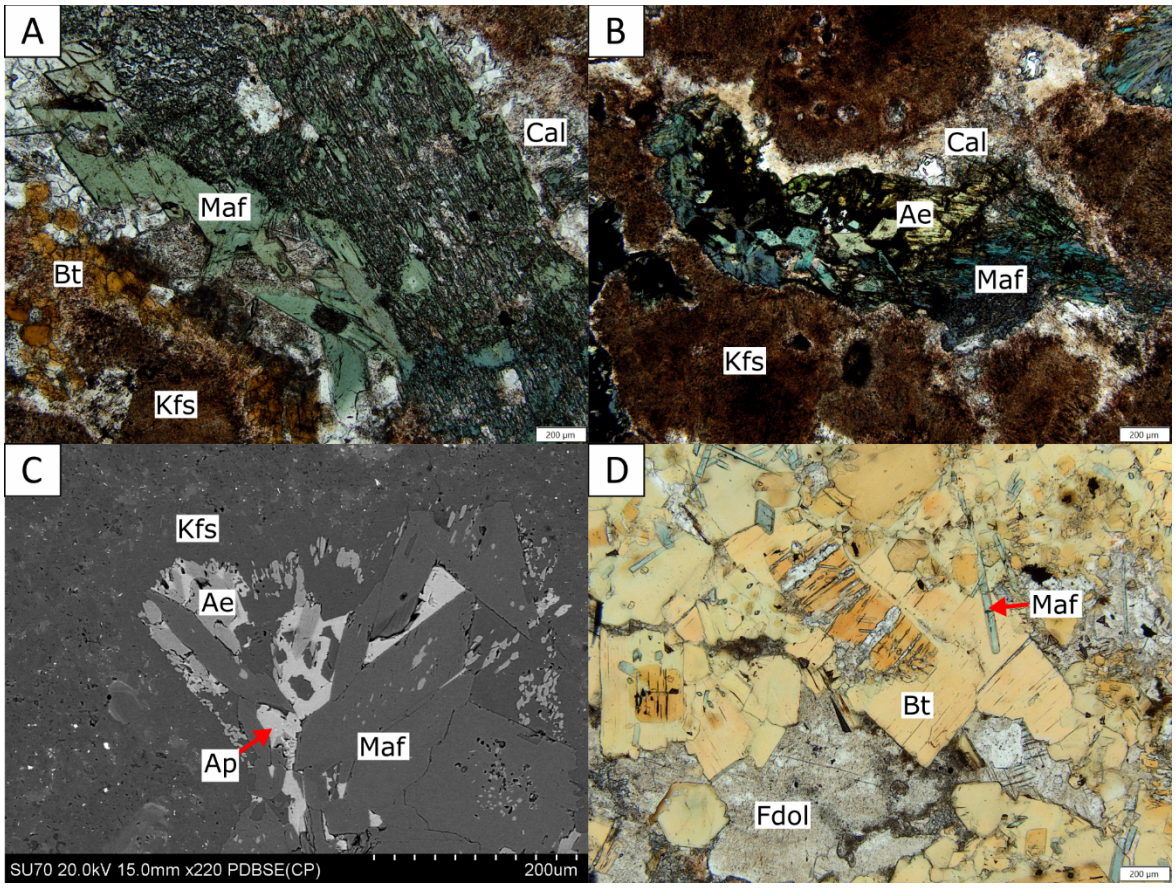

Figure 4.28: Photomicrographs of magnesio-arfvedsonite in plane-polarized light (a), (b), and (d) (scale bar at the bottom right is 200 µm) and BSE image (c). (a) magnesio-arfvedsonite within a syenite xenolith, both pitted and fresh (DDH-03-251). (b) magnesio-arfvedsonite associated with aegirine within a syenite xenolith (DDH-03-251). (c) inclusions of aegirine within the overgrowing magnesio-arfvedsonite (DDH-03-251). (d) reaction rind of a syenite xenolith composed of phlogopite-biotite with unaltered magnesio-arfvedsonite (DDH-04-177). Abbreviations: magnesio-arfvedsonite (Maf), biotite (Bt), K-feldspar (Kfs), calcite (Cal), apatite (Ap), aegirine (Ae), quartz (Qz), and ferroan dolomite (Fdol).

Within the calcite carbonatite, the magnesio-arfvedsonite typically occurs within apatitite clasts and disaggregated apatitite forming acicular crystals that are 100-to-400 µm in length (Figure 4.29b). These acicular magnesio-arfvedsonite are commonly aligned parallel to the elongation of the apatitite clasts and have been observed defining folding within an apatitite clast (Figure 4.29c). These apatitite clasts variably contain disseminated pyrochlore (Figure 4.29c). Magnesio-arfvedsonite that forms within the calcite groundmass away from the apatite is variably mantled by quartz (Figure 4.29d).

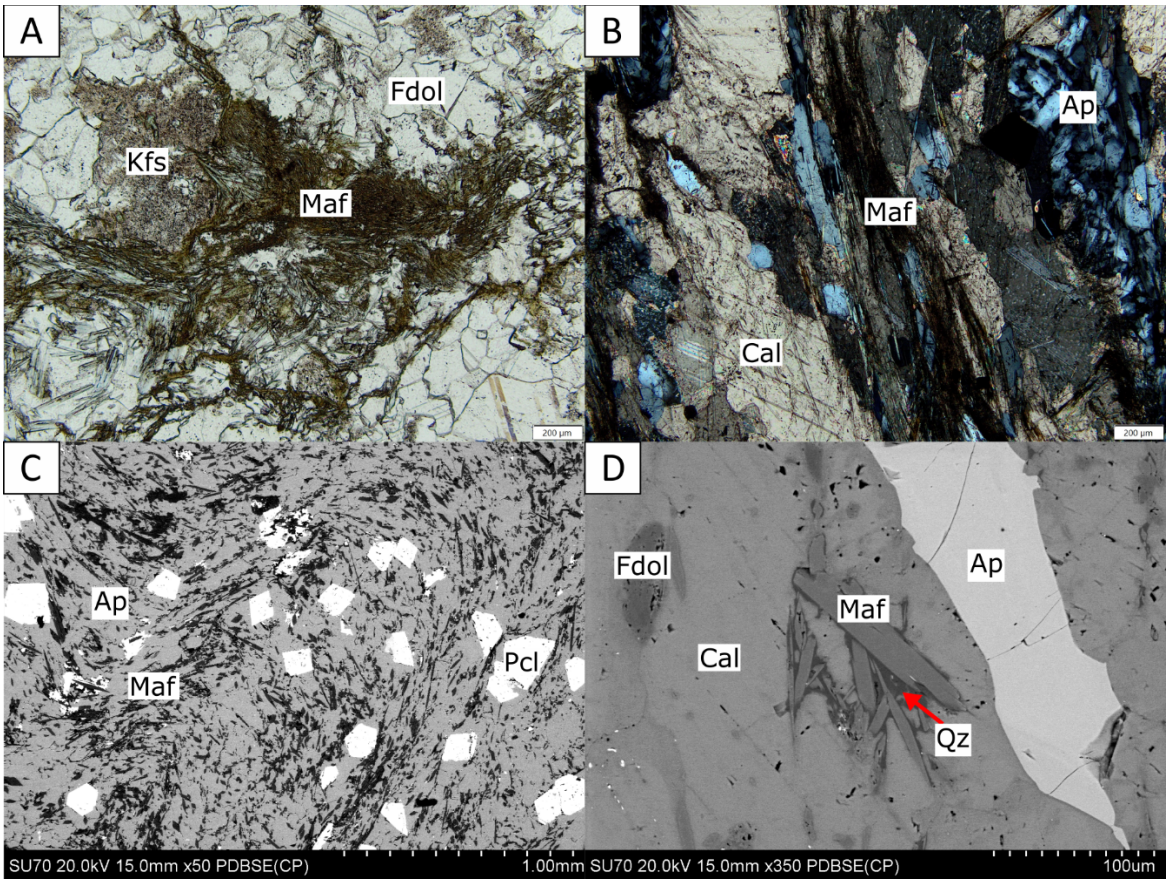

Figure 4.29: Photomicrographs of magnesio-arfvedsonite in plane-polarized light (a) and cross-polarized light (b) and BSE images (c) and (d). (a) acicular magnesio-arfvedsonite associated with disaggregated K-feldspar within a ferroan dolomite groundmass (DDH-04-606). (b) acicular magnesio-arfvedsonite aligned parallel to the elongate apatitite clasts and disaggregated apatite (DDH-03-192). (c) acicular magnesio-arfvedsonite defining folding within an apatitite clast with disseminated pyrochlore (DDH-09-457B). (d) acicular mgnesio-arfvedsonite mantled by quartz within the calcite groundmass (DDH-03-192). Abbreviations: magnesio-arfvedsonite (Maf), K-feldspar (Kfs), ferroan dolomite (Fdol), apatite (Ap), calcite (Cal), pyrochlore (Pcl), and quartz (Qz).

Compositional data for magnesio-arfvedsonite from Good Hope were obtained from 25 EDS analyses and are presented in Appendix I. Representative compositions are presented in Table 4.6 with structural formulae calculated on the basis of twenty-three atoms of oxygen. The compositional ranges are restrictive in the magnesio-arfvedsonite with the major oxides ranging from 5.7-to-9.8 wt. % (Na_2O), 10.7-to-19.8 wt. % (MgO), 51.4-to-56.5 wt. % (SiO_2), 3.1-to-10.1 wt. % (FeO), and 0.4-to-9.1 wt. % (Fe_2O_3). All these compositions contain potassium,

ranging from 1.8-to-3.9 wt. % (K_2O). They also contain variable amounts of Al_2O_3 (b.d.-to-1.4 wt. %), CaO (b.d.-to-6.7 wt. %), MnO (b.d.-to-4.2 wt. %), and TiO_2 (b.d.-to-4.2 wt. %).

Table 4.6: Representative compositions of magnesio-arfvedsonite from Good Hope.

	DDH-09-457B N = 5	DDH-09-457B N = 1	DDH-03-192 N = 2	DDH-03-192 N = 1	DDH-04-606 N = 2	DDH-03-251 N = 2	DDH-04-177 N = 4
Wt. %							
Na_2O	6.62	8.74	8.24	7.78	9.66	8.75	8.80
MgO	18.60	14.52	16.54	17.30	14.38	15.79	14.63
Al_2O_3	0.44	-	0.47	-	0.17	0.48	-
SiO_2	55.93	55.56	56.02	55.81	54.70	54.91	54.72
K_2O	2.63	3.82	2.58	2.45	2.24	2.28	2.06
CaO	4.60	-	2.43	3.26	-	1.00	0.52
TiO_2	0.34	1.47	-	0.29	-	0.09	0.49
V_2O_5	-	-	-	-	0.13	0.26	-
MnO	1.56	-	-	-	-	0.14	0.81
Fe_2O_3	3.73	6.12	6.41	5.45	8.51	6.84	5.90
FeO	4.85	6.21	5.20	5.24	4.76	5.63	7.55
Total	99.31	96.44	97.88	97.58	94.53	96.15	95.47
Structural formulae calculated on the basis of 23 oxygens							
Na	1.81	2.47	2.28	2.16	2.77	2.46	2.51
Mg	3.90	3.15	3.52	3.68	3.17	3.42	3.21
Al	0.07	-	0.08	-	0.03	0.08	-
Si	7.87	8.09	7.99	7.97	8.08	7.98	8.07
K	0.47	0.71	0.47	0.45	0.42	0.42	0.39
Ca	0.69	-	0.37	0.50	-	0.16	0.08
Ti	0.04	0.16	-	0.03	-	0.01	0.05
V	-	-	-	-	0.01	0.02	-
Mn	0.18	-	-	-	-	0.02	0.10
Fe^{3+}	0.39	0.67	0.69	0.59	0.95	0.75	0.65
Fe^{2+}	0.57	0.76	0.62	0.63	0.59	0.68	0.93
Total	16.00	16.00	16.00	16.00	16.01	16.00	16.00

Dash (-) – Indicates values are b.d. limits

The magnesio-arfvedsonite are not commonly zoned. The zoned grains that are observed typically consist of a dominant core composition and a thin, indistinct rim. From the core to the rim the Na and Fe increase while the Ca and Mg decrease. It was observed in some grains that the core lacked Al that was present in the rim, however this compositional variation is not consistent across all zoned grains. Increase in Na and Fe with a decrease in Ca and Mg is consistent with 'normal' zoning as defined by Hogarth (1989). Figure 4.30 is a bivariate plot of Ca + Mg + Fe^{2+} (a.p.f.u.) versus Na + Fe^{3+} (a.p.f.u.) that shows a strong negative correlation (R^2 = 0.93) representing the zoning within these grains is a continuum rather than two distinct populations.

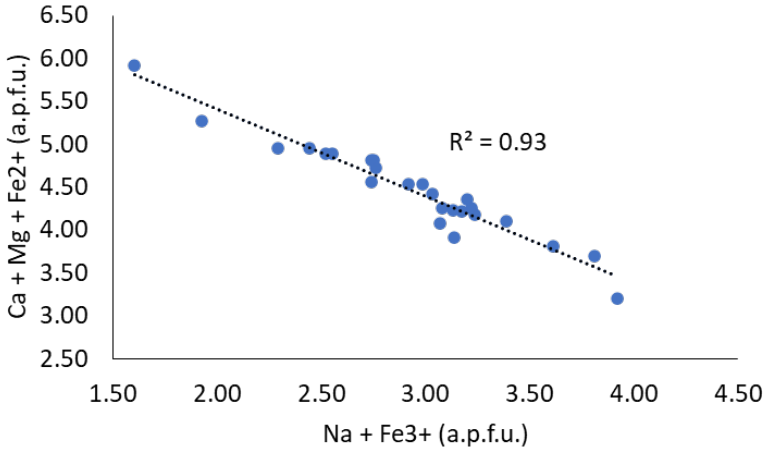

Figure 4.30: Bivariate plot of (Ca + Mg + Fe^{2+}) (a.p.f.u.) versus (Na + Fe^{3+}) (a.p.f.u.) from magnesio-arfvedsonite showing a negative correlation (R^2 = 0.93), consistent with the substitution active from the core to the rim, with higher Na and Fe^{3+} in the rim compared to the core.

A general formula for amphiboles can be defined as $A\,B_2\,C_5\,T_8\,O_{22}\,W_2$, where A = Na, K, or Ca; B = Na, Mg, Fe^{2+}, Mn^{2+}, or Ca; C = Mg, Fe^{2+}, Mn^{2+}, Al, Fe^{3+}, Mn^{3+}, V^{3+}, or Ti^{4+}; T = Si, Al, Ti^{4+}; and W = (OH), F, Cl, or O. Figure 4.31a is a bivariate plot of Mg (a.p.f.u.) versus Na (a.p.f.u.) that has a negative trend (R^2 = 0.77) indicating a substitution between Na and Mg that likely occurs

at the B-site. Figure 4.31b is a bivariate plot of Na + K (a.p.f.u.) versus Ca (a.p.f.u.) that contains a negative trend (R^2 = 0.88) that suggests a substitution of Ca for Na + K at the A-site. Calcium can also substitute at the B-site, however the positive correlation (R^2 = 0.8) of Ca (a.p.f.u.) versus Mg (a.p.f.u.) (Figure 4.31c) suggests that Ca is substituting at the A-site. Figure 4.31d is a bivariate plot of ∑Fe (a.p.f.u.) versus Mg (a.p.f.u.) that shows a negative correlation (R^2 = 0.89) that is consistent with the substitution at both the B- and C-sites.

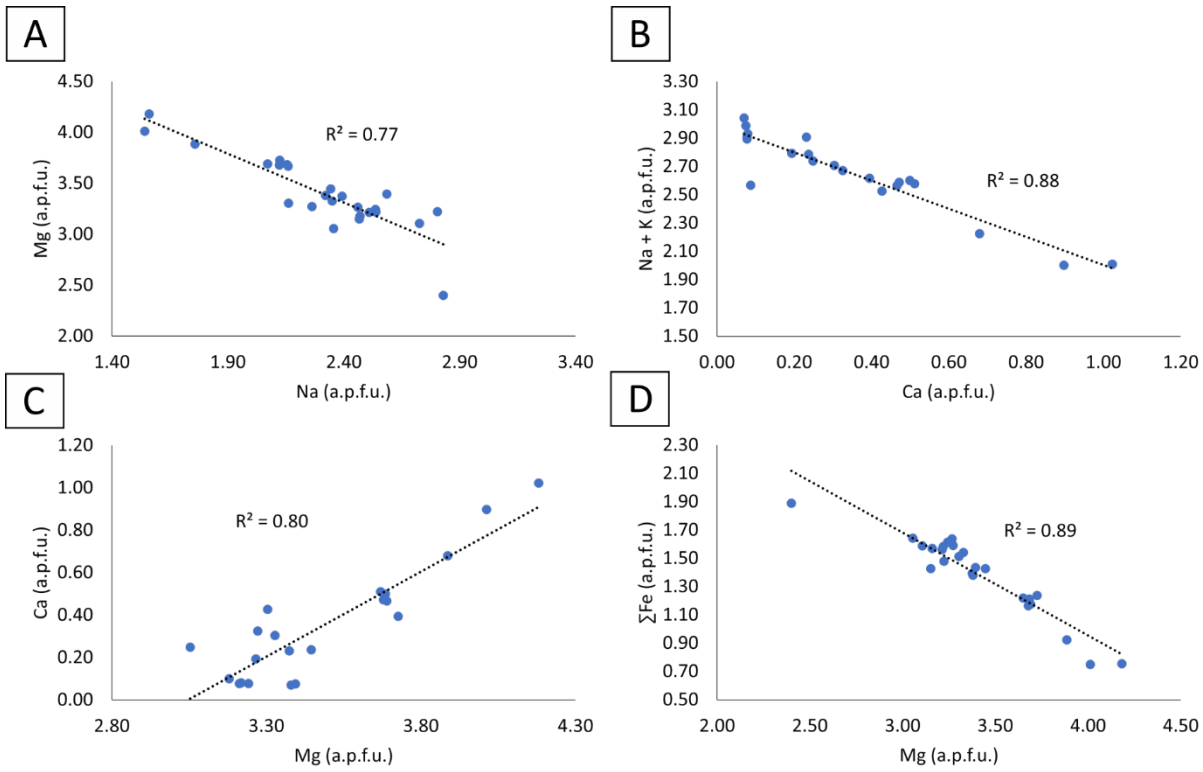

Figure 4.31: Magnesio-arfvedsonite compositions from Good Hope. (a) bivariate plot of Mg (a.p.f.u.) versus Na (a.p.f.u.) that shows a negative correlation (R^2 = 0.77). (b) bivariate plot of (Na + K) (a.p.f.u.) versus Ca (a.p.f.u.) that shows a negative correlation (R^2 = 0.88). (c) bivariate plot of Ca (a.p.f.u.) versus Mg (a.p.f.u.) that shows a positive correlation (R^2 = 0.80). (d) bivariate plot of ∑Fe (a.p.f.u.) versus Mg (a.p.f.u.) that shows a negative correlation (R^2 = 0.89).

The little to moderate correlation between Mg and either Fe^{2+} (Figure 4.32a) or Fe^{3+} (Figure 4.32b) would support that most of the Fe substitution is occurring at the C-site. This is also

supported by the strong correlation between Na and Mg (Figure 4.31a) that suggests the dominant substitution at the B-site is between Na and Mg.

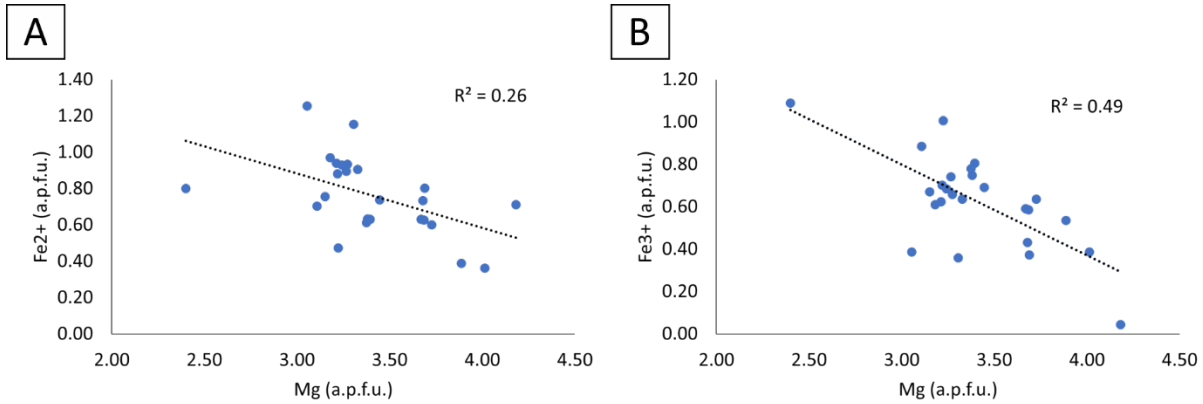

Figure 4.32: C-site substitution in magnesio-arfvedsonite from Good Hope. (a) bivariate plot of Fe^{2+} (a.p.f.u.) versus Mg (a.p.f.u.) that shows a negative trend with little correlation (R^2 = 0.26). (b) bivariate plot of Fe^{3+} (a.p.f.u.) versus Mg (a.p.f.u.) that shows a negative trend with a moderate correlation (R^2 = 0.49).

4.7 Aegirine

Aegirine is not an abundant phase, ranging up to 10 vol. % in only a few samples within the syenite xenoliths, the calcite carbonatite, and the ferroan dolomite carbonatite. It is also a component of the rare orbicular sample (PGH-18-06-416), making up greater than 20 vol. % of the sample. The aegirine are typically subhedral-to-anhedral, ranging from 25-to-200 µm in size. Within the syenite xenoliths, aegirine tends to form stubby prisms associated with magnesio-arfvedsonite (Figure 4.28b). Magnesio-arfvedsonite is also observed overgrowing aegirine, with many crystals containing very fine-grained inclusions of aegirine (Figure 4.28c). Fibrous aegirine aggregates were also observed within the syenite xenoliths that might have formed at the expense of biotite (Figure 4.33a). Within the calcite carbonatite, aegirine occurs as fine-grained subhedral, isolated laths. More commonly, aegirine occurs as disaggregated or acicular crystals within the ferroan dolomite carbonatite. The disaggregated aegirine is typically

associated with K-feldspar ± magnesio-arfvedsonite and forms stubby prisms (Figure 4.33b). This aegirine variably contain inclusions of synchysite-(Ce) and can be associated with rutile. The acicular aegirine occurs associated with ferroan dolomite + apatite that typically occurs within the calcite carbonatite (Figure 4.33c).

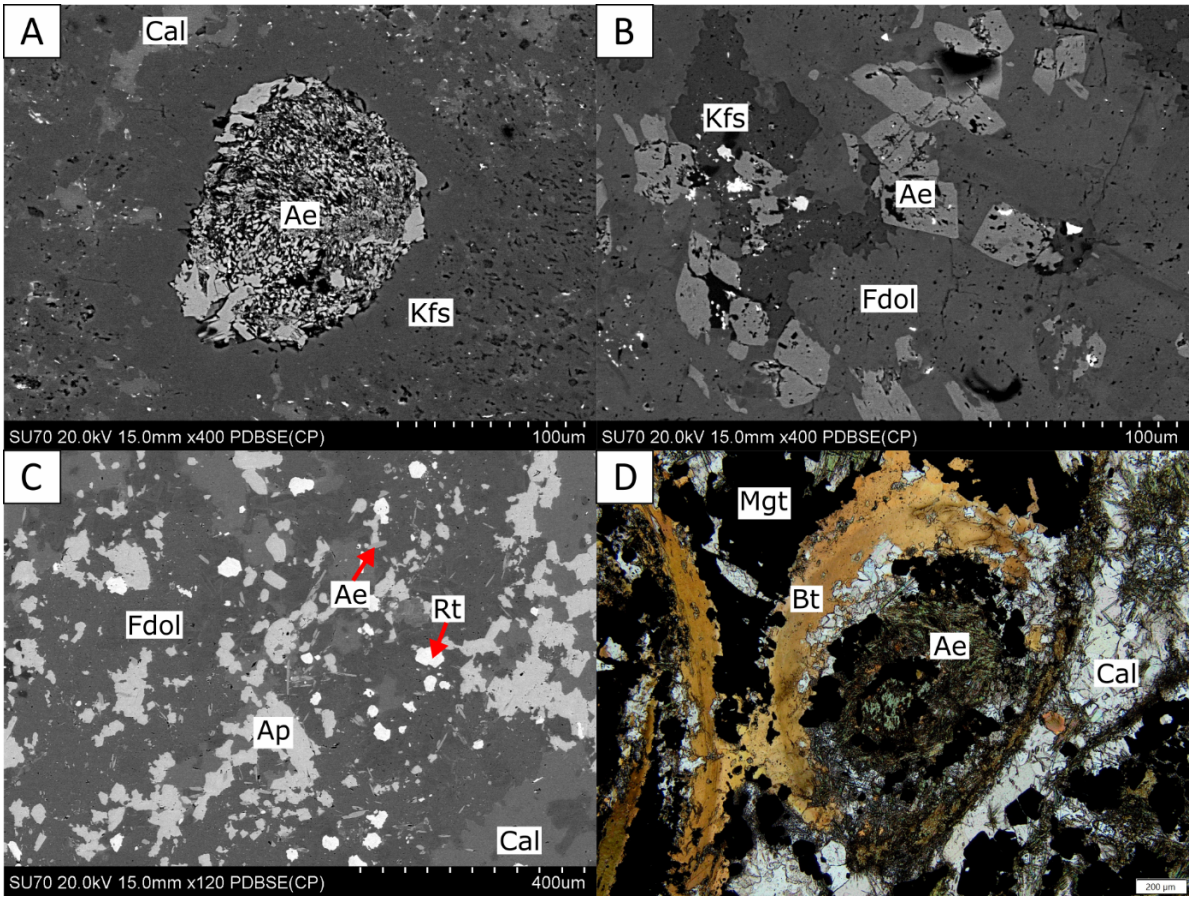

Figure 4.33: Aegirine BSE images (a), (b), and (c) and a photomicrograph in plane-polarized light (d) (scale bar in the bottom right is 200 µm). (a) fibrous aegirine aggregate that may have formed at the expense of biotite in a syenite xenolith (DDH-03-251). (b) stubby prisms of subhedral-to-anhedral aegirine within a ferroan dolomite carbonatite with associated K-feldspar (DDH-04-37). (c) acicular aegirine disseminated within ferroan dolomite with associated apatite and clasts of calcite (PGH-18-01-79). (d) acicular aegirine within the carbonate groundmass and within an orbicule that may have formed at the expense of biotite associated with magnetite and mantled by biotite (PGH-18-06-416). Abbreviations; aegirine (Ae), K-feldspar (Kfs), calcite (Cal), ferroan dolomite (Fdol), apatite (Ap), rutile (Rt), magnetite (Mgt), and biotite (Bt).

The orbicular sample contains acicular and elongate laths of aegirine that occur within the orbicules as well as in the groundmass carbonate. The aegirine is typically isolated but is

intergrown with biotite within the orbicules and might be forming at the expense of biotite (Figure 4.33d).

Compositional data for aegirine from Good Hope were obtained from 24 EDS analyses and are presented in Appendix I. Representative compositions are presented in Table 4.7 with structural formulae calculated on the basis of six atoms of oxygen and ferric iron calculated by stoichiometry using the Droop (1987) method. The compositional range of aegirine ($NaFe^{3+}Si_2O_6$) from Good Hope is limited, with the major oxides varying from 10.0-to-13.9 wt. % (Na_2O), 50.4-to-54.5 wt. % (SiO_2), and 20.8-to-31.8 wt. % (Fe_2O_3). The minor elements, with the exception of CaO (0.1-to-5.9 wt. %), all range from below detection up to 6.5 wt. % (MgO), 1.0 wt. % (Al_2O_3), 0.8 wt. % (K_2O), 2.3 wt. % (TiO_2), 4.6 wt. % (MnO), and 6.1 wt. % (FeO). Calcium, Mg, and Fe^{2+} are accounted for by the diopside ($CaMgSi_2O_6$) and hedenbergite ($CaFe^{2+}Si_2O_6$) endmembers. The minor Al, Ti, and Mn represent the endmembers $CaAl_2SiO_6$, $CaTiAl_2O_6$, and $CaMnSi_2O_6$, respectively. Within the syenite xenoliths and the carbonatite most of the compositions are aegirine with only a few that could be classified as aegirine-augite according to the aegirine – diopside – hedenbergite ternary diagram (Figure 4.34). The aegirine compositions within the orbicular sample all plot in a tight cluster that are nearly pure aegirine with a small trend toward hedenbergite (Figure 4.34). The aegirine compositions from the orbicular occurrence also contain V (0.5-to-2.8 wt. %) (Table 4.7). The compositions from the syenite xenoliths and from the disseminated samples have a wider range with a larger contribution from the diopside component and lack V (Figure 4.34).

Table 4.7: Representative compositions of aegirine from Good Hope.

	DDH-03-251	DDH-03-251	DDH-04-34	PGH-18-06-416
Wt. %				
Na_2O	11.33	11.28	12.04	13.67
MgO	1.79	6.53	2.02	0.41
Al_2O_3	0.39	0.91	-	0.28
SiO_2	52.24	54.50	52.57	53.06
K_2O	-	0.82	0.24	-
CaO	3.80	2.29	0.42	0.47
TiO_2	0.58	0.31	0.71	1.12
V_2O_5	-	-	-	0.65
MnO	-	-	-	0.06
Fe_2O_3	26.98	24.85	24.64	28.76
FeO	2.31	-	4.33	2.77
Total	**99.41**	**101.49**	**96.97**	**101.24**
Structural formulae calculated on the basis of 6 oxygens				
Na	0.84	0.81	0.92	1.00
Mg	0.10	0.36	0.12	0.02
Al	0.02	0.04	-	0.01
Si	2.01	2.01	2.06	2.01
K	-	0.04	0.01	-
Ca	0.16	0.09	0.02	0.02
Ti	0.02	0.01	0.02	0.03
V	-	-	-	0.02
Mn	-	-	-	-
Fe^{3+}	0.78	0.69	0.73	0.82
Fe^{2+}	0.07	-	0.14	0.09
Total	**4.00**	**4.04**	**4.02**	**4.02**
Mol % aegirine – hedenbergite - diopside				
Ae	83.08	76.92	85.49	93.33
Hd	6.97	-	7.81	5.45
Di	9.95	23.08	6.70	1.21

Dash (-) - indicates values are b.d. limits

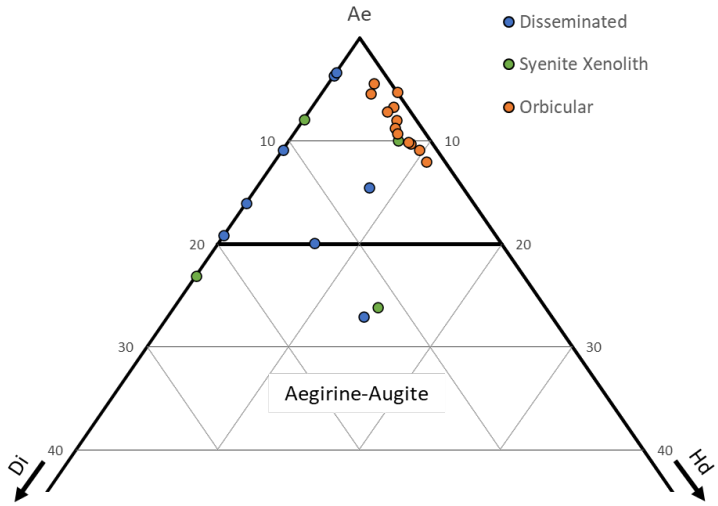

Figure 4.34: The Good Hope aegirine compositions plotted in the aegirine – diopside – hedenbergite ternary diagram.

4.8 Biotite

Biotite at Good Hope occurs in the syenite xenoliths, as the major phase in the reaction rinds along the margins of the syenite xenoliths, as isolated grains in the carbonatite, and within the rare orbicular occurrence. The biotite ranges from 50-to-600 µm in size and ranges from unaltered to extensively replaced by chlorite. Within the syenite xenoliths the biotite is subhedral-to-anhedral and slightly-to-moderately replaced, typically by ferroan dolomite ± K-feldspar. It is commonly associated with magnesio-arfvedsonite and K-feldspar and occurs principally adjacent to ferroan dolomite (Figure 4.35a). Biotite is also the dominant phase within the reaction rinds at the margins of the syenite xenoliths. This biotite is typically fresh, forming euhedral-to-subhedral crystals that are commonly zoned with anhedral cores and euhedral-to-subhedral rims (Figure 4.35b). These can contain ferroan dolomite, K-feldspar, and/or rutile forming along the cleavage planes of the cores of the grains (Figure 4.35c). Within the carbonatite, the biotite are typically isolated, forming subhedral-to-anhedral crystals that

are slightly-to-extensively replaced (Figure 4.35d), by either ferroan dolomite ± K-feldspar or chlorite, with most being completely pseudomorphed when replaced by chlorite.

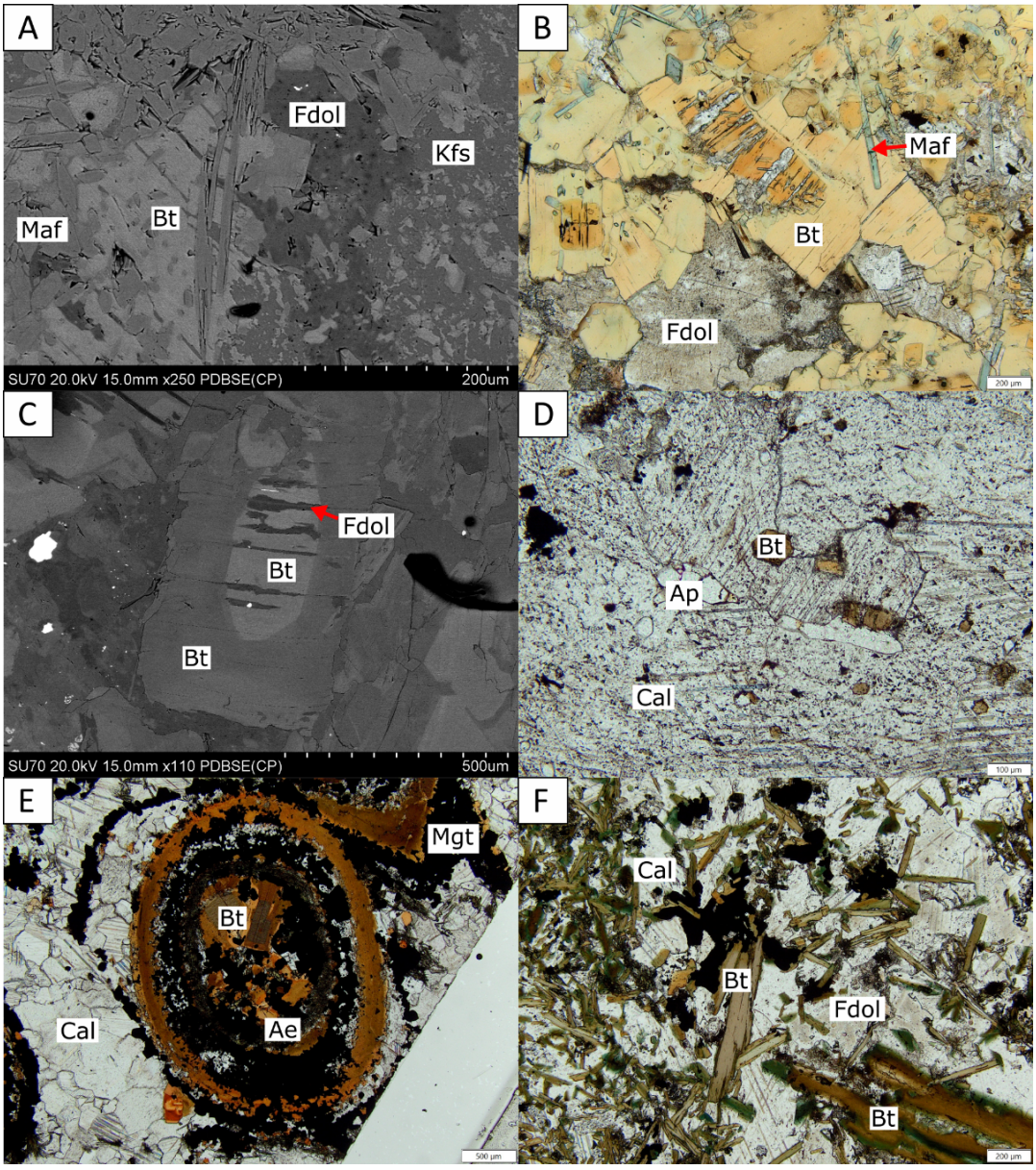

Figure 4.35: BSE images (a) and (c) and photomicrographs in plane-polarized light (b), (d), (e), and (f) of biotite from Good Hope (scale bar in the bottom right corner is 200 µm (b) and (f), 500 µm (d) and (e)). (a) biotite intergrown with magnesio-arfvedsonite and disaggregated in K-feldspar (DDH-04-177). (b) zoned biotite in the reaction rind of a syenite xenolith with an annite-rich core and phlogopite-rich rim (DDH-04-177). (c) zoned biotite in the reaction rind of a syenite xenolith with ferroan dolomite and rutile forming along the cleavage planes in the core (DDH-04-177). (d) isolated biotite within a calcite carbonatite (RHM-10). (e) orbicule with laths of weakly -zoned biotite in the core and tangential biotite in the outer rim (PGH-18-06-416). (f) laths of biotite with annite-rich rims (DDH-04-34). Abbreviations; biotite (Bt), K-feldspar (Kfs), ferroan dolomite (Fdol), magnesio-arfvedsonite (Maf), calcite (Cal), apatite (Ap), aegirine (Ae), and magnetite (Mgt).

These are observed in both calcite and ferroan dolomite carbonatite but are more commonly associated with K-feldspar within the ferroan dolomite carbonatite. In the orbicular occurrence, the biotite is a major component of the orbicules and does not occur in the surrounding groundmass. It forms in both the core, as 200-to-600 μm laths that are variably zoned, and in the rims, as 50-to-200 μm aggregates and tangential laths up to a millimeter in length (Figure 4.35e). These grains are typically subhedral-to-anhedral, associated with magnetite and overgrown by aegirine.

Compositional data for biotite were obtained from 74 EDS analyses and are presented in Appendix I. Representative compositions are presented in Table 4.8 with structural formulae calculated on the basis of twenty-two atoms of oxygen. The compositions for the biotite from Good Hope have variation in the major cations ranging from 32.2-to-46.7 wt. % (SiO_2), 5.5-to-14.8 wt. % (Al_2O_3), 10.3-to-24.5 wt. % (MgO), 3.5-to-22.6 wt. % (FeO), and 4.1-to-11.0 wt. % (K_2O). All the iron is assumed to be Fe^{2+} as stoichiometric calculation following Droop (1987) indicated no Fe^{3+}. All biotite plot close to the phlogopite – annite line in the Al – Mg – Fe ternary diagram (Figure 4.36). The compositions in the carbonatite are mostly phlogopite-rich and in the syenite xenoliths and disaggregated in the carbonatite are typically zonation-free. The reaction rind biotite, at the margins of the syenite xenoliths, are commonly zoned with annite-rich cores and phlogopite-rich rims. This zoning is consistent throughout the carbonatite except in one sample, DDH-04-34. This sample contains laths of biotite of variable grain size that are typically zoned with a similar composition to other zoned grains in the core, with more annite-rich rims (Figure 4.35f). These compositions are separated in the ternary diagram Al – Mg – Fe (Figure 4.36), which shows the compositions of the cores from both the carbonatite and DDH-

04-34 cluster together and the rims of DDH-04-34 plot toward annite while the rims in the reaction rinds plot toward phlogopite.

Table 4.8: Representative compositions of biotite from Good Hope.

	DDH-04-34	RW-PL-06	RW-PL-06	PGH-18-06-416	DDH-03-251	DDH-04-34	DDH-04-34
Wt. %							
Na_2O	-	0.57	0.23	-	0.26	0.24	0.32
MgO	14.91	21.60	8.66	17.68	14.70	12.15	14.11
Al_2O_3	10.97	9.23	22.23	11.09	13.54	13.26	13.88
SiO_2	32.30	43.98	47.39	38.90	37.29	34.23	34.65
K_2O	5.03	10.80	10.43	10.04	10.15	9.49	9.42
TiO_2	0.22	0.54	-	2.19	2.20	4.44	4.19
MnO	1.81	0.06	-	-	0.34	0.79	0.50
FeO	22.55	6.95	2.56	14.44	15.48	18.15	15.43
BaO	-	-	-	-	-	-	0.88
Total	**87.78**	**93.71**	**91.50**	**94.34**	**93.93**	**92.82**	**93.37**
Structural formulae calculated on the basis of 22 oxygens							
Na	-	0.16	0.06	-	0.08	0.07	0.09
Mg	3.72	4.70	1.82	3.98	3.35	2.86	3.24
Al	2.16	1.59	3.69	1.98	2.44	2.47	2.52
Si	5.40	6.42	6.68	5.88	5.71	5.42	5.35
K	1.07	2.01	1.88	1.94	1.98	1.92	1.85
Ti	0.03	0.06	-	0.25	0.25	0.53	0.49
Mn	0.25	0.01	-	-	0.04	0.11	0.07
Fe	3.15	0.85	0.30	1.83	1.98	2.41	2.00
Ba	-	-	-	-	-	-	0.27
Total	**15.77**	**15.81**	**14.44**	**15.85**	**15.84**	**15.81**	**15.88**

Dash (-) - indicates values are b.d. limits

The compositions of the biotite from the orbicular sample are also shown on this plot, and although these grains can be zoned, the compositions of the cores and rims all plot together, with the rims typically containing more Fe than the cores. The disseminated biotite plots with a

similar composition to the phlogopite rims in the syenite xenolith reaction rinds and the biotite in the orbicular sample (Figure 4.36).

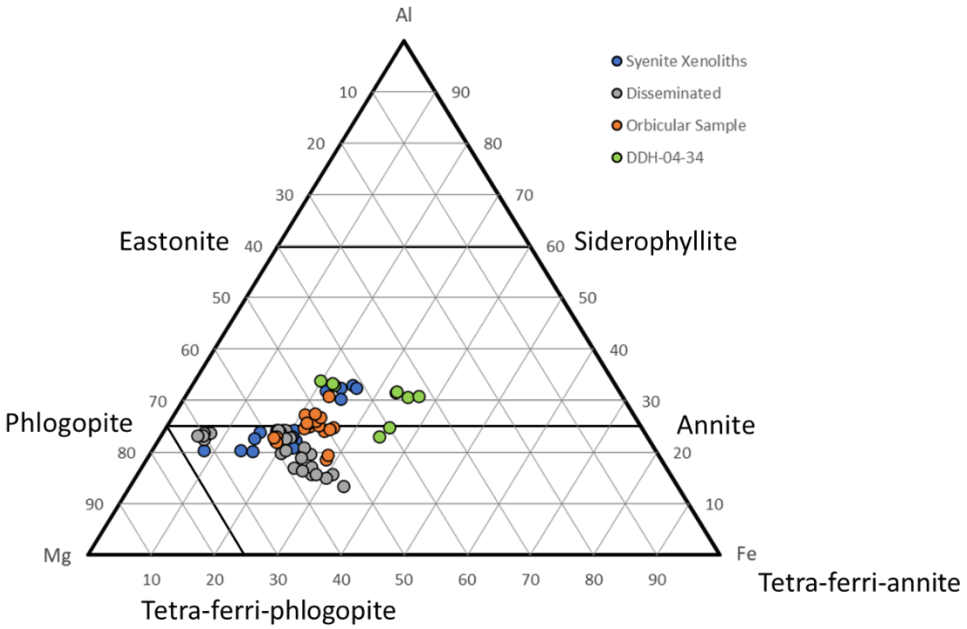

Figure 4.36: Good Hope biotite compositions plotted in the Al – Mg – Fe ternary diagram with compositions from the syenite xenoliths (blue), the disseminated samples (gray), the orbicular sample (orange), and sample DDH-04-34 (green).

The compositional variation in the biotite could also be due to the variable degrees of chloritization observed in the samples. Chloritization is characterized by the increase in Mg, Fe, and Mn and the decrease in Si, K, and Ti (Yamini et al., 2017). Calcium, K, and Na can also occur as impurities in chlorite (Yamini et al., 2017). The ternary diagram TiO_2 – FeO – MgO (Figure 4.37) after Yamini et al. (2017) shows the variation from primary biotite, assumed to have crystallized from a silicate melt to secondary biotite that exhibit strong chloritization. The compositions from sample DDH-04-34 all plot in the primary field of the diagram and the compositions from the syenite xenoliths, disseminated samples, and orbicular sample all plot

principally in the re-equilibrated primary biotite field with some in the secondary biotite field (Figure 4.37).

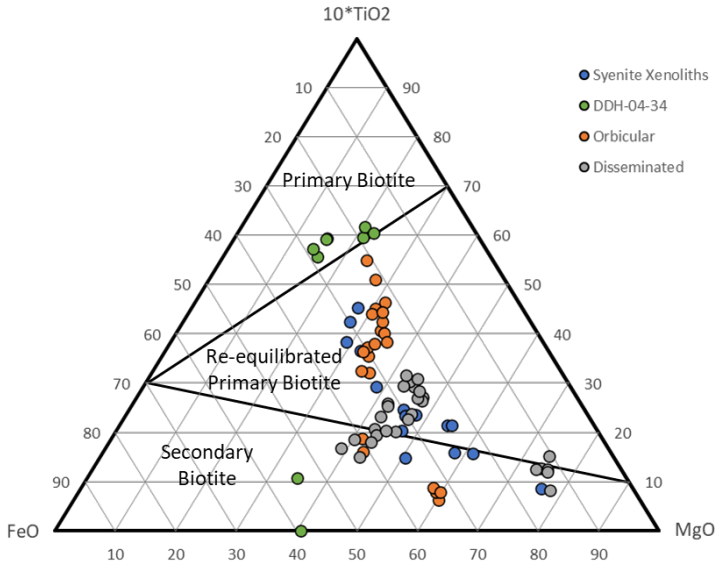

Figure 4.37: Good Hope biotite compositions plotted in the $10*TiO_2$ – FeO_T – MgO ternary diagram with compositions from the syenite xenoliths (blue), the disseminated samples (gray), the orbicular sample (orange), and sample DDH-04-34 (green) (*after* Yamini et al., 2017). "primary" biotite is inferred to have crystallized from a silicate melt and "secondary" biotite locally exhibit strong chloritization (Yamini et al., 2017).

4.9 Chlorite

Chlorite occurs within the calcite and ferroan dolomite carbonatite and can range from trace amounts-to-20 vol. %. It is typically very fine-grained forming fibrous-to-acicular aggregates or isolated, disaggregated acicular grains. Fibrous aggregates of chlorite are observed intergrown with fibrous magnetite and syntaxial intergrowths of REE-fluorocarbonates and occur interstitial to euhedral calcite (Figure 4.38a). Euhedral ferroan dolomite occurs in contact with radial-to-colloidal chlorite that is observed surrounding anhedral, disaggregated apatite with associated laths of REE-fluorocarbonates (Figure 4.38b). The fibrous chlorite also commonly occurs as veins that crosscut the carbonatite (Figure 4.38c)

and the apatitite clasts. Fibrous-to-acicular chlorite replaces biotite, retaining the original crystal habit, and occurs within the apatitite clasts and the ferroan dolomite carbonatite (Figure 4.38d).

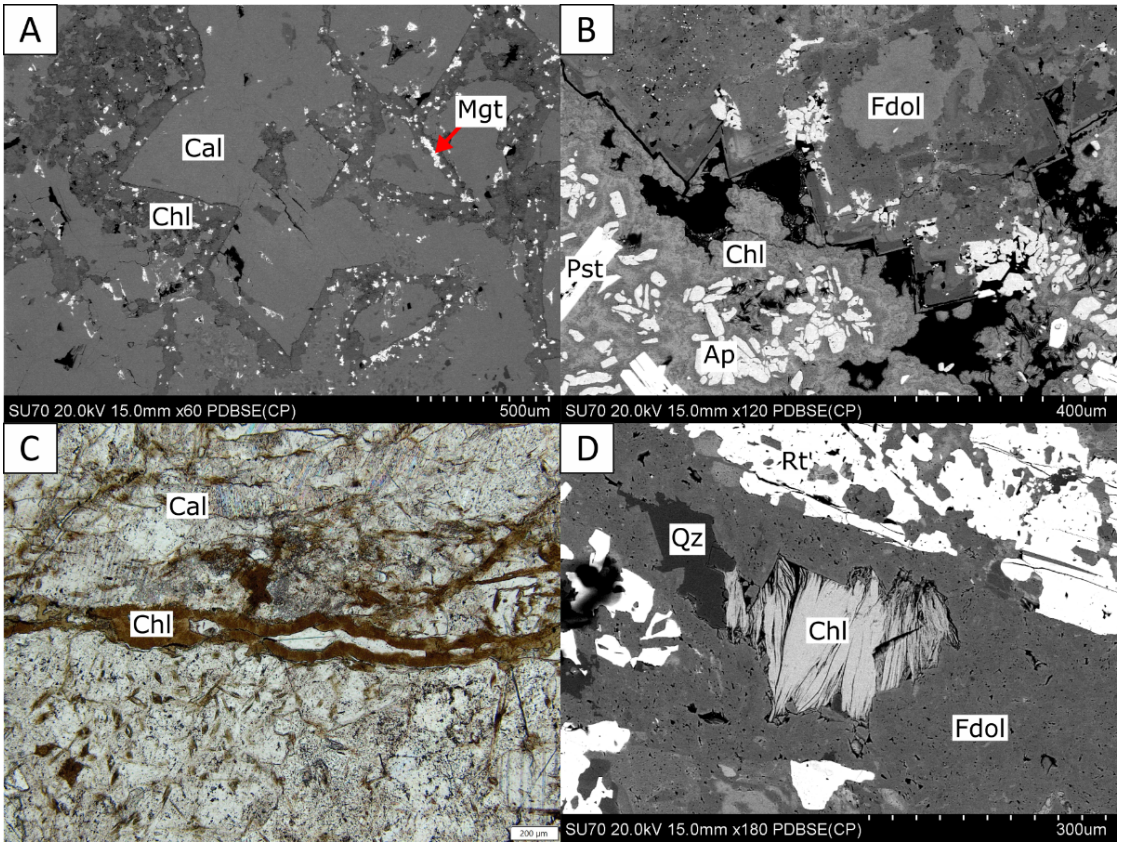

Figure 4.38: BSE images (a), (b), and (d) of chlorite from Good Hope and photomicrograph (c) in plane-polarized light (scale bar at the bottom right is 200 µm). (a) euhedral calcite with interstitial, fibrous chlorite intergrown with magnetite (RHM-06). (b) radial-to-colloidal chlorite forming around disaggregated apatite (DDH-08-13). (c) vein of chlorite crosscutting calcite (PGH-18-06-384). (d) chlorite replacing biotite within ferroan dolomite (PGH-18-06-384). Abbreviations; calcite (Cal), chlorite (Chl), magnetite (Mgt), ferroan dolomite (Fdol), dolomite (Dol), parisite-(Ce) (Pst), apatite (Ap), quartz (Qz), and rutile (Rt).

Commonly, chlorite is intergrown or adjacent to other phases, including quartz, barite, strontianite, apatite, magnetite, calcite, and REE-fluorocarbonates. Barite is observed along the margins of some of the chlorite veins, poikilitic calcite with interstitial chlorite surrounds fine-grained apatite, and chlorite can mantle the REE-fluorocarbonates.

Compositional data for chlorite from Good Hope were obtained from 22 EDS analyses and are presented in Appendix I. Representative compositions are presented in Table 4.9 with structural formulae calculated on the basis of twenty-eight atoms of oxygen.

Table 4.9: Representative compositions of chlorite from Good Hope.

	PGH-18-06-384	**DDH-04-666**	**RW-PL-08**	**DDH-04-606**	**RHM-06**	**RW-PL-06**
Wt. %						
Na_2O	0.09	0.78	0.50	-	-	-
MgO	12.97	1.36	11.90	12.87	18.07	15.27
Al_2O_3	9.06	3.65	13.68	10.14	13.07	16.04
SiO_2	31.85	36.18	41.74	31.42	32.74	30.86
P_2O_5	-	0.23	-	-	-	-
K_2O	-	0.77	4.88	0.08	0.23	-
CaO	0.44	0.57	5.14	0.68	0.98	0.34
V_2O_5	0.28	-	-	-	0.22	-
Cr_2O_3	-	-	4.65	-	-	-
MnO	-	1.03	-	-	-	-
FeO	30.58	31.31	4.79	26.51	17.49	24.80
Total	**85.26**	**75.88**	**87.28**	**81.70**	**82.80**	**87.31**
Structural formulae calculated on the basis of 28 oxygens						
Na	0.04	0.38	0.19	-	-	-
Mg	4.31	0.52	3.45	4.37	5.72	4.76
Al	2.38	1.09	3.13	2.72	3.27	3.95
Si	7.10	9.20	8.11	7.16	6.96	6.46
P	-	0.05	-	-	-	-
K	-	0.25	1.21	0.02	0.06	-
Ca	0.11	0.16	1.07	0.17	0.22	0.08
V	0.04	-	-	-	0.03	-
Cr	-	-	0.71	-	-	-
Mn	-	0.22	-	-	-	-
Fe	5.70	6.66	0.78	5.05	3.11	4.34
Total	**19.67**	**18.52**	**18.66**	**19.49**	**19.38**	**19.59**

Dash (-) - indicates values are b.d. limits

The compositional range for the chlorite from Good Hope have some variation and are generally iron-rich. The major cations vary from 29.1-to-39.0 wt. % (SiO_2), 8.7-to-18.2 wt. % (Al_2O_3), 10.3-to-20.8 wt. % (MgO), and 13.8-to-32.6 wt. % (FeO). The compositions plot within the trioctahedral-type chlorite field in the Al – Fe – Mg ternary diagram (Figure 4.39), ranging from chamosite to clinochlore.

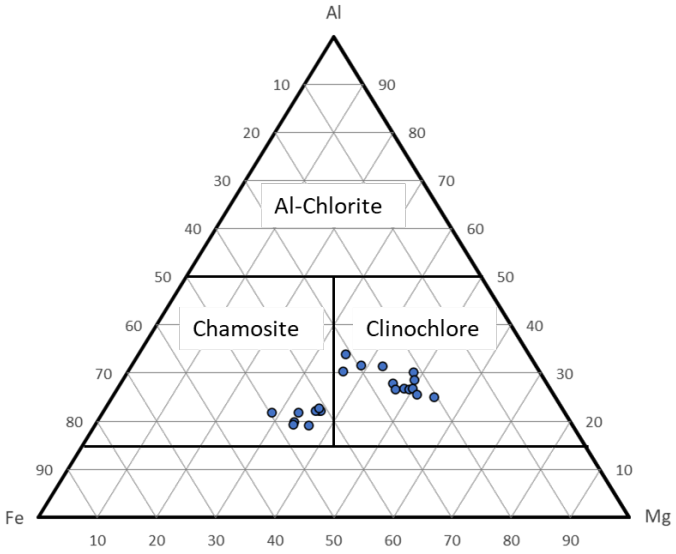

Figure 4.39: Compositions of chlorite from Good Hope plotted in the Al – Fe – Mg ternary diagram indicating the compositions fall in both the chamosite and clinochlore fields.

Further classification of the chlorite uses the bivariate discrimination plot of Fe (a.p.f.u.) versus Si (a.p.f.u.) (Figure 4.40), which indicates the compositions are diabantite.

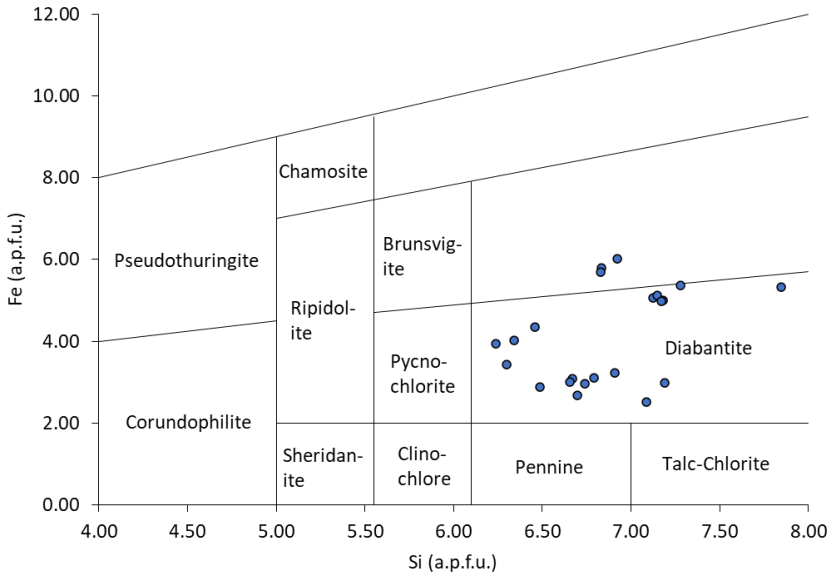

Figure 4.40: Chlorite compositions from Good Hope plotted on the Fe (a.p.f.u.) versus Si (a.p.f.u.) discrimination diagram for chlorite, indicating a diabantite composition (*after* Hey, 1954).

4.10 REE-carbonates

Synchysite-(Ce) and parisite-(Ce) are the most common REE-fluorocarbonates at Good Hope. Bastnaesite-(Ce) is present in minor amounts as syntaxial intergrowths within either synchysite-(Ce) or parisite-(Ce). Burbankite occurs as inclusions in ferroan dolomite and is less common in calcite. Synchysite-(Ce) and parisite-(Ce) also occur as inclusions within calcite and ferroan dolomite and are typically associated or intergrown with strontianite. Synchysite-(Ce) and parisite-(Ce) occur as very fine-grained syntaxial intergrowths, as medium-grained laths, and euhedral-prismatic crystals (Figure 4.41a). The bastnaesite-(Ce) commonly forms syntaxial intergrowths in the laths (Figure 4.41b). The REE-fluorocarbonates occur within both the calcite and ferroan dolomite (Figure 4.41c). They are typically associated with other phases including quartz, chlorite, barite, thorite, magnetite, and strontianite, and less commonly apatite and pyrite. Strontianite and magnetite are commonly intergrown with the REE-fluorocarbonates but

can also occur as inclusions (strontianite) and mantling the REE-fluorocarbonates (magnetite) (Figure 4.41d).

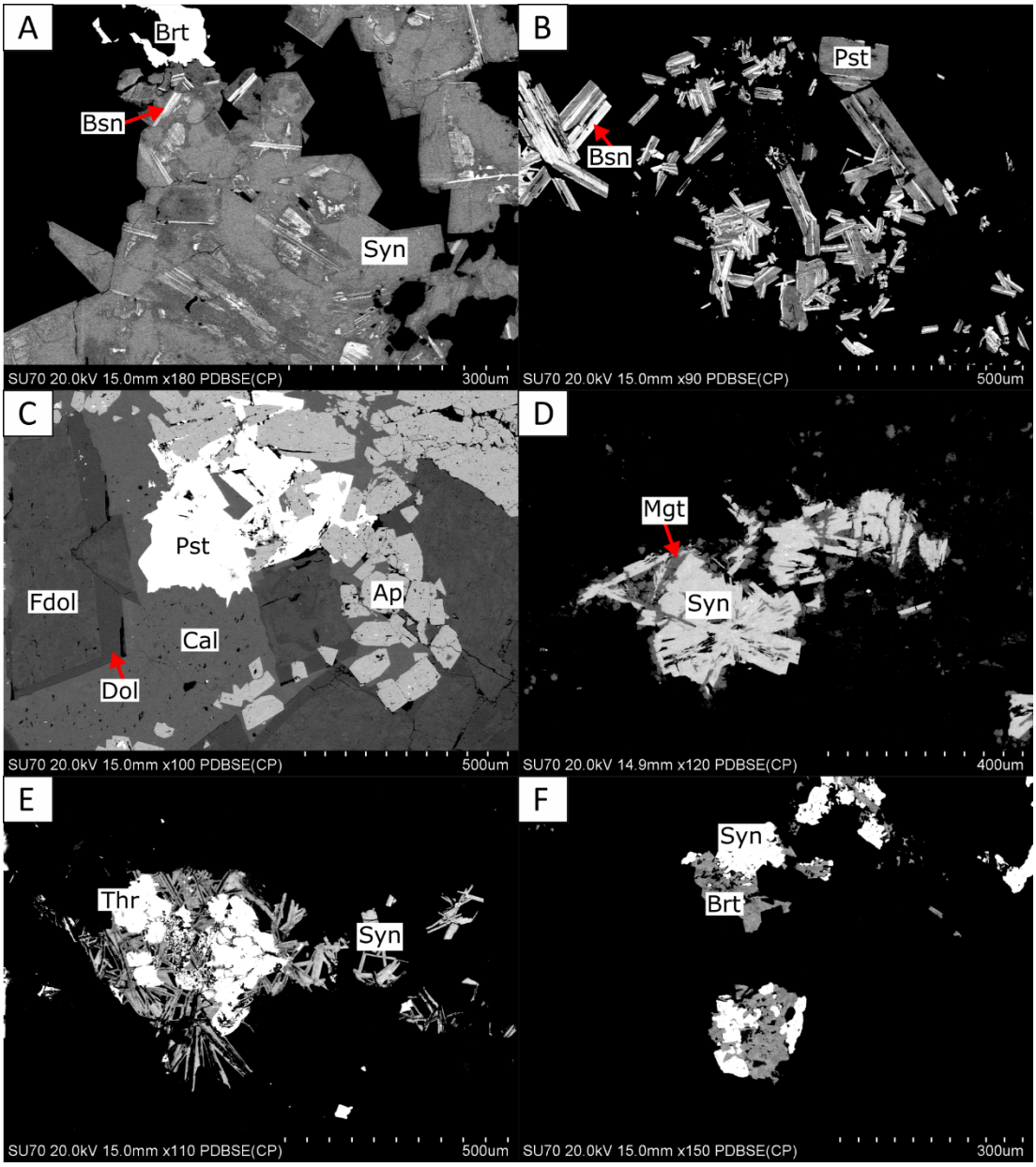

Figure 4.41: BSE images of REE-fluorocarbonates from Good Hope. (a) euhedral-prismatic synchysite-(Ce) with syntaxial intergrowths of bastnaesite-(Ce) (PGH-18-07-174). (b) laths of parisite-(Ce) with syntaxial intergrowths of bastnaesite-(Ce) (DDH-08-13). (c) parisite-(Ce) within calcite carbonatite with associated ferroan dolomite and apatite (RHM-12). (d) parisite-(Ce) mantled by fibrous magnetite (RHM-06). (e) syntaxial synchysite-(Ce) associated with thorite (PL-S2-PI-2). (f) synchysite-(Ce) intergrown with barite (DDH-07-103). Abbreviations; synchysite-(Ce) (Syn), bastnaesite-(Ce) (Bsn), barite (Brt), parisite-(Ce) (Pst), ferroan dolomite (Fdol), dolomite (Dol), calcite (Cal), apatite (Ap), magnetite (Mgt), and thorite (Thr).

Thorite can occur as inclusions or adjacent to the REE-fluorocarbonates (Figure 4.41e). Quartz and barite (Figure 4.41f) are typically observed adjacent to the REE-fluorocarbonates, while chlorite can be mantling the grains. Apatite is found associated with the REE-fluorocarbonates but rarely without magnetite, and where the REE-fluorocarbonates occur within the apatitite clasts they are almost always associated with magnetite.

Compositional data for the REE-fluorocarbonates from Good Hope were obtained from 38 EDS analyses and are presented in Appendix I. The number of analyses is limited as the compositions were difficult to analyze due to the presence of common iron oxide/hydroxide overgrowths. Representative compositions are presented in Table 4.10 with structural formulae calculated on the basis of 3 CO_3 groups (pst), 2 CO_3 groups (syn), and 1 CO_3 group (bsn). The classification of synchysite, parisite, and bastnaesite are determined by the content of $CaCO_3$ and subsequently the content of $(REY)_2(CO_3)_3$, the ternary diagram $CaCO_3$ – $BaCO_3$ – $(REY)_2(CO_3)_3$ (Figure 4.42) illustrates this. The REE-fluorocarbonates from Good Hope have CaO and $(REY)_2O_3$ varying from 16.2-to-17.7 wt. % and 43.5-to-57.7 wt. % (syn), 10.4-to-15.1 wt. % and 48.4-to-66.5 wt. % (pst), and 0.4-to-1.4 wt. % and 79.0-to-81.3 wt. % (bsn), respectively. The predominant REE in the REE-fluorocarbonates is Ce, followed by La, Nd, and Pr. Some synchysite compositions contain Sm and/or Gd, some parisite compositions contain Sm, and bastnaesite contains both Sm and Gd below detection. Synchysite and parisite can both contain Y_2O_3 (b.d.-to-1.4 wt. %, syn; b.d.-to-0.5 wt. %, pst), with Y contents in bastnaesite below detection. Synchysite and bastnaesite can both contain ThO_2 (b.d.-to-2.3 wt. %, syn; b.d.-to-1.1 wt. %, bsn), with Th in parisite below detection.

Table 4.10: Representative compositions of REE-fluorocarbonates from Good Hope.

	PGH-18-07-174 (Syn)	**DDH-03-474** (Syn)	**DDH-03-474** (Syn)	**PGH-18-07-174** (Pst)	**PGH-18-07-174** (Pst)	**PGH-18-07-174** (Bsn)	**PGH-18-07-174** (Bsn)
Wt. %							
CaO	16.63	17.07	16.75	11.27	15.10	1.09	0.87
SrO	0.50	0.71	-	0.59	0.80	-	0.34
Y_2O_3	-	1.23	0.96	-	0.47	-	-
La_2O_3	17.33	9.47	9.72	19.63	15.23	27.90	27.29
Ce_2O_3	28.03	23.27	24.64	32.34	27.27	40.46	39.48
Pr_2O_3	2.48	2.98	2.86	3.04	2.80	3.35	3.13
Nd_2O_3	7.62	12.55	13.40	8.87	9.61	9.39	9.47
Sm_2O_3	-	2.30	2.41	-	1.26	-	-
Gd_2O_3	-	1.46	-	-	-	-	-
ThO_2	-	1.48	-	-	-	-	0.90
F	3.59	3.41	3.35	4.28	4.03	6.01	6.20
-O = F	1.51	1.44	1.41	1.80	1.70	2.53	2.61
Total	**74.67**	**74.48**	**72.67**	**78.07**	**74.88**	**85.66**	**85.08**
Structural formulae calculated on the basis of 3 (Pst), 2 (Syn), and 1 (Bsn) CO_3 group(s)							
Ca	0.83	0.85	0.85	0.89	1.17	0.03	0.03
Sr	0.01	0.02	-	0.03	0.03	-	0.01
Y	-	0.03	0.02	-	0.02	-	-
La	0.30	0.16	0.17	0.53	0.41	0.28	0.29
Ce	0.48	0.39	0.43	0.87	0.72	0.41	0.41
Pr	0.04	0.05	0.05	0.08	0.07	0.03	0.03
Nd	0.13	0.21	0.23	0.23	0.25	0.09	0.10
Sm	-	0.04	0.04	-	0.03	-	-
Gd	-	0.02	-	-	-	-	-
Th	-	0.02	-	-	-	-	0.01
F	0.53	0.50	0.50	1.00	0.92	0.52	0.56
Total	**1.79**	**1.78**	**1.78**	**2.64**	**2.71**	**0.85**	**0.86**

Dash (-) - indicates values are b.d. limits
Syn - Synchysite-(Ce)
Pst - Parisite-(Ce)
Bsn - Bastnaesite-(Ce)

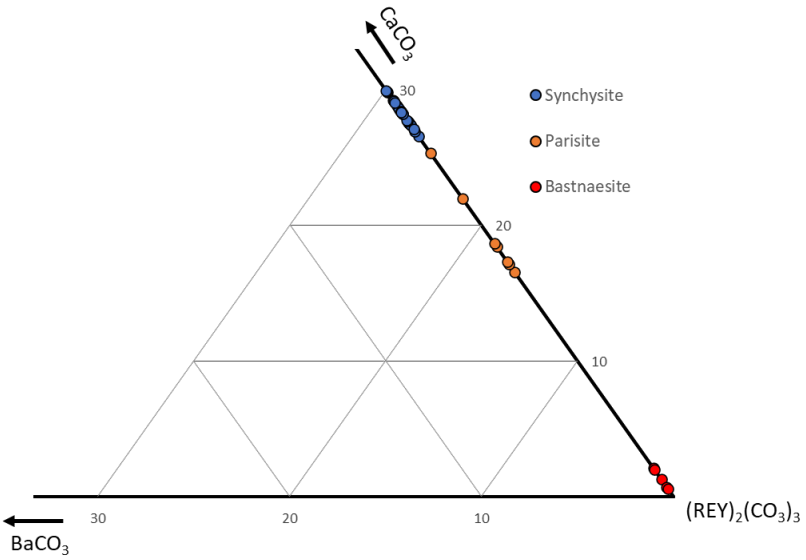

Figure 4.42: Ternary diagram $CaCO_3$ – $BaCO_3$ – $(REY)_2(CO_3)_3$ for the REE-fluorocarbonate compositions from Good Hope.

All the REE-fluorocarbonates can contain SrO with compositions varying from b.d.-to-0.8 wt. % (syn), 0.3-to-1.0 wt. % (pst), and b.d.-to-0.4 wt. % (bsn). Like the REY, the F compositions have an inverse relation to the Ca content, with the F content varying from 2.9-to-4.2 wt. % (syn), 4-to-4.6 wt. % (pst), and 5.9-to-6.3 wt. % (bsn) (Figure 4.43).

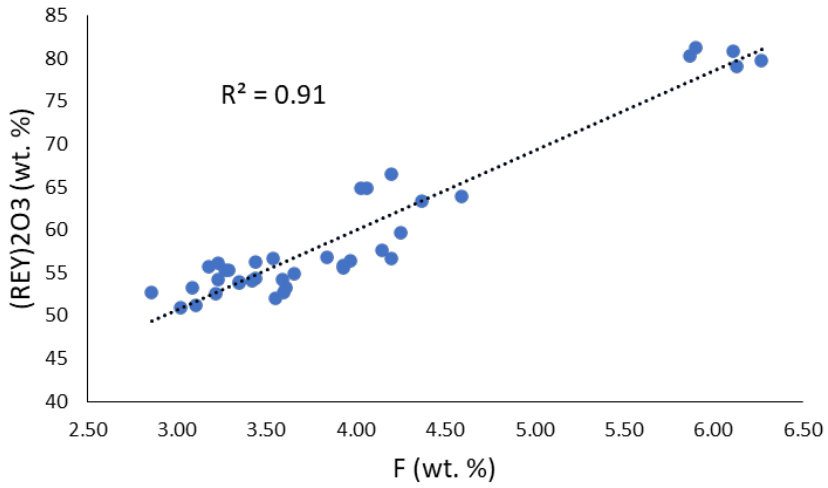

Figure 4.43: REE-fluorocarbonate compositions from Good Hope plotted in the bivariate plot of $(REY)_2O_3$ (wt. %) versus F (wt. %) that shows a strong positive correlation (R^2 = 0.91).

Compositional data for the burbankite from Good Hope were obtained from 22 EDS analyses and are presented in Appendix I. Representative compositions are presented in Table 4.11 with structural formulae calculated on the basis of 1 CO_3 group.

Table 4.11: Representative compositions of burbankite from Good Hope.

	DDH-03-192	DDH-02-42	DDH-07-179	DDH-08-13
Wt. %				
$Na_2(CO_3)$	11.41	16.76	16.98	16.09
$MgCO_3$	-	-	-	2.22
$CaCO_3$	61.00	16.53	25.88	23.16
$MnCO_3$	0.52	-	-	-
$FeCO_3$	-	-	0.66	0.74
$SrCO_3$	27.81	48.54	33.95	38.17
$BaCO_3$	-	1.22	5.87	8.51
$La_2(CO_3)_3$	-	4.52	0.72	2.59
$Ce_2(CO_3)_3$	-	9.56	6.17	5.57
$Pr_2(CO_3)_3$	-	0.71	1.60	-
$Nd_2(CO_3)_3$	-	3.48	7.17	2.17
$Sm_2(CO_3)_3$	-	-	1.34	-
Total	**100.73**	**101.33**	**100.32**	**99.21**
Structural formulae calculated on the basis of 1 CO_3 group				
Na	0.24	0.41	0.40	0.39
Mg	-	-	-	0.03
Ca	0.67	0.21	0.33	0.29
Mn	-	-	-	-
Fe	-	-	0.01	0.01
Sr	0.21	0.42	0.29	0.33
Ba	-	0.01	0.04	0.05
La	-	0.03	-	0.01
Ce	-	0.05	0.03	0.03
Pr	-	-	0.01	-
Nd	-	0.02	0.04	0.01
Sm	-	-	0.01	-
Total	**1.12**	**1.15**	**1.16**	**1.16**

Dash (-) - indicates values are b.d. limits

Burbankite has a large compositional variation with the major carbonates ranging from 11.4-to-19 wt. % (Na_2CO_3), 15.6-to-61 wt. % ($CaCO_3$), 27.8-to-53 wt. % ($SrCO_3$), b.d.-to-11.8 wt. % ($BaCO_3$), and b.d.-to-28.3 wt. % ($REE_2(CO_3)_3$). The minor carbonates range from b.d.-to-2.6 ($MgCO_3$), b.d.-to-0.5 wt. % ($MnCO_3$), and b.d.-to-0.8 wt. % ($FeCO_3$). The REE contents vary from b.d.-to-5.6 wt. % ($La_2(CO_3)_3$), b.d.-to-12.6 wt. % ($Ce_2(CO_3)_3$), b.d.-to-1.6 wt. % ($Pr_2(CO_3)_3$), b.d.-to-7.2 wt. % ($Nd_2(CO_3)_3$), b.d.-to-1.3 wt. % ($Sm_2(CO_3)_3$).

4.11 Rutile

Rutile from Good Hope occurs disseminated in the syenite xenoliths and the carbonatite in trace amounts and can occur as aggregates up to 5 vol. %. The disseminated rutile is subhedral-to-anhedral, ranging from 25-to-150 µm in size, and can be granular or elongate. The aggregate rutile consists of crystals that range from 100-to-300 µm in size and occur in a calcite groundmass (Figure 4.44).

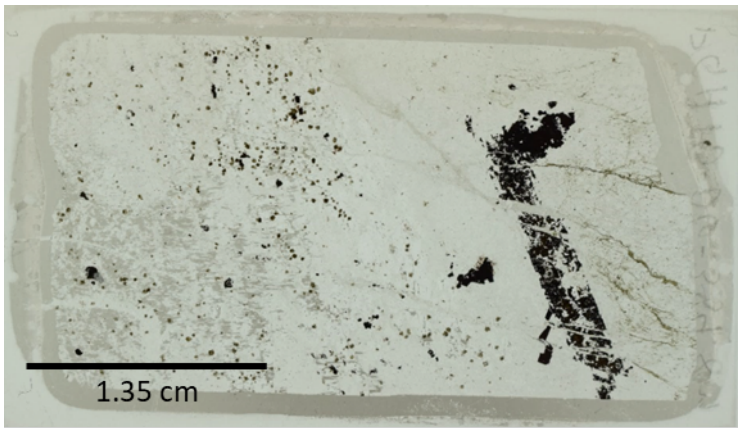

Figure 4.44: Scanned thin section from the Good Hope carbonatite of a rutile aggregate within calcite carbonatite that is cut by veins of ferroan dolomite (PGH-18-06-384).

The disseminated rutile is observed in both the calcite and ferroan dolomite and is commonly associated with silicate phases including K-feldspar, biotite, aegirine, and magnesio-arfvedsonite (Figure 4.45). It can occur as inclusions in apatite and K-feldspar and has been

observed forming along cleavage planes in the core of zoned biotite (Figure 4.35c). Other common associations include apatite, quartz, fluorite, barite, and zircon.

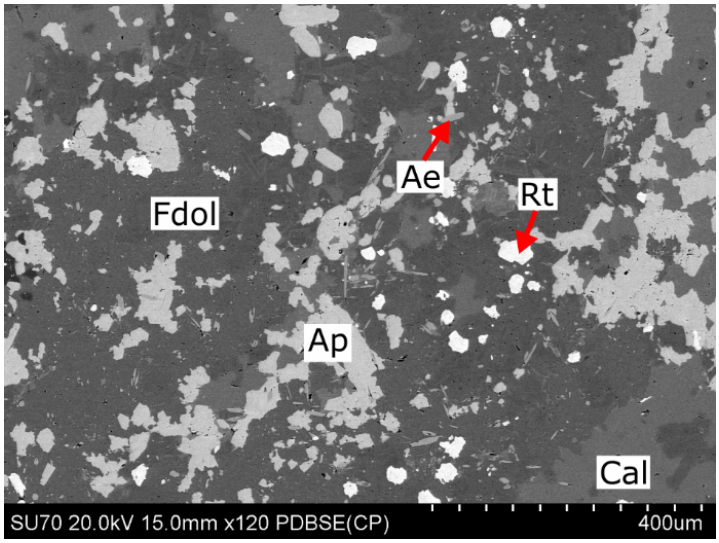

Figure 4.45: BSE image of disseminated rutile from the Good Hope carbonatite with ferroan dolomite + apatite within a calcite groundmass and acicular aegirine (PGH-18-01-79). Abbreviations; rutile (Rt), ferroan dolomite (Fdol), apatite (Ap), calcite (Cal), and aegirine (Ae).

Compositional data for rutile from Good Hope was obtained from 32 EDS analyses and are presented in Appendix I. Representative compositions are presented in Table 4.12 with structural formulae calculated on the basis of two atoms of oxygen. There is a large compositional range for TiO_2 (68.1-to-101.8 wt. %) owing to the variation in Nb_2O_5 (0.5-to-16.1 wt. %) and FeO (b.d.-to-6.2 wt. %). There are several trace elements that are variably incorporated into the rutile structure that range from b.d. to 3.8 wt. % (MgO), 4.2 wt. % (CaO), 1.6 wt. % (Al_2O_3), 6.9 wt. % (V_2O_5), 2.9 wt. % (Cr_2O_3), 6.6 wt. % (SiO_2), 4.2 wt. % (ZrO_2), and 4.1 wt. % (WO_3). Zirconium is only observed in one sample where the rutile occurs with calcite, quartz, and magnetite that are replacing a relict phase (Figure 4.46a).

Table 4.12: Representative compositions of rutile from Good Hope.

	DDH-04-37	02-45.78	PL-S2-PI-2	RW-PL-06	DDH-04-177
Wt. %					
MgO	-	-	-	-	-
Al_2O_3	-	-	-	0.19	-
SiO_2	0.41	-	-	0.35	0.89
CaO	0.63	0.39	3.24	-	-
TiO_2	95.75	81.13	93.79	94.84	78.01
V_2O_5	-	-	-	-	-
Cr_2O_3	-	-	-	2.94	-
FeO	0.57	3.61	-	-	5.39
ZrO_2	-	-	-	-	-
Nb_2O_5	3.20	16.06	4.29	0.56	13.64
WO_3	-	-	-	-	1.71
Total	**100.56**	**101.19**	**101.32**	**98.88**	**99.64**
Structural formulae calculated on the basis of 2 oxygens					
Mg	-	-	-	-	-
Al	-	-	-	-	-
Si	0.01	-	-	-	0.01
Ca	0.01	0.01	0.05	-	-
Ti	0.96	0.85	0.94	0.97	0.84
V	-	-	-	-	-
Cr	-	-	-	0.03	-
Fe	0.01	0.04	-	-	0.06
Zr	-	-	-	-	-
Nb	0.02	0.10	0.03	-	0.09
W	-	-	-	-	0.01
Total	**1.00**	**1.00**	**1.02**	**1.01**	**1.01**

Dash (-) - indicates values are b.d. limits

The rutile can be homogeneous in composition but are more commonly zoned. The zoning is typically patchy due to variation in the Nb content (Figure 4.46b). Concentrically zoned rutile is rarely observed and is not very distinct, with compositional variation mostly in the Nb content.

There are a few concentrically zoned grains within RW-PL-06 and DDH-04-177 that contain a discontinuous, thin outer rim that contains W (Figure 4.46c).

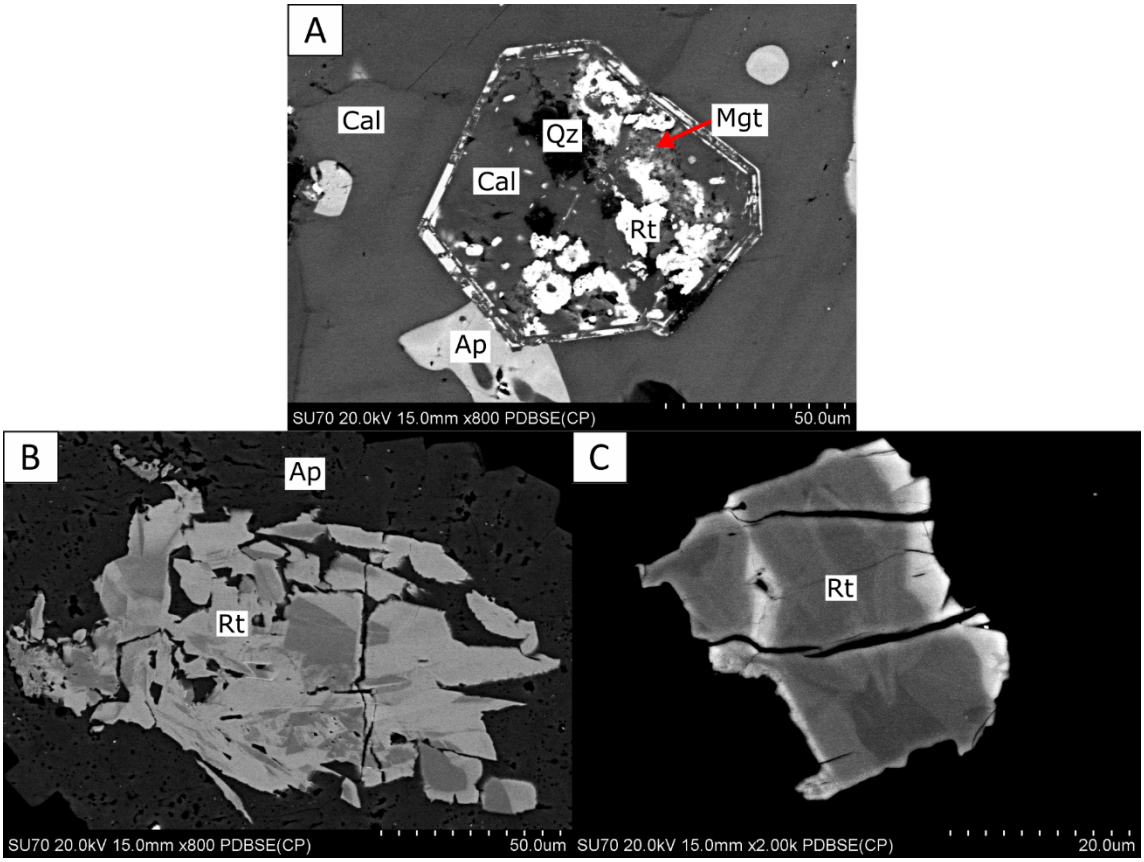

Figure 4.46: BSE images of rutile from the Good Hope carbonatite. (a) Zr-bearing rutile + magnetite + quartz + calcite replace an unknown relict phase (DDH-04-34). (b) rutile in apatite with patchy zonation due to variation in the Nb content (02-45.78). (c) concentric zoned rutile with variation in the Nb content in the core and W-bearing rutile as a discontinuous rim (RW-PL-06). Abbreviations; rutile (Rt), magnetite (Mgt), quartz (Qz), calcite (Cal), and apatite (Ap).

The variation of Nb in rutile is associated with the incorporation of other trace elements that accommodate the substitution of Nb for Ti. The two principal substitution reactions involve either divalent or trivalent cations for charge balance (Win et al., 2017):

$$(1) \qquad 3Ti^{4+} = 2Nb^{5+} + M^{2+}$$

$$(2) \qquad 2Ti^{4+} = Nb^{5+} + M^{3+}$$

The most common element for these substitutions is Fe as it can occur as either a divalent (ferrous) or trivalent (ferric) cation. The bivariate plot of FeO_T (wt. % oxide) versus Nb_2O_5 (wt. % oxide) (Figure 4.47) shows the weak-to-moderate positive correlation ($R^2 = 0.45$) of the Fe and Nb (dashed line). The solid lines show the two possible substitutions with either ferrous or ferric iron (Chakhmouradian et al., 2015).

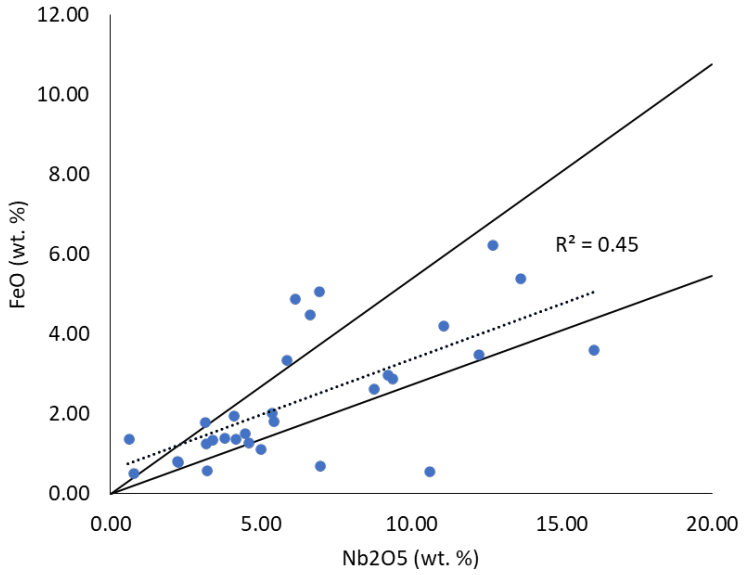

Figure 4.47: Compositions of rutile from Good Hope plotted in the FeO (wt. % oxide) versus Nb_2O_5 (wt. % oxide) bivariate plot showing a weak-to-moderate positive correlation ($R^2 = 0.45$) (dashed line) and the two principal substitution reactions (solid lines) where Nb is accommodated with Fe^{2+} or Fe^{3+}.

Since the compositions do not follow either substitution line there is likely a component of both ferrous and ferric iron. The weak-to-moderate correlation between the Fe and Nb also suggests that other divalent and trivalent cations are participating in the substitution of Nb. The bivariate plot of the divalent cations present in the rutile from Good Hope (Mg and Ca) with Nb (a.p.f.u.) versus Ti (a.p.f.u.) (Figure 4.48a) shows a good negative correlation ($R^2 = 0.82$). The bivariate plot of the trivalent cations present in the rutile from Good Hope (Al, V, and Cr) with Nb (a.p.f.u.) versus Ti (a.p.f.u.) (Figure 4.48b) shows a moderate negative correlation ($R^2 =$

0.68). This suggests the divalent substitution reaction is dominant with less of the Nb being accommodated by the trivalent substitution reaction.

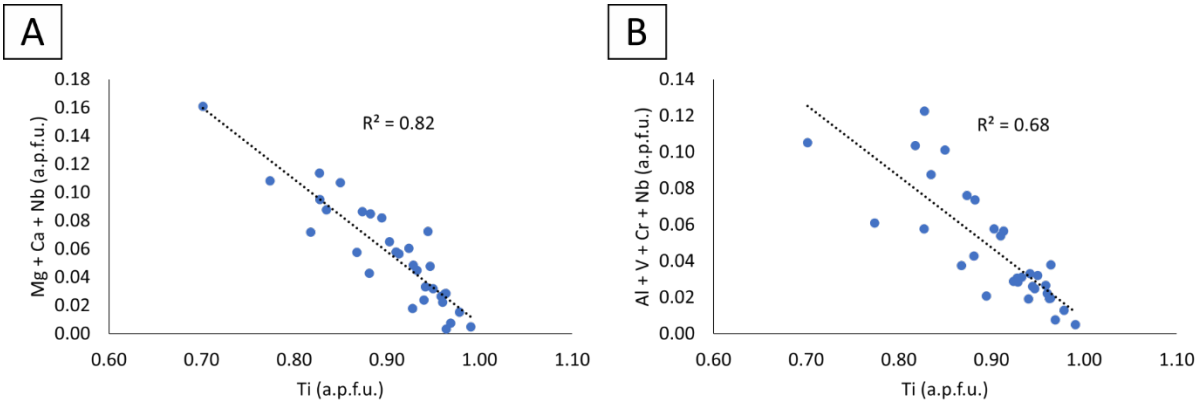

Figure 4.48: Compositions of rutile from Good Hope. (a) Bivariate plot of the divalent cations (Mg and Ca) + Nb (a.p.f.u.) versus Ti (a.p.f.u.) that shows a good negative correlation (R^2 = 0.82). (b) Bivariate plot of the trivalent cations (Al, V, and Cr) + Nb (a.p.f.u.) versus Ti (a.p.f.u.) that shows a moderate negative correlation (R^2 = 0.68).

Tungsten can be accommodated in rutile by a variety of substitutions using the same cations that accommodate Nb. The rare occurrence of W-bearing rutile at Good Hope limited the number of analyses and no substitution could be confirmed.

4.12 Magnetite and Ilmenite

Magnetite occurs in the Good Hope carbonatite from trace amounts up to 5 vol. %. Ilmenite is not observed in the Good Hope carbonatite, but it does occur within the orbicular carbonatite. Within the Good Hope carbonatite the magnetite is dominantly an interstitial phase associated with hydrothermal phases, either as inclusions and intergrowths with calcite, or isolated crystals within the syenite xenoliths associated with quartz, barite, and calcite. These grains can be fibrous-to-acicular or anhedral ranging from 10-to-50 µm in size, rarely up to 100 µm. Inclusions of magnetite occur in apatite, calcite, ferroan dolomite, quartz, K-feldspar, and rarely rutile. It occurs as an interstitial phase in the apatitite clasts (Figure 4.49a),

mantling isolated apatite, and intergrown with calcite that mantles some of the apatitite clasts (Figure 4.49b). Disseminated magnetite is also observed in chlorite aggregates. Associated with the REE-fluorocarbonates, it forms syntaxial intergrowths (Figure 4.49c), mantling the REE phases (Figure 4.49d), or forming very fine-grained clasts entrained in calcite and ferroan dolomite. Magnetite is observed along contacts with different phases, typically forming semi-spherical aggregates of radiating crystals. This is observed at the contact with apatite extending into quartz (Figure 4.49e), at the contact with K-feldspar extending into calcite, at the contact with quartz extending into calcite (Figure 4.49f), and at the contact with ferroan dolomite extending into calcite.

Magnetite is also observed in the orbicular sample from the Good Hope carbonatite, where it occurs within the core and rims. These grains are subhedral-to-anhedral ranging from 50-to-500 µm in size. Two types of magnetite were observed in the orbicular sample: (1) Ti-poor fine-grained crystals, typically occurring in the rims of the orbicules; and (2) Ti-bearing medium-to-coarse-grained crystals that contain trellis-type ilmenite lamellae. The latter typically occur in the core or inner rims of the orbicules (Figure 4.50a).

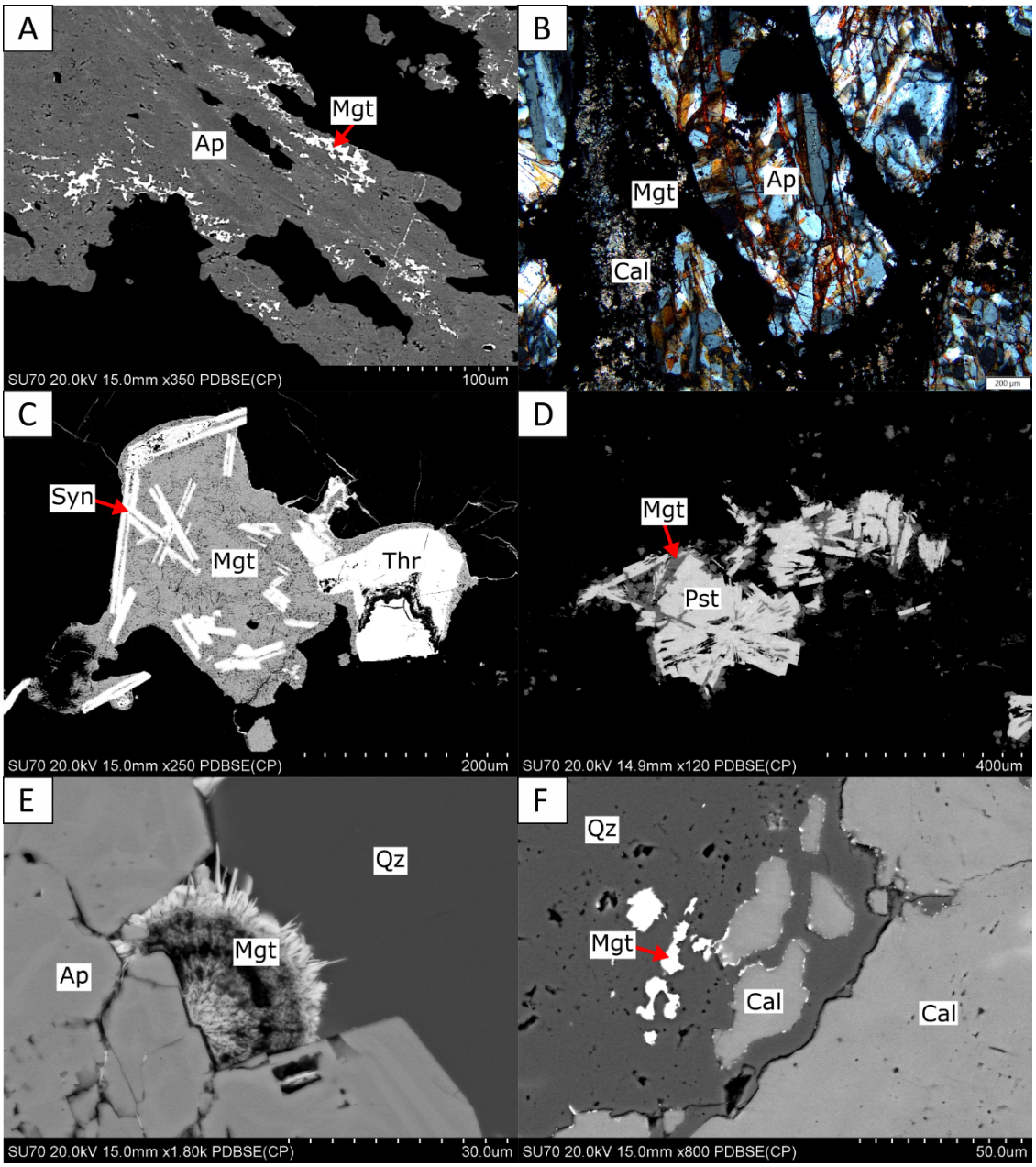

Figure 4.49: BSE images (a), (c)-to-(f) and photomicrograph (b) in cross-polarized light (scale bar in the bottom right is 200 µm) of magnetite from Good Hope. (a) apatitite clast with interstitial magnetite (02-118). (b) magnetite + calcite mantling apatitite clasts (DDH-02-42). (c) fibrous magnetite intergrown with syntaxial synchysite-(Ce) (PL-S2-PI-1). (d) fibrous magnetite mantling lathes of parisite-(Ce) (RHM-06). (e) radiating, globular magnetite at the contact with apatite and quartz (DDH-07-179). (f) globular magnetite forming at the margin of calcite in contact with quartz (PL-S2-PI-1). Abbreviations; apatite (Ap), magnetite (Mgt), calcite (Cal), synchysite-(Ce) (Syn), thorite (Thr), parisite-(Ce) (Pst), and quartz (Qz).

Both types can be associated with fine-grained, granular ilmenite grains that typically occur in contact with the magnetite (Figure 4.50b). It commonly occurs intergrown with the carbonate phases and adjacent to the biotite.

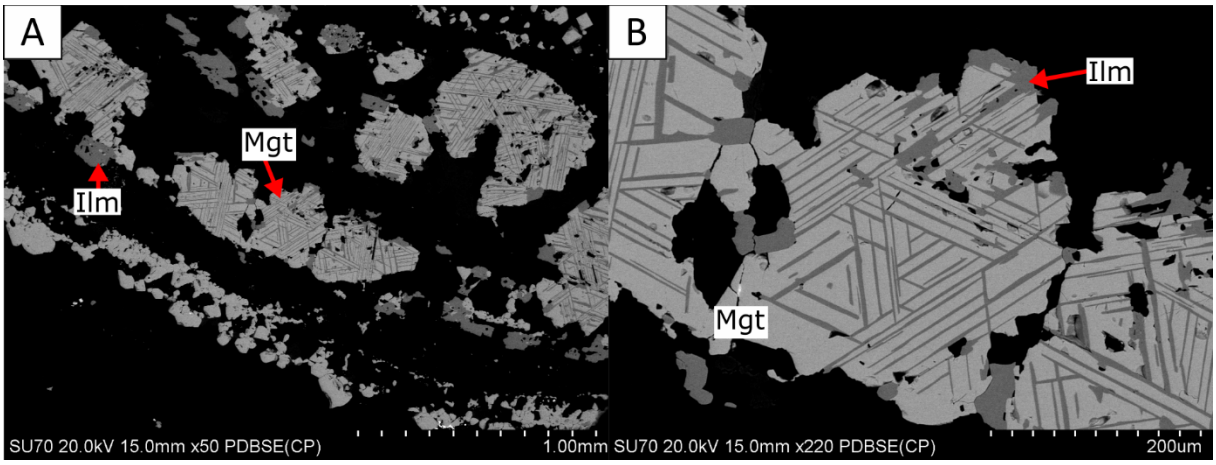

Figure 4.50: Magnetite from the orbicular sample at Good Hope. (a) Two types of magnetite, the fine-grained magnetite in the outer rim and the medium-to-coarse-grained magnetite with trellis-type ilmenite lamellae in the core and inner rim. (b) fine-grained, granular ilmenite at the margins of the magnetite. Abbreviations; magnetite (Mgt) and ilmenite (Ilm).

Compositional data for magnetite from Good Hope were obtained from 42 EDS analyses and for ilmenite from 14 EDS analyses and are presented in Appendix I. The ilmenite compositions are exclusively measured from the orbicular sample as ilmenite is not observed elsewhere. Representative compositions are presented in Table 4.13 with structural formulae calculated on the basis of 4 atoms of oxygen (magnetite) and 3 atoms of oxygen (ilmenite). The compositional ranges are limited for magnetite with the major oxides varying 54.4-to-65.1 wt. % Fe_2O_3 and 24.5-to-31.7 wt. % FeO, with ferric iron calculated by stoichiometry using the method of Droop (1987). The minor oxides within magnetite all vary from b.d. to 1 wt. % (MgO), 2.6 wt. % (Al_2O_3), 7.3 wt. % (SiO_2), 2.5 wt. % (CaO), 1.3 wt. % (TiO_2), 1.2 wt. % (MnO), 3.5 wt. % (Nb_2O_5), and 1.2 wt. % (SnO). Due to the small grain size the analyses likely contain some

contamination from the adjacent phases. The compositional range for ilmenite is more restrictive with the major oxides varying from 48.1-to-49.4 wt. % TiO_2 and 48.5-to-51.1 wt. % FeO. The minor elements include MnO and Nb_2O_5 that range from 0.5-to-0.8 wt. % and 0.3-to-1 wt. %, respectively.

Table 4.13: Representative composition of magnetite and ilmenite from Good Hope.

	DDH-07-179 (Mgt)	**DDH-03-251** (Mgt)	**RHM-12** (Mgt)	**02-118** (Mgt)	**PGH-18-06-416** (Mgt)	**PGH-18-06-416** (Mgt)	**PGH-18-06-416** (Ilm)
Wt. %							
Al_2O_3	0.48	0.58	0.83	0.41	-	-	-
SiO_2	1.79	5.46	6.22	2.08	-	-	-
CaO	1.26	0.34	0.88	0.69	-	-	-
TiO_2	0.33	1.29	-	0.53	0.65	-	48.58
V_2O_5	-	1.96	-	0.23	0.93	1.02	-
MnO	-	-	-	-	-	-	0.61
FeO	26.11	25.95	24.74	26.57	31.08	31.55	50.09
Fe_2O_3	58.03	57.67	54.99	59.01	62.16	63.09	-
Nb_2O_5	-	-	-	3.02	-	-	0.76
SnO_2	-	1.22	-	-	-	-	-
Total	**88.00**	**94.47**	**87.66**	**92.53**	**94.83**	**95.66**	**100.03**
Structural formulae calculated on the basis of 4 oxygens (magnetite) and 3 oxygens (ilmenite)							
Al	0.02	0.03	0.04	0.02	-	-	-
Si	0.08	0.21	0.25	0.08	-	-	-
Ca	0.06	0.01	0.04	0.03	-	-	-
Ti	0.01	0.04	-	0.02	0.02	-	0.94
V	-	0.05	-	0.01	0.02	0.03	-
Mn	-	-	-	-	-	-	0.01
Fe^{2+}	0.93	0.82	0.85	0.90	1.05	1.06	1.08
Fe^{3+}	1.87	1.65	1.70	1.79	1.90	1.91	-
Nb	-	-	-	0.06	-	-	0.01
Sn	-	0.02	-	-	-	-	-
Total	**2.97**	**2.83**	**2.88**	**2.90**	**2.99**	**3.00**	**2.04**

Dash (-) - indicates values are b.d. limits

4.13 Barite

Barite is a late-forming mineral observed in both the calcite and ferroan dolomite carbonatites, as isolated and interstitial anhedral crystals ranging from 50-to-500 µm in size, rarely up to 2 mm (Figure 4.51a). Barite can also occur as inclusions and elongate stringers in the calcite and ferroan dolomite (Figure 4.51b), and as interstitial grains in apatitite clasts. The barite is typically associated with other late-crystallizing minerals, including quartz, chlorite, fluorite, REE-fluorocarbonates, and calcite. Isolated grains occur in veins of chlorite and calcite, intergrown with REE-fluorocarbonates (Figure 4.51c), and intergrown with magnetite ± quartz ± calcite (Figure 4.51d). The barite can occur with pyrite and rutile, where it forms along grain boundaries and as fracture fill. The barite can also form as veins that are commonly discontinuous and are observed cutting earlier quartz veins (Figure 4.51e). In addition to occurring in the carbonatite, barite is also observed in the syenite xenoliths, associated with quartz + magnetite + calcite and in the fluorite clasts associated with calcite + K-feldspar + quartz + thorite + REE-fluorocarbonates (Figure 4.51f).

Compositional data for barite from Good Hope were obtained from 18 EDS analyses and are presented in Appendix I. Representative compositions are presented in Table 4.14 with structural formulae calculated on the basis of four atoms of oxygen. The compositional range is restricted with SO_3 varying from 32.9-to-35.5 wt. % and BaO varying from 60.8-to-68.2 wt. %. The elements that are present in trace amounts include SrO (b.d.-to-3.2 wt. %), CaO (b.d.-to-3.9 wt. %), and FeO (b.d.-to-0.5 wt. %). Some rare compositions have a greater component of celestine and contain up to 33 wt. % SrO. Strontium, Ca, and Fe easily substitute in the Ba site as they have the same valence.

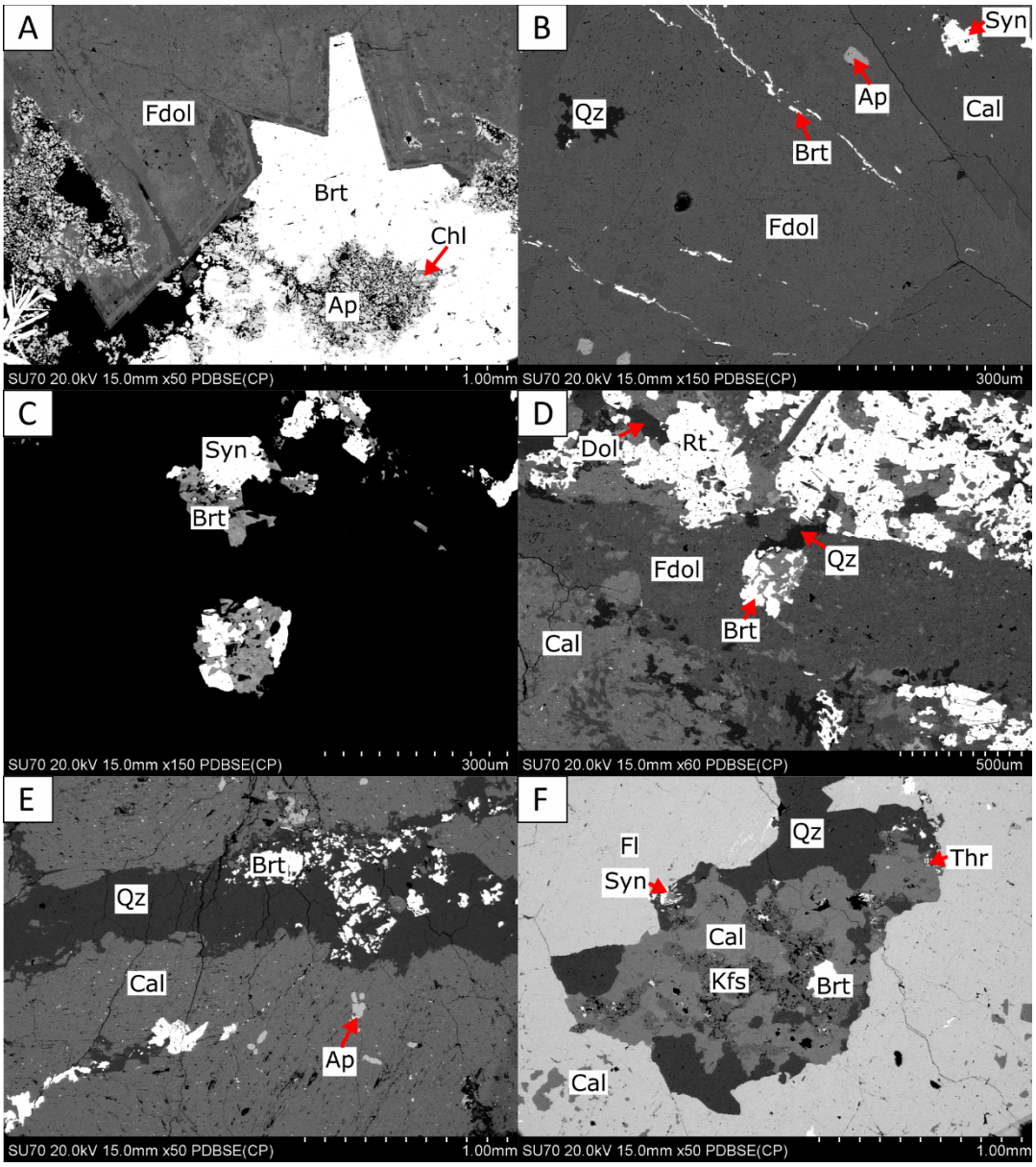

Figure 4.51: BSE images of barite from Good Hope. (a) coarse-grained interstitial barite intergrown with apatite + chlorite (DDH-08-13). (b) stringers of barite within ferroan dolomite (DDH-04-37). (c) intergrown barite + synchysite-(Ce) (DDH-07-103). (d) intergrown barite + calcite within a ferroan dolomite vein (PGH-18-06-384). (e) discontinuous barite vein cutting an earlier quartz vein (RW-PL-02). (f) isolated barite in a clast of calcite + K-feldspar + quartz that is entrained in a fluorite clast (PL-S2-PI-1). Abbreviations; ferroan dolomite (Fdol), barite (Brt), apatite (Ap), chlorite (Chl), quartz (Qz), calcite (Cal), synchysite-(Ce) (Syn), dolomite (Dol), rutile (Rt), K-feldspar (Kfs), fluorite (Fl), and thorite (Thr).

Table 4.14: Representative compositions of barite from Good Hope.

	02-118	DDH-04-37	DDH-08-13	DDH-04-666	PGH-18-06-384
Wt. %					
SO_3	34.50	34.42	33.16	35.00	33.90
CaO	-	0.41	0.65	-	-
FeO	-	-	0.32	0.36	-
SrO	1.56	-	-	-	-
BaO	64.40	67.94	66.22	66.41	66.54
Total	**100.46**	**102.77**	**100.35**	**101.77**	**100.44**
Structural formulae calculated on the basis of 4 oxygens					
S	1.00	0.99	0.98	1.00	0.99
Ca	-	0.02	0.03	-	-
Fe	-	-	0.01	0.01	-
Sr	0.03	-	-	-	-
Ba	0.97	1.02	1.02	0.99	1.02
Total	**2.00**	**2.02**	**2.04**	**2.00**	**2.01**

Dash (-) – indicates values are b.d. limits

4.14 Quartz

Quartz occurs in most of the samples from Good Hope, in both the carbonatite and as a minor component in the syenite xenoliths. It typically forms an interstitial phase that may be poikilitic, entraining grains of calcite, ferroan dolomite, and apatite (Figure 4.52a). It is common for the quartz to form anhedral blebs, however there is one occurrence of euhedral quartz that forms extending into calcite at the margin with an aggregate of quartz + chlorite + magnetite ± apatite (Figure 4.52b). More typical is that the carbonate phases are euhedral extending into the interstitial quartz (Figure 4.8a). The quartz can also occur within the apatitite clasts, typically forming along the grain boundaries of the apatite, that may form a network-type texture (Figure 4.52c). It is common for the quartz to form veins that cut the apatitite clasts and

carbonatite and typically have anastomosing margins that will entrain grains of the groundmass (Figure 4.52d).

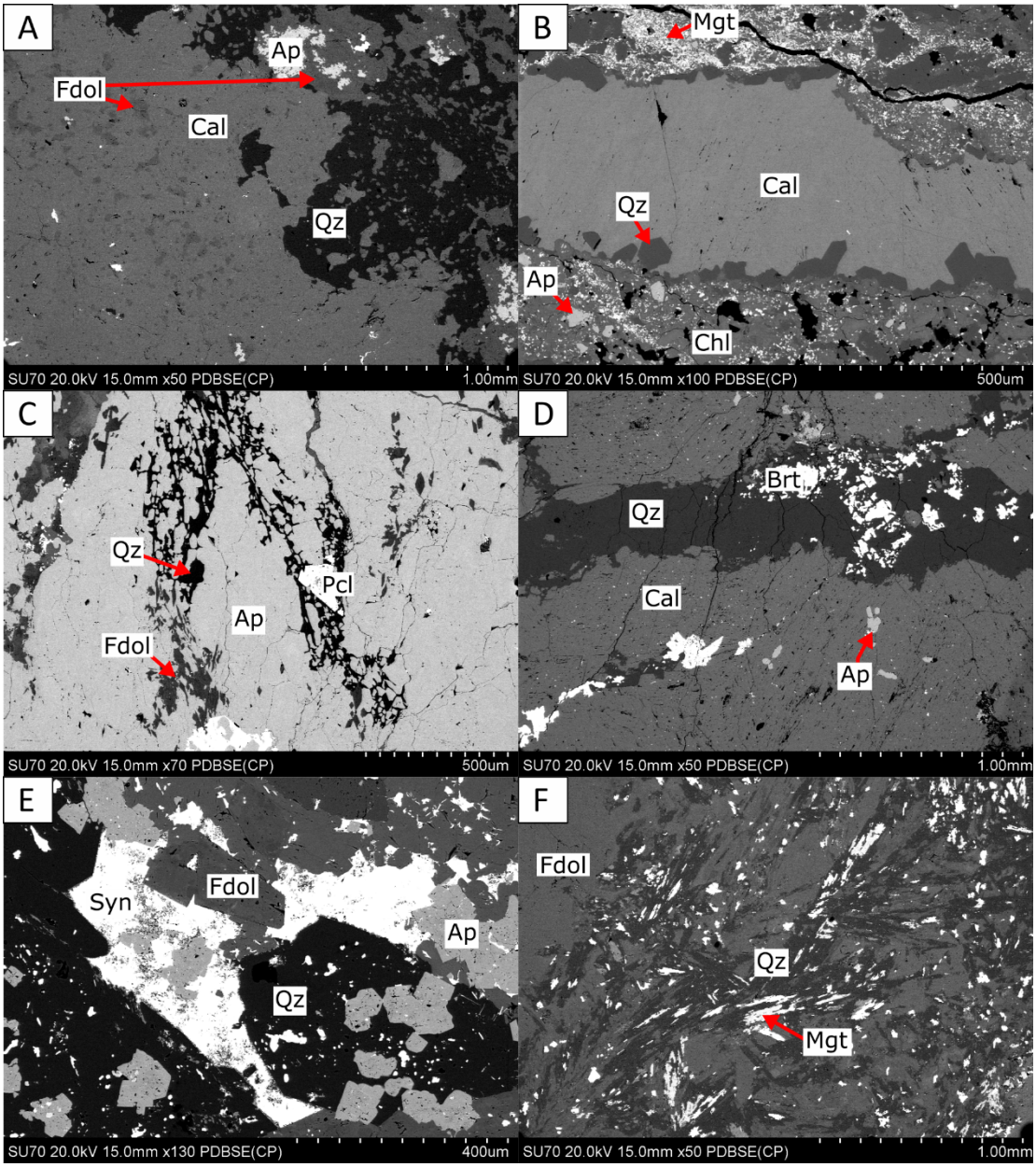

Figure 4.52: BSE images of quartz from Good Hope. (a) poikilitic quartz with entrained calcite and ferroan dolomite (02-118). (b) euhedral quartz extending into calcite (RHM-07). (c) network-type texture of quartz within an apatitite clast (PGH-18-06-384). (d) quartz vein with anastomosing margins cutting a calcite carbonatite (RW-PL-02). (e) quartz associated with synchysite-(Ce), ferroan dolomite, and apatite, the quartz contains inclusions of synchysite-(Ce) (DDH-04-666). (f) dendritic quartz with intergrown magnetite (RW-PL-06). Abbreviations; calcite (Cal), ferroan dolomite (Fdol), apatite (Ap), quartz (Qz), chlorite (Chl), magnetite (Mgt), pyrochlore (Pcl), barite (Brt), and synchysite-(Ce) (Syn).

The quartz occasionally contains inclusions or very fine, entrained grains of strontianite, chlorite, magnetite, REE-fluorocarbonates, and aegirine. Quartz is commonly intergrown with other phases forming clasts in the carbonatite groundmass including chlorite + apatite, chlorite + magnetite, ferroan dolomite + apatite + REE-fluorocarbonates (Figure 4.52e), calcite + barite, and thorite. Quartz is observed forming dendritic crystals within ferroan dolomite with associated magnetite (Figure 4.52f). Within the calcite carbonatite quartz occurs mantling acicular magnesio-arfvedsonite and has also been observed mantling REE-fluorocarbonates. The quartz is typically associated with the medium-grained REE-fluorocarbonates throughout the carbonatite. It is also a common phase adjacent and intergrown with the fluorite clasts that are typically associated with some REE-fluorocarbonates (Figure 4.8d).

4.15 Fluorite

Fluorite occurs as an interstitial phase as anhedral crystals 10-to-200 μm in size, and ~2 cm clasts consisting of aggregates of crystals (Figure 4.53). The fluorite clasts typically entrain isolated grains and aggregates of quartz ± calcite ± K-feldspar ± barite ± thorite ± REE-fluorocarbonates (Figure 4.54a).

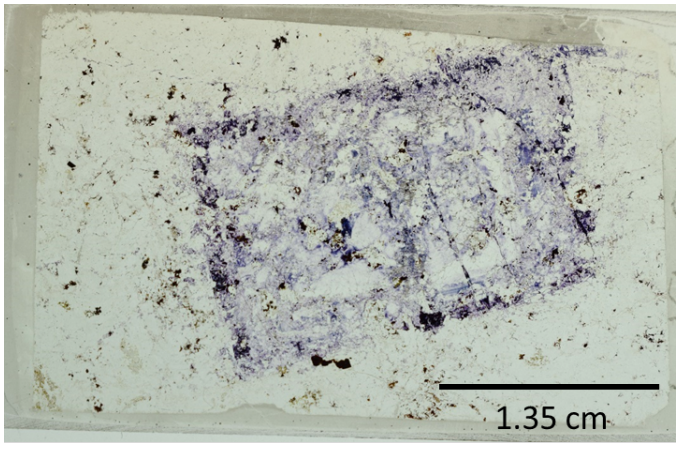

Figure 4.53: Scanned petrographic thin section of sample PL-S2-PI-1 showing fluorite that occurs within a calcite carbonatite with abundant quartz veins.

Fluorite is commonly associated with quartz and can occur as isolated grains within quartz veins. Although occurring in the ferroan dolomite, it is more commonly observed in the calcite carbonatite. Within the calcite carbonatite, the fluorite can occur as isolated crystals and rarely as inclusions, and as intergrowths with REE-fluorocarbonates ± thorite. Fluorite is also interstitial to the elongate apatitite clasts within the calcite carbonatite. Within the ferroan dolomite and K-feldspar groundmass, fluorite is observed in trace amounts in clasts with intergrown quartz ± ferroan dolomite ± chlorite ± biotite (Figure 4.54b).

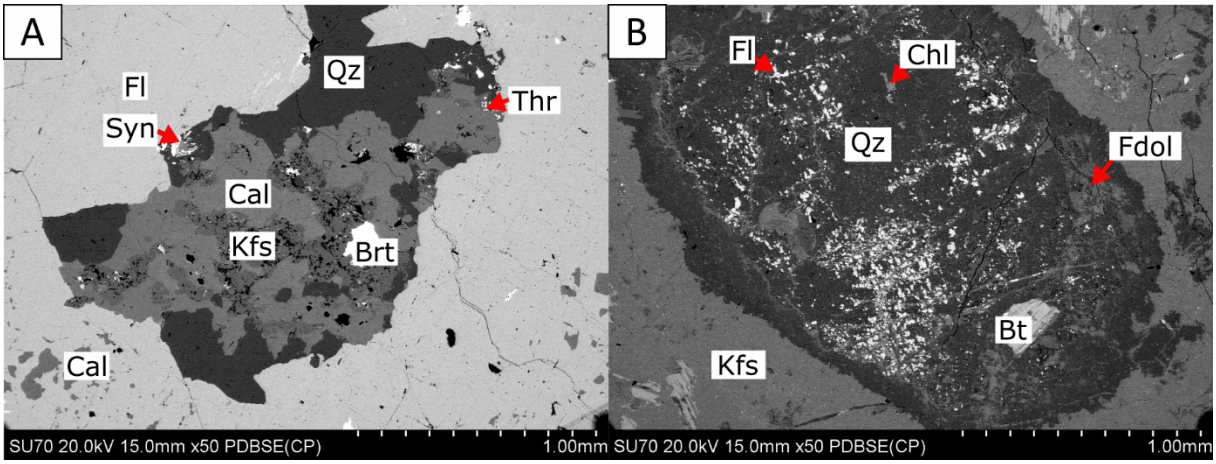

Figure 4.54: BSE images of fluorite from Good Hope. (a) clast of calcite + K-feldspar + quartz + barite + thorite + synchysite-(Ce) within the fluorite clast (PL-S2-PI-1). (b) quartz clast with intergrown fluorite + ferroan dolomite and isolated chlorite and biotite within the ferroan dolomite + K-feldspar groundmass (RW-PL-06). Abbreviations; calcite (Cal), K-feldspar (Kfs), quartz (Qz), synchysite-(Ce) (Syn), thorite (Thr), barite (Brt), fluorite (Fl), ferroan dolomite (Fdol), chlorite (Chl), and biotite (Bt).

Chapter 5. Orbicular Carbonatite Occurrence

The Good Hope carbonatite hosts xenolith clasts of an orbicular carbonatite whose source and relationship to the Good Hope carbonatite is unknown. This occurrence is of particular interest as the adjacent Prairie Lake complex also contains bands of this unusual texture within the ijolite and may support a relationship between Prairie Lake and Good Hope. A description of the orbicular carbonatite from Good Hope and a summary of the description by Zurevinski and Mitchell (2015) of the orbicular ijolite from Prairie Lake are presented. A general comparison of the two orbicular occurrences and a possible model of formation for the Good Hope orbicular carbonatite is discussed.

Good Hope Orbicular Carbonatite

The orbicular carbonatite occurrence was found at depth (~416 m depth) in the drill core (PGH-18-06) as xenolith clasts, 5-to-10 cm in size, entrained within the Good Hope carbonatite complex (Figure 5.1). The orbicules are millimetre in size and spherical-to-oblate in shape with random orientations (Figure 5.2). The elongate shape with random orientation is suggested to be caused by plastic deformation in a turbulent environment in a low viscosity host.

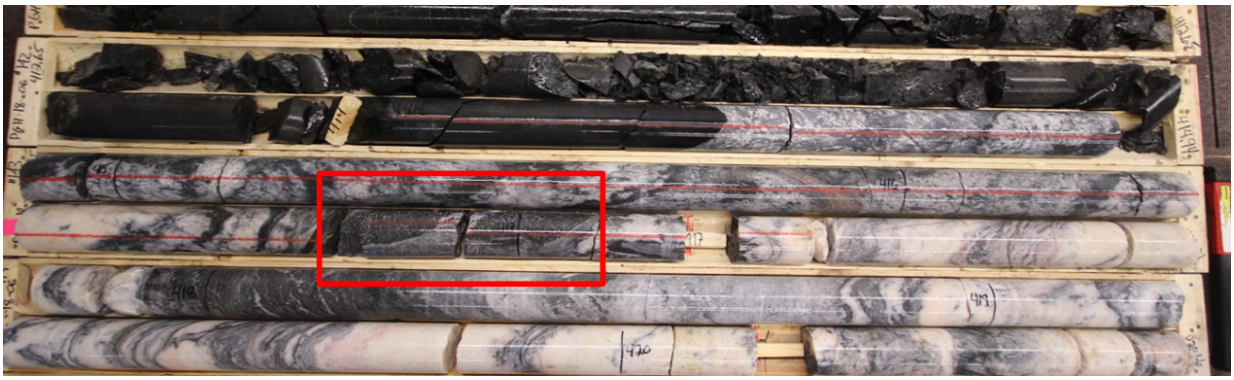

Figure 5.1: Wetted drill core PGH-18-06 (412.6-to-420.6 m) showing the location of the xenolith clasts of the orbicular carbonatite (red box) entrained within the host Good Hope carbonatite.

The orbicules predominantly consist of multiple discrete shells, although they can occur as spherical aggregates with indistinct shells (Figure 5.3a and b). The shells typically surround an indistinct core that has a similar texture to the shells. The shells consist of granular, anhedral minerals with no preferred orientation and of tangential minerals aligned parallel to the margins of the orbicules (Figure 5.3a). The host carbonatite is equigranular, medium-grained, and anhedral with 120° triple points defining an allotriomorphic equilibrated texture (Figure 5.3c). The contacts between the orbicules and the host is variable and can be sharp and distinct or intergrown and discontinuous (Figure 5.3d). The host can also be entrained as one of the outer shells in the orbicules with distinct shells and intergrown in the core of the spherical, indistinct aggregates.

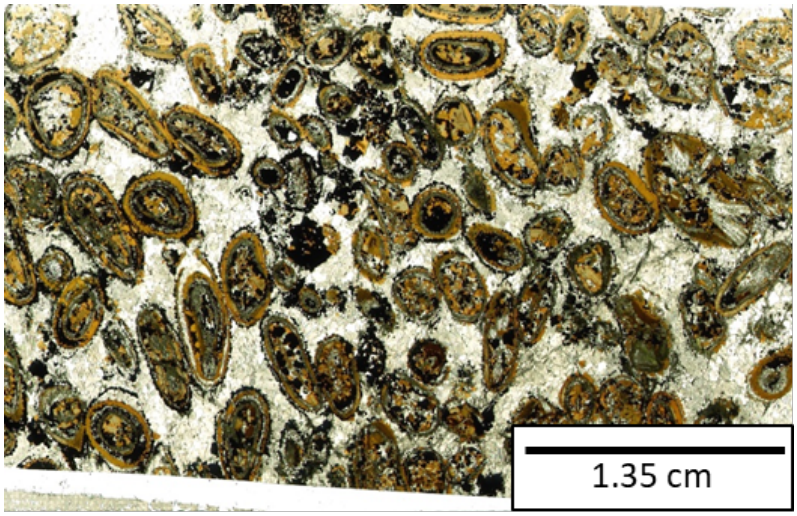

Figure 5.2: Scanned petrographic thin section of sample PGH-18-06-416, the single orbicular occurrence at the Good Hope carbonatite complex.

The orbicules consist of magnetite, ilmenite, aegirine, ferroan dolomite, and phlogopite and occur in a calcite carbonatite host. They are devoid of a distinct core however the cores sometimes contain entrained material of the host calcite carbonatite. There are two types of

magnetite: (1) medium-grained, granular that is Ti-bearing with trellis-type ilmenite exsolution lamellae; and (2) fine-grained, granular that has little to no Ti (Figure 4.50). The type 1 magnetite, with associated ilmenite, commonly occurs in the cores of the orbicules that can also contain phlogopite and rarely calcite. The orbicules tend to develop monomineralic shells composed of aegirine ± ferroan dolomite, tangential phlogopite, type 2 magnetite, or rarely calcite. The composition of the phlogopite in the core and shells of the orbicules is similar, with both containing variable zonation in the Fe and Ti content (Figure 5.3b).

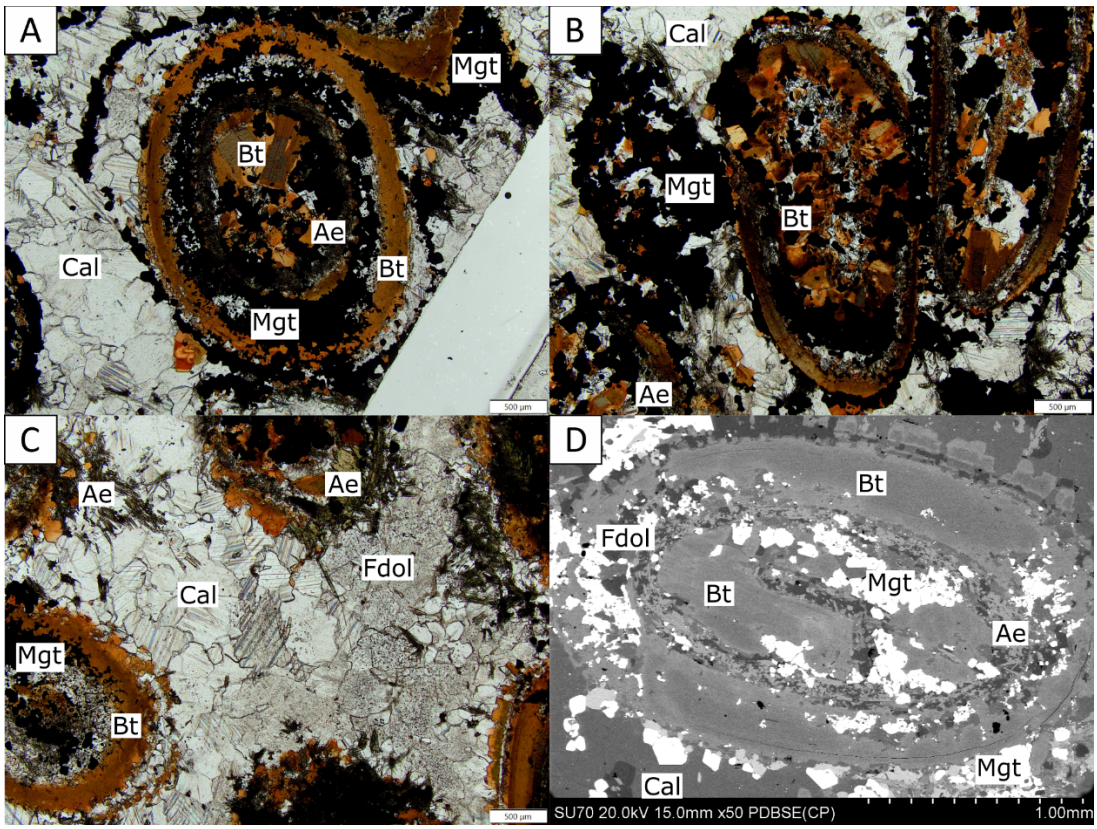

Figure 5.3: Photomicrographs in plane-polarized light (a), (b), and (c) (scale bar in the bottom right is 500 µm) and BSE image (d) of the orbicular carbonatite. (a) orbicule with thin, distinct shells. (b) orbicule with indistinct shells. (c) host calcite that have irregular grain boundaries, but several 120° triple points. (d) orbicule contact with the host is variable and can be sharp or intergrown and discontinuous. Abbreviations; calcite (Cal), biotite (Bt), aegirine (Ae), magnetite (Mgt), and ferroan dolomite (Fdol).

The margins of the orbicules in contact with the calcite carbonatite tend to be sharp if the external shell is tangential phlogopite. Where the external shell is Ti-poor magnetite, the contact is typically discontinuous and intergrown with the host calcite. The calcite carbonatite host contains isolated, anhedral ferroan dolomite and disaggregated Ti-poor magnetite and aegirine (Figure 5.3c).

Prairie Lake Orbicular Ijolite

Zurevinski and Mitchell (2015) have described the orbicular ijolite that occurs within the Prairie Lake carbonatite complex. This occurrence is predominantly found in frost-heaved blocks but is also observed in drill core at depth (~115 m depth). Both types of occurrences are found in distinct bands less than a meter wide. The host of the Prairie Lake orbicules is medium-grained nepheline ijolite. The occurrence consists of two populations of orbicules, large (3-to-5 cm diameter) and mini (1-to-1.5 cm) that commonly have a slight oblate shape. Zurevinski and Mitchell (2015) interpret this oblate shape to represent loading and subsequent plastic deformation of the orbicules during magmatic sedimentation.

The Prairie Lake large and mini orbicules occur in close spatial proximity but are not observed in the same sample. They have the same mineralogy and texture, except the mini orbicules are devoid of the equigranular core that is common in the large orbicules. The equigranular core is leucocratic and mineralogically distinct resembling the host ijolite. The Prairie Lake orbicules are characterized by contrasting concentric bands of leucocratic and melanocratic minerals and can contain up to 30 bands (large orbicules). In addition to the concentric bands, some orbicules contain radial outward zoning from their core that terminate and are surrounded by a subsequent concentric zone. The orbicules that contain a core also

commonly contain radial, skeletal-like growth in contact with the concentric shells indicative of rapid crystallization consistent with quenching. The shells in the large and mini orbicules can be thin and monomineralic or wider and composed of several minerals with each of the orbicules being unique, exhibiting variable thickness and quantity of shells.

The dominant phases in the cores of the Prairie Lake orbicules are diopside and calcite, while apatite occurs in close association with garnet. The quench phases include diopside, calcite, K-feldspar, and melilite with minor Ti-magnetite, sphalerite, and perovskite. The radial zone consists predominantly of nepheline and garnet where the garnet contains inclusions of Ti-magnetite. Each concentric band contains a dominant mineral, either garnet, phlogopite, or nepheline. Alteration assemblages are also recognized and include zeolites, calcite, and cancrinite that are likely altering nepheline and K-feldspar. The contact between the orbicules and the host ijolite is interlocking and dominated by the fine-grained quenching textures. The texture and common composition between the Prairie Lake orbicules and host suggests the orbicular ijolite is the result of interaction between partially crystallized, quenched ijolite melt in contact with subsequent pulses of ijolitic magma. This interaction would result in annealing recrystallization that produced monomineralic layers sequentially from the margins to the core.

Discussion

The Good Hope orbicular carbonatite has a distinctly different texture and mineralogy from the Prairie Lake orbicular ijolite, suggesting a different process of formation. The most distinct difference from the Prairie Lake orbicular ijolite, is the variation in the composition of the orbicules and the host in the orbicular carbonatite. The orbicules are dominated by silicates

and magnetite whereas the host is dominantly calcite, which suggests they are a transported assemblage. In addition to containing evolved minerals (i.e., aegirine), the orbicules also contain two types of magnetite: Ti-bearing magnetite with ilmenite lamellae and granular magnetite with Ti contents below the detection limit (< 0.1 wt. % TiO_2). This could indicate the magnetite crystallized at different times under different conditions as elements such as Ti are generally immobile, thus physical conditions can influence their incorporation into magnetite (Chen et al., 2019). The Ti contents of the granular magnetite are below detection limits (Ti < 600 ppm) suggesting they are hydrothermal magnetite. The Ti contents for the magnetite with ilmenite lamellae range from 1800 ppm to 7000 ppm suggesting a magmatic origin. This is supported by the magmatic magnetite generally occurring in the core or inner shells of the orbicules while the hydrothermal magnetite occurs in the outer shells.

The composition of magnetite and ilmenite pairs are useful geothermometers and can be used to determine the fO_2 of the magma at the time of crystallization. The magnetite and ilmenite data for the orbicular occurrence are within the scope of the original calibration for the method by Yavuz (2021) and results in a temperature range of 517-to-575°C and an fO_2 range of log -19.8-to- -22.7 for the Ti-bearing magnetite and associated ilmenite. The temperature and oxygen fugacity values are consistent with values observed for other carbonatites (Phalaborwa, South Africa; Milani et al., 2017). Figure 5.4 indicates that as temperatures decrease the oxygen fugacity also decreases, with values that fall along the nickel-nickel oxide fugacity buffer (Milani et al., 2017). This supports the Ti-bearing magnetite being a magmatic phase and that the orbicular occurrence is a xenolith. The lack of associated ilmenite with the Ti-poor, granular magnetite prevents the determination of the temperature at the time of crystallization. The

generally lower concentrations of Ti in hydrothermal magnetite from carbonatites supports it being hydrothermal and likely formed at lower temperatures.

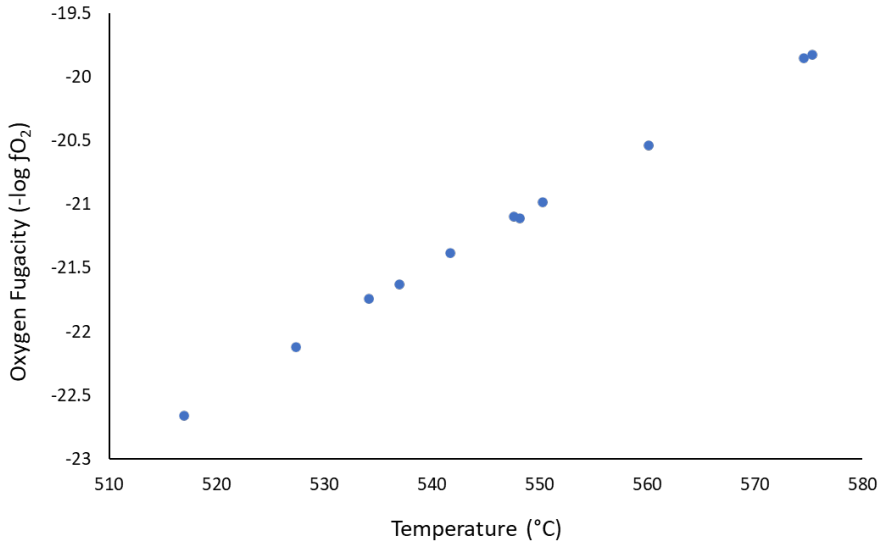

Figure 5.4: Plot of oxygen fugacity (-log fO_2) versus temperature (°C) for the Ti-bearing magnetite and associated ilmenite using the WinMIgob software created by Yavuz (2021) for the orbicular carbonatite from the Good Hope carbonatite.

In general, the models for orbicular formation can fit into three groups: (1) liquid immiscibility; (2) superheating that lowers the nucleation rate and increases the growth rate; (3) quenched recrystallization following the injection of magma. The absence of xenolith cores, radial growth of minerals in the shells, and fractional crystallization in the formation of the shells and host suggests there was no magma mixing or superheating of the host that supressed nucleation. The presence of trellis-type ilmenite lamellae within Ti-bearing magnetite, magnetite with Ti contents below detection limits, as well as V-bearing aegirine suggest there was an influx of hydrothermal fluids. The degree to which these fluids played in the formation of this orbicular occurrence remains speculative. Surface tension effects could have aided in the formation of the orbicules as they are significant in silicate-carbonate melts. If the Ti-bearing

magnetite is magmatic, it may have crystallized elsewhere and been entrained in the current host and suggests that the fluids that formed the hydrothermal magnetite were not enriched in Ti. The Ti-poor magnetite and aegirine within the host and in the orbicules have similar compositions, suggesting disaggregation of some orbicules, or they crystallized late in the host and were not incorporated into the orbicules. Either could be true, with the disaggregation supported by the soft-shell deformation observed in the elongation and oblate shape of the orbicules present. It is also easy to see the possibility of the more evolved aegirine and Ti-poor magnetite being late to crystallize and not being incorporated into the orbicules due to the more crystalline host. The presence of the intergrown host calcite and Ti-poor magnetite in some of the contacts between the host and the orbicules also supports the Ti-poor magnetite crystallizing late in a more crystalline host. This would support fractional crystallization playing a role in the formation of this orbicular occurrence.

Chapter 6. Discussion

6.1 Paragenesis

The primary objectives of this research are to characterize the carbonate and silicate mineralogy of the Good Hope carbonatite, to classify the carbonatite and discuss the petrogenesis of this occurrence. The secondary objectives are to provide a general comparison with the Prairie Lake carbonatite complex, including a comparison of the orbicular occurrences from each complex, and discuss the possible implications of a genetic link.

Good Hope Carbonatite Mineralogy

The major minerals in the Good Hope carbonatite include calcite, ferroan dolomite, and apatite. The apatite typically occurs as apatitite clasts or disaggregated clasts and can occur in either a calcite groundmass or a ferroan dolomite groundmass. It is also common for the ferroan dolomite to mantle the apatitite clasts within a calcite groundmass (Figure 4.3a). The minor phases, which in some samples can comprise up to 20 vol. % of the rock, include K-feldspar, magnesio-arfvedsonite, biotite-phlogopite, aegirine, quartz, chlorite, magnetite, barite, pyrochlore, albite, and fluorite. The accessory minerals include pyrite, synchysite-(Ce), rutile, strontianite, thorite, parisite-(Ce), bastnaesite-(Ce), burbankite, and zircon. These commonly occur as inclusions in the carbonates and occur as isolated grains that can be up to a few millimeters. Syenite xenoliths occur in the carbonatites and range from cm-to-tens of cm in size and typically contain a reaction rim of fresh phlogopite. These xenoliths consist of K-feldspar, magnesio-arfvedsonite, biotite-phlogopite, aegirine, and quartz.

The Good Hope occurrence can be classified as a carbonatite using the IUGS classification that defines a carbonatite as any igneous rock that contains more than 50 vol. %

magmatic carbonate and less than 20 vol. % silicate minerals (Le Maitre, 2002). Using the genetic classification of Mitchell (2005), it can be further classified as containing both calcite carbonatite and ferroan dolomite carbonatite. Due to the modal mineralogical differences that vary extensively over short distances it is more beneficial to classify the Good Hope carbonatite on the basis of the genetically related rocks that make up the complex. This classification will be further discussed in section 6.2 of this chapter that considers the relationship to the Prairie Lake carbonatite.

Apatite is an early crystallizing phase as evidenced by its “pill-like” morphology (Figure 4.1a), the cumulate clasts of apatitite, and the association with pyrochlore. This “pill-like” morphology is characteristic of apatite that crystallized early in plutonic carbonatite complexes (Chakhmouradian et al., 2017) and is observed at the Aley Nb deposit, Canada (Chakhmouradian et al., 2015), the Ambadongar carbonatite complex, India (Dhote et al., 2021), the Oka carbonatite complex, Canada (Chen and Simonetti, 2013), and the Okorusu carbonatite complex, Namibia (Cangelosi et al., 2020). Mitchell et al. (2020) provide REE distribution patterns for apatite from four apatitite clasts from Good Hope that show similar trends with a flat-to-slight positive slope from La-Nd and a steep, straight, negative slope from Sm-Yb (Figure 6.1). Chakhmouradian et al. (2017) show that REE are compatible with respect to apatite and expect the residual melt to become depleted, especially in the LREE, as the apatite would be expected to incorporate the LREE readily during early crystallization. There is also evidence of dissolution of the apatite which could influence the REE budget of the apatite (Figure 4.4a).

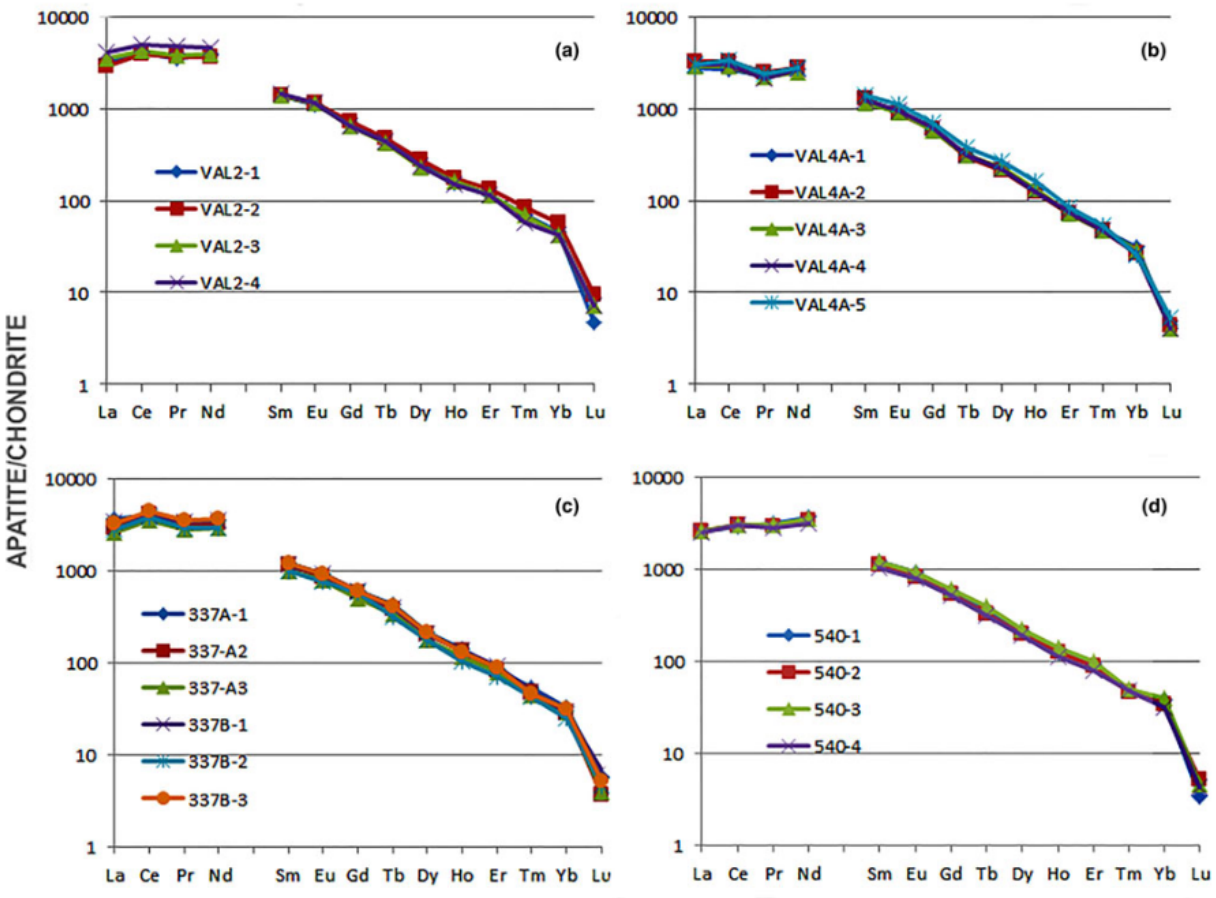

Figure 6.1: Chondrite-normalized REE distribution patterns for apatite from Good Hope taken from four different apatitite clasts (from Mitchell et al., 2020). Samples (a) VAL2 and (b) VAL4A are from near surface exploration pits. Samples (c) 337 and (d) 540 are from different depths (m) within the complex from 60° and 50° inclined drill cores.

The CL images of apatite show crystallization of apatite followed by a period of dissolution prior to further crystallization and dissolution (Figure 4.3b and c). This unusual morphology of carbonatitic apatite is proposed to be due to interaction with the host melt and other cumulus phases that result in the erosion of the euhedral crystal faces (Chakhmouradian et al., 2017). The rounded to elongate nature of the majority of the apatitite clasts and the disaggregated nature of the apatite within the carbonatitic groundmass supports the

accumulation and subsequent remobilization within the carbonatite magma (Figure 4.1b). This further supports multiple pulses of carbonatitic magma within the system.

From the CL spectra of apatite, the broad blue peak is centred around 450 nm, which may indicate the presence of Eu^{2+} in the apatite structure (Figure 4.3d). This broad peak in the blue portion of the spectrum is difficult to resolve and could also indicate the presence of Ce and Dy. If there is Eu^{2+} substituting in the apatite structure for Ca^{2+} this would suggest reducing conditions. The presence of oxides, such as magnetite and sulfates, such as barite, which incorporates oxidized sulfur species, supports an oxidizing environment (Farrell et al., 2010). Changing conditions from a reducing environment to an oxidizing one is suggested to occur at the Amba Dongar carbonatite complex (Dhote et al., 2021). Mitchell and Krouse (1975), propose that decreasing temperatures in carbonatite magmas results in the formation of increased oxidized species at the expense of reduced species. Crystallization of calcite and apatite occurs early in the magmatic sequence, while precipitation of magnetite and barite are late, during the hydrothermal phase. This supports an initially reducing system at higher temperature that progressively changes to an oxidizing one with decreasing temperature.

The pyrochlore associated with the apatitite clasts are euhedral-to-subhedral, ranging from 25-to-1000 μm and up to 3 mm in size (Figure 4.18). The association with the apatitite clasts and the euhedral habit suggests the pyrochlore was an early crystallizing phase. Smaller pyrochlore crystals also occur within the ferroan dolomite and later-stage carbonatites and can contain inclusions of magnesio-arfvedsonite and barite (Figure 4.19f). These pyrochlore are not derived from the disaggregation of the apatitite clasts and appear to be primary in the late-stage carbonatites. Both types of pyrochlore commonly have some degree of concentric or

patchy zonation and are typically replaced by either fersmite, columbite-(Fe) or both (Figure 4.19). The zonation is mostly patchy and due to slight variation in the Sr, Na, Ca, or Ti content. The larger compositional variations result from alteration to fersmite or columbite-(Fe), with increased Ba and Sr contents in fersmite and higher Fe contents in the columbite-(Fe). These elements are accommodated in the pyrochlore structure by the loss of Na and Ca and the formation of A-site vacancies (Figure 4.22). Some of the replaced pyrochlore can have a pitted appearance that could be attributed to dissolution (Figure 4.19e). Interestingly, the pyrochlore are rarely completely replaced and some of the grains have a thin inner rim of fersmite surrounded by an outer rim of magmatic pyrochlore (Figure 4.19a and f). Similarly, some of the pyrochlore may only contain columbite-(Fe) alteration in the core of the grain and retain an outer rim of magmatic pyrochlore (Figure 4.19d). The presence of columbite-(Fe) cores and fersmite inner rims surrounded by outer rims of magmatic pyrochlore suggest magmatic crystallization of pyrochlore continued following a period of alteration. This supports multiple episodes of primary crystallization of pyrochlore with intermittent alteration, probably caused by multiple pulses of magma into the system.

The carbonates include calcite and ferroan dolomite. The calcite is magmatic as it is Sr-rich and contains abundant strontianite inclusions (Thompson et al., 2002; Chakhmouradian et al., 2016; Chebotarev et al., 2019) (Figure 4.9c and d). The presence of burbankite inclusions could support a primary magmatic origin or suggest Na may be present in a hydrothermal fluid that precipitated hydrothermal calcite since burbankite inclusions are interpreted to be primary with the host carbonate (Chakhmouradian et al., 2016). The calcite that lacks inclusions could be recrystallized magmatic calcite, as carbonate minerals are susceptible to recrystallization,

however recrystallization also typically results in straight grain boundaries and abundant 120° triple points that are rarely observed at Good Hope. The presence of calcite veins as well as euhedral, distinctly zoned crystals in CL imaging, further rules out recrystallization and supports a hydrothermal origin of some of the calcite (Chakhmouradian et al., 2016).

The abundance of burbankite inclusions in some of the ferroan dolomite supports that the ferroan dolomite was also a primary crystallizing phase and suggests that the carbonatite magma was enriched in Na (Chakhmouradian and Dhalgren, 2021). The compositional variation of the ferroan dolomite shows a consistent transition from Fe-poor dolomite to Fe-rich ferroan dolomite, which is consistent with fractional crystallization. The zoned ferroan dolomite typically has an Fe-poor core that is more likely to contain inclusions of burbankite and strontianite surrounded by rims with higher Fe content that typically lack inclusions (Figure 4.14b). This observation supports the idea that the rims crystallized as either a late magmatic or hydrothermal mineral. Some of the euhedral zoned ferroan dolomite crystals contain thin outer rims of Fe-poor dolomite (Figure 4.14b). The euhedral habit of the ferroan dolomite crystals that commonly extend into hydrothermal phases (e.g., calcite, chlorite, etc.) also supports a hydrothermal origin for some of the ferroan dolomite (Chakhmourdaian et al., 2016).

Ferroan dolomite has a strong association with the apatitite clasts and can be observed at the contact between groundmass calcite and the apatitite clasts (Figure 4.3a). Some calcite is intergrown with magnetite at the contact with apatite, which could represent an Fe-rich carbonatitic fluid that was at temperatures above the stability field for Fe-carbonates that instead crystallized calcite + magnetite (Figure 4.49b). The stability field for Fe-carbonates begins at temperatures of 500°C (Mitchell et al., 2017), indicating the temperatures of the

magma were likely higher. The temperatures may not have been significantly higher since there are commonly Fe-carbonates adjacent to the calcite + magnetite aggregate. The composition of the magma can also influence the crystallizing assemblage, independent of temperature. The ferroan dolomite associated with the apatitite clasts is a later stage of crystallization as the ferroan dolomite transects the groundmass calcite and would likely form at lower temperatures. Rosenberg (1967) determined “ankerite”, or better termed ferroan dolomite, will break down into a three phase assemblage of calcite, dolomite, and siderite if the ratio of Fe/(Mg + Fe) is > 0.7. This is supported by the ferroan dolomite compositions containing Fe/(Mg + Fe) ratios that range up to 0.7, indicating Fe contents reached this level, and likely higher. This is consistent with the ferro-carbonatites being the low temperature products of fractional crystallization of Ca-Mg carbonate melts (Giovannini et al., 2020).

The ferroan dolomite appears to be coeval with dissolution-reprecipitation of apatite from the association of the ferroan dolomite with the blue-violet luminescent apatite (Figure 4.3b). This blue-violet luminescing apatite typically surrounds the magmatic, zoned, green, orange, and violet luminescent apatite. Alkali-metasomatism can form zoned apatite that has similar morphological and luminescent characteristics to the zoned apatite from Good Hope (Elliott et al., 2018). This apatite contains green and orange-pink luminescent cores that are surrounded by purple luminescent apatite and is observed in the fenites in Nkalonge, Malawi (Figure 6.2) (Elliott et al., 2018). Broom-Fendley et al. (2016) inferred breakdown and dissolution of previously formed apatite by the presence of turbid cores and growth of pink luminescent apatite rims. Pink luminescent apatite occurs along the grain boundaries of apatite in the apatitite clasts and suggests the dissolved apatite only travelled short distances before

being reprecipitated (Figure 4.4a). The blue-violet apatite may represent precipitation of hydrothermal apatite with late ferroan dolomite. The inferred late-hydrothermal apatite from Good Hope contains measurable REE concentrations (EDS), is associated with quartz, chlorite, barite, and euhedral ferroan dolomite and shows distinct REE emission lines in the CL spectra (Figure 4.3e and f).

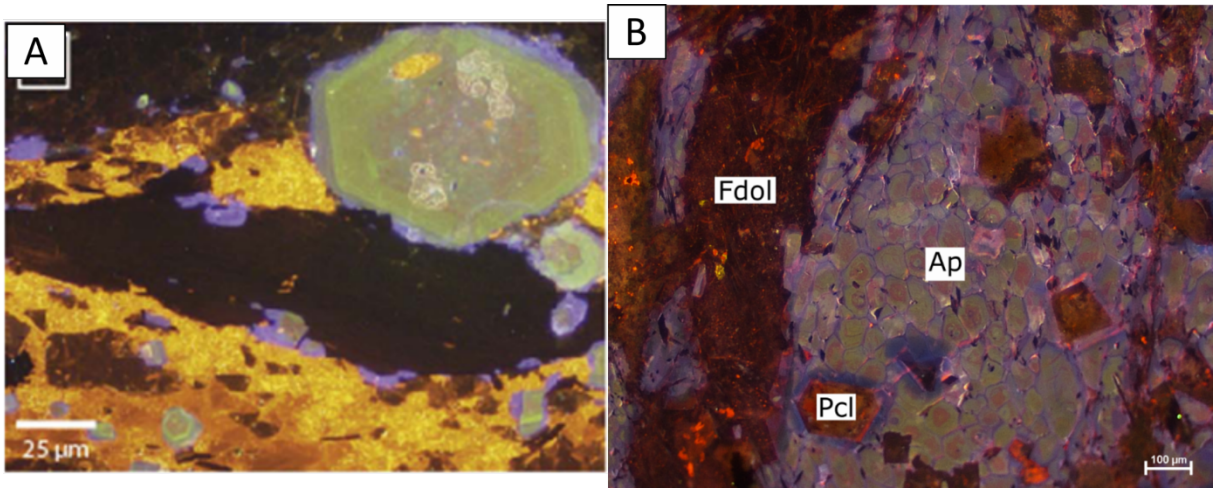

Figure 6.2: Cathodoluminescence images of zoned apatite. (a) From the fenite aureole in Nkalonje, Malawi, green, orange-pink, and purple luminescent apatite adjacent to calcite (yellow-orange luminescence) and a pyroxene vein (black) (Elliott et al., 2018). (b) Comparable green, orange, and purple luminescent apatite from the Good Hope carbonatite that is adjacent to ferroan dolomite (dark red-brown luminescence) (DDH-09-457B).

The REE-fluorocarbonates show textures, including syntaxial intergrowths, characteristic of magmatic crystallization (Dalsin et al., 2015) as well as associations that suggest late hydrothermal precipitation (Figure 4.41b). The common association of the REE-fluorocarbonates with other hydrothermal phases, such as calcite, chlorite, magnetite, etc. suggests the REE-fluorocarbonates are also hydrothermal. The presence of burbankite inclusions supports burbankite crystallization early in the crystallization sequence. Burbankite, however, is highly susceptible to dissolution by hydrothermal fluids that result in the crystallization of secondary Sr, LREE, and Ba minerals. Zaitsev et al. (1998) suggest syntaxial

intergrowths are evidence for the REE-fluorocarbonates being primary and related to changes in the composition of the host fluid. This could also be due to changes in the composition of a hydrothermal fluid or the result of later hydrothermal metasomatic reactions, as suggested by Yang et al. (2000). If burbankite did crystallize early, thereby depleting the primary melt in REEs, they would not be available for formation of the REE-fluorocarbonates until after the hydrothermal alteration of the burbankite crystals. The common intergrowth of the REE-fluorocarbonates with strontianite and thorite further support the precipitation of the REE-fluorocarbonates during the late-magmatic to hydrothermal stage (Forster, 2001) (Figure 4.41e). Anenburg et al. (2020a) show experimentally that REE behave incompatibly throughout igneous differentiation of carbonatites, leading to REE enrichment in the magma and precipitation of REE-fluorocarbonates late in the hydrothermal stage. The presence of alkalis in the carbonatitic magma promotes incorporation of LREE in fluorapatite over the HREE contributing to higher HREE concentrations in late-stage fluids (Anenburg et al., 2020b), which could support the presence of Y-bearing REE-fluorocarbonates. Yttrium also has an affinity to F and Y-F complexes are stable in hydrothermal fluids (Anenburg et al., 2020b).

Syenite Xenoliths

The syenite xenoliths centimeter-to-tens of centimeters in size consist of K-feldspar, aegirine, magnesio-arfvedsonite, and phlogopite. They show evidence for alteration by the red colouration of the anhedral K-feldspar and the reaction rind of zoned phlogopite with fresh euhedral rims (Figure 4.35b and c). The source of these xenoliths remains unknown, but it is possible that they have undergone fenitization due to the interaction with the host carbonatite. These xenoliths might be derived from an early crystallizing silicate magma associated with the

complex. This association is similar to the occurrence of syenites in the Wicheeda carbonatite complex that contain dominantly K-feldspar, aegirine, and biotite (Dalsin et al., 2015). The Good Hope syenite xenoliths also show evidence for alteration, possibly by the fluids related to the carbonatitic magma, including the replacement of the aegirine by magnesio-arfvedsonite and the fresh phlogopite rims (Figure 4.28b and c). Chipman Lake fenites occur north of the Good Hope carbonatite complex along the northern extension of the Big Bay – Ashburton fault system (Figure 2.1.) (Platt and Woolley, 1990). There are several similarities between the fenites at Chipman Lake and the syenite xenoliths at Good Hope, including the red colour, the composition of albite and microcline + magnesio-arfvedsonite + phlogopite + carbonate ± aegirine, and the phlogopite-rich zones at the dyke-fenite contact (Platt and Woolley, 1990). The presence of Nb in rutile that is typically within or adjacent to the syenite xenoliths at Good Hope further supports a metasomatic origin as Nb-rutile can be common in silicate rocks, with higher Nb content associated with metasomatic silicate rocks (Chakhmouradian et al., 2015).

The crystallization of this complex likely involves multiple pulses of carbonatitic magma and possibly followed the sequence: (1) crystallization of the syenite from an unknown alkaline parental magma; (2) crystallization of the initial magmatic Ca-Na pyrochlore + apatite from the carbonatitic magma; (3) entrapment and alteration of the crystalline syenite as xenoliths with replacement of aegirine by magnesio-arfvedsonite and formation of the phlogopite rims; (4) alteration of the pyrochlore and dissolution-reprecipitation of the apatite followed by resumption of magmatic Ca-Na pyrochlore and apatite crystallization with a subsequent pulse of carbonatitic magma; (5) crystallization of the alkali-rich silicate phases (i.e., aegirine and magnesio-arfvedsonite); (6) accumulation of the apatite + pyrochlore ± magnesio-arfvedsonite

followed by the disaggregation and flow deformation of the clasts with a subsequent magma pulse; (7) crystallization of the primary magmatic calcite as the groundmass phase; (8) the crystallization of the primary magmatic dolomite and subsequent crystallization of increasingly Fe-rich ferroan dolomite; (9) late crystallizing ferroan dolomite with associated late-hydrothermal apatite + pyrochlore; (10) the hydrothermal precipitation of quartz, chlorite, calcite, REE-fluorocarbonates, magnetite, and fluorite; and (11) the precipitation of Fe-overgrowths on the REE-fluorocarbonates and the Fe-oxides/hydroxides in some of the apatitite clasts.

6.2 Brief comparison of the Prairie Lake and Good Hope occurrences

The Prairie Lake alkaline-rock carbonatite complex is subdivided into four rock suites: (1) biotite pyroxenites and calcite carbonatite-I, (2) ijolite-suite rocks, (3) malignites, and (4) calcite carbonatite-II (herein referred to as carbonatite) (Wu et al., 2017; Savard and Mitchell, 2021). The mineralogical and textural descriptions of the Prairie Lake carbonatite used in this section are summarized by Mitchell (unpub. data). The silicate units all contain similar mineralogy, with most of the variation in the modal %. For simplicity, the silicate units are described together under the term “silicate rocks”, a further description can be found in Savard and Mitchell (2021). The mineral table (Table 6.1) lists the phases present within the Prairie Lake and Good Hope occurrences. The mineralogy of the two occurrences is vastly different, however both the silicate rocks and the carbonatite from Prairie Lake have a few minerals in common with the Good Hope carbonatite.

The minerals of the Prairie Lake silicate rocks in common with the Good Hope carbonatite include calcite, apatite, K-feldspar, biotite, magnetite, aegirine, pyrochlore,

fersmite, strontianite, and pyrite. The calcite from the Prairie Lake silicates is considered a late-stage mineral, with all of the compositions containing Sr ranging from 1.3-to-1.5 wt. % SrO.

Table 6.1: Mineral list of the Good Hope occurrence carbonatite and the Prairie Lake occurrence carbonatite and silicate rocks. Minerals are listed in relative order of abundance in their respective occurrences.

Good Hope Occurrence	**Prairie Lake Occurrence**	
Carbonatite	Carbonatite	Silicate Rocks
Calcite	Olivine	Diopside-Hedenbergite
Ferroan Dolomite	Calcite	Nepheline
Fluorapatite	Fluorapatite	Apatite
K-feldspar	Ti-magnetite	Andradite-Morimotoite
Biotite -Phlogopite	Phlogopite-Barian Phlogopite	Biotite-Annite
Magnesio-Arfvedsonite	Phlogopite-Tetraferriphlogopite	Calcite
Magnetite	Pyrite	Pyrite
Quartz	Na-Ca Pyrochlore	K-feldspar
Pyrite	U-Ta Pyrochlore	Wollastonite
Chlorite	Pb Pyrochlore	Pyrochlore
Aegirine	Niobian Zirconolite	Fersmite
Dolomite	Perovskite-latrappite-loparite	Marianoite
Na-Ca Pyrochlore	Baddeleyite	Hedenbergite-Aegirine
Fersmite	Thorianite	Zeolite
Columbite-Fe	Calzirtite	Cancrinite
Barite	Pyrrhotite	Strontianite
Synchysite-(Ce)	Galena	Bartyocalcite
Parisite-(Ce)	Co-Pentlandite	Ti-magnetite
Bastnaesite-(Ce)	Chalcopyrite	Wadeite
Fluorite	Ancylite-(Ce)	Catapleiite
Strontianite	Rhabdophane-(Ce)	Calzertite
Burbankite	Mn-ilmenite	Zircon
Rutile		Baddeleyite
Albite		

In contrast, the Good Hope calcite, which is a major phase that crystallized at several stages of the carbonatite evolution, contains a larger range of Sr values from b.d.-to-3.4 wt. % SrO. Within the Prairie Lake silicate rocks the apatite is F-bearing but is not referred to as fluorapatite and occurs associated with the late-stage calcite and wollastonite within the malignites. In common with Good Hope, the apatite is also observed forming apatitites. The

Good Hope carbonatite contains K-feldspar as a primary crystallizing phase, while the Prairie Lake silicate rocks only contain K-feldspar as an alteration product after nepheline. The biotite present in the Prairie Lake silicate rocks is almost exclusively annite, in contrast to Good Hope biotite that is predominantly phlogopite. The biotite from both occurrences, however, contain varying degrees of chloritization. The magnetite from the Prairie Lake silicate rocks contains Ti, which is uncommon for the magnetite at Good Hope. Aegirine is the only pyroxene observed in the Good Hope carbonatite and although there is some aegirine present in the malignites of the Prairie Lake occurrence, the pyroxene more commonly range between diopside and hedenbergite compositions. The pyrochlore and fersmite present in the Prairie Lake silicate rocks occurs exclusively in the biotite pyroxenites.

The minerals of the Prairie Lake carbonatite in common with the Good Hope carbonatite includes calcite, fluorapatite, biotite, magnetite, pyrochlore, and pyrite. Although common in name, these minerals tend to have variation in composition between the two occurrences. The Prairie Lake carbonatite magnetite, for instance, always contains Ti, with values ranging from 3-to-12 wt. % TiO_2, compared with Good Hope magnetite that commonly lacks Ti. Good Hope also lacks ilmenite that is present in the Prairie Lake carbonatite and instead incorporates the Ti into rutile, which is absent from the Prairie Lake carbonatite. Calcite is the dominant carbonate in the Prairie Lake carbonatite, consistently containing 1-to-2 wt. % SrO, while Good Hope calcite ranges from b.d.-to-3.4 wt. % SrO. The fluorapatite compositions are slightly different as well, although they are both relatively REE- and Sr-poor, Prairie Lake apatite compositions never have more than 1 wt. % SrO or TREO, where Good Hope fluorapatite can contain up to 1.7 wt. % SrO and 4.1 wt. % TREO. Further geochemical evaluation using LA-ICP-MS will be useful in

further comparing the Prairie Lake and Good Hope apatite, especially with regards to the specific REE present in each. The biotite present in the Prairie Lake carbonatite ranges in composition from phlogopite-barian phlogopite-to-phlogopite-tetraferriphlogopite while the Good Hope biotite is typically phlogopite with some compositions ranging up to 50 % annite. There are several types of pyrochlore present in the Prairie Lake carbonatite, including Na-Ca pyrochlore, U-Ta pyrochlore, and Pb-pyrochlore, with only Na-Ca pyrochlore in common with the Good Hope carbonatite.

The Prairie Lake carbonatite is also texturally distinct from the Good Hope carbonatite. The Prairie Lake carbonatite is typically banded on the cm- to mm-scale with the layering defined by modal variation in the olivine, calcite, apatite, mica, and magnetite. The calcite commonly contains straight grain boundaries and abundant 120° triple points, resulting in an allotriomorphic, equilibrated texture that is absent at Good Hope. Any banding within the Good Hope carbonatite is defined by the preferred elongation of the apatitite clasts. In common with the Good Hope carbonatite, the Prairie Lake carbonatite contains cm- to dm-scale clasts, however in contrast these are ultramafic rocks including, ijolite, biotite pyroxenite, wollastonite ijolite, micro-melaijolite, or alnoitic lamprophyre.

6.3 Relationship to the Prairie Lake Occurrence

All the rock units within the Prairie Lake complex are contemporaneous and have identical Sr and Nd isotopic compositions, indicating they were derived from a common parental magma (Wu et al., 2017; Savard and Mitchell, 2021). The complex is considered a consanguineous assemblage of ijolite and carbonatite suggesting derivation from a nephelinitic magma (Savard and Mitchell, 2021). Savard and Mitchell (2021) provide a petrogenetic model

(Figure 6.3) for the Prairie Lake complex, which represents a series of anastomosing channels that segregated small batches of the common parental magma resulting in different evolutions for each. They also suggest a variety of emplacement processes were active including magma mixing, crystal settling and differentiation, solid-state deformation and re-equilibration, and deuteric alteration.

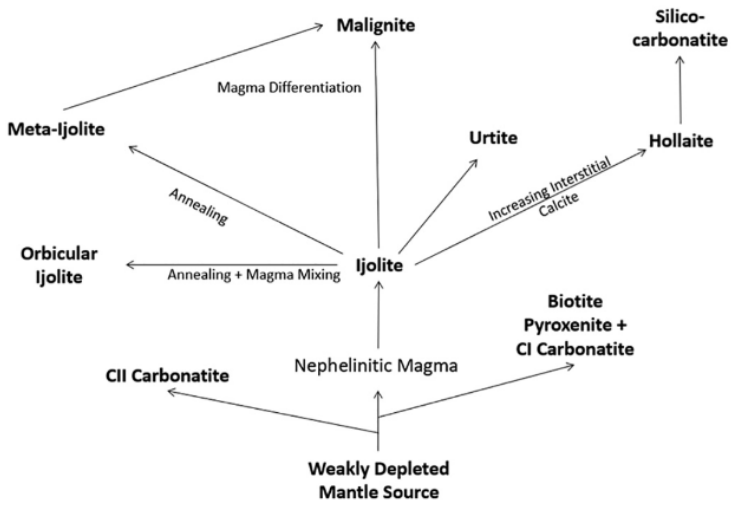

Figure 6.3: Petrogenetic model for the Prairie Lake carbonatite complex, from Savard and Mitchell (2021).

From the petrogenetic model presented for Prairie Lake, the carbonatite magma is removed early in the evolution of the complex, but from the presence of the ultramafic clasts of the later evolved ijolite, biotite pyroxenite, and malignite indicates the carbonatite was likely the last phase to crystallize. The nephelinite clan carbonatites can contain later ankerite carbonatites as well as late-stage carbothermal residua that forms Sr-, Ba-, and REE-bearing carbonates (Mitchell, 2005). Mitchell (2005) proposes two processes for formation of these late carbonatites: (1) interaction of pre-existing carbonatites with groundwater, or (2) they represent residual fractions of the parental magma. Prairie Lake has been compared to the Fen

complex, Norway, which contain hematite-calcite-dolomite carbonatite (rodberg) and ankerite carbonatite that are assumed to be formed by the interaction of the carbonatites with groundwater (Mitchell, 2005).

The Good Hope carbonatite could be related in some manner to the parental magma of the Prairie Lake carbonatite, although geological and mineralogical evidence are not conclusive as to the exact relationship. The Prairie Lake carbonatite has a cumulate texture, which may have separated from a residual carbonatitic magma that produced the Good Hope carbonatite. Ionov and Harmer (2002) inferred the crystallization of calcite would concentrate REE and lithophile elements, with the exception of Sr, in the residual melt if apatite was not crystallizing from observations at the Spitskop Complex (South Africa). Pyrochlore are also expected to crystallize as U- and Ta-rich, as observed in Prairie Lake, prior to crystallization of Na-Ca pyrochlore, observed in Good Hope (Viladkar et al., 2017). The textural differences between Prairie Lake and Good Hope suggest the former crystallized in a more quiescent environment with the formation of modal layering attributable to rheological processes, while the latter appears to be emplaced in a more turbulent environment.

The presence of both calcite and ferroan dolomite as the groundmass phase in different samples indicates the different parts of Good Hope carbonatite can be classified as calcite carbonatite and a dolomitic carbonatite. The amount of Fe within the ferroan dolomite may be considered sufficient in classifying it as a ferroan dolomite carbonatite. Several of the samples contain up to 20 vol. % of silicates and could be termed magnesio-arfvedsonite calcite carbonatites and aegirine biotite ferroan dolomite carbonatites. As a consequence of changes in modal mineralogy over small distances, several types of carbonatite can be identified at

Good Hope. Following Mitchell (2005), it would be worthwhile classifying the carbonatite as a group of genetically related units as opposed to classifying each specific rock type. These groups are largely dependant on the associated silicate rocks, however the syenite xenoliths have not crystallized from the same magma and might not be genetically related, suggesting the Good Hope carbonatite could belong to the group of carbonatites that lack associated silicate rocks. Alternatively, the Good Hope carbonatite could be a carbothermal residual deposit. Carbothermal residua refers to low-temperature fluids derived from a fractionated magma containing CO_2 as well as F and H_2O in variable proportions (Mitchell, 2005). The Good Hope carbonatite consists of areas that crystallized magmatic calcite + magnetite rather than ferroan dolomite which could support temperatures above 500°C that would not support them being solely carbothermal residua. Many alkaline rock carbonatite complexes typically progress from crystallizing silicate melts (i.e., ijolite or biotite pyroxenite, observed in Prairie Lake), followed by the crystallization of calcite carbonatite (observed in Prairie Lake and Good Hope), crystallization of dolomite carbonatite (observed in Good Hope and Prairie Lake), crystallization of ferroan dolomite (observed in Good Hope), and precipitation of carbothermal residua (i.e., Sr-, Ba-, and REE-bearing carbonates, observed at Good Hope). The Prairie Lake carbonatite is genetically associated with the ijolites and potassic nepheline syenites (Wu et al., 2017), indicating Prairie Lake is a member of the nephelinite clan. If Good Hope is derived from fractionated magma related to the Prairie Lake carbonatite, then it too would be considered a member of the nephelinite clan.

Chapter 7. Conclusions

7.1 Orbicular carbonatite occurrence

The orbicular carbonatite consists of spherical-to-oblate, millimeter-scale orbicules which occur within an equilibrated calcite carbonatite host. The orbicules are composed of Ti-bearing magnetite (type 1) with associated ilmenite, Ti-poor magnetite (type 2), phlogopite, V-bearing aegirine, and ferroan dolomite. They predominantly consist of discrete shells of aegirine ± ferroan dolomite, tangential phlogopite, type 2 magnetite, and rarely calcite. They can also form spherical aggregates with indistinct shells. Orbicules lack a distinct core, containing entrained host calcite, type 1 magnetite, and zoned phlogopite. The two types of magnetite are interpreted to have crystallized at different times under different conditions. The Ti-bearing magnetite (type 1) containing ilmenite lamellae is magmatic, crystallizing at temperatures around 517-to-575°C with fO_2 of -19.8-to- -22.7. The Ti-poor magnetite (type 2) is hydrothermal, possibly crystallizing after the type-I magnetite and associated with the crystallization of the more evolved V-bearing aegirine. The orbicular carbonatite from Good Hope is texturally and mineralogically distinct from the orbicular ijolite found at the Prairie Lake carbonatite complex. With respect to these, the absence of xenolith cores, radial growth of the minerals in the shells, and fractional crystallization of the shells and host suggests there was no magma mixing or super heating of the host that supressed nucleation. The differences in the composition of the orbicules and the host suggests they could be a transported assemblage. The degree to which the hydrothermal fluids played in the formation of the orbicules is unknown but might have been introduced after the orbicules were entrained in the host calcite, as the type 2 magnetite and aegirine can occur disaggregated in the host. The difference in

composition of the orbicules and host could also suggest surface tension effects played a role in the orbicule formation.

7.2 Mineralogy and petrology

The Good Hope carbonatite is composed predominantly of calcite carbonatite and lesser ferroan dolomite carbonatite containing elongate apatitite clasts that commonly contain pyrochlore. Entrained within the carbonatite are subangular clasts of syenite composed of K-feldspar, magnesio-arfvedsonite, biotite-phlogopite, aegirine, and quartz. They typically exhibit a reaction rim of phlogopite. The minor phases occurring and disseminated in the carbonatite can comprise up to 20 vol. % of the rock and include K-feldspar, magnesio-arfvedsonite, biotite-phlogopite, aegirine, quartz, chlorite, magnetite, barite, pyrochlore, albite, and fluorite. The accessory minerals include pyrite, synchysite-(Ce), rutile, strontianite, thorite, parisite-(Ce), bastnaesite-(Ce), burbankite, and zircon. These commonly occur as inclusions in the carbonates or as isolated crystals 50-to-200 μm in size, rarely up to 2 mm. The Good Hope carbonatite exhibits significant modal heterogeneity over short distances, thus several types of carbonatite can be identified. Generally, Good Hope can be classified as a calcite carbonatite and a ferroan dolomite carbonatite.

Cathodoluminescence imaging shows evidence for multiple periods of crystallization and dissolution with the erosion of the euhedral crystal faces due to interaction with later pulses of carbonatitic magma. The pyrochlore crystallized early with the apatite and have concentric to patchy zonation resulting from alteration to fersmite and columbite-(Fe). Pyrochlore are also primary in the late-stage carbonatite as evidenced by magmatic Ca-Na pyrochlore forming the outer rims of altered grains, inclusions of magnesio-arfvedsonite and

barite in the pyrochlore, and small magmatic pyrochlore occurring in the ferroan dolomite carbonatite.

The dominant carbonates within the Good Hope carbonatite are magmatic, Sr-rich calcite, and hydrothermal, Sr- and Mg-poor, near endmember $CaCO_3$. Ferroan dolomite can also occur as a groundmass phase and is commonly zoned with increasing Fe content from core to rim, consistent with fractional crystallization. Inconsistent zonation patterns throughout the carbonatite suggests multiple pulses of variably Fe-rich carbonatite magmas. The euhedral habit of some ferroan dolomite crystals extending into hydrothermal phases (e.g., chlorite, calcite, etc.) supports the presence of some hydrothermal ferroan dolomite. The ferroan dolomite has a strong association with the apatitite clasts, although calcite intergrown with magnetite can also occur at the contacts with the apatitite clasts. This could indicate Fe-rich carbonatite-forming magma above the temperature of stability for Fe-carbonates (500°C) and instead crystallized calcite + magnetite. Alternatively, the composition of the magma might have been too Fe-rich ($Fe/(Mg + Fe) > 0.7$) to crystallize ferroan dolomite.

Ferroan dolomite is coeval with the precipitation of hydrothermal apatite that has blue-violet CL luminescence. This hydrothermal apatite contains measurable REE contents (EDS), is associated with quartz, chlorite, barite, and ferroan dolomite, and has distinct REE emission lines in the CL spectra. The REE-fluorocarbonates commonly contain syntaxial intergrowths and are typically associated with the hydrothermal phases (e.g., quartz, fluorite, chlorite, magnetite, etc.), suggesting they are hydrothermal in origin. Y-bearing REE-fluorocarbonates indicate the presence of HREE in the hydrothermal fluids. The replacement of aegirine by magnesio-

arfvedsonite, fresh phlogopite rims, and the red colouration of the K-feldspar is evidence for alteration of the syenite xenoliths, possibly by the fluids related to the carbonatitic magma.

7.3 Paragenesis

The Good Hope carbonatite consists of multiple pulses of magmatism that entrained an early syenite phase and low temperature carbothermal residua. The crystallization of this complex possibly followed the sequence: (1) crystallization of the syenite from an unknown alkaline parental magma; (2) crystallization of the initial magmatic Ca-Na pyrochlore + apatite from a carbonatitic magma; (3) entrapment and alteration of the crystalline syenite as xenoliths with replacement of aegirine by magnesio-arfvedsonite and formation of the phlogopite rims; (4) alteration of the pyrochlore and dissolution-reprecipitation of the apatite followed by resumption of magmatic Ca-Na pyrochlore and apatite crystallization with a subsequent pulse of carbonatitic magma; (5) crystallization of the alkali-rich silicate phases (i.e., aegirine and magnesio-arfvedsonite); (6) accumulation of the apatite + pyrochlore ± magnesio-arfvedsonite followed by the disaggregation and flow deformation of the clasts with a subsequent magma pulse; (7) crystallization of the primary magmatic calcite as the groundmass phase; (8) the crystallization of the primary magmatic dolomite and subsequent crystallization of increasingly Fe-rich ferroan dolomite; (9) late crystallizing ferroan dolomite with associated late-hydrothermal apatite + pyrochlore; (10) the hydrothermal precipitation of quartz, chlorite, calcite, REE-fluorocarbonates, magnetite, and fluorite; and (11) the precipitation of Fe-overgrowths on the REE-fluorocarbonates and the Fe-oxides/hydroxides in some of the apatitite clasts.

Although the Good Hope carbonatite is spatially associated with the Prairie Lake carbonatite complex it differs significantly in its mineralogy and lacks ijolite-suite rocks. It is possible that the Good Hope carbonatites are ultimately related to the magmatism that gave rise to this complex however, these major differences preclude any simple differentiation relationship to the Prairie Lake complex. Any speculation as to a genetic relationship is premature and requires further studies such Sr and Nd isotopic compositions for the apatite in both complexes. A U/Pb age determination for apatite will also be useful in evaluating this relationship. Further evaluation by LA-ICP-MS of the trace elements in the zoned apatite from Good Hope and Prairie Lake defined by CL imaging will help to better understand their relationship.

References

Anenburg, M., Mavrogenes, J. A., and Bennett, V. C. 2020a. The Fluorapatite P-REE-Th Vein Deposit at Nolans Bore: Genesis by Carbonatite Metasomatism. Journal of Petrology, 61: 1. https://doi.org/10.1093/petrology/egaa003

Anenburg, M., Mavrogenes, J. A., Frigo, C., and Wall, F. 2020b. Rare earth element mobility in and around carbonatites controlled by sodium, potassium, and silica. Scientific Advances, 6. http://advances.sciencemag.org/

Ayer, J. A., Goutier, J., Thurston, P. C., Dube, B., and Kamber, B. S. 2010. Tectonic and Metallogenic Evolution of the Abitibi and Wawa Subprovinces; *in* Summary of Field Work and Other Activities 2010, Ontario Geological Survey, Open File Report 6260, 3-1 to 3-6.

Barker, D. S. 1996. Carbonatite volcanism. In: *Undersaturated Alkaline Rocks: Mineralogy, Petrogenesis, and Economic Potential,* Mitchell, R. H. (ed.), Mineralogical Association of Canada, Short Course, 24, 45-61.

Binder, G. and Troll, G. 1989. Coupled anion substitution in natural carbon-bearing apatites. Contributions to Mineralogy and Petrology, 101, 394-401.

Broom-Fendley, S., Styles, M. T., Appleton, J. D., Gunn, G., and Wall, F. 2016. Evidence for dissolution-reprecipitation of apatite and preferential LREE mobility in carbonatite-derived late-stage hydrothermal processes. American Mineralogist, 101: 3, 596–611. https://doi.org/10.2138/am-2016-5502CCBY

Cangelosi, D., Broom-Fendley, S., Banks, D., Morgan, D., and Yardley, B. 2020. Light rare earth element redistribution during hydrothermal alteration at the Okorusu carbonatite complex, Namibia. Mineralogical Magazine, 84, 49-64. DOI: 10.1180/mgm.2019.54

Chakhmouradian, A. R. and Dahlgren, S. 2021. Primary inclusions of burbankite in carbonatites from the Fen complex, southern Norway. Mineralogy and Petrology, 115, 161–171. https://doi.org/10.1007/s00710-021-00736-0/Published

Chakhmouradian, A. R., Reguir, E. P., and Zaitsev, A. N. 2016. Calcite and dolomite in intrusive carbonatites. I. Textural variations. Mineralogy and Petrology, 110: 2–3, 333–360. https://doi.org/10.1007/s00710-015-0390-6

Chakhmouradian, A. R., Reguir, E. P., Kressall, R. D., Crozier, J., Pisiak, L. K., Sidhu, R., and Yang, P. 2015. Carbonatite-hosted niobium deposit at Aley, northern British Columbia (Canada): Mineralogy, geochemistry and petrogenesis. Ore Geology Reviews, 64, 642–666. https://doi.org/10.1016/j.oregeorev.2014.04.020

Chakhmouradian, A. R., Reguir, E. P., Zaitsev, A. N., Couëslan, C., Xu, C., Kynický, J., Mumin, A. H., and Yang, P. 2017. Apatite in carbonatitic rocks: Compositional variation, zoning, element partitioning and petrogenetic significance. Lithos, 274–275, 188–213. https://doi.org/10.1016/j.lithos.2016.12.037

Chebotarev, D. A., Veksler, I. V., Wohlgemuth-Ueberwasser, C., Doroshkevich, A. G., and Koch-Müller, M. 2019. Experimental study of trace element distribution between calcite, fluorite and carbonatitic melt in the system CaCO3 + CaF2 + Na2CO3 ± Ca3(PO4)2 at

100 MPa. Contributions to Mineralogy and Petrology, 174: 1. https://doi.org/10.1007/s00410-018-1530-x

Chen, W. and Simonetti, A. 2013. In-situ determination of major and trace elements in calcite and apatite, and U-Pb ages of apatite from the Oka carbonatite complex: Insights into a complex crystallization history. Chemical Geology, 353, 151-172. DOI: 10.1016/j.chemgeo.2012.04.022

Chen, W., Ying, Y., Bai, T., Zhang, J., Jiang, S., Zhao, K., Shin, D., and Kynicky, J. 2019. In situ major and trace element analysis of magnetite from carbonatite-related complexes: Implication for petrogenesis and ore genesis. Ore Geology Reviews, 107, 30-40. DOI: 10.1016/j.oregeorev.2019.01.029

Cleaver, A. 2017. Mineralogy and Petrology of the Good Hope Carbonatite Occurrence, Marathon, ON. HBSc. thesis, Lakehead University, Thunder Bay, Ontario.

Cooper, A. F. and Reid, D. L. 1998. Nepheline sovites as parental magmas in carbonatite complexes: evidence from Dicker Willem, Southwest Namibia. Journal of Petrology, 39, 2123-2136.

Dalsin, M. L., Groat, L. A., Creighton, S., and Evans, R. J. 2015. The mineralogy and geochemistry of the Wicheeda Carbonatite Complex, British Columbia, Canada. Ore Geology Reviews, 64, 523–542. https://doi.org/10.1016/j.oregeorev.2014.02.013

Dey, M., Mitchell, R. H., Bhattacharjee, S., Chakrabarty, A., Pal, S., Pal, S., and Kumar Sen, A. 2021. Composition and genesis of albitite-hosted antecrystic pyrochlore from the

Sevattur carbonatite complex, India. Mineralogical Magazine, 1-20. DOI: 10.1180.mgm.2021.6

Dhote, P., Bhan, U., and Verma, D. 2021. Genetic model of carbonatite hosted rare earth elements mineralization from Ambadongar Carbonatite Complex, Deccan Volcanic Province, India. Ore Geology Reviews, 135. https://doi.org/10.1016/j.oregeorev.2021.104215

Droop, G. T. R. 1987. A general equation for estimating Fe^{3+} concentrations in ferromagnesian silicates and oxides from microprobe analyses, using stoichiometric criteria. Mineralogical Magazine, 51, 431-435.

Eggler, D. H. 1978. The effect of CO_2 upon partial melting of peridotite in the system Na_2O-CaO-Al_2O_3-MgO-SiO_2-CO_2 to 35 kb, with an analysis of melting in peridotite-H_2O-CO_2 system. American Journal of Science, 278, 305-343.

Elliott, H. A. L., Wall, F., Chakhmouradian, A. R., Siegfried, P. R., Dahlgren, S., Weatherley, S., Finch, A. A., Marks, M. A. W., Dowman, E., and Deady, E. 2018. Fenites associated with carbonatite complexes: A review. Ore Geology Reviews, 93, 38–59). Elsevier B.V. https://doi.org/10.1016/j.oregeorev.2017.12.003

Ernst, R. E. and Bell, K. 2010. Large igneous provinces (LIPs) and carbonatites. Mineralogy and Petrology, 98: 1–2, 55–76. https://doi.org/10.1007/s00710-009-0074-1

Farrell, S., Bell, K., and Clark, I. 2010. Sulphur isotopes in carbonatites and associated silicate rocks from the Superior Province, Canada. Mineralogy and Petrology, 98: 1–2, 209–226. https://doi.org/10.1007/s00710-009-0101-2

Forster, H. J. 2001. Synchysite-(Y) ± synchysite-(Ce) solid solutions from Markersbach, Erzgebirge, Germany: REE and Th mobility during high-T alteration of highly fractionated aluminous A-type granites. Mineralogy and Petrology, 72, 259-280.

Giebel, R. J., Marks, M. A. W., Gauert, C. D. K., and Markl, G. 2019. A model for the formation of carbonatite-phoscorite assemblages based on the compositional variations of mica and apatite from the Palabora Carbonatite Complex, South Africa. Lithos, 324–325, 89–104. https://doi.org/10.1016/j.lithos.2018.10.030

Giovannini, A. L., Mitchell, R. H., Bastos Neto, A. C., Moura, C. A. V., Pereira, V. P., and Porto, C. G. 2020. Mineralogy and geochemistry of the Morro dos Seis Lagos siderite carbonatite, Amazonas, Brazil. Lithos, 360–361. https://doi.org/10.1016/j.lithos.2020.105433

Gittins, J. 1989. The origin and evolution of carbonatite magmas. In: *Carbonatites: Genesis and Evolution,* Bell, K. (ed) Unwin Hyman, London, 580-600.

Hamilton, D. L., Bedson, P., and Esson, J. 1989. The behaviour of trace elements in the evolution of carbonatites. In: *Carbonatites: Genesis and Evolution,* Bell, K. (ed), Unwin Hyman, London, 405-427

Hey, M. H. 1954. A new review of the chlorites. Mineralogical Magazine, 30, 277-292.

Hughes, J. M., Cameron, M., and Mariano, A. N. 1991. Rare-earth-element ordering and structural variations in natural rare-earth-bearing apatite. American Mineralogist, 76, 1165-1173.

Ionov, D. and Harmer, R. E. 2002. Trace element distribution in calcite-dolomite carbonatites from Spitskop: inferences from differentiation of carbonatite magmas and the origin of carbonates in mantle xenoliths. Earth and Planetary Science Letters, 198, 495-510.

Le Bas, M. J. 1977. Carbonatite – Nephelinite Volcanism. John Wiley and Sons, London.

Le Bas, M. J. 2008. Fenites associated with carbonatites. The Canadian Mineralogist, 46, 915-932. DOI: 10.3749/canmin.46.4.915

Lee, W. J. and Wyllie, P. J. 1998. Processes of Crustal Carbonatite Formation by Liquid Immiscibility and Differentiation, Elucidated by Model Systems. Journal of Petrology, 39: 11-12, 2005-2013.

Le Maitre, R. W. 2002. Igneous Rocks: a classification and glossary of terms. Cambridge University Press, Cambridge, U.K.

Mason, H. E., McCubbin, F. M., Smirnov, A., and Phillips, B. L. 2009. Solid-state NMR and IR spectroscopic investigation of the role of structural water and F in carbonate-rich fluorapatite. American Mineralogist, 94, 507-516.

Milani, L., Bolhar, R., Cawthorn, R. G., and Frei, D. 2017. In situ LA-ICP-MS and EPMA trace element characterization of Fe-Ti oxides from the phoscorite-carbonatite association at

Phalaborwa, South Africa. Miner Deposita, 52: 747-768. Doi: 10.1007/s00126-016-0696-2

Mitchell, R. H. Unpublished Data. Prairie Lake carbonatite complex: Mineralogy of the heterogeneous carbonatites.

Mitchell, R. H. 2005. CARBONATITES AND CARBONATITES AND CARBONATITES. The Canadian Mineralogist, 43.

Mitchell, R. H. 2014: Cathodoluminescence of apatite. In: *Cathodoluminescence and its Application to Geoscience,* Coulson, I. M. (ed.). Mineralogical Association of Canada, Short Course, 45, 143-167.

Mitchell, R. H. 2015. Primary and secondary niobium mineral deposits associated with carbonatites. Ore Geology Reviews, 64, 626–641. https://doi.org/10.1016/j.oregeorev.2014.03.010

Mitchell, R. H., Chudy, T., McFarlane, C. R. M., and Wu, F. Y. 2017. Trace element and isotopic composition of apatite in carbonatites from the Blue River area (British Columbia, Canada) and mineralogy of associated silicate rocks. Lithos, 286–287, 75–91. https://doi.org/10.1016/j.lithos.2017.06.008

Mitchell, R. H. and Krouse, H. R. 1975. Sulphur isotope geochemistry of carbonatites. Geochimica et Cosmochimica Acta, 39, 1505 – 1513.

Mitchell, R.H., Wahl, R., and Cohen A. 2020. Mineralogy and genesis of pyrochlore apatitite from The Good Hope Carbonatite, Ontario: A potential niobium deposit. Mineralogical Magazine, 84: 81-91. Doi: 10.1180/mgm.2019.64

Néron, A., Bédard, L. P., and Gaboury, D. 2018. The Saint-Honoré carbonatite REE zone, Québec, Canada: Combied magmatic and hydrothermal processes. Minerals, 8: 9. https://doi.org/10.3390/min8090397

Pan, Y. and Fleet, M. E. 2002. Compositions of the Apatite-Group Minerals: Substitution Mechanisms and Controlling Factors. DOI: 10.2138/rmg.2002.48.2

Pirajno, F. 2015. Intracontinental anorogenic alkaline magmatism and carbonatites, associated mineral systems and the mantle plume connection. Gondwana Research, 27: 3, 1181 – 1216. https://doi.org/10.1016/j.gr.2014.09.008

Plato Gold. 2018. 'Good Hope Niobium Project' [online]. Available at: https://www.platogold.com/projects/good-hope-niobium-project/ (Accessed: 16 July 2021)

Platt, R. G. and Woolley, A. R. 1990. THE CARBONATITES AND FENITES OF CHIPMAN LAKE, ONTARIO. The Canadian Mineralogist, 28. https://pubs.geoscienceworld.org/canmin/article-pdf/28/2/241/3446169/241.pdf?casa_token=HGiNH_q70JEAAAAA:MID9ofsdMOFNDhWm91lwspJOmdZL

Roeder, P. L., MacArthur, D., Ma, X., Palmer, G. R., and Mariano, A. N. 1987. Cathodoluminescence and microprobe study of rare-earth elements in apatite. American Mineralogist, 72, 801-811.

Ronsbo, J. G. 1989. Coupled susbstitution involving REEs and Na and Si in apatite in alkaline rocks from the Illimanaussaq intrusion, South Greenland, and the petrologic implications. American Mineralogist, 74, 869-901.

Rosenberg, P. E. 1967. Subsolidus relations in the system $CaCO_3$ – $MgCO_3$ – $FeCO_3$ between 350°C and 550°C. American Mineralogist, 52, 787 – 797.

Sage, R. P. 1987. Geology of carbonatite – Alkalic rock complexes in Ontario: Prairie Lake carbonatite complex, District of Thunder Bay. Ministry of Northern Development and Mines, Ontario Geological Survey, Study 46.

Savard, J. J. and Mitchell, R. H. 2021. Petrology of ijolite series rocks from the Prairie Lake (Canada) and Fen (Norway) alkaline rock-carbonatite complexes. Lithos, 396–397. https://doi.org/10.1016/j.lithos.2021.106188

Stott, G. M. 2011. A Revised Terrane Subdivision of the Superior Province of Ontario: Ontario Geological Survey. Miscellaneous Release - Data. p. 278.

Stott, G. M., Corkery, M. T., Percival, J. A., Simard, M., and Goutier, J. 2010. A revised terrane subdivision of the Superior Province; *in* Summary of Field Work and Other Activities 2010, Ontario Geological Survey, Open File Report 6260, 20-1 to 20-10.

Thompson, R. N., Smith, P. M., Gibson, S. A., Mattey, D. P., and Dickin, A. P. 2002. Ankerite carbonatite from Swartbooisdrif, Namibia: The first evidence for magmatic ferrocarbonatite. Contributions to Mineralogy and Petrology, 143: 3, 377–396. https://doi.org/10.1007/s00410-002-0350-0

Veksler, I. V., Petibon, C., Jenner, G. A., Dorfman, A. M., and Dingwell, D. B. 1998. Trace element partitioning in immiscible silicate-carbonate liquid systems: an initial experimental study using a centrifuge autoclave. Journal of Petrology, 39.

Viladkar, S. G., Bismayer, U., and Ziietlow, P. 2017. Metamict U-rich pyrochlore of Newania carbonatite, Udaipur, Rajasthan. Journal Geological Society of India, 89, 133-138.

Viladkar, S. G. and Sorokhtina, N. V. 2021. Evolution of pyrochlore in carbonatites of the Amba Dongar complex, India. Mineralogical Magazine, 85: 4, 554–567. https://doi.org/10.1180/mgm.2021.50

Win, M. M., Enami, M., Kato, T., and Thu, Y. K. 2017. A mechanism for Nb incorporation in rutile and application of Zr-in-rutile thermometry: A case study from granulite facies paragneisses of the Mogok metamorphic belt, Myanmar. Mineralogical Magazine, 81: 6, 1503–1521. https://doi.org/10.1180/minmag.2017.081.014

Woodruff, L. G., Schulz, K. J., Nicholson, S. W., and Dicken, C. L. 2020. Mineral deposits of the Mesoproterozoic Midcontinent Rift system in the Lake Superior region – A space and time classification. Ore Geology Reviews, 126. Elsevier B.V. https://doi.org/10.1016/j.oregeorev.2020.103716

Woolley, A. R. and Kempe, D. R. C. 1989. Carbonatites: nomenclature, average chemical compositions, and element distribution. In: *Carbonatites: Genesis and Evolution,* Bell, K (ed.), Unwin Hyman, London, 1-14.

Woolley, A. R. and Kjarsgaard, B. A. 2008. Paragenetic types of carbonatite as indicated by the diversity and relative abundance from a global database. The Canadian Mineralogist, 46: 741-752. Doi: 10.3749/canmin.46.4.741

Wu, F-Y., Mitchell, R.H., Li Q-L., Zhang C., and Yang Y-H. 2017. Emplacement age and isotopic composition of the Prairie Lake carbonatite complex, Northwestern Ontario, Canada. Geological Magazine, 154: 2: 217-236. Doi: 10.1017/S0016756815001120

Wyllie, P. J. and Huang, W. 1976. Carbonation and melting reactions in the system CaO – MgO – SiO_2 – CO_2 at mantle pressures with geophysical and petrological applications. Contributions to Mineralogy and Petrology, 54, 79-107.

Wyllie, P. J. and Tuttle, O. F. 1960. The system CaO-CO_2-H_2O and the origin of carbonatites. Journal of Petrology, 1, 1-46.

Yamini, M.A., Tutti, F., Aminoroayaei Yamini, M. R., Ahmadian, J., and Wan, B. 2017. Examination of chloritization of biotite as a tool for reconstructing the physicochemical parameters of mineralization and associated alteration in the Zafarghand porphyry copper system, Ardestan, Central Iran: mineral-chemistry and stable isotope analyses. Mineralogy and Petrology, 111: 5, 747–759. https://doi.org/10.1007/s00710-016-0486-7

Yang, X. M., Yang, X. Y., Zhang, P. S., and Le Bas, M. J. 2000. Ba-REE fluorcarbonate minerals from a carbonatite dyke at Bayan Obo, Inner Mongolia, North China. Mineralogy and Petrology, 70, 221-234.

Yavuz, F. 2021. WinMIgob: A Windows program for magnetite-ilmenite geothermometer and oxygen barometer. Journal of Geosciences, 66 (1): 51-70. http://doi.org/10.3190/jgeosci.319

Yi, H., Balan, E., Gervais, C., Segalen, L., Fayon, F., Roche, D., Person, A., Morin, G., Guillaumet, M., Blanchard, M., Lazzeri, M., and Babonneau, F. 2013. A carbonate-fluoride defect model for carbonate-rich fluorapatite. American Mineralogist, 98: 5–6, 1066–1069. https://doi.org/10.2138/am.2013.4445

Zaitsev, A. N., Wall, F., and Le Bas, M. J. 1998. REE-Sr-Ba mineral from the Khibina carbonatites, Kola Peninsula, Russia: their mineralogy, paragenesis and evolution. Mineralogical Magazine, 62: 2, 225-250.

Zurevinski, S. E. and Mitchell, R. H. 2015. Petrogenesis of orbicular ijolites from the Prairie Lake complex, Marathon, Ontario: Textural evidence from rare processes of carbonatitic magmatism. Lithos, 239, 234–244. https://doi.org/10.1016/j.lithos.2015.11.003

Appendix I Mineral chemistry

I-I Apatite

	DDH-07-103 N = 3	DDH-04-37 N = 4	DDH-04-37 N = 2	DDH-09-457B N = 4	DDH-03-192 N = 3	DDH-03-192 N = 1	DDH-03-192 N = 1
Wt. %							
Na_2O	-	0.31	-	-	-	-	0.34
MgO	-	-	-	-	-	-	-
Al_2O_3	-	-	-	-	-	-	-
SiO_2	-	-	-	-	-	-	-
P_2O_5	40.00	39.26	39.26	42.01	42.43	42.16	42.22
K_2O	-	-	-	-	-	-	-
CaO	56.58	55.24	55.53	55.65	55.83	55.30	55.73
FeO	-	-	0.17	-	-	-	-
SrO	0.86	0.88	-	0.81	1.15	1.16	1.16
Y_2O_3	-	-	-	-	-	-	-
La_2O_3	-	-	-	-	-	-	-
Ce_2O_3	-	-	-	-	-	-	-
Nd_2O_3	-	-	-	-	-	0.54	-
Dy_2O_3	-	-	-	-	-	-	-
Yb_2O_3	-	-	-	-	-	-	-
ThO_2	-	-	-	-	-	-	-
F	4.30	3.75	4.65	3.91	3.83	4.56	4.02
Total	**101.75**	**99.71**	**99.96**	**102.37**	**103.23**	**103.71**	**103.47**
-O=F	1.81	1.58	1.96	1.64	1.61	1.92	1.69
Total	**99.93**	**98.14**	**98.00**	**100.72**	**101.62**	**101.79**	**101.78**

	DDH-07-103 N = 3	DDH-04-37 N = 4	DDH-04-37 N = 2	DDH-09-457B N = 4	DDH-03-192 N = 3	DDH-03-192 N = 1	DDH-03-192 N = 1
Structural formulae calculated on the basis of 12.5 oxygen							
Na	-	0.05	-	-	-	-	0.06
Mg	-	-	-	-	-	-	-
Al	-	-	-	-	-	-	-
Si	-	-	-	-	-	-	-
P	3.05	3.03	3.07	3.11	3.11	3.14	3.11
K	-	-	-	-	-	-	-
Ca	5.45	5.39	5.49	5.22	5.18	5.21	5.19
Fe	-	-	0.01	-	-	-	-
Sr	0.04	0.05	-	0.04	0.06	0.06	0.06
Y	-	-	-	-	-	-	-
La	-	-	-	-	-	-	-
Ce	-	-	-	-	-	-	-
Nd	-	-	-	-	-	0.02	-
Dy	-	-	-	-	-	-	-
Yb	-	-	-	-	-	-	-
Th	-	-	-	-	-	-	-
F	1.22	1.08	1.36	1.08	1.05	1.27	1.11
Total Cations	**8.54**	**8.52**	**8.58**	**8.37**	**8.36**	**8.42**	**8.42**

	PL-S2-PI N = 3	PL-S2-PI N = 2	RW-PL-02 N = 7	02-45.78 N = 3	DDH-04-495 N = 1	DDH-04-495 N = 1	DDH-04-666 N = 3
Wt. %							
Na_2O	-	0.30	-	-	-	0.20	0.22
MgO	-	-	-	-	-	-	-
Al_2O_3	-	-	-	-	-	-	-
SiO_2	-	-	-	-	-	-	-
P_2O_5	40.77	40.22	41.59	41.11	40.78	41.55	40.91
K_2O	-	-	-	-	-	-	-
CaO	54.72	54.26	54.79	55.89	55.30	55.44	54.63
FeO	-	-	-	-	-	-	-
SrO	0.60	0.57	1.10	0.61	1.66	1.64	0.57
Y_2O_3	-	-	-	-	-	-	-
La_2O_3	-	-	-	-	-	-	-
Ce_2O_3	-	-	-	-	-	-	-
Nd_2O_3	-	-	-	-	-	0.66	-
Dy_2O_3	-	-	-	-	-	-	-
Yb_2O_3	-	-	-	-	-	-	-
ThO_2	-	-	-	-	-	-	-
F	4.46	4.85	4.04	4.46	4.66	3.95	4.16
Total	**100.55**	**100.20**	**101.52**	**102.20**	**102.40**	**103.45**	**100.48**
-O=F	1.88	2.04	1.70	1.88	1.96	1.66	1.75
Total	**98.67**	**98.15**	**99.82**	**100.32**	**100.44**	**101.79**	**98.72**

	PL-S2-PI N = 3	PL-S2-PI N = 2	RW-PL-02 N = 7	02-45.78 N = 3	DDH-04-495 N = 1	DDH-04-495 N = 1	DDH-04-666 N = 3
Structural formulae calculated on the basis of 12.5 oxygen							
Na	-	0.05	-	-	-	0.03	0.04
Mg	-	-	-	-	-	-	-
Al	-	-	-	-	-	-	-
Si	-	-	-	-	-	-	-
P	3.12	3.12	3.12	3.10	3.10	3.08	3.11
K	-	-	-	-	-	-	-
Ca	5.30	5.34	5.21	5.34	5.32	5.21	5.26
Fe	-	-	-	-	-	-	-
Sr	0.03	0.03	0.06	0.03	0.09	0.08	0.03
Y	-	-	-	-	-	-	-
La	-	-	-	-	-	-	-
Ce	-	-	-	-	-	-	-
Nd	-	-	-	-	-	0.02	-
Dy	-	-	-	-	-	-	-
Yb	-	-	-	-	-	-	-
Th	-	-	-	-	-	-	-
F	1.28	1.41	1.13	1.26	1.32	1.10	1.18
Total Cations	**8.46**	**8.54**	**8.38**	**8.47**	**8.51**	**8.43**	**8.44**

	PL-S2-PI-2 N = 3	DDH-02-42.3 N = 4	DDH-02-42.3 N = 1	DDH-02-42.3 N = 1	02-260B N = 9	DDH-04-177 N = 2	DDH-04-177 N = 2
Wt. %							
Na_2O	0.44	0.32	-	-	0.24	-	0.24
MgO	-	-	-	-	-	-	-
Al_2O_3	-	-	-	-	-	-	-
SiO_2	-	-	-	-	-	-	-
P_2O_5	41.16	41.24	41.72	41.76	41.17	40.53	40.86
K_2O	-	-	-	-	-	-	-
CaO	54.24	54.26	54.63	54.75	54.41	55.02	55.11
FeO	-	-	0.45	-	-	-	-
SrO	0.96	0.61	-	0.86	0.91	0.42	-
Y_2O_3	-	-	-	-	-	-	-
La_2O_3	-	-	-	-	-	-	-
Ce_2O_3	0.32	-	-	-	-	-	-
Nd_2O_3	0.46	-	-	0.60	0.45	-	-
Dy_2O_3	-	-	-	-	-	-	-
Yb_2O_3	-	-	-	-	-	-	-
ThO_2	-	-	-	-	-	-	-
F	4.55	4.09	3.93	3.48	4.25	4.85	4.51
Total	**102.12**	**100.50**	**100.74**	**101.45**	**101.43**	**100.82**	**100.71**
-O=F	1.92	1.72	1.65	1.47	1.79	2.04	1.90
Total	**100.20**	**98.78**	**99.09**	**99.98**	**99.64**	**98.77**	**98.81**

	PL-S2-PI-2 N = 3	DDH-02-42.3 N = 4	DDH-02-42.3 N = 1	DDH-02-42.3 N = 1	02-260B N = 9	DDH-04-177 N = 2	DDH-04-177 N = 2
Structural formulae calculated on the basis of 12.5 oxygen							
Na	0.08	0.06	-	-	0.04	-	0.04
Mg	-	-	-	-	-	-	-
Al	-	-	-	-	-	-	-
Si	-	-	-	-	-	-	-
P	3.12	3.13	3.13	3.10	3.12	3.12	3.12
K	-	-	-	-	-	-	-
Ca	5.21	5.21	5.19	5.15	5.22	5.37	5.32
Fe	-	-	0.03	-	-	-	-
Sr	0.05	0.03	-	0.04	0.05	0.02	-
Y	-	-	-	-	-	-	-
La	-	-	-	-	-	-	-
Ce	0.01	-	-	-	-	-	-
Nd	0.01	-	-	0.02	0.01	-	-
Dy	-	-	-	-	-	-	-
Yb	-	-	-	-	-	-	-
Th	-	-	-	-	-	-	-
F	1.29	1.16	1.10	0.97	1.20	1.40	1.29
Total Cations	**8.49**	**8.42**	**8.35**	**8.32**	**8.44**	**8.51**	**8.49**

	DDH-03-251 N = 3	PL-S2-PI-1 N = 2	PL-S2-PI-1 N = 2	PL-S2-PI-1 N = 1	DDH-04-34 N = 2	02-118 N = 4	02-118 N = 2
Wt. %							
Na_2O	0.22	0.28	-	1.12	-	0.48	-
MgO	-	-	-	-	-	-	-
Al_2O_3	-	-	-	-	-	-	-
SiO_2	-	-	-	-	1.22	0.41	0.22
P_2O_5	42.11	41.24	41.08	39.46	38.97	40.16	41.64
K_2O	-	-	-	-	-	-	-
CaO	54.62	54.98	54.80	49.66	53.40	54.18	54.70
FeO	-	-	-	-	-	-	-
SrO	0.80	0.95	0.80	1.01	1.59	0.98	1.00
Y_2O_3	-	-	-	-	-	-	-
La_2O_3	-	-	-	-	-	-	-
Ce_2O_3	-	-	-	-	0.53	-	-
Nd_2O_3	-	-	-	1.20	-	-	-
Dy_2O_3	-	-	-	0.48	-	-	-
Yb_2O_3	0.38	-	0.60	-	-	-	-
ThO_2	-	-	-	-	-	-	-
F	3.72	3.89	4.44	4.66	3.54	4.51	4.04
Total	**102.52**	**101.32**	**101.72**	**97.58**	**99.22**	**100.72**	**101.60**
-O=F	1.56	1.64	1.87	1.96	1.49	1.90	1.70
Total	**100.95**	**99.68**	**99.85**	**95.62**	**97.73**	**98.82**	**99.89**

	DDH-03-251 N = 3	PL-S2-PI-1 N = 2	PL-S2-PI-1 N = 2	PL-S2-PI-1 N = 1	DDH-04-34 N = 2	02-118 N = 4	02-118 N = 2
Structural formulae calculated on the basis of 12.5 oxygen							
Na	0.04	0.05	-	0.21	-	0.08	-
Mg	-	-	-	-	-	-	-
Al	-	-	-	-	-	-	-
Si	-	-	-	-	0.11	0.04	0.02
P	3.12	3.10	3.12	3.17	2.99	3.08	3.12
K	-	-	-	-	-	-	-
Ca	5.13	5.23	5.27	5.04	5.19	5.27	5.18
Fe	-	-	-	-	-	-	-
Sr	0.04	0.05	0.04	0.06	0.08	0.05	0.05
Y	-	-	-	-	-	-	-
La	-	-	-	-	-	-	-
Ce	-	-	-	-	0.02	-	-
Nd	-	-	-	0.04	-	-	-
Dy	-	-	-	0.01	-	-	-
Yb	0.01	-	0.02	-	-	-	-
Th	-	-	-	-	-	-	-
F	1.03	1.09	1.26	1.40	1.02	1.29	1.13
Total Cations	**8.34**	**8.42**	**8.44**	**8.52**	**8.40**	**8.52**	**8.37**

	02-118 N = 2	PL-S1-P3-1 N = 6	PL-S1-P3-1 N = 3	PGH-18-06-199 N = 3	PGH-18-07-427 N = 4	PGH-18-07-427 N = 3	PGH-18-06-384 N = 2
Wt. %							
Na_2O	0.40	0.55	-	0.07	0.34	0.17	0.12
MgO	-	-	-	-	-	0.26	-
Al_2O_3	-	-	-	-	-	-	-
SiO_2	-	-	-	-	-	1.46	-
P_2O_5	39.12	40.55	41.19	41.75	40.20	38.52	41.23
K_2O	-	-	-	-	-	-	-
CaO	53.63	52.48	55.18	55.07	53.87	52.08	54.29
FeO	-	-	-	-	-	-	-
SrO	0.95	0.89	0.63	0.90	0.81	1.27	0.90
Y_2O_3	-	-	-	-	-	-	-
La_2O_3	-	-	-	-	-	0.42	-
Ce_2O_3	-	0.12	-	0.29	-	1.35	-
Nd_2O_3	-	0.11	-	0.32	-	0.76	-
Dy_2O_3	-	-	-	-	-	-	-
Yb_2O_3	-	0.25	-	-	-	-	-
ThO_2	-	-	-	-	-	-	-
F	4.87	4.57	4.57	3.85	3.54	3.07	4.01
Total	**98.96**	**99.51**	**101.57**	**102.25**	**98.74**	**99.36**	**100.53**
-O=F	2.05	1.92	1.93	1.62	1.49	1.29	1.69
Total	**96.91**	**97.59**	**99.65**	**100.63**	**97.25**	**98.06**	**98.84**

	02-118 N = 2	PL-S1-P3-1 N = 6	PL-S1-P3-1 N = 2	PGH-18-06-199 N = 3	PGH-18-07-427 N = 4	PGH-18-07-427 N = 3	PGH-18-06-384 N = 2
Structural formulae calculated on the basis of 12.5 oxygen							
Na	0.07	0.10	-	0.01	0.06	0.03	0.02
Mg	-	-	-	-	-	0.04	-
Al	-	-	-	-	-	-	-
Si	-	-	-	-	-	0.13	-
P	3.10	3.15	3.13	3.11	3.08	2.95	3.12
K	-	-	-	-	-	-	-
Ca	5.38	5.16	5.30	5.19	5.23	5.05	5.20
Fe	-	-	-	-	-	-	-
Sr	0.05	0.05	0.03	0.05	0.04	0.07	0.05
Y	-	-	-	-	-	-	-
La	-	-	-	-	-	0.01	-
Ce	-	-	-	0.01	-	0.04	-
Nd	-	-	-	0.01	-	0.02	-
Dy	-	-	-	-	-	-	-
Yb	-	0.01	-	-	-	-	-
Th	-	-	-	-	-	-	-
F	1.44	1.33	1.30	1.07	1.01	0.88	1.13
Total Cations	**8.61**	**8.48**	**8.46**	**8.37**	**8.41**	**8.35**	**8.39**

	DDH-07-179 N = 3	DDH-07-179 N = 2	RW-PL-08 N = 3	DDH-08-13 N = 3	DDH-08-13 N = 2	DDH-08-13 N = 2	RHM-12 N = 5
Wt. %							
Na_2O	0.24	0.11	-	0.19	1.35	0.12	0.21
MgO	-	-	0.10	-	-	-	-
Al_2O_3	-	-	-	-	-	-	-
SiO_2	-	-	1.29	0.31	-	-	-
P_2O_5	40.98	41.67	39.70	41.58	40.45	41.42	41.01
K_2O	-	-	-	-	-	-	-
CaO	54.43	54.84	53.45	55.26	50.48	54.99	54.69
FeO	-	-	-	-	-	-	-
SrO	0.42	0.58	-	0.40	0.33	0.44	0.74
Y_2O_3	-	-	-	0.39	2.64	0.65	-
La_2O_3	-	-	0.15	0.11	-	-	-
Ce_2O_3	0.20	-	0.49	0.26	0.69	-	-
Nd_2O_3	0.62	-	-	0.12	0.73	0.22	-
Dy_2O_3	-	-	-	-	-	-	-
Yb_2O_3	-	-	-	-	-	-	-
ThO_2	-	-	-	-	-	-	-
F	4.77	4.62	3.01	4.36	4.15	4.28	4.57
Total	**101.67**	**101.81**	**98.18**	**102.98**	**100.80**	**102.10**	**101.21**
-O=F	2.01	1.94	1.27	1.83	1.75	1.80	1.92
Total	**99.66**	**99.86**	**96.92**	**101.14**	**99.05**	**100.30**	**99.29**

	DDH-07-179 N = 3	DDH-07-179 N = 2	RW-PL-08 N = 3	DDH-08-13 N = 3	DDH-08-13 N = 2	DDH-08-13 N = 2	RHM-12 N = 5
Structural formulae calculated on the basis of 12.5 oxygen							
Na	0.04	0.02	-	0.03	0.24	0.02	0.04
Mg	-	-	0.01	-	-	-	-
Al	-	-	-	-	-	-	-
Si	-	-	0.12	0.03	-	-	-
P	3.13	3.15	3.01	3.10	3.11	3.11	3.13
K	-	-	-	-	-	-	-
Ca	5.27	5.24	5.13	5.21	4.92	5.23	5.28
Fe	-	-	-	-	-	-	-
Sr	0.02	0.03	-	0.02	0.02	0.02	0.04
Y	-	-	-	0.02	0.13	0.03	-
La	-	-	-	-	-	-	-
Ce	0.01	-	0.02	0.01	0.02	-	-
Nd	0.02	-	-	-	0.02	0.01	-
Dy	-	-	-	-	-	-	-
Yb	-	-	-	-	-	-	-
Th	-	-	-	-	-	-	-
F	1.36	1.30	0.85	1.21	1.19	1.20	1.30
Total Cations	**8.49**	**8.44**	**8.29**	**8.43**	**8.46**	**8.42**	**8.48**

	PGH-18-07-174 N = 4	PGH-18-07-174 N = 3
Wt. %		
Na_2O	0.55	-
MgO	-	-
Al_2O_3	-	-
SiO_2	0.10	-
P_2O_5	40.26	41.16
K_2O	-	-
CaO	52.57	54.72
FeO	-	-
SrO	0.59	0.70
Y_2O_3	-	-
La_2O_3	0.10	-
Ce_2O_3	0.75	-
Nd_2O_3	0.59	-
Dy_2O_3	-	-
Yb_2O_3	-	-
ThO_2	0.09	-
F	4.79	4.70
Total	**100.40**	**101.28**
-O=F	2.02	1.98
Total	**98.38**	**99.31**

	PGH-18-07-174 N = 4	PGH-18-07-174 N = 3
Structural formulae calculated on the basis of 12.5 oxygen		
Na	0.10	-
Mg	-	-
Al	-	-
Si	0.01	-
P	3.14	3.14
K	-	-
Ca	5.18	5.28
Fe	-	-
Sr	0.03	0.04
Y	-	-
La	-	-
Ce	0.03	-
Nd	0.02	-
Dy	-	-
Yb	-	-
Th	-	-
F	1.39	1.34
Total Cations	**8.51**	**8.46**

I-II Calcite

	RHM-07 n = 3	RHM-07 n = 4	RHM-07 n = 1	RHM-10 n = 3	RHM-10 n = 1	DDH-07-103 n = 4	DDH-07-103 n = 1	DDH-07-103 n = 1	DDH-04-37 n = 2	DDH-04-37 n = 1
Wt. %										
$Mg(CO_3)$	0.52	-	-	-	0.88	-	-	-	-	-
$Ca(CO_3)$	92.63	93.25	94.00	96.73	94.09	96.62	97.44	97.73	94.17	96.44
$Mn(CO_3)$	4.50	5.63	4.02	1.06	1.30	0.60	0.55	-	3.40	-
$Fe(CO_3)$	-	-	-	0.78	1.77	0.61	-	-	0.59	0.84
$Sr(CO_3)$	1.65	-	1.21	-	0.91	-	-	-	-	0.83
Total	**99.31**	**98.89**	**99.23**	**98.58**	**98.95**	**97.83**	**97.99**	**97.73**	**98.16**	**98.11**
Structural formulae calculated on the basis of 6 oxygens										
Mg	0.04	-	-	-	0.06	-	-	-	-	-
Ca	5.65	5.70	5.74	5.90	5.74	5.94	5.97	6.00	5.79	5.92
Mn	0.24	0.30	0.21	0.06	0.07	0.03	0.03	-	0.18	-
Fe	-	-	-	0.04	0.09	0.03	-	-	0.03	0.04
Sr	0.07	-	0.05	-	0.04	-	-	-	-	0.03
Total	**6.00**	**6.00**	**6.00**	**6.00**	**6.00**	**6.00**	**6.00**	**6.00**	**6.00**	**6.00**

	DDH-04-37 n = 1	DDH-09-457B n = 3	DDH-03-192 n = 5	RW-PL-02 n = 3	RW-PL-02 n = 2	RW-PL-02 n = 1	02-45.78 n = 3	DDH-04-495 n = 3	DDH-04-495 n = 3	DDH-04-495 n = 1
Wt. %										
$Mg(CO_3)$	-	1.11	1.40	-	-	-	-	0.93	-	-
$Ca(CO_3)$	96.80	90.97	93.70	93.48	94.68	90.64	95.22	91.31	94.69	94.37
$Mn(CO_3)$	-	6.13	1.17	6.03	4.46	6.16	0.58	0.69	0.46	0.58
$Fe(CO_3)$	0.71	0.91	1.07	-	0.55	0.74	-	0.99	0.60	0.55
$Sr(CO_3)$	-	1.56	2.13	-	-	0.71	-	1.25	-	0.51
Total	**97.51**	**100.68**	**99.46**	**99.51**	**99.69**	**98.25**	**95.80**	**95.18**	**95.75**	**96.02**
Structural formulae calculated on the basis of 6 oxygens										
Mg	-	0.08	0.10	-	-	-	-	0.07	-	-
Ca	5.96	5.49	5.69	5.68	5.74	5.60	5.97	5.78	5.94	5.92
Mn	-	0.32	0.06	0.32	0.23	0.33	0.03	0.04	0.03	0.03
Fe	0.04	0.05	0.06	-	0.03	0.04	-	0.05	0.03	0.03
Sr	-	0.06	0.09	-	-	0.03	-	0.05	-	0.02
Total	**6.00**	**6.00**	**6.00**	**6.00**	**6.00**	**6.00**	**6.00**	**6.00**	**6.00**	**6.00**

	DDH-04-495 n = 1	DDH-04-666 n = 4	PL-S2-PI-2 n = 3	PL-S2-PI-2 n = 1	PL-S2-PI-2 n = 1	PL-S2-PI-2 n = 1	DDH-04-606 n = 2	DDH-04-606 n = 2	DDH-04-606 n = 1	DDH-02-42 n = 1
Wt. %										
$Mg(CO_3)$	0.25	-	0.36	-	-	-	0.43	-	0.63	-
$Ca(CO_3)$	94.34	91.86	92.66	95.39	95.66	93.35	92.41	93.06	86.09	91.91
$Mn(CO_3)$	0.32	0.75	0.93	1.05	1.57	1.33	0.83	0.67	-	1.04
$Fe(CO_3)$	0.73	1.00	0.95	-	0.40	-	0.89	0.53	2.64	1.16
$Sr(CO_3)$	-	0.92	0.65	-	0.46	0.57	0.65	0.61	-	-
Total	**95.64**	**94.53**	**95.56**	**96.44**	**98.09**	**95.25**	**95.21**	**94.87**	**89.36**	**94.11**
Structural formulae calculated on the basis of 6 oxygens										
Mg	0.02	-	0.03	-	-	-	0.03	-	0.05	-
Ca	5.92	5.86	5.84	5.94	5.88	5.90	5.84	5.91	5.80	5.88
Mn	0.02	0.04	0.05	0.06	0.08	0.07	0.05	0.04	-	0.06
Fe	0.04	0.06	0.05	-	0.02	-	0.05	0.03	0.15	0.06
Sr	-	0.04	0.03	-	0.02	0.02	0.03	0.03	-	-
Total	**6.00**	**6.00**	**6.00**	**6.00**	**6.00**	**6.00**	**6.00**	**6.00**	**6.00**	**6.00**

	DDH-02-42 n = 1	RW-PL-06 n = 1	RW-PL-06 n = 1	RW-PL-06 n = 1	DDH-04-177 n = 1	DDH-04-177 n = 1	DDH-04-177 n = 1	DDH-03-251 n = 2	DDH-03-251 n = 1	PL-S2-PI-1 n = 3
Wt. %										
$Mg(CO_3)$	-	-	0.48	1.00	0.54	-	-	0.96	0.36	-
$Ca(CO_3)$	96.01	91.87	92.51	91.30	91.60	94.57	97.64	89.64	93.48	94.48
$Mn(CO_3)$	-	0.70	0.55	1.04	0.44	0.70	0.42	0.50	-	1.03
$Fe(CO_3)$	-	0.53	0.97	1.02	0.40	0.52	-	1.25	-	0.41
$Sr(CO_3)$	-	0.66	0.90	-	1.80	-	-	1.41	1.48	0.38
Total	**96.01**	**93.76**	**95.41**	**94.36**	**94.78**	**95.78**	**98.06**	**93.77**	**95.32**	**96.30**
Structural formulae calculated on the basis of 6 oxygens										
Mg	-	-	0.04	0.08	0.04	-	-	0.07	0.03	-
Ca	6.00	5.90	5.84	5.81	5.83	5.93	5.98	5.77	5.91	5.91
Mn	-	0.04	0.03	0.06	0.02	0.04	0.02	0.03	-	0.06
Fe	-	0.03	0.05	0.06	0.02	0.03	-	0.07	-	0.02
Sr	-	0.03	0.04	-	0.08	-	-	0.06	0.06	0.02
Total	**6.00**	**6.00**	**6.00**	**6.00**	**6.00**	**6.00**	**6.00**	**6.00**	**6.00**	**6.00**

	PL-S2-PI-1 n = 2	PL-S2-PI-1 n = 1	PL-S2-PI-1 n = 1	DDH-04-34 n = 2	DDH-04-34 n = 1	DDH-04-34 n = 1	02-118 n = 2	02-118 n = 1	02-118 n = 1	PL-S1-P3-1 n = 1
Wt. %										
$Mg(CO_3)$	-	-	-	-	-	-	-	-	2.47	3.35
$Ca(CO_3)$	92.61	92.53	93.84	93.37	90.25	91.30	93.51	93.46	88.71	91.73
$Mn(CO_3)$	1.17	1.49	0.91	0.49	0.53	-	0.45	0.70	1.69	-
$Fe(CO_3)$	-	0.44	-	1.14	1.34	-	-	0.37	0.94	1.60
$Sr(CO_3)$	-	-	0.34	-	2.14	2.21	-	-	0.56	-
Total	**93.78**	**94.46**	**95.08**	**95.00**	**94.26**	**93.51**	**93.96**	**94.53**	**94.36**	**96.67**
Structural formulae calculated on the basis of 6 oxygens										
Mg	-	-	-	-	-	-	-	-	0.19	0.25
Ca	5.93	5.89	5.94	5.91	5.80	5.90	5.97	5.94	5.64	5.67
Mn	0.07	0.08	0.05	0.03	0.03	-	0.03	0.04	0.09	-
Fe	-	0.02	-	0.06	0.07	-	-	0.02	0.05	0.09
Sr	-	-	0.01	-	0.09	0.10	-	-	0.02	-
Total	**6.00**	**6.00**	**6.00**	**6.00**	**6.00**	**6.00**	**6.00**	**6.00**	**6.00**	**6.00**

	PL-S1-P3-1 n = 1	PGH-18-06-199 n = 4	PGH-18-06-199 n = 1	PGH-18-07-427 n = 2	PGH-18-07-427 n = 4	PGH-18-07-427 n = 1	PGH-18-06-384 n = 3	PGH-18-06-384 n = 1	DDH-07-179 n = 4	DDH-07-179 n = 2
Wt. %										
$Mg(CO_3)$	-	0.78	-	-	1.65	1.42	0.39	-	-	-
$Ca(CO_3)$	93.85	91.92	95.50	91.83	87.43	89.39	90.54	93.92	94.31	93.56
$Mn(CO_3)$	0.89	0.93	0.39	1.50	0.62	1.05	0.95	0.29	0.65	0.68
$Fe(CO_3)$	-	1.06	0.69	1.37	1.40	-	0.55	0.56	-	0.36
$Sr(CO_3)$	-	1.03	-	1.38	3.08	1.99	1.72	0.28	-	-
Total	**94.74**	**95.73**	**96.58**	**96.08**	**94.18**	**93.86**	**94.15**	**95.07**	**94.96**	**94.60**
Structural formulae calculated on the basis of 6 oxygens										
Mg	-	0.06	-	-	0.13	0.11	0.03	-	-	-
Ca	5.95	5.79	5.94	5.78	5.63	5.75	5.81	5.94	5.96	5.94
Mn	0.05	0.05	0.02	0.08	0.03	0.06	0.05	0.02	0.04	0.04
Fe	-	0.06	0.04	0.07	0.08	-	0.03	0.03	-	0.02
Sr	-	0.04	-	0.06	0.13	0.09	0.08	0.01	-	-
Total	**6.00**	**6.00**	**6.00**	**6.00**	**6.00**	**6.00**	**6.00**	**6.00**	**6.00**	**6.00**

	DDH-08-13 n = 2	DDH-08-13 n = 1	DDH-08-13 n = 1	RHM-06 n = 4	RHM-06 n = 1	RHM-06 n = 1	RHM-06 n = 1	RHM-12 n = 2	RHM-12 n = 1	PGH-18-07-174 n = 2
Wt. %										
$Mg(CO_3)$	4.99	0.48	0.92	0.51	-	-	0.61	-	-	-
$Ca(CO_3)$	92.26	92.39	84.50	85.43	85.88	87.21	84.22	96.57	96.76	92.76
$Mn(CO_3)$	-	1.91	0.75	2.79	2.71	1.57	0.75	-	0.52	0.73
$Fe(CO_3)$	-	-	0.79	0.58	-	0.44	-	-	-	0.62
$Sr(CO_3)$	-	-	4.86	1.54	1.47	0.97	5.44	-	0.41	-
Total	**97.25**	**94.78**	**91.82**	**90.85**	**90.05**	**90.19**	**91.01**	**96.57**	**97.69**	**94.11**
Structural formulae calculated on the basis of 6 oxygens										
Mg	0.36	0.04	0.07	0.04	-	-	0.05	-	-	-
Ca	5.64	5.86	5.62	5.69	5.77	5.84	5.66	6.00	5.95	5.93
Mn	-	0.11	0.04	0.16	0.16	0.09	0.04	-	0.03	0.04
Fe	-	-	0.05	0.03	-	0.03	-	-	-	0.03
Sr	-	-	0.22	0.07	0.07	0.04	0.25	-	0.02	-
Total	**6.00**	**6.00**	**6.00**	**6.00**	**6.00**	**6.00**	**6.00**	**6.00**	**6.00**	**6.00**

	PGH-18-07-174 n = 2	PGH-18-07-174 n = 1	PGH-18-07-174 n = 1	PGH-18-06-416 n = 7
Wt. %				
$Mg(CO_3)$	-	-	-	1.40
$Ca(CO_3)$	93.01	92.57	93.01	89.78
$Mn(CO_3)$	1.33	1.28	0.86	0.91
$Fe(CO_3)$	0.77	-	-	2.24
$Sr(CO_3)$	0.54	0.24	-	1.29
Total	**95.66**	**94.09**	**93.87**	**95.62**
Structural formulae calculated on the basis of 6 oxygens				
Mg	-	-	-	0.10
Ca	5.86	5.92	5.95	5.67
Mn	0.07	0.07	0.05	0.05
Fe	0.04	-	-	0.12
Sr	0.02	0.01	-	0.06
Total	**6.00**	**6.00**	**6.00**	**6.00**

I-III Ferroan dolomite and dolomite

	DDH-07-103 n = 2	DDH-07-103 n = 7	DDH-07-103 n = 9	DDH-07-103 n = 6	DDH-04-37 n = 4	DDH-09-457B n = 3	DDH-03-192 n = 2	DDH-03-192 n = 2	PL-S2-PI n = 3	PL-S2-PI n = 1
Wt. %										
$Mg(CO_3)$	32.58	31.68	26.21	38.17	17.95	31.49	28.43	31.92	25.60	18.85
$Ca(CO_3)$	53.31	54.18	52.81	54.40	52.74	52.80	57.12	53.37	50.94	49.58
$Mn(CO_3)$	2.55	1.88	2.84	1.49	2.58	0.92	1.71	1.85	4.19	1.07
$Fe(CO_3)$	12.31	13.00	19.39	2.80	27.47	14.74	14.31	14.08	19.45	29.77
$Sr(CO_3)$	1.13	-	-	1.13	-	-	-	0.64	-	-
Total	**101.87**	**100.74**	**101.25**	**97.99**	**100.74**	**99.95**	**101.56**	**101.86**	**100.18**	**99.26**
Structural formulae calculated on the basis of 6 oxygens										
Mg	2.15	2.16	1.81	2.61	1.28	2.16	1.93	2.16	1.79	1.36
Ca	3.07	3.11	3.07	3.13	3.16	3.05	3.27	3.04	3.00	3.02
Mn	0.13	0.09	0.14	0.07	0.14	0.05	0.09	0.09	0.22	0.06
Fe	0.61	0.64	0.97	0.14	1.42	0.74	0.71	0.69	0.99	1.56
Sr	0.05	-	-	0.04	-	-	-	0.03	-	-
Total	**6.00**	**6.00**	**6.00**	**6.00**	**6.00**	**6.00**	**6.00**	**6.00**	**6.00**	**6.00**

	02-45.78 n = 4	02-45.78 n = 2	DDH-04-495 n = 3	DDH-04-495 n = 3	DDH-04-495 n = 2	DDH-04-666 n = 10	DDH-04-666 n = 9	PL-S2-PI-2 n = 3	PL-S2-PI-2 n = 6	PL-S2-PI-2 n = 7
Wt. %										
$Mg(CO_3)$	25.81	36.18	30.89	28.25	31.02	21.49	27.26	29.43	33.38	38.69
$Ca(CO_3)$	51.88	55.34	52.50	53.61	52.66	50.26	51.74	51.48	52.68	53.25
$Mn(CO_3)$	2.58	1.22	0.67	1.64	0.80	1.26	2.00	0.76	0.96	0.55
$Fe(CO_3)$	19.43	3.49	14.61	15.91	12.88	25.96	17.68	16.02	11.06	2.73
$Sr(CO_3)$	0.21	-	-	0.63	-	-	0.45	0.38	0.42	0.49
Total	**99.91**	**96.23**	**98.68**	**100.04**	**97.37**	**98.97**	**99.12**	**98.07**	**98.51**	**95.71**
Structural formulae calculated on the basis of 6 oxygens										
Mg	1.81	2.52	2.15	1.96	2.18	1.54	1.92	2.07	2.31	2.69
Ca	3.06	3.25	3.08	3.13	3.12	3.04	3.06	3.05	3.07	3.12
Mn	0.14	0.06	0.04	0.08	0.04	0.07	0.10	0.04	0.05	0.03
Fe	0.99	0.18	0.74	0.80	0.66	1.36	0.91	0.82	0.56	0.14
Sr	0.01	-	-	0.02	-	-	0.02	0.02	0.02	0.02
Total	**6.00**	**6.00**	**6.00**	**6.00**	**6.00**	**6.00**	**6.00**	**6.00**	**6.00**	**6.00**

	DDH-04-606 n = 5	DDH-04-606 n = 5	DDH-02-42 n = 2	DDH-02-42 n = 2	DDH-02-42 n = 2	02-260B n = 8	02-260B n = 5	RW-PL-06 n = 8	DDH-04-177 n = 4	DDH-04-177 n = 6
Wt. %										
$Mg(CO_3)$	30.53	26.15	27.90	25.97	33.70	28.76	24.00	32.06	23.51	29.96
$Ca(CO_3)$	52.42	51.17	50.06	50.52	53.02	51.76	50.52	51.28	51.89	52.67
$Mn(CO_3)$	1.11	1.72	2.24	2.36	1.77	2.02	2.14	1.42	2.49	0.78
$Fe(CO_3)$	13.93	19.45	17.56	19.52	9.05	15.99	22.64	12.77	21.39	13.59
$Sr(CO_3)$	0.32	0.05	-	-	-	-	-	0.45	-	0.07
Total	**98.30**	**98.54**	**97.77**	**98.37**	**97.54**	**98.53**	**99.30**	**97.99**	**99.25**	**97.06**
Structural formulae calculated on the basis of 6 oxygens										
Mg	2.13	1.85	1.98	1.85	2.35	2.02	1.70	2.24	1.67	2.12
Ca	3.09	3.06	2.99	3.02	3.11	3.06	3.02	3.02	3.10	3.14
Mn	0.06	0.09	0.12	0.13	0.09	0.11	0.11	0.07	0.13	0.04
Fe	0.71	1.00	0.91	1.01	0.46	0.82	1.17	0.65	1.11	0.70
Sr	0.01	-	-	-	-	-	-	0.02	-	-
Total	**6.00**	**6.00**	**6.00**	**6.00**	**6.00**	**6.00**	**6.00**	**6.00**	**6.00**	**6.00**

	DDH-04-177 n = 3	DDH-03-251 n = 3	DDH-03-251 n = 4	DDH-03-251 n = 1	PL-S2-PI-1 n = 1	PL-S2-PI-1 n = 1	DDH-04-34 n = 3	02-118 n = 3	02-118 n = 3	02-118 n = 1
Wt. %										
$Mg(CO_3)$	38.56	21.71	31.54	34.58	29.18	34.14	24.39	24.86	28.70	34.49
$Ca(CO_3)$	54.14	51.18	52.38	53.45	51.83	51.45	50.52	50.49	51.10	52.29
$Mn(CO_3)$	0.86	1.81	1.00	-	2.75	2.07	2.58	6.37	2.38	6.97
$Fe(CO_3)$	2.62	24.43	13.96	10.53	14.43	6.53	20.95	16.43	14.76	0.95
$Sr(CO_3)$	-	0.31	-	-	0.56	1.80	-	-	0.37	0.30
Total	**96.18**	**99.45**	**98.88**	**98.55**	**98.75**	**95.99**	**98.44**	**98.15**	**97.31**	**95.00**
Structural formulae calculated on the basis of 6 oxygens										
Mg	2.67	1.55	2.19	2.38	2.04	2.42	1.74	1.78	2.04	2.45
Ca	3.15	3.07	3.06	3.10	3.06	3.07	3.03	3.04	3.06	3.13
Mn	0.05	0.10	0.05	-	0.14	0.11	0.13	0.33	0.13	0.36
Fe	0.13	1.27	0.71	0.53	0.74	0.34	1.09	0.85	0.76	0.05
Sr	-	0.01	-	-	0.02	0.07	-	-	0.01	0.01
Total	**6.00**	**6.00**	**6.00**	**6.00**	**6.00**	**6.00**	**6.00**	**6.00**	**6.00**	**6.00**

	PL-S3-PI-1 n = 3	PL-S3-PI-1 n = 3	PL-S3-PI-1 n = 2	PL-S3-PI-1 n = 1	PGH-18-06-199 n = 3	PGH-18-06-199 n = 6	PGH-18-07-427 n = 3	PGH-18-07-427 n = 2	PGH-18-06-384 n = 4	PGH-18-06-384 n = 5
Wt. %										
$Mg(CO_3)$	28.77	26.56	36.83	15.99	32.59	24.03	29.19	17.17	29.73	26.31
$Ca(CO_3)$	50.90	50.86	51.70	29.28	52.34	51.29	51.95	49.65	52.62	51.14
$Mn(CO_3)$	1.63	2.00	3.13	0.78	2.24	2.14	2.46	2.41	1.30	1.53
$Fe(CO_3)$	16.24	19.25	3.24	6.62	10.99	22.77	14.23	29.52	14.40	19.77
$Sr(CO_3)$	0.50	-	-	0.24	0.84	-	0.91	0.40	0.32	0.05
Total	**98.05**	**98.66**	**94.90**	**52.90**	**98.99**	**100.23**	**98.74**	**99.16**	**98.37**	**98.79**
Structural formulae calculated on the basis of 6 oxygens										
Mg	2.03	1.88	2.60	2.32	2.26	1.69	2.04	1.24	2.08	1.86
Ca	3.03	3.03	3.08	3.06	3.05	3.04	3.07	3.04	3.11	3.04
Mn	0.08	0.10	0.16	0.06	0.11	0.11	0.13	0.13	0.07	0.08
Fe	0.84	0.99	0.17	0.54	0.55	1.17	0.73	1.58	0.74	1.02
Sr	0.02	-	-	0.01	0.03	-	0.03	0.02	0.01	-
Total	**6.00**	**6.00**	**6.00**	**6.00**	**6.00**	**6.00**	**6.00**	**6.00**	**6.00**	**6.00**

	PGH-18-06-384 n = 1	DDH-07-179 n = 2	DDH-07-179 n = 3	DDH-07-179 n = 4	DDH-08-13 n = 6	DDH-08-13 n = 4	DDH-08-13 n = 6	RHM-06 n = 6	RHM-12 n = 4	RHM-12 n = 2
Wt. %										
$Mg(CO_3)$	36.27	32.24	29.34	34.04	32.22	27.29	39.03	27.42	33.93	27.53
$Ca(CO_3)$	52.08	51.58	51.46	52.47	52.12	51.42	53.90	49.51	52.34	51.58
$Mn(CO_3)$	1.52	2.03	3.57	2.29	3.08	1.46	0.79	1.93	3.07	3.95
$Fe(CO_3)$	5.21	9.51	13.96	8.42	11.61	19.09	2.09	15.57	9.32	16.90
$Sr(CO_3)$	0.94	0.33	0.47	0.88	0.29	-	0.15	0.08	0.76	-
Total	**96.02**	**95.69**	**98.80**	**98.11**	**99.32**	**99.39**	**95.96**	**94.51**	**99.43**	**99.95**
Structural formulae calculated on the basis of 6 oxygens										
Mg	2.54	2.29	2.06	2.36	2.22	1.91	2.70	2.01	2.33	1.92
Ca	3.08	3.09	3.03	3.06	3.03	3.04	3.15	3.06	3.03	3.03
Mn	0.08	0.11	0.19	0.12	0.16	0.08	0.04	0.10	0.15	0.20
Fe	0.27	0.49	0.71	0.43	0.58	0.97	0.11	0.83	0.47	0.86
Sr	0.04	0.01	0.02	0.04	0.01	-	0.01	-	0.03	-
Total	**6.00**	**6.00**	**6.00**	**6.00**	**6.00**	**6.00**	**6.00**	**6.00**	**6.00**	**6.00**

	RHM-12 n = 2	PGH-18-07-174 n = 1	PGH-18-07-174 n = 1	PGH-18-06-416 n = 5
Wt. %				
$Mg(CO_3)$	39.20	24.03	30.29	30.51
$Ca(CO_3)$	53.58	51.61	51.74	52.80
$Mn(CO_3)$	0.44	4.78	2.01	1.61
$Fe(CO_3)$	0.89	20.24	14.45	15.18
$Sr(CO_3)$	-	-	0.30	0.64
Total	**94.11**	**100.66**	**98.78**	**100.74**
Structural formulae calculated on the basis of 6 oxygens				
Mg	2.76	1.68	2.11	2.09
Ca	3.18	3.04	3.04	3.05
Mn	0.03	0.25	0.10	0.08
Fe	0.05	1.03	0.73	0.76
Sr	-	-	0.01	0.03
Total	**6.00**	**6.00**	**6.00**	**6.00**

I-IV Pyrochlore

	DDH-03-192 n = 2 Pcl	RW-PL-02 n = 1 Pcl	RW-PL-02 n = 1 Frs	RW-PL-02 n = 1 Frs	RW-PL-02 n = 2 Frs	RW-PL-02 n = 1 Frs	RW-PL-02 n = 1 Frs	02-45 n = 1 Pcl	02-45 n = 2 Frs	02-45 n = 1 Frs
Wt. %										
Na_2O	7.71	7.94	5.53	4.69	-	-	-	6.49	1.38	-
CaO	16.08	17.35	15.27	12.88	8.30	10.04	16.41	14.72	11.57	8.63
MnO	-	-	1.78	4.80	11.24	8.81	1.61	-	-	0.54
SrO	1.04	0.87	1.17	0.35	-	-	-	2.44	6.45	5.38
BaO	-	-	-	-	-	-	-	-	-	-
FeO	-	-	0.68	2.19	6.23	4.21	1.13	0.95	1.00	5.06
Ce_2O_3	-	-	-	1.31	1.72	1.35	0.52	-	-	-
Nd_2O_3	-	-	-	0.82	0.27	-	-	-	-	-
UO_3	-	-	-	-	-	-	-	-	-	1.16
MgO	-	-	-	-	-	-	-	-	-	-
Al_2O_3	-	-	-	-	-	-	-	-	-	-
SiO_2	-	-	-	-	-	-	-	-	1.11	1.88
TiO_2	3.34	3.67	3.16	2.56	3.84	7.04	2.87	2.73	2.96	4.68
Nb_2O_5	70.02	66.10	70.61	66.41	70.57	71.37	79.84	69.37	67.31	61.10
Ta_2O_5	-	-	-	-	-	-	-	-	-	-
F	6.27	5.82	-	-	-	-	-	5.42	1.36	-
-O=F	2.64	2.45	-	-	-	-	-	2.28	0.57	-
Total	**101.81**	**99.30**	**98.20**	**96.01**	**102.15**	**102.82**	**102.38**	**99.84**	**92.54**	**88.43**

	DDH-03-192 n = 2 Pcl	RW-PL-02 n = 1 Pcl	RW-PL-02 n = 1 Frs	RW-PL-02 n = 1 Frs	RW-PL-02 n = 2 Frs	RW-PL-02 n = 1 Frs	RW-PL-02 n = 1 Frs	02-45 n = 1 Pcl	02-45 n = 2 Frs	02-45 n = 1 Frs
Structural formula calculated on the basis of 6 oxygen normalized to 2 B-site cations										
Na	0.88	0.94	0.63	0.57	-	-	-	0.75	0.16	-
Ca	1.01	1.14	0.95	0.86	0.51	0.57	0.92	0.94	0.73	0.56
Mn	-	-	0.09	0.25	0.55	0.40	0.07	-	-	0.03
Sr	0.04	0.03	0.04	0.01	-	-	-	0.08	0.22	0.19
Ba	-	-	-	-	-	-	-	-	-	-
Fe	-	-	0.03	0.11	0.30	0.19	0.05	0.05	0.05	0.26
Ce	-	-	-	0.03	0.04	0.03	0.01	-	-	-
Nd	-	-	-	0.02	0.01	-	-	-	-	-
U	-	-	-	-	-	-	-	-	-	0.01
A-Site Total	**1.92**	**2.11**	**1.74**	**1.86**	**1.40**	**1.18**	**1.05**	**1.83**	**1.16**	**1.05**
A-Site Vacancy	0.08	-0.11	0.26	0.14	0.60	0.82	0.95	0.17	0.84	0.95
Mg	-	-	-	-	-	-	-	-	-	-
Al	-	-	-	-	-	-	-	-	-	-
Si	-	-	-	-	-	-	-	-	0.07	0.11
Ti	0.15	0.17	0.14	0.12	0.17	0.28	0.11	0.12	0.13	0.21
Nb	1.85	1.83	1.86	1.88	1.83	1.72	1.89	1.88	1.80	1.67
Ta	-	-	-	-	-	-	-	-	-	-
B-Site Total	**2.00**	**2.00**	**2.00**	**2.00**	**2.00**	**2.00**	**2.00**	**2.00**	**2.00**	**2.00**
F	1.16	1.13	-	-	-	-	-	1.03	0.25	-

	PL-S2-PI-2 n = 1 Pcl	DDH-04-606 n = 2 Frs	DDH-04-606 n = 2 Pcl	DDH-02-42 n = 3 Pcl	DDH-02-42 n = 1 Frs	DDH-02-42 n = 1 Pcl	02-260B n = 2 Frs	02-260B n = 1 Clf	02-260B n = 1 Frs	02-260B n = 1 Frs
Wt. %										
Na_2O	8.40	5.36	8.02	7.47	4.23	7.66	6.18	-	0.83	1.28
CaO	15.68	13.29	15.41	15.27	12.67	15.64	13.30	7.74	6.40	3.96
MnO	-	-	-	-	-	-	-	-	-	-
SrO	1.13	2.23	0.54	1.25	4.14	-	3.88	-	9.92	7.69
BaO	-	-	-	-	-	-	0.49	1.97	4.58	7.04
FeO	-	0.88	-	0.19	0.56	0.34	1.53	15.10	4.30	2.71
Ce_2O_3	-	-	-	-	-	-	-	-	-	-
Nd_2O_3	-	-	-	-	-	-	-	-	-	-
UO_3	-	0.93	-	-	-	-	-	-	2.70	7.92
MgO	-	-	-	-	-	-	-	-	-	0.28
Al_2O_3	-	-	-	-	-	-	-	-	-	0.35
SiO_2	2.08	1.15	-	-	0.82	-	2.52	2.43	2.78	9.46
TiO_2	5.99	2.93	3.70	2.71	1.96	4.60	3.33	3.23	3.09	1.04
Nb_2O_5	64.02	66.92	67.50	69.08	67.25	65.59	65.18	55.04	53.04	41.18
Ta_2O_5	-	-	-	-	-	-	-	-	-	3.14
F	6.80	4.30	4.82	5.91	4.34	6.44	5.06	-	2.10	-
-O=F	2.86	1.81	2.03	2.49	1.83	2.71	2.13	-	0.88	-
Total	**101.24**	**96.16**	**97.95**	**99.38**	**94.14**	**97.56**	**99.33**	**85.51**	**88.86**	**86.05**

	PL-S2-PI-2 n = 1 Pcl	DDH-04-606 n = 2 Frs	DDH-04-606 n = 2 Pcl	DDH-02-42 n = 3 Pcl	DDH-02-42 n = 1 Frs	DDH-02-42 n = 1 Pcl	02-260B n = 2 Frs	02-260B n = 1 Clf	02-260B n = 1 Frs	02-260B n = 1 Frs
Structural formula calculated on the basis of 6 oxygen normalized to 2 B-site cations										
Na	0.92	0.62	0.93	0.87	0.50	0.90	0.69	-	0.11	0.16
Ca	0.95	0.85	0.99	0.98	0.83	1.01	0.83	0.56	0.47	0.28
Mn	-	-	-	-	-	-	-	-	-	-
Sr	0.04	0.08	0.02	0.04	0.15	-	0.13	-	0.40	0.29
Ba	-	-	-	-	-	-	0.01	0.05	0.12	0.18
Fe	-	0.04	-	0.01	0.03	0.02	0.07	0.85	0.25	0.15
Ce	-	-	-	-	-	-	-	-	-	-
Nd	-	-	-	-	-	-	-	-	-	-
U	-	0.01	-	-	-	-	-	-	0.04	0.11
A-Site Total	**1.90**	**1.60**	**1.94**	**1.91**	**1.51**	**1.93**	**1.73**	**1.46**	**1.39**	**1.17**
A-Site Vacancy	0.10	0.40	0.06	0.09	0.49	0.07	0.27	0.54	0.61	0.83
Mg	-	-	-	-	-	-	-	-	-	0.03
Al	-	-	-	-	-	-	-	-	-	0.03
Si	0.12	0.07	-	-	0.05	-	0.14	0.16	0.19	0.62
Ti	0.25	0.13	0.17	0.12	0.09	0.21	0.15	0.16	0.16	0.05
Nb	1.63	1.80	1.83	1.88	1.86	1.79	1.71	1.67	1.65	1.22
Ta	-	-	-	-	-	-	-	-	-	0.06
B-Site Total	**2.00**	**2.00**	**2.00**	**2.00**	**2.00**	**2.00**	**2.00**	**2.00**	**2.00**	**2.00**
F	1.21	0.81	0.91	1.12	0.84	1.23	0.92	-	0.46	-

	02-260B n = 1 Frs	DDH-04-177 n = 1 Pcl	DDH-03-251 n = 1 Frs	DDH-03-251 n = 1 Frs	DDH-03-251 n = 1 Clf	02-118 n = 3 Pcl	02-118 n = 1 Frs	PL-S1-P3-1 n = 2 Pcl	Pl-S1-P3-1 n = 1 Frs	PL-S1-P3-1 n = 1 Clf
Wt. %										
Na_2O	2.12	7.46	2.32	4.33	1.55	7.80	0.29	7.38	1.19	-
CaO	8.57	16.01	13.77	14.11	5.41	15.42	4.46	15.60	9.89	3.95
MnO	-	-	-	-	1.27	-	-	-	-	1.03
SrO	8.57	-	1.97	2.20	-	1.07	6.40	1.17	6.24	-
BaO	3.45	-	-	-	1.47	-	4.33	-	4.79	3.19
FeO	2.98	-	-	-	17.53	-	3.17	-	-	17.84
Ce_2O_3	-	-	-	-	0.41	-	-	-	-	-
Nd_2O_3	-	-	-	-	0.76	-	-	-	-	-
UO_3	3.44	-	1.45	0.91	0.85	-	3.23	-	-	1.25
MgO	-	-	-	-	3.65	-	-	-	-	-
Al_2O_3	-	-	-	-	-	-	-	-	-	-
SiO_2	3.01	-	0.94	0.97	7.65	-	2.42	-	2.19	0.58
TiO_2	1.46	3.96	3.97	3.20	3.33	4.42	4.98	2.75	2.32	2.61
Nb_2O_5	58.92	69.55	68.21	68.65	52.06	66.48	59.51	71.21	62.67	64.09
Ta_2O_5	1.00	-	-	-	-	-	-	-	-	-
F	2.29	6.24	3.76	4.46	-	6.17	-	5.61	2.25	-
-O=F	0.96	2.63	1.58	1.88	-	2.60	-	2.36	0.95	-
Total	**94.85**	**100.59**	**94.81**	**96.95**	**95.94**	**98.77**	**88.79**	**101.34**	**90.59**	**94.54**

	02-260B n = 1 Frs	DDH-04-177 n = 1 Pcl	DDH-03-251 n = 1 Frs	DDH-03-251 n = 1 Frs	DDH-03-251 n = 1 Clf	02-118 n = 3 Pcl	02-118 n = 1 Frs	PL-S1-P3-1 n = 2 Pcl	Pl-S1-P3-1 n = 1 Frs	PL-S1-P3-1 n = 1 Clf
Structural formula calculated on the basis of 6 oxygen normalized to 2 B-site cations										
Na	0.27	0.84	0.26	0.49	0.15	0.91	0.03	0.83	0.14	-
Ca	0.59	1.00	0.85	0.88	0.30	0.99	0.29	0.98	0.66	0.27
Mn	-	-	-	-	0.05	-	-	-	-	0.06
Sr	0.32	-	0.07	0.07	-	0.04	0.22	0.04	0.22	-
Ba	0.09	-	-	-	0.03	-	0.10	-	0.12	0.08
Fe	0.16	-	-	-	0.74	-	0.16	-	-	0.95
Ce	-	-	-	-	0.01	-	-	-	-	-
Nd	-	-	-	-	0.01	-	-	-	-	-
U	0.05	-	0.02	0.01	0.01	-	0.04	-	-	0.02
A-Site Total	**1.47**	**1.84**	**1.19**	**1.45**	**1.31**	**1.93**	**0.85**	**1.85**	**1.14**	**1.37**
A-Site Vacancy	0.53	0.16	0.81	0.55	0.69	0.07	1.15	0.15	0.86	0.63
Mg	-	-	-	-	0.28	-	-	-	-	-
Al	-	-	-	-	-	-	-	-	-	-
Si	0.19	-	0.05	0.06	0.39	-	0.15	-	0.14	0.04
Ti	0.07	0.17	0.17	0.14	0.13	0.20	0.23	0.12	0.11	0.12
Nb	1.72	1.83	1.77	1.80	1.20	1.80	1.63	1.88	1.76	1.84
Ta	0.02	-	-	-	-	-	-	-	-	-
B-Site Total	**2.00**	**2.00**	**2.00**	**2.00**	**2.00**	**2.00**	**2.00**	**2.00**	**2.00**	**2.00**
F	0.47	1.15	0.68	0.82	-	1.17	-	1.04	0.44	-

	PL-S1-P3-1 n = 1 Pcl	**PL-S1-P3-1 n = 1** Frs	**PGH-18-06-199 n = 1** Pcl	**PGH-18-06-384 n = 2** Pcl	**PGH-18-06-384 n = 1** Frs	**PGH-18-06-384 n = 1** Clf	**RHM-06 n = 3** Pcl	**RHM-06 n = 1** Frs	**DDH-03-474 n = 3** Pcl
Wt. %									
Na_2O	6.51	0.28	7.65	7.70	0.55	0.50	6.93	0.76	7.77
CaO	14.24	11.18	14.24	15.50	9.74	5.92	14.88	15.17	16.03
MnO	-	0.96	-	-	0.92	0.85	-	-	-
SrO	2.46	0.35	2.16	0.80	-	0.32	1.91	0.31	1.09
BaO	1.17	2.59	-	-	1.40	2.14	-	-	-
FeO	-	5.88	1.19	-	6.35	11.57	-	1.06	-
Ce_2O_3	-	-	-	-	-	-	-	-	-
Nd_2O_3	-	-	-	-	1.34	-	-	-	-
UO_3	-	-	-	-	-	-	-	-	-
MgO	-	-	-	-	-	-	-	-	-
Al_2O_3	-	-	-	-	-	-	-	-	-
SiO_2	-	0.88	0.55	-	1.21	1.08	-	-	-
TiO_2	2.20	2.41	1.10	3.60	2.84	1.94	1.29	1.28	3.74
Nb_2O_5	69.40	71.65	73.61	69.30	69.38	69.92	70.16	73.32	70.17
Ta_2O_5	-	-	-	-	-	-	-	-	-
F	4.88	-	-	6.13	-	-	5.04	-	6.25
-O=F	2.05	-	-	2.58	-	-	2.12	-	2.63
Total	**98.81**	**96.18**	**100.50**	**100.43**	**93.73**	**94.24**	**98.08**	**91.90**	**102.42**

	PL-S1-P3-1 n = 1 Pcl	PL-S1-P3-1 n = 1 Frs	PGH-18-06-199 n = 1 Pcl	PGH-18-06-384 n = 2 Pcl	PGH-18-06-384 n = 1 Frs	PGH-18-06-384 n = 1 Clf	RHM-06 n = 3 Pcl	RHM-06 n = 1 Frs	DDH-03-474 n = 3 Pcl
Structural formula calculated on the basis of 6 oxygen normalized to 2 B-site cations									
Na	0.76	0.03	0.86	0.88	0.06	0.06	0.82	0.09	0.87
Ca	0.92	0.68	0.88	0.98	0.60	0.37	0.98	0.95	0.99
Mn	-	0.05	-	-	0.04	0.04	-	-	-
Sr	0.09	0.01	0.07	0.03	-	0.01	0.07	0.01	0.04
Ba	0.03	0.06	-	-	0.03	0.05	-	-	-
Fe	-	0.28	0.06	-	0.31	0.57	-	0.05	-
Ce	-	-	-	-	-	-	-	-	-
Nd	-	-	-	-	0.03	-	-	-	-
U	-	-	-	-	-	-	-	-	-
A-Site Total	**1.80**	**1.11**	**1.87**	**1.88**	**1.07**	**1.10**	**1.87**	**1.10**	**1.90**
A-Site Vacancy	0.20	0.89	0.13	0.12	0.93	0.90	0.13	0.90	0.10
Mg	-	-	-	-	-	-	-	-	-
Al	-	-	-	-	-	-	-	-	-
Si	-	0.05	0.03	-	0.07	0.06	-	-	-
Ti	0.10	0.10	0.05	0.16	0.12	0.09	0.06	0.06	0.16
Nb	1.90	1.85	1.92	1.84	1.81	1.85	1.94	1.94	1.84
Ta	-	-	-	-	-	-	-	-	-
B-Site Total	**2.00**	**2.00**	**2.00**	**2.00**	**2.00**	**2.00**	**2.00**	**2.00**	**2.00**
F	0.93	-	-	1.14	-	-	0.98	-	1.15

I-V Feldspar

	DDH-04-37 n = 3 Kfs	**PL-S2-PI-2 n = 4** Alb	**DDH-04-666 n = 2** Kfs	**DDH-04-606 n = 3** Kfs	**02-260B n = 3** Kfs	**RW-PL-06 n = 4** Kfs	**RW-PL-06 n = 2** Alb
Wt. %							
Na_2O	0.16	11.63	0.42	0.26	0.34	0.50	11.32
Al_2O_3	17.71	19.00	17.72	17.74	17.91	17.92	18.92
SiO_2	64.35	68.36	63.51	63.44	64.01	64.01	67.57
K_2O	16.17	-	16.28	16.37	16.52	16.18	0.09
CaO	-	0.06	-	-	-	-	-
Fe_2O_3	0.54	0.13	0.14	-	0.10	0.09	0.15
BaO	-	-	-	-	-	-	-
Total	98.93	99.18	98.06	97.82	98.87	98.70	98.04
Structural formulae calculated on the basis of 8 oxygens							
Na	0.01	0.99	0.04	0.02	0.03	0.05	0.98
Al	0.98	0.99	0.99	0.99	0.99	0.99	0.99
Si	3.01	3.01	3.00	3.00	3.00	3.00	3.01
K	0.96	-	0.98	0.99	0.99	0.97	-
Ca	-	-	-	-	-	-	-
Fe^{3+}	0.02	-	-	-	-	-	-
Ba	-	-	-	-	-	-	-
Total	4.98	4.99	5.01	5.01	5.01	5.01	4.99

	DDH-04-177 n = 4 Kfs	**DDH-04-177 n = 2** Alb	**DDH-04-177 n = 1** Kfs	**DDH-03-251 n = 3** Kfs	**DDH-03-251 n = 1** Kfs	**PL-S2-PI-1 n = 1** Kfs	**DDH-04-34 n = 1** Kfs
Wt. %							
Na_2O	0.50	11.18	-	0.49	0.47	0.23	0.27
Al_2O_3	17.81	18.94	21.26	17.98	18.15	17.81	17.27
SiO_2	63.49	67.40	54.88	64.54	64.17	63.66	61.80
K_2O	15.99	0.20	11.06	16.38	16.43	16.56	16.13
CaO	0.34	0.13	-	-	-	-	1.39
Fe_2O_3	0.26	0.20	0.61	0.32	-	-	0.54
BaO	0.12	-	13.88	-	0.39	-	-
Total	98.50	98.05	101.69	99.72	99.61	98.26	97.40
Structural formulae calculated on the basis of 8 oxygens							
Na	0.05	0.97	-	0.04	0.04	0.02	0.03
Al	0.99	0.99	1.10	0.98	0.99	0.99	0.98
Si	2.99	3.00	2.41	3.00	2.98	3.00	2.96
K	0.96	0.01	0.62	0.97	0.97	1.00	0.99
Ca	0.02	0.01	-	-	-	-	0.07
Fe^{3+}	0.01	0.01	0.02	0.01	-	-	0.02
Ba	0.01	-	1.19	-	0.04	-	-
Total	5.02	4.99	5.34	5.01	5.03	5.01	5.04

	DDH-04-34 n = 1 Kfs	02-118 n = 1 Kfs
Wt. %		
Na_2O	0.30	0.27
Al_2O_3	17.52	17.72
SiO_2	62.30	64.30
K_2O	16.17	16.60
CaO	-	-
Fe_2O_3	0.72	0.30
BaO	-	-
Total	97.01	99.19
Structural formulae calculated on the basis of 8 oxygens		
Na	0.03	0.02
Al	0.99	0.98
Si	2.98	3.01
K	0.99	0.99
Ca	-	-
Fe^{3+}	0.03	0.01
Ba	-	-
Total	5.02	5.01

I-VI Magnesio-arfvedsonite

	DDH-09-457B n = 5	DDH-09-457B n = 1	DDH-03-192 n = 2	DDH-03-192 n = 1	DDH-04-606 n = 2	DDH-04-606 n = 1	DDH-04-177 n = 4
Wt. %							
Na_2O	6.62	8.74	8.24	7.78	9.66	9.75	8.80
MgO	18.60	14.52	16.54	17.30	14.38	10.74	14.63
Al_2O_3	0.44	-	0.47	-	0.17	-	-
SiO_2	55.93	55.56	56.02	55.81	54.70	54.29	54.72
K_2O	2.63	3.82	2.58	2.45	2.24	3.68	2.06
CaO	4.60	-	2.43	3.26	-	-	0.52
TiO_2	0.34	1.47	-	0.29	-	0.48	0.49
V_2O_5	-	-	-	-	0.13	0.22	-
MnO	1.56	-	-	-	-	-	0.81
Fe_2O_3	3.73	6.12	6.41	5.45	8.51	4.96	5.90
FeO	4.85	6.21	5.20	5.24	4.76	5.53	7.55
Total	99.31	96.44	97.88	97.58	94.53	89.65	95.47
Structural formulae calculated on the basis of 6 oxygens							
Na	1.81	2.47	2.28	2.16	2.77	2.94	2.51
Mg	3.90	3.15	3.52	3.68	3.17	2.49	3.21
Al	0.07	-	0.08	-	0.03	-	-
Si	7.87	8.09	7.99	7.97	8.08	8.45	8.07
K	0.47	0.71	0.47	0.45	0.42	0.73	0.39
Ca	0.69	-	0.37	0.50	-	-	0.08
Ti	0.04	0.16	-	0.03	-	0.06	0.05
V	-	-	-	-	0.01	0.02	-
Mn	0.18	-	-	-	-	-	0.10
Fe^{3+}	0.39	0.67	0.69	0.59	0.95	0.58	0.65
Fe^{2+}	0.57	0.76	0.62	0.63	0.59	0.72	0.93
Total	16.00	16.00	16.00	16.00	16.01	16.00	16.00

	DDH-04-177 n = 1	DDH-03-251 n = 4	DDH-03-251 n = 2	PGH-18-06-199 n = 1	PGH-18-06-199 n = 1
Wt. %					
Na_2O	8.22	8.14	8.75	8.27	7.66
MgO	13.86	15.10	15.79	15.66	17.27
Al_2O_3	1.16	1.14	0.48	-	0.41
SiO_2	51.42	54.03	54.91	55.92	55.91
K_2O	2.03	1.96	2.28	3.90	2.55
CaO	1.57	1.99	1.00	0.45	3.08
TiO_2	4.25	0.30	0.09	0.13	0.18
V_2O_5	-	-	0.26	0.22	0.24
MnO	0.33	0.16	0.14	-	-
Fe_2O_3	3.48	5.44	6.84	6.86	4.01
FeO	10.15	7.95	5.63	5.22	6.14
Total	96.47	96.19	96.15	96.63	97.45
Structural formulae calculated on the basis of 6 oxygens					
Na	2.36	2.31	2.46	2.32	2.12
Mg	3.05	3.29	3.42	3.38	3.68
Al	0.20	0.20	0.08	-	0.07
Si	7.60	7.90	7.98	8.10	7.99
K	0.38	0.37	0.42	0.72	0.46
Ca	0.25	0.31	0.16	0.07	0.47
Ti	0.47	0.03	0.01	0.01	0.02
V	-	-	0.02	0.02	0.02
Mn	0.04	0.02	0.02	-	-
Fe^{3+}	0.39	0.60	0.75	0.75	0.43
Fe^{2+}	1.25	0.97	0.68	0.63	0.73
Total	16.00	16.00	16.00	16.00	16.00

I-VII Aegirine

	DDH-04-37 n = 2	DDH-04-37 n = 1	DDH-03-251 n = 2	DDH-03-251 n = 1	DDH-03-251 n = 1	DDH-04-34 n = 2	DDH-04-34 n = 1
Wt. %							
Na_2O	11.77	10.47	11.33	11.28	12.97	10.41	12.04
MgO	2.25	2.62	1.79	6.53	0.70	2.08	2.02
Al_2O_3	-	-	0.39	0.91	0.89	0.52	-
SiO_2	52.80	52.58	52.24	54.50	52.24	50.63	52.57
K_2O	-	0.17	-	0.82	-	-	0.24
CaO	3.27	5.37	3.80	2.29	0.30	5.70	0.42
TiO_2	0.79	0.32	0.58	0.31	1.24	0.43	0.71
V_2O_5	-	-	-	-	-	-	-
MnO	3.59	-	-	-	-	0.61	-
Fe_2O_3	28.57	20.83	26.98	24.85	26.15	24.03	24.64
FeO	-	5.72	2.31	-	4.27	3.02	4.33
Total	**103.02**	**98.08**	**99.41**	**101.49**	**98.76**	**97.41**	**96.97**
Structural formulae calculated on the basis of 6 oxygens							
Na	0.85	0.77	0.84	0.81	0.97	0.79	0.92
Mg	0.12	0.15	0.10	0.36	0.04	0.12	0.12
Al	-	-	0.02	0.04	0.04	0.02	-
Si	1.96	1.99	2.01	2.01	2.01	1.99	2.06
K	-	0.01	-	0.04	-	-	0.01
Ca	0.13	0.22	0.16	0.09	0.01	0.24	0.02
Ti	0.02	0.01	0.02	0.01	0.04	0.01	0.02
V	-	-	-	-	-	-	-
Mn	0.11	-	-	-	-	0.02	-
Fe^{3+}	0.80	0.77	0.78	0.69	0.76	0.71	0.73
Fe^{2+}	-	-	0.07	-	0.14	0.10	0.14
Total	**4.00**	**3.92**	**4.00**	**4.04**	**4.01**	**4.01**	**4.02**
Mol % aegirine – hedenbergite – diopside							
Ae	86.84	80.63	83.08	76.92	90.10	76.53	85.49
Hd	-	-	6.97	-	7.70	10.67	7.81
Di	13.16	19.37	9.95	23.08	2.20	12.80	6.70

	PGH-18-07-427 n = 2	PGH-18-06-416 n = 1	PGH-18-06-416 n = 3	PGH-18-06-416 n = 8
Wt. %				
Na_2O	13.12	13.67	13.67	13.64
MgO	0.52	-	0.41	0.49
Al_2O_3	0.69	0.31	0.28	0.24
SiO_2	52.02	52.61	53.06	53.01
K_2O	-	-	-	-
CaO	0.93	0.30	0.47	0.31
TiO_2	0.36	0.92	1.12	1.63
V_2O_5	-	0.49	0.65	1.41
MnO	-	-	0.06	-
Fe_2O_3	31.43	28.61	28.76	26.21
FeO	-	2.80	2.77	4.24
Total	**99.06**	**99.70**	**101.24**	**101.17**
Structural formulae calculated on the basis of 6 oxygens				
Na	0.98	1.02	1.00	1.00
Mg	0.03	-	0.02	0.03
Al	0.03	0.01	0.01	0.01
Si	1.99	2.02	2.01	2.00
K	-	-	-	-
Ca	0.04	0.01	0.02	0.01
Ti	0.01	0.03	0.03	0.05
V	-	0.01	0.02	0.04
Mn	-	-	-	-
Fe^{3+}	0.91	0.83	0.82	0.75
Fe^{2+}	-	0.09	0.09	0.13
Total	**3.99**	**4.02**	**4.02**	**4.02**
Mol % aegirine – hedenbergite - diopside				
Ae	96.43	94.87	93.33	89.74
Hd	-	5.13	5.45	8.33
Di	3.57	-	1.21	1.92

I-VIII Biotite

	RW-PL-06 n = 3	RW-PL-06 n = 2	RW-PL-06 n = 1	DDH-04-177 n = 8	DDH-03-251 n = 2	DDH-04-34 n = 4	DDH-04-34 n = 3
Wt. %							
Na_2O	-	0.57	0.23	0.45	0.26	0.24	0.32
MgO	14.87	21.60	8.66	19.44	14.70	12.15	14.11
Al_2O_3	13.87	9.23	22.23	9.29	13.54	13.26	13.88
SiO_2	37.39	43.98	47.39	41.48	37.29	34.23	34.65
K_2O	9.90	10.80	10.43	10.47	10.15	9.49	9.42
CaO	-	-	-	-	-	0.08	-
TiO_2	1.67	0.54	-	0.77	2.20	4.44	4.19
MnO	0.31	0.06	-	0.06	0.34	0.79	0.50
FeO	14.18	6.95	2.56	10.97	15.48	18.15	15.43
BaO	-	-	-	-	-	-	0.88
Total	**92.19**	**93.71**	**91.50**	**92.93**	**93.93**	**92.82**	**93.37**
Structural formulae calculated on the basis of 6 oxygens							
Na	-	0.16	0.06	0.13	0.08	0.07	0.09
Mg	3.42	4.70	1.82	4.37	3.35	2.86	3.24
Al	2.53	1.59	3.69	1.65	2.44	2.47	2.52
Si	5.78	6.42	6.68	6.25	5.71	5.42	5.35
K	1.95	2.01	1.88	2.01	1.98	1.92	1.85
Ca	-	-	-	-	-	0.01	-
Ti	0.19	0.06	-	0.09	0.25	0.53	0.49
Mn	0.04	0.01	-	0.01	0.04	0.11	0.07
Fe	1.83	0.85	0.30	1.38	1.98	2.41	2.00
Ba	-	-	-	-	-	-	0.27
Total	**15.74**	**15.81**	**14.44**	**15.89**	**15.84**	**15.81**	**15.88**

	DDH-04-34 n = 2	PGH-18-06-416 n = 3	PGH-18-06-416 n = 6	PGH-18-06-416 n = 13	PGH-18-08-464 n = 13	PGH-18-07-645 n = 9	DDH-04-451A n = 6
Wt. %							
Na_2O	-	-	-	-	0.45	0.55	0.36
MgO	14.91	17.24	19.62	17.68	18.65	19.79	23.80
Al_2O_3	10.97	12.09	9.29	11.09	7.29	10.37	10.00
SiO_2	32.30	38.14	41.26	38.90	39.94	39.36	43.46
K_2O	5.03	9.91	10.36	10.04	9.71	9.65	10.84
CaO	-	-	-	-	-	-	-
TiO_2	0.22	2.73	0.43	2.19	0.90	1.28	0.39
MnO	1.81	0.14	-	-	-	0.41	-
FeO	22.55	14.12	13.32	14.44	15.45	11.45	4.06
BaO	-	-	-	-	-	-	-
Total	**87.78**	**94.38**	**94.27**	**94.34**	**92.39**	**92.85**	**92.91**
Structural formulae calculated on the basis of 6 oxygens							
Na	-	-	-	-	0.14	0.16	0.10
Mg	3.72	3.88	4.39	3.98	4.32	4.47	5.16
Al	2.16	2.15	1.64	1.98	1.33	1.85	1.71
Si	5.40	5.76	6.19	5.88	6.21	5.97	6.32
K	1.07	1.91	1.98	1.94	1.93	1.87	2.01
Ca	-	-	-	-	-	-	-
Ti	0.03	0.31	0.05	0.25	0.10	0.15	0.04
Mn	0.25	0.02	-	-	-	0.05	-
Fe	3.15	1.78	1.67	1.83	2.01	1.45	0.49
Ba	-	-	-	-	-	-	-
Total	**15.77**	**15.81**	**15.93**	**15.85**	**16.05**	**15.97**	**15.84**

I-IX Chlorite

	DDH-04-666 n = 1	DDH-04-666 n = 1	DDH-04-606 n = 2	DDH-04-606 n = 2	RW-PL-06 n = 3	PGH-18-06-199 n = 1	PGH-18-06-199 n = 1
Wt. %							
Na_2O	-	0.78	-	-	-	-	-
MgO	12.74	1.36	12.94	12.87	18.07	10.27	12.55
Al_2O_3	10.59	3.65	9.88	10.14	13.07	9.92	9.48
SiO_2	30.52	36.18	30.98	31.42	32.74	38.98	31.46
P_2O_5	-	0.23	-	-	-	-	1.23
K_2O	-	0.77	0.17	0.08	0.23	1.39	-
CaO	-	0.57	0.68	0.68	0.98	0.86	1.64
V_2O_5	0.27	-	-	-	0.22	-	-
Cr_2O_3	-	-	-	-	-	-	-
MnO	-	1.03	-	-	-	-	-
FeO	30.90	31.31	26.05	26.51	17.49	31.66	31.41
Total	**85.02**	**75.88**	**80.68**	**81.70**	**82.80**	**93.08**	**87.77**
Structural formulae calculated on the basis of 28 oxygens							
Na	-	0.38	-	-	-	-	-
Mg	4.25	0.52	4.45	4.37	5.72	3.08	4.06
Al	2.79	1.09	2.69	2.72	3.27	2.35	2.42
Si	6.83	9.20	7.15	7.16	6.96	7.85	6.83
P	-	0.05	-	-	-	-	0.23
K	-	0.25	0.05	0.02	0.06	0.36	-
Ca	-	0.16	0.17	0.17	0.22	0.19	0.38
V	0.04	-	-	-	0.03	-	-
Cr	-	-	-	-	-	-	-
Mn	-	0.22	-	-	-	-	-
Fe	5.79	6.66	5.03	5.05	3.11	5.33	5.70
Total	**19.71**	**18.52**	**19.55**	**19.49**	**19.38**	**19.15**	**19.62**

	PGH-18-06-384 n = 2	RW-PL-08 n = 1	RW-PL-08 n = 1	DDH-08-13 n = 4	RHM-06 n = 5	PGH-18-07-174 n = 1
Wt. %						
Na_2O	0.09	-	0.50	-	-	-
MgO	12.97	27.00	11.90	17.05	20.40	15.27
Al_2O_3	9.06	13.74	13.68	16.73	13.47	16.04
SiO_2	31.85	34.45	41.74	30.42	31.49	30.86
P_2O_5	-	-	-	-	-	-
K_2O	-	0.15	4.88	-	-	-
CaO	0.44	-	5.14	0.57	0.33	0.34
V_2O_5	0.28	-	-	-	-	-
Cr_2O_3	-	-	4.65	-	-	-
MnO	-	-	-	-	-	-
FeO	30.58	10.67	4.79	20.04	16.18	24.80
Total	**85.26**	**86.01**	**87.28**	**84.80**	**81.88**	**87.31**
Structural formulae calculated on the basis of 28 oxygens						
Na	0.04	-	0.19	-	-	-
Mg	4.31	7.91	3.45	5.35	6.50	4.76
Al	2.38	3.18	3.13	4.14	3.39	3.95
Si	7.10	6.77	8.11	6.39	6.73	6.46
P	-	-	-	-	-	-
K	-	0.04	1.21	-	-	-
Ca	0.11	-	1.07	0.13	0.08	0.08
V	0.04	-	-	-	-	-
Cr	-	-	0.71	-	-	-
Mn	-	-	-	-	-	-
Fe	5.70	1.75	0.78	3.52	2.89	4.34
Total	**19.67**	**19.66**	**18.66**	**19.53**	**19.58**	**19.59**

I-X REE-Fluorocarbonate

	PGH-18-07-174 n = 6 (Syn)	**PGH-18-07-174 n = 2** (Syn)	**PGH-18-07-174 n = 1** (Syn)	**DDH-03-474 n = 4** (Syn)	**DDH-03-474 n = 1** (Syn)	**DDH-03-474 n = 1** (Syn)	**RW-PL-04 n = 1** (Syn)
Wt. %							
CaO	16.63	16.41	16.53	17.07	17.11	16.75	16.26
SrO	0.50	0.43	0.39	0.71	0.63	-	0.7
Y_2O_3	-	-	-	1.23	0.94	0.96	-
La_2O_3	17.33	16.08	16.02	9.47	9.57	9.72	15.55
Ce_2O_3	28.03	27.86	27.41	23.27	23.58	24.64	26.66
Pr_2O_3	2.48	3.26	2.97	2.98	2.62	2.86	2.56
Nd_2O_3	7.62	8.82	8.85	12.55	12.92	13.40	8.42
Sm_2O_3	-	1.24	-	2.30	1.57	2.41	0.91
Gd_2O_3	-	-	-	1.46	-	-	-
ThO_2	-	-	0.32	1.48	0.96	-	-
F	3.59	4.00	3.29	3.41	3.11	3.35	3.42
-O = F	1.51	1.68	1.39	1.44	1.31	1.41	1.44
Total	**74.67**	**76.39**	**74.40**	**74.48**	**71.70**	**72.67**	**73.04**
Structural formulae calculated on the basis of 3 (Pst), 2 (Syn), and 1 (Bsn) CO_3 group(s)							
Ca	0.83	0.82	0.82	0.85	0.87	0.85	0.83
Sr	0.01	0.01	0.01	0.02	0.02	-	0.02
Y	-	-	-	0.03	0.02	0.02	-
La	0.30	0.28	0.27	0.16	0.17	0.17	0.27
Ce	0.48	0.48	0.47	0.39	0.41	0.43	0.46
Pr	0.04	0.06	0.05	0.05	0.05	0.05	0.04
Nd	0.13	0.15	0.15	0.21	0.22	0.23	0.14
Sm	-	0.02	-	0.04	0.03	0.04	0.01
Gd	-	-	-	0.02	-	-	-
Th	-	-	-	0.02	0.01	-	-
F	0.53	0.59	0.48	0.50	0.46	0.50	0.51
Total	**1.79**	**1.81**	**1.77**	**1.78**	**1.78**	**1.78**	**1.79**

	RW-PL-04 n = 1 (Syn)	**RW-PL-04 n = 1** (Syn)	**RHM-12 n = 3** (Syn)	**RHM-12 n = 3** (Syn)	**RHM-12 n = 1** (Syn)	**RHM-12 n = 1** (Syn)	**PGH-18-07-174 n = 6** (Pst)
Wt. %							
CaO	17.1	16.55	16.95	16.94	17.24	16.97	11.27
SrO	0.74	0.81	0.55	0.59	-	0.56	0.59
Y_2O_3	-	-	0.64	0.57	0.45	-	-
La_2O_3	12.35	13.11	13.67	12.51	13.81	12.53	19.63
Ce_2O_3	27.74	25.69	28.00	26.90	27.78	28.72	32.34
Pr_2O_3	2.17	2.51	2.94	2.88	2.63	2.71	3.04
Nd_2O_3	8.69	8.97	9.89	9.38	9.52	9.93	8.87
Sm_2O_3	-	0.97	0.98	0.92	1.14	1.03	-
Gd_2O_3	-	0.76	-	-	-	-	-
ThO_2	0.78	1.16	-	1.11	-	-	-
F	3.02	3.55	3.57	3.10	3.27	3.66	4.28
-O = F	1.27	1.49	1.50	1.31	1.38	1.54	1.80
Total	**71.81**	**73.01**	**76.01**	**73.60**	**74.47**	**74.57**	**78.22**
Structural formulae calculated on the basis of 3 (Pst), 2 (Syn), and 1 (Bsn) CO_3 group(s)							
Ca	0.85	0.85	0.82	0.84	0.85	0.85	0.89
Sr	0.02	0.02	0.01	0.02	-	0.02	0.03
Y	-	-	0.02	0.01	0.01	-	-
La	0.21	0.23	0.23	0.21	0.23	0.22	0.53
Ce	0.47	0.45	0.46	0.45	0.47	0.49	0.87
Pr	0.04	0.04	0.05	0.05	0.04	0.05	0.08
Nd	0.14	0.15	0.16	0.15	0.16	0.17	0.23
Sm	-	0.01	0.02	0.01	0.02	0.02	-
Gd	-	-	-	-	-	-	-
Th	0.01	0.01	-	0.01	-	-	-
F	0.44	0.54	0.51	0.45	0.47	0.54	1.00
Total	**1.74**	**1.77**	**1.76**	**1.77**	**1.77**	**1.80**	**2.64**

	PGH-18-07-174 n = 1 (Pst)	PGH-18-07-174 n = 2 (Bsn)	PGH-18-07-174 n = 2 (Bsn)	PGH-18-07-174 n = 1 (Bsn)
Wt. %				
CaO	15.10	1.09	0.87	0.36
SrO	0.80	-	0.34	0.29
Y_2O_3	0.47	-	-	-
La_2O_3	15.23	27.90	27.29	25.74
Ce_2O_3	27.27	40.46	39.48	40.44
Pr_2O_3	2.80	3.35	3.13	3.75
Nd_2O_3	9.61	9.39	9.47	10.40
Sm_2O_3	1.26	-	-	-
Gd_2O_3	-	-	0.90	-
ThO_2	-	-	1.20	-
F	4.03	6.01	6.20	5.87
-O = F	1.70	2.53	2.61	2.47
Total	**74.88**	**85.66**	**85.08**	**84.39**
Structural formulae calculated on the basis of 3 (Pst), 2 (Syn), and 1 (Bsn) CO_3 group(s)				
Ca	1.17	0.03	0.03	0.01
Sr	0.03	-	0.01	-
Y	0.02	-	-	-
La	0.41	0.28	0.29	0.27
Ce	0.72	0.41	0.41	0.42
Pr	0.07	0.03	0.03	0.04
Nd	0.25	0.09	0.10	0.11
Sm	0.03	-	-	-
Gd	-	-	-	-
Th	-	-	0.01	-
F	0.92	0.52	0.56	0.53
Total	**2.71**	**0.85**	**0.86**	**0.85**

I-XI Burbankite

	DDH-03-192 n = 2	DDH-03-192 n = 1	DDH-02-42 n = 2	DDH-02-42 n = 1	PGH-18-06-199 n = 1	PGH-18-06-199 n = 1	PGH-18-06-199 n = 1
Wt. %							
$Na_2(CO_3)$	16.25	11.41	16.76	17.36	18.96	16.95	15.47
$MgCO_3$	-	-	-	-	-	-	-
$CaCO_3$	27.99	61.00	16.53	34.12	25.61	34.26	31.05
$MnCO_3$	-	0.52	-	-	-	-	-
$FeCO_3$	-	-	-	-	-	-	-
$SrCO_3$	41.71	27.81	48.54	28.04	34.73	37.62	44.36
$BaCO_3$	3.41	-	1.22	7.71	5.84	4.75	3.56
$La_2(CO_3)_3$	2.22	-	4.52	2.64	4.45	0.77	-
$Ce_2(CO_3)_3$	4.75	-	9.56	5.83	9.24	2.26	1.15
$Pr_2(CO_3)_3$	-	-	0.71	-	1.41	-	-
$Nd_2(CO_3)_3$	1.90	-	3.48	2.12	2.71	0.68	0.72
$Sm_2(CO_3)_3$	-	-	-	-	-	-	-
Total	**98.23**	**100.73**	**101.33**	**97.81**	**102.97**	**97.30**	**96.33**
Structural formulae calculated on the basis of 1 CO_3 group							
Na	0.39	0.24	0.41	0.41	0.44	0.40	0.37
Mg	-	-	-	-	-	-	-
Ca	0.35	0.67	0.21	0.42	0.31	0.43	0.39
Mn	-	-	-	-	-	-	-
Fe	-	-	-	-	-	-	-
Sr	0.36	0.21	0.42	0.24	0.29	0.32	0.38
Ba	0.02	-	0.01	0.05	0.04	0.03	0.02
La	0.01	-	0.03	0.01	0.02	-	-
Ce	0.03	-	0.05	0.03	0.05	0.01	0.01
Pr	-	-	-	-	0.01	-	-
Nd	0.01	-	0.02	0.01	0.01	-	-
Sm	-	-	-	-	-	-	-
Total	**1.17**	**1.12**	**1.15**	**1.18**	**1.17**	**1.19**	**1.18**

	PGH-18-06-199 n = 1	DDH-07-179 n = 1	DDH-07-179 n = 1	DDH-07-179 n = 1	DDH-08-13 n = 1	DDH-08-13 n = 1	DDH-08-13 n = 1
Wt. %							
$Na_2(CO_3)$	14.16	16.98	16.57	15.10	15.18	15.83	16.09
$MgCO_3$	-	-	-	-	0.92	-	2.22
$CaCO_3$	27.00	25.88	30.95	26.16	33.57	18.01	23.16
$MnCO_3$	-	-	-	-	-	-	-
$FeCO_3$	-	0.66	0.40	0.34	0.77	-	0.74
$SrCO_3$	51.91	33.95	30.67	49.81	39.56	49.52	38.17
$BaCO_3$	2.88	5.87	9.03	2.20	4.34	8.00	8.51
$La_2(CO_3)_3$	-	0.72	1.15	0.53	-	2.01	2.59
$Ce_2(CO_3)_3$	0.81	6.17	4.39	1.65	2.12	4.09	5.57
$Pr_2(CO_3)_3$	-	1.60	0.50	-	-	-	-
$Nd_2(CO_3)_3$	-	7.17	3.51	-	-	1.10	2.17
$Sm_2(CO_3)_3$	-	1.34	-	-	-	-	-
Total	**96.77**	**100.32**	**97.18**	**95.79**	**96.46**	**98.57**	**99.21**
Structural formulae calculated on the basis of 1 CO_3 group							
Na	0.34	0.40	0.40	0.37	0.36	0.40	0.39
Mg	-	-	-	-	0.01	-	0.03
Ca	0.35	0.33	0.39	0.34	0.42	0.24	0.29
Mn	-	-	-	-	-	-	-
Fe	-	0.01	-	-	0.01	-	0.01
Sr	0.45	0.29	0.26	0.44	0.33	0.45	0.33
Ba	0.02	0.04	0.06	0.01	0.03	0.05	0.05
La	-	-	0.01	-	-	0.01	0.01
Ce	-	0.03	0.02	0.01	0.01	0.02	0.03
Pr	-	0.01	-	-	-	-	-
Nd	-	0.04	0.02	-	-	0.01	0.01
Sm	-	0.01	-	-	-	-	-
Total	**1.17**	**1.16**	**1.17**	**1.18**	**1.17**	**1.18**	**1.16**

	RHM-12 n = 1	RHM-12 n = 1	RHM-12 n = 1	RHM-12 n = 1	PGH-18-07-174 n = 1	PGH-18-07-174 n = 1
Wt. %						
$Na_2(CO_3)$	16.12	14.64	16.65	15.70	16.69	15.35
$MgCO_3$	-	2.61	-	0.59	-	-
$CaCO_3$	26.57	32.37	16.13	30.30	20.02	25.18
$MnCO_3$	-	-	-	-	-	-
$FeCO_3$	-	0.76	0.39	0.48	0.35	-
$SrCO_3$	32.38	41.43	51.49	35.93	39.93	45.63
$BaCO_3$	8.26	4.57	4.35	7.63	11.75	10.40
$La_2(CO_3)_3$	3.39	-	3.18	1.91	2.07	-
$Ce_2(CO_3)_3$	7.32	-	6.28	3.65	3.70	1.09
$Pr_2(CO_3)_3$	-	-	0.84	-	-	-
$Nd_2(CO_3)_3$	2.06	-	1.89	1.04	1.23	0.71
$Sm_2(CO_3)_3$	-	-	-	-	-	-
Total	**96.11**	**96.38**	**101.20**	**97.23**	**95.74**	**98.37**
Structural formulae calculated on the basis of 1 CO_3 group						
Na	0.40	0.34	0.41	0.38	0.43	0.38
Mg	-	0.04	-	0.01	-	-
Ca	0.35	0.40	0.21	0.38	0.27	0.33
Mn	-	-	-	-	-	-
Fe	-	0.01	-	0.01	-	-
Sr	0.29	0.35	0.45	0.31	0.37	0.40
Ba	0.05	0.03	0.03	0.05	0.08	0.07
La	0.02	-	0.02	0.01	0.01	-
Ce	0.04	-	0.04	0.02	0.02	0.01
Pr	-	-	-	-	-	-
Nd	0.01	-	0.01	0.01	0.01	-
Sm	-	-	-	-	-	-
Total	**1.16**	**1.17**	**1.17**	**1.17**	**1.19**	**1.18**

I-XII Rutile

	DDH-04-37 n = 1	02-45.78 n = 1	02-45.78 n = 1	PL-S2-PI-2 n = 1	PL-S2-PI-2 n = 2	DDH-04-606 n = 1	DDH-04-606 n = 1
Wt. %							
MgO	-	-	-	-	-	-	-
Al_2O_3	-	-	-	-	-	-	-
SiO_2	0.41	0.41	-	-	-	0.33	-
CaO	0.63	0.27	0.39	3.24	2.71	-	0.16
TiO_2	95.75	88.72	81.13	93.79	86.92	98.25	101.77
V_2O_5	-	-	-	-	5.34	-	-
Cr_2O_3	-	-	-	-	-	-	-
FeO	0.57	2.62	3.61	-	0.63	1.39	0.80
ZrO_2	-	-	-	-	-	-	-
Nb_2O_5	3.20	8.76	16.06	4.29	8.79	3.78	2.25
WO_3	-	-	-	-	-	-	-
Total	**100.56**	**100.78**	**101.19**	**101.32**	**104.38**	**103.75**	**104.98**
Structural formulae calculated on the basis of 2 oxygens							
Mg	-	-	-	-	-	-	-
Al	-	-	-	-	-	-	-
Si	0.01	0.01	-	-	-	-	-
Ca	0.01	-	0.01	0.05	0.04	-	-
Ti	0.96	0.91	0.85	0.94	0.86	0.96	0.98
V	-	-	-	-	0.05	-	-
Cr	-	-	-	-	-	-	-
Fe	0.01	0.03	0.04	-	0.01	0.02	0.01
Zr	-	-	-	-	-	-	-
Nb	0.02	0.05	0.10	0.03	0.05	0.02	0.01
W	-	-	-	-	-	-	-
Total	**1.00**	**1.00**	**1.00**	**1.02**	**1.00**	**1.00**	**1.00**

	DDH-04-606 n = 2	RW-PL-06 n = 1	RW-PL-06 n = 1	RW-PL-06 n = 1	RW-PL-06 n = 1	RW-PL-06 n = 1	RW-PL-06 n = 1
Wt. %							
MgO	-	-	-	-	-	-	1.26
Al_2O_3	-	-	0.19	0.18	-	-	-
SiO_2	-	0.35	0.35	1.14	0.29	-	0.87
CaO	-	-	-	-	0.49	0.62	2.57
TiO_2	94.02	91.33	94.84	75.48	86.40	94.35	75.11
V_2O_5	-	-	-	-	-	-	1.22
Cr_2O_3	-	-	2.94	2.50	-	-	-
FeO	2.34	2.01	-	4.20	2.98	1.26	5.06
ZrO_2	-	-	-	-	-	-	-
Nb_2O_5	7.42	5.36	0.56	11.06	9.21	3.18	6.94
WO_3	-	-	-	4.07	-	-	4.05
Total	**103.77**	**99.05**	**98.88**	**98.63**	**99.37**	**99.41**	**97.08**
Structural formulae calculated on the basis of 2 oxygens							
Mg	-	-	-	-	-	-	0.03
Al	-	-	-	-	-	-	-
Si	-	-	-	0.02	-	-	0.01
Ca	-	-	-	-	0.01	0.01	0.04
Ti	0.93	0.94	0.97	0.82	0.90	0.96	0.83
V	-	-	-	-	-	-	0.01
Cr	-	-	0.03	0.03	-	-	-
Fe	0.03	0.02	-	0.05	0.03	0.01	0.06
Zr	-	-	-	-	-	-	-
Nb	0.04	0.03	-	0.07	0.06	0.02	0.05
W	-	-	-	0.02	-	-	0.02
Total	**1.00**	**1.00**	**1.01**	**1.01**	**1.01**	**1.01**	**1.04**

	RW-PL-06 n = 1	DDH-04-177 n = 1	DDH-04-177 n = 1	DDH-04-177 n = 2	DDH-03-251 n = 1	DDH-03-251 n = 1	DDH-03-251 n = 1
Wt. %							
MgO	0.18	-	-	3.53	-	-	-
Al_2O_3	0.24	-	-	1.55	0.77	-	-
SiO_2	0.99	2.04	0.89	6.57	2.44	-	1.26
CaO	-	-	-	0.31	0.32	1.61	0.33
TiO_2	94.27	81.91	78.01	71.78	93.36	93.90	93.42
V_2O_5	-	-	-	-	-	-	-
Cr_2O_3	-	-	-	-	0.51	-	-
FeO	1.37	4.48	5.39	5.56	0.82	1.94	1.80
ZrO_2	-	-	-	-	-	-	-
Nb_2O_5	0.63	6.63	13.64	9.43	2.23	4.09	3.16
WO_3	-	0.87	1.71	0.43	-	-	-
Total	**97.68**	**95.93**	**99.64**	**99.13**	**100.45**	**101.54**	**99.97**
Structural formulae calculated on the basis of 2 oxygens							
Mg	-	-	-	0.07	-	-	-
Al	-	-	-	0.02	0.01	-	-
Si	0.01	0.03	0.01	0.09	0.03	-	0.02
Ca	-	-	-	-	-	0.02	-
Ti	0.97	0.89	0.84	0.74	0.93	0.95	0.95
V	-	-	-	-	-	-	-
Cr	-	-	-	-	0.01	-	-
Fe	0.02	0.05	0.06	0.06	0.01	0.02	0.02
Zr	-	-	-	-	-	-	-
Nb	-	0.04	0.09	0.06	0.01	0.02	0.02
W	-	-	0.01	-	-	-	-
Total	**1.01**	**1.01**	**1.01**	**1.06**	**1.01**	**1.02**	**1.01**

	DDH-03-251 n = 1	DDH-04-34 n = 1	DDH-04-34 n = 3	PGH-18-06-384 n = 2
Wt. %				
MgO	-	-	-	-
Al_2O_3	-	-	-	-
SiO_2	0.43	1.85	1.08	-
CaO	0.70	1.31	1.47	-
TiO_2	84.44	81.08	88.87	91.64
V_2O_5	-	-	-	-
Cr_2O_3	-	-	-	-
FeO	3.49	3.34	1.30	0.94
ZrO_2	-	4.23	-	-
Nb_2O_5	12.25	5.85	4.69	2.48
WO_3	-	-	-	-
Total	**101.31**	**97.66**	**97.41**	**95.06**
Structural formulae calculated on the basis of 2 oxygens				
Mg	-	-	-	-
Al	-	-	-	-
Si	0.01	0.03	0.01	-
Ca	0.01	0.02	0.02	-
Ti	0.87	0.87	0.93	0.97
V	-	-	-	-
Cr	-	-	-	-
Fe	0.04	0.04	0.02	0.01
Zr	-	0.03	-	-
Nb	0.08	0.04	0.03	0.02
W	-	-	-	-
Total	**1.01**	**1.02**	**1.01**	**1.00**

I-XIII Magnetite and Ilmenite

	RW-PL-06 n = 2	RW-PL-06 n = 1	DDH-03-251 n = 1	DDH-04-34 n = 1	DDH-08-13 n = 1	PGH-18-07-174 n = 1	PL-S2-PI-1 n = 1
Wt. %							
Al_2O_3	-	-	0.58	0.26	1.08	2.59	1.42
SiO_2	0.45	0.55	5.46	4.64	0.65	6.68	2.79
CaO	0.30	0.19	0.34	0.26	0.31	0.47	0.25
TiO_2	-	0.48	1.29	-	0.23	-	-
V_2O_5	1.18	0.41	1.96	-	0.52	-	-
MnO	-	-	-	-	-	-	-
FeO	28.48	28.73	25.95	27.19	26.46	25.01	26.95
Fe_2O_3	63.29	63.85	57.67	60.44	58.81	55.58	59.91
Nb_2O_5	-	-	-	-	0.68	-	-
SnO_2	-	-	1.22	-	-	-	-
Total	**93.70**	**94.20**	**94.466**	**92.79**	**88.74**	**90.33**	**91.32**
Structural formulae calculated on the basis of 4 oxygens (magnetite) and 3 oxygens (ilmenite)							
Al	-	-	0.03	0.01	0.05	0.12	0.07
Si	0.02	0.02	0.21	0.18	0.03	0.26	0.11
Ca	0.01	0.01	0.01	0.01	0.01	0.02	0.01
Ti	-	0.01	0.04	-	0.01	-	-
V	0.03	0.01	0.05	-	0.01	-	-
Mn	-	-	-	-	-	-	-
Fe^{2+}	0.97	0.97	0.82	0.90	0.94	0.82	0.92
Fe^{3+}	1.94	1.95	1.65	1.80	1.88	1.64	1.83
Nb	-	-	-	-	0.01	-	-
Sn	-	-	0.02	-	-	-	-
Total	**2.97**	**2.97**	**2.83**	**2.91**	**2.96**	**2.86**	**2.94**

	PL-S2-PI-1 n = 1	02-118 n = 2	02-118 n = 2	02-118 n = 1	PL-S1-P3-1 n = 2	PGH-18-07-427 n = 1	PGH-18-07-427 n = 1
Wt. %							
Al_2O_3	0.44	0.62	0.41	-	0.41	-	1.05
SiO_2	0.75	1.39	2.08	-	1.45	-	-
CaO	0.17	1.31	0.69	2.51	0.33	1.42	1.69
TiO_2	-	-	0.53	-	-	-	-
V_2O_5	0.28	-	0.23	0.40	-	0.46	0.46
MnO	-	-	-	-	-	1.24	-
FeO	27.84	27.88	26.57	27.91	28.36	28.77	29.30
Fe_2O_3	61.87	61.96	59.01	62.03	63.04	63.94	65.12
Nb_2O_5	-	-	3.02	-	-	-	-
SnO_2	-	-	-	-	-	-	-
Total	**91.35**	**93.15**	**92.53**	**92.84**	**93.58**	**95.83**	**97.61**
Structural formulae calculated on the basis of 4 oxygens (magnetite) and 3 oxygens (ilmenite)							
Al	0.02	0.03	0.02	-	0.02	-	0.05
Si	0.03	0.06	0.08	-	0.06	-	-
Ca	0.01	0.06	0.03	0.11	0.01	0.06	0.07
Ti	-	-	0.02	-	-	-	-
V	0.01	-	0.01	0.01	-	0.01	0.01
Mn	-	-	-	-	-	0.04	-
Fe^{2+}	0.97	0.95	0.90	0.97	0.96	0.95	0.96
Fe^{3+}	1.94	1.89	1.79	1.93	1.92	1.90	1.91
Nb	-	-	0.06	-	-	-	-
Sn	-	-	-	-	-	-	-
Total	**2.98**	**2.98**	**2.90**	**3.02**	**2.97**	**2.97**	**3.00**

	DDH-07-179 n = 3	DDH-07-179 n = 2	RHM-12 n = 2	PGH-18-06-416 n = 12	PGH-18-06-416 n = 5	PGH-18-06-416 n = 14 (Ilm)
Wt. %						
Al_2O_3	0.48	0.63	0.83	-	-	-
SiO_2	1.79	2.32	6.22	-	-	-
CaO	1.26	1.25	0.88	-	-	-
TiO_2	0.33	-	-	0.65	-	48.58
V_2O_5	-	-	-	0.93	1.02	-
MnO	-	-	-	-	-	0.61
FeO	26.11	26.68	24.74	31.08	31.55	50.09
Fe_2O_3	58.03	59.30	54.99	62.16	63.09	-
Nb_2O_5	-	-	-	-	-	0.76
SnO_2	-	-	-	-	-	-
Total	**88.00**	**90.16**	**87.66**	**94.83**	**95.66**	**100.03**
Structural formulae calculated on the basis of 4 oxygens (magnetite) and 3 oxygens (ilmenite)						
Al	0.02	0.03	0.04	-	-	-
Si	0.08	0.10	0.25	-	-	-
Ca	0.06	0.06	0.04	-	-	-
Ti	0.01	-	-	0.02	-	0.94
V	-	-	-	0.02	0.03	-
Mn	-	-	-	-	-	0.01
Fe^{2+}	0.93	0.93	0.85	1.05	1.06	1.08
Fe^{3+}	1.87	1.85	1.70	1.90	1.91	-
Nb	-	-	-	-	-	0.01
Sn	-	-	-	-	-	-
Total	**2.97**	**2.96**	**2.88**	**2.99**	**3.00**	**2.04**

I-XIV Barite

	DDH-07-103 n = 1	DDH-04-37 n = 1	02-45.78 n = 1	02-45.78 n = 1	DDH-04-666 n = 1	PL-S2-PI-2 n = 1	DDH-03-251 n = 1	PL-S2-PI-1 n = 1	PL-S2-PI-1 n = 1
Wt. %									
SO_3	34.77	34.42	34.73	35.48	35.00	35.01	34.22	33.71	34.02
CaO	-	0.41	1.62	-	-	-	-	0.25	-
FeO	-	-	-	-	0.36	-	-	0.47	-
SrO	-	-	-	-	-	0.73	1.10	-	-
BaO	67.19	67.94	67.56	67.42	66.41	68.24	65.67	66.39	66.76
Total	**101.96**	**102.77**	**103.91**	**102.90**	**101.77**	**103.98**	**100.99**	**100.82**	**100.78**
Structural formulae calculated on the basis of 4 oxygens									
S	1.00	0.99	0.98	1.00	1.00	0.99	0.99	0.99	0.99
Ca	-	0.02	0.07	-	-	-	-	0.01	-
Fe	-	-	-	-	0.01	-	-	0.02	-
Sr	-	-	-	-	-	0.02	0.02	-	-
Ba	1.01	1.02	1.00	0.99	0.99	1.01	1.00	1.01	1.02
Total	**2.00**	**2.02**	**2.04**	**2.00**	**2.00**	**2.02**	**2.01**	**2.03**	**2.01**

	02-118 n = 1	DDH-08-13 n = 1	DDH-08-13 n = 1	PGH-18-06-384 n = 2	PGH-18-06-384 n = 1
Wt. %					
SO_3	34.50	34.24	33.16	33.21	33.90
CaO	-	-	0.65	2.63	-
FeO	-	-	0.32	-	-
SrO	1.56	0.34	-	1.85	-
BaO	64.40	67.47	66.22	63.41	66.54
Total	**100.46**	**102.05**	**100.35**	**101.09**	**100.44**
Structural formulae calculated on the basis of 4 oxygens					
S	1.00	0.99	0.98	0.96	0.99
Ca	-	-	0.03	0.11	-
Fe	-	-	0.01	-	-
Sr	0.03	0.01	-	0.04	-
Ba	0.97	1.02	1.02	0.96	1.02
Total	**2.00**	**2.02**	**2.04**	**2.07**	**2.01**

Appendix II Cathodoluminescence

II-I Imaging (University of Manitoba)

DDH-02-42

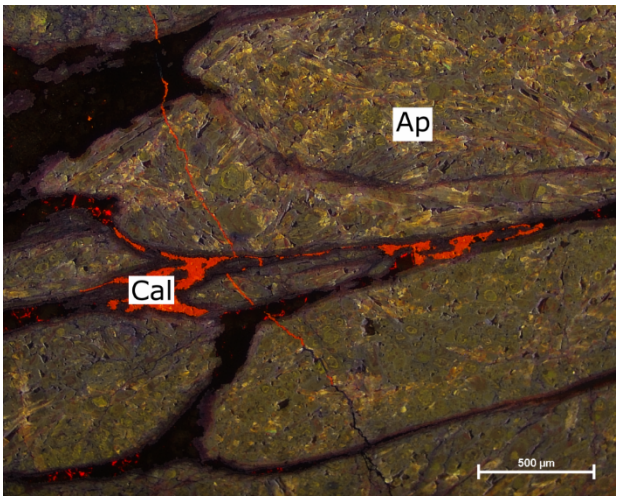

DDH-02-42

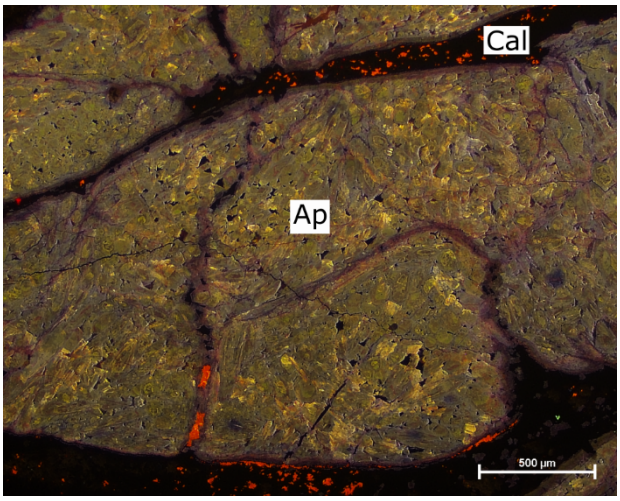

DDH-04-37

DDH-04-37

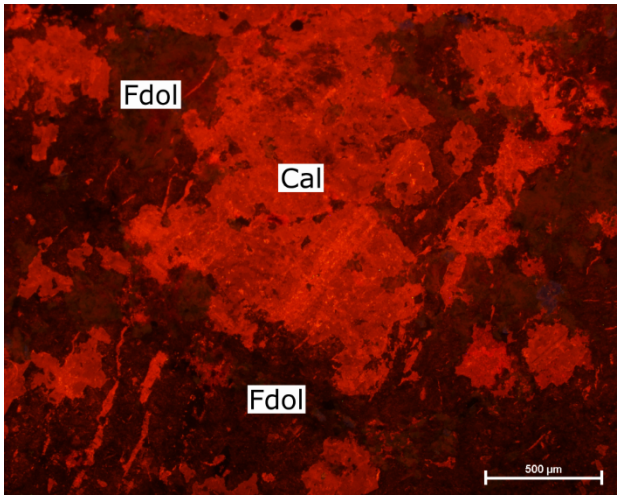

DDH-04-495

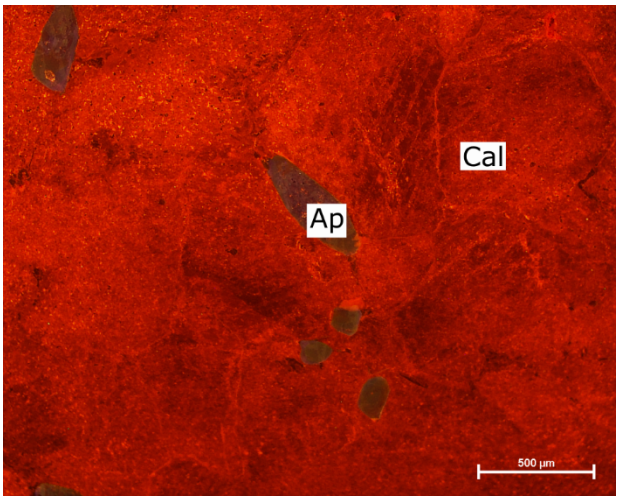

DDH-04-495

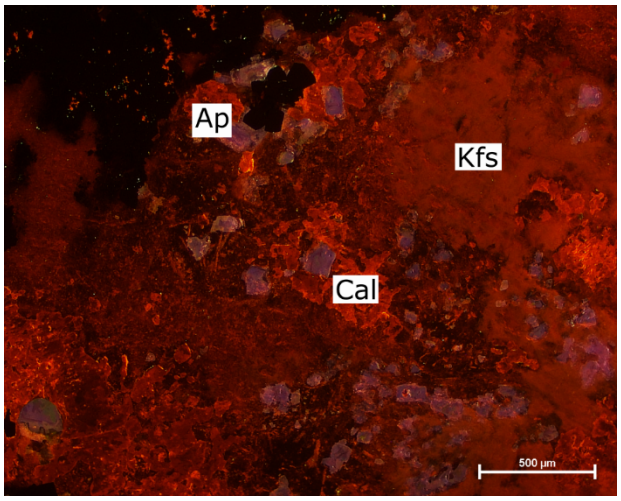

DDH-09-457B

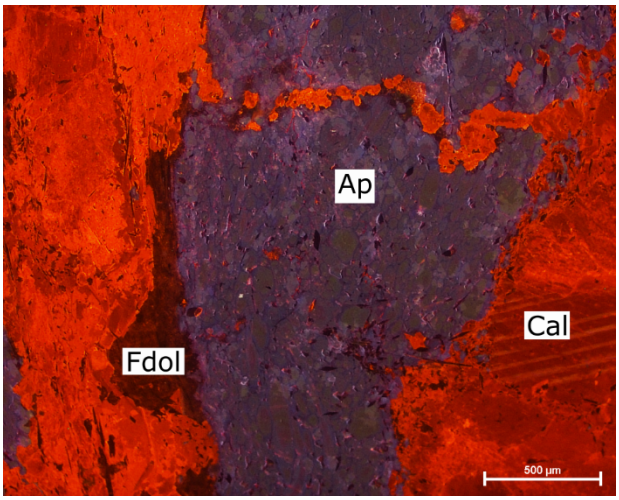

DDH-09-457B

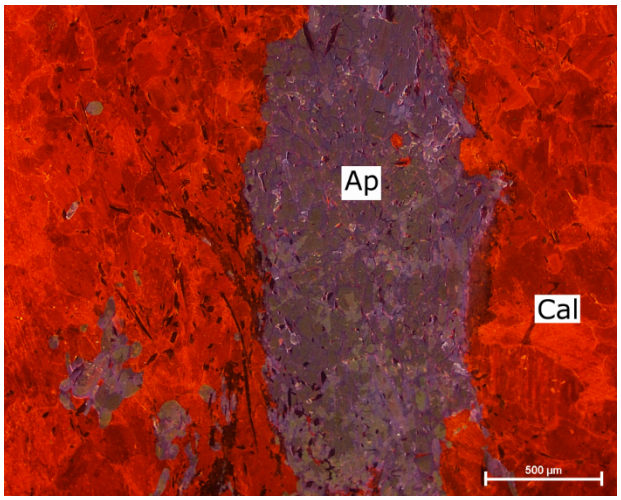

DDH-09-457B

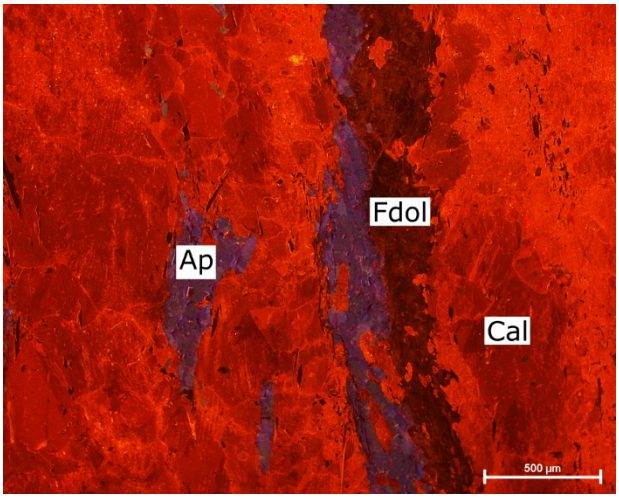

DDH-09-457B

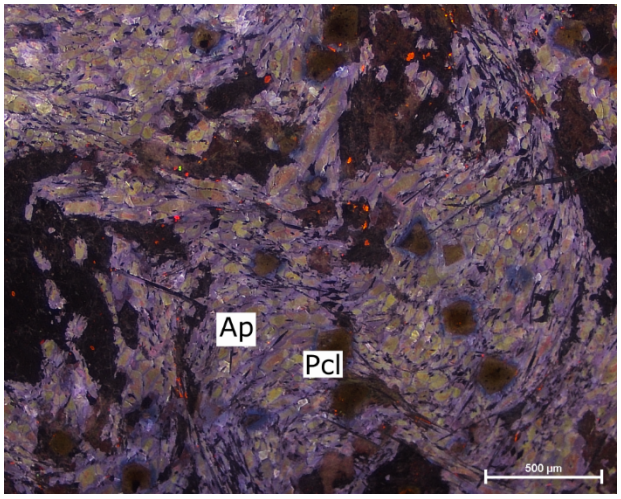

DDH-09-457B

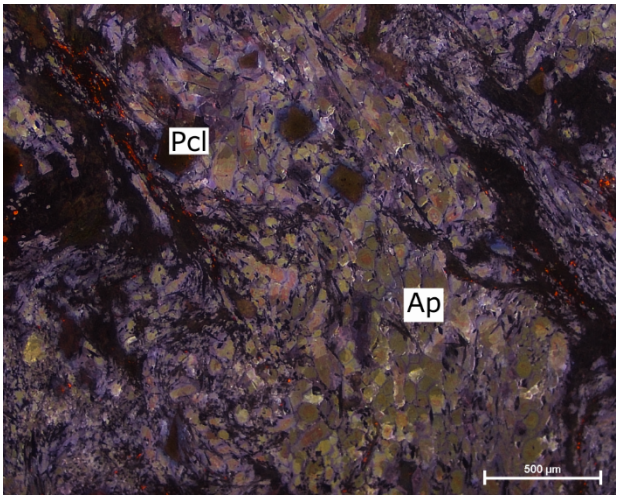

DDH-09-457B

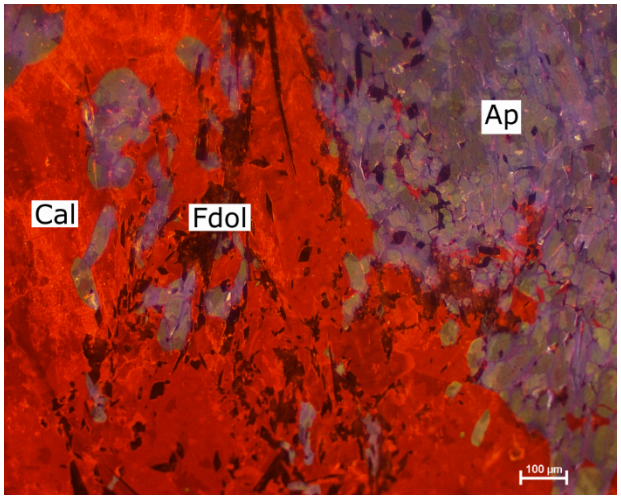

DDH-09-457B

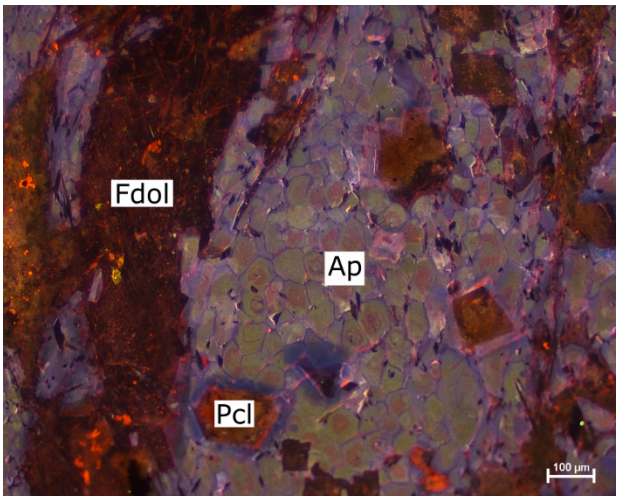

02-118

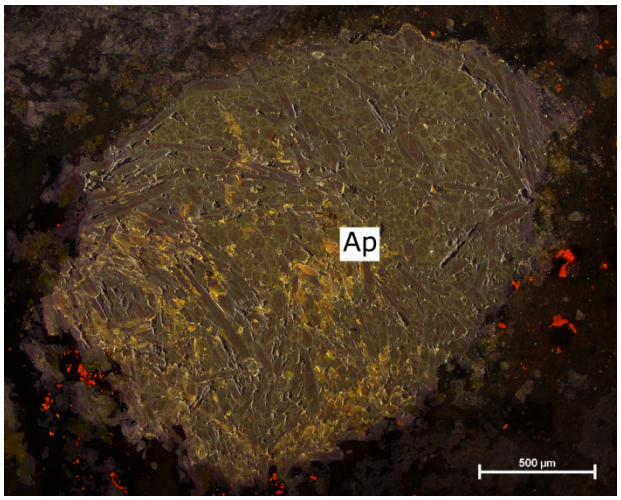

02-118

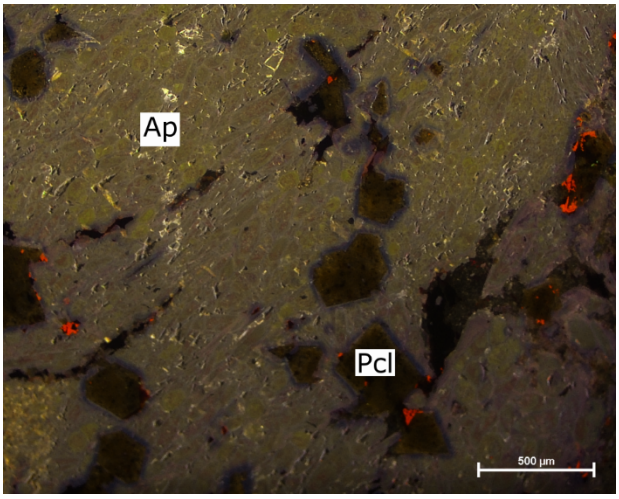

02-118

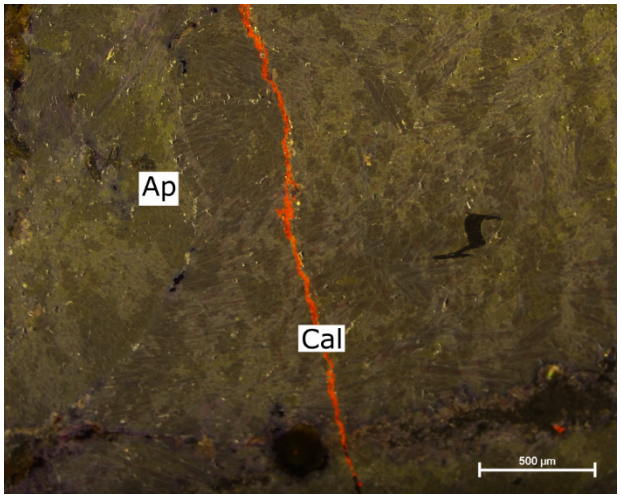

02-118

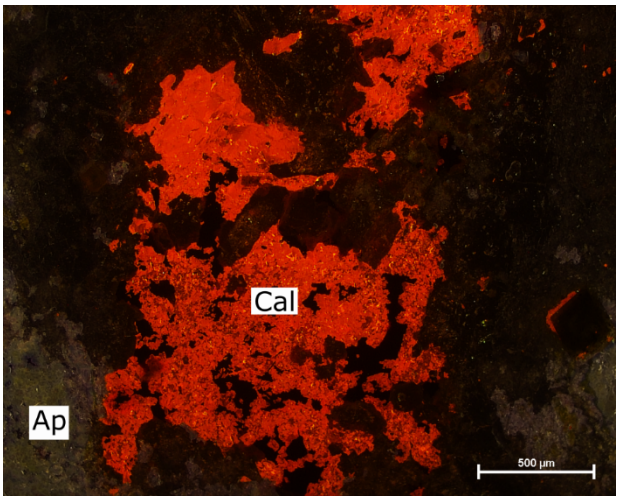

02-118

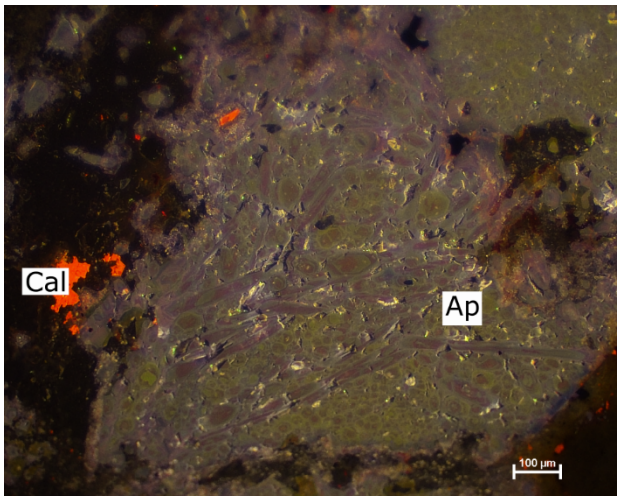

02-118

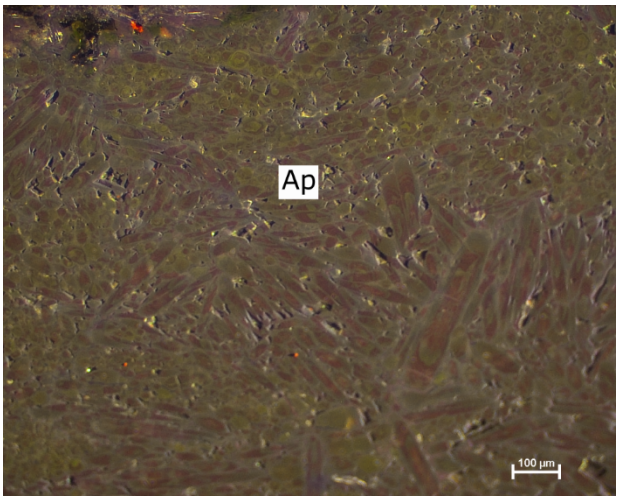

DDH-03-251

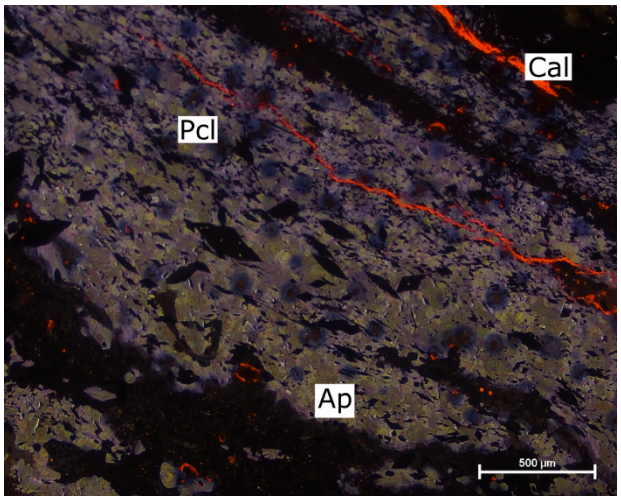

DDH-03-251

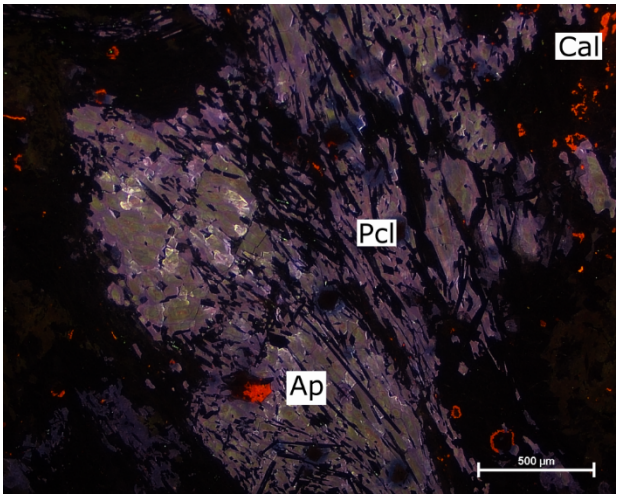

DDH-03-251

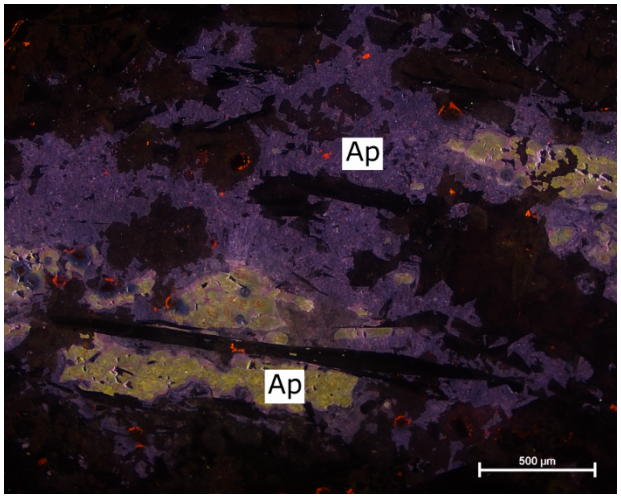

DDH-03-251

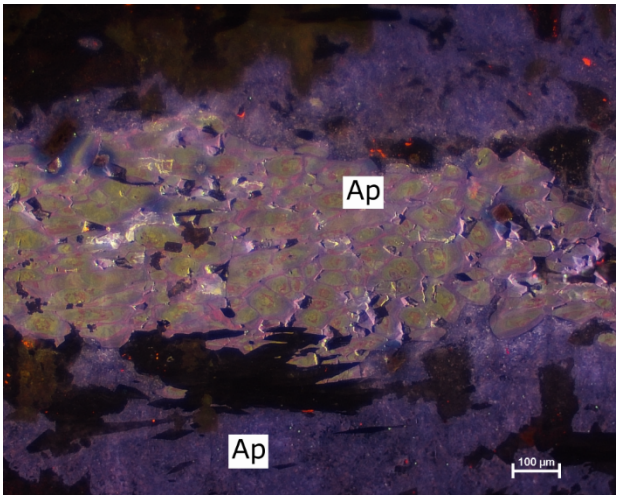

DDH-04-171

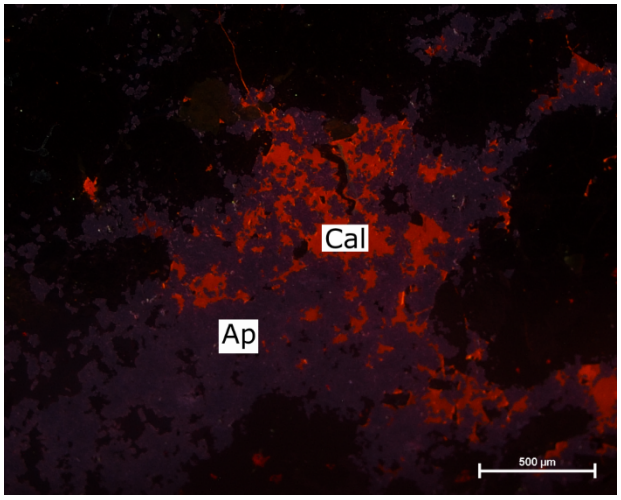

DDH-04-171

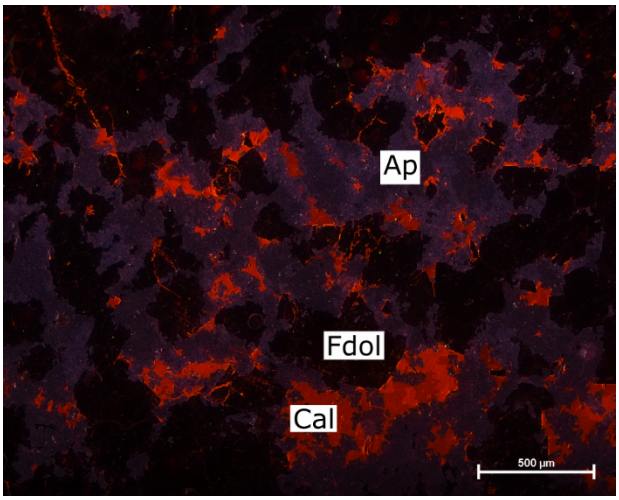

DDH-04-171

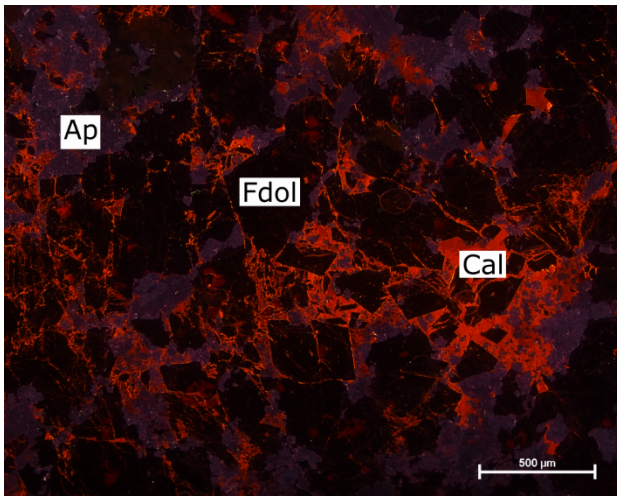

DDH-04-171

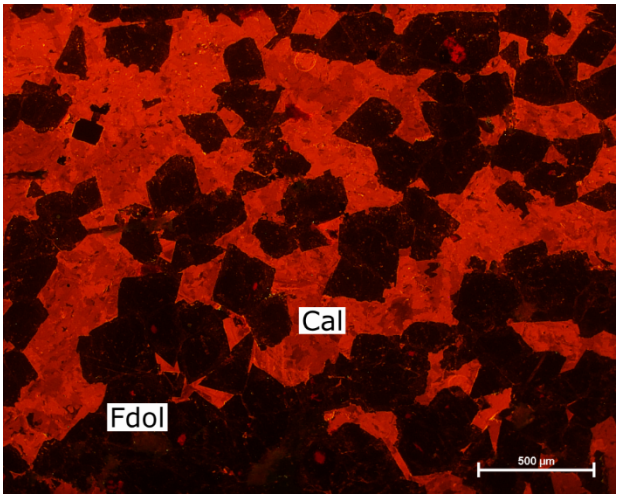

DDH-04-495

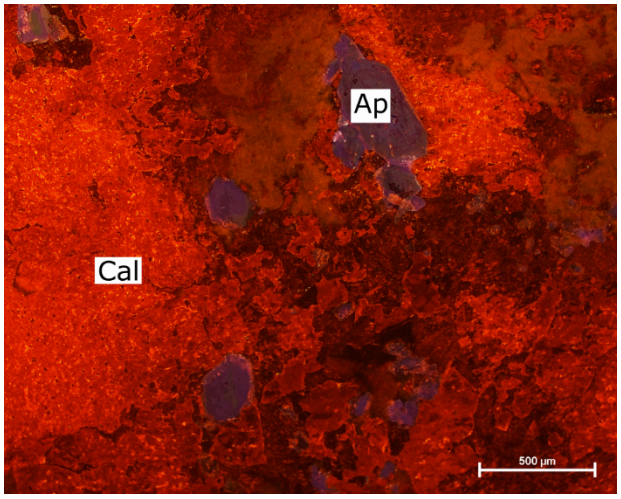

DDH-04-495

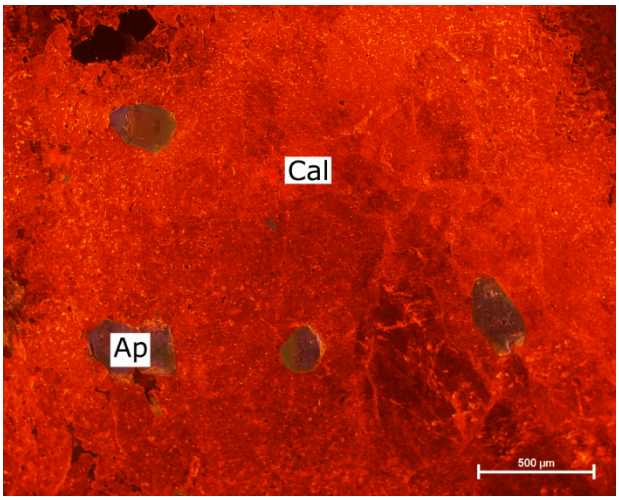

DDH-04-495

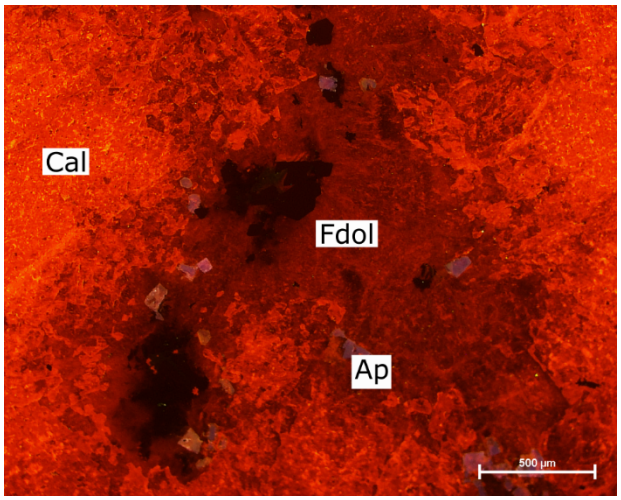

DDH-04-495

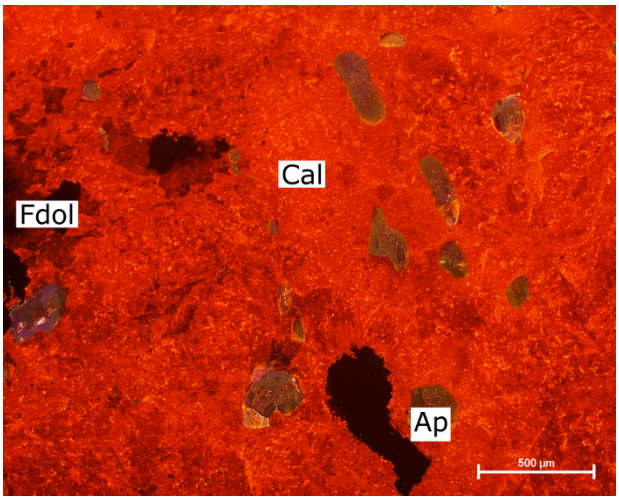

DDH-04-495

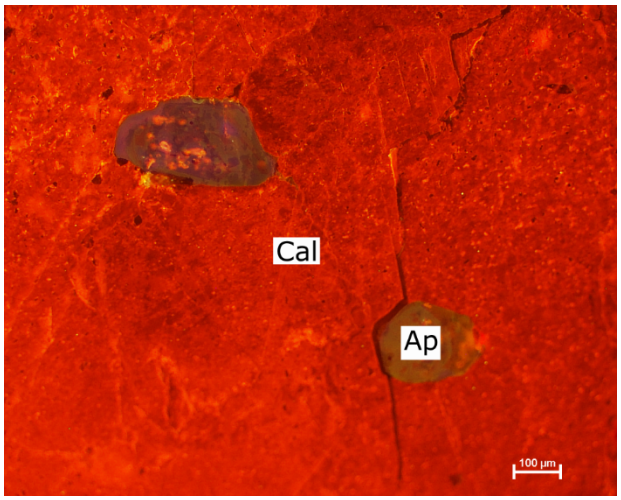

DDH-04-495

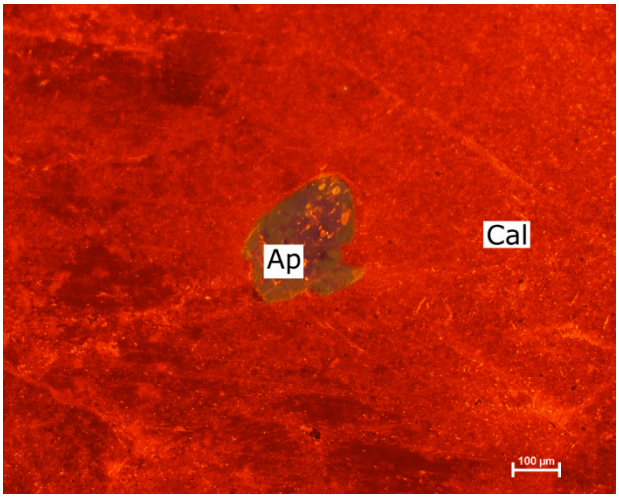

DDH-04-495

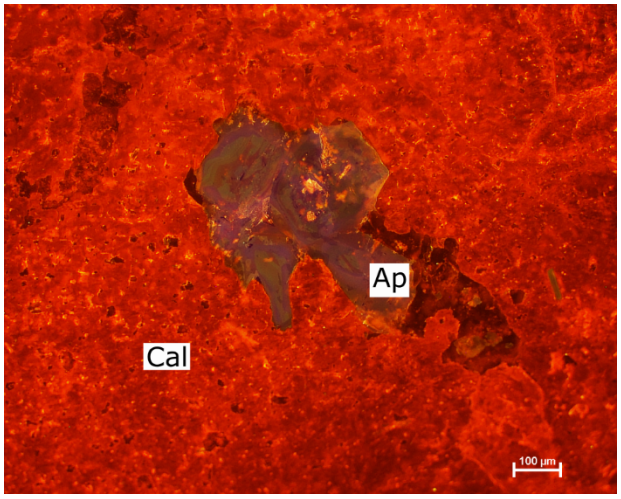

DDH-04-495

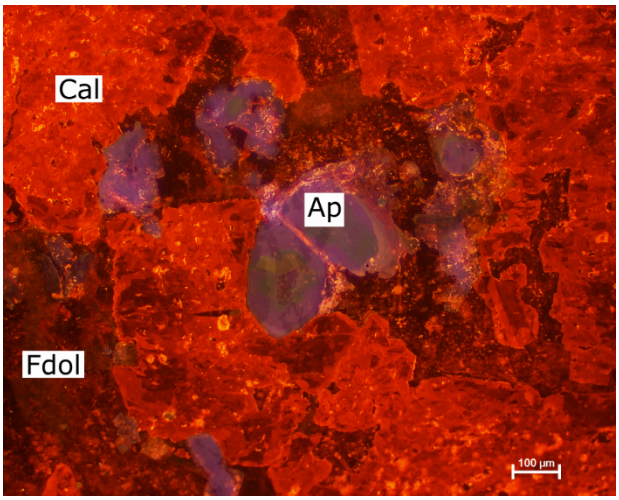

DDH-04-495

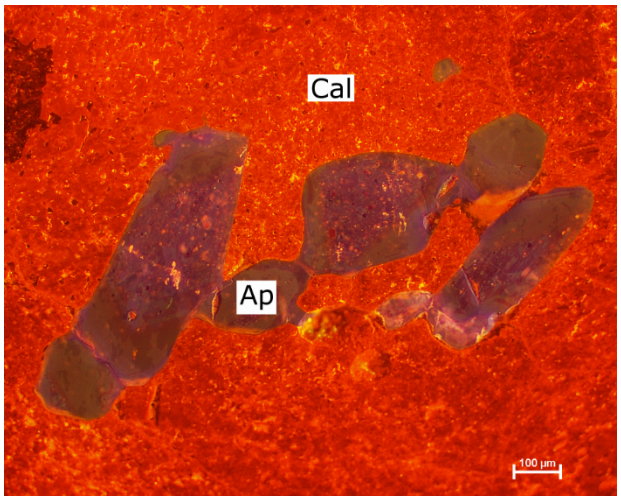

DDH-04-666

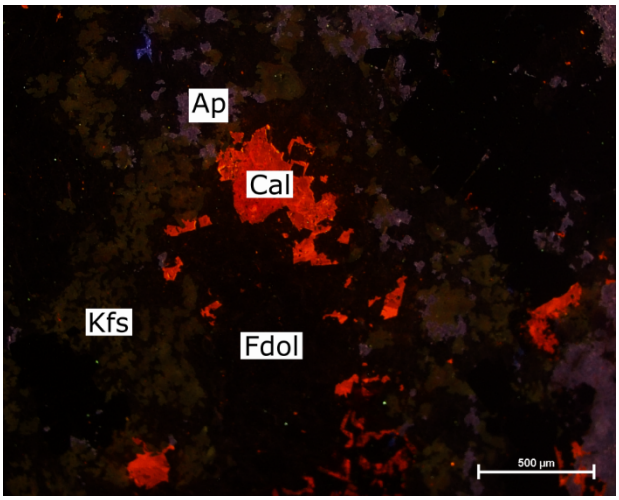

DDH-04-666

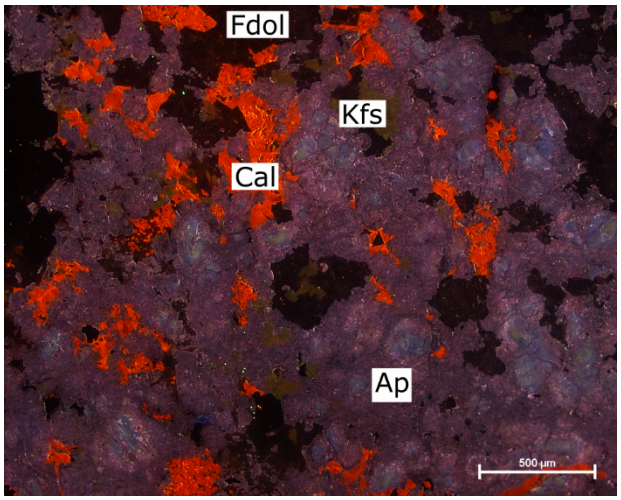

DDH-04-666

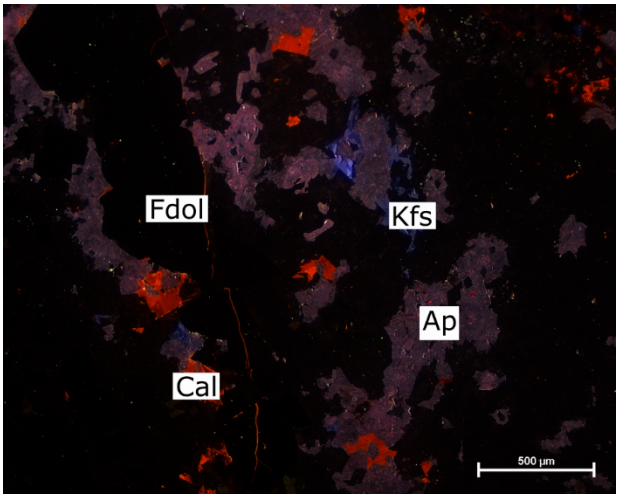

DDH-04-666

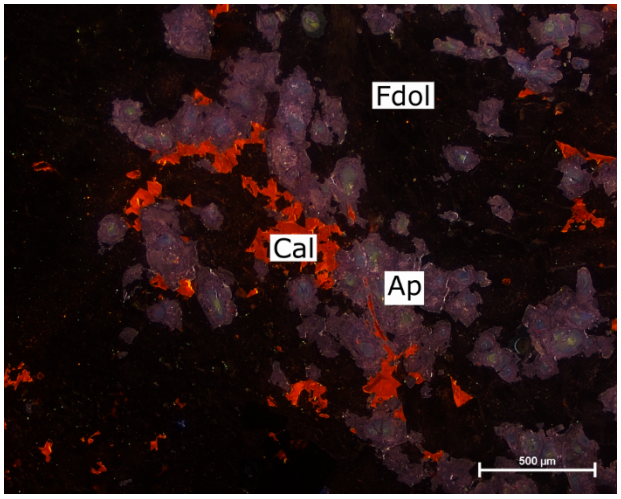

DDH-04-666

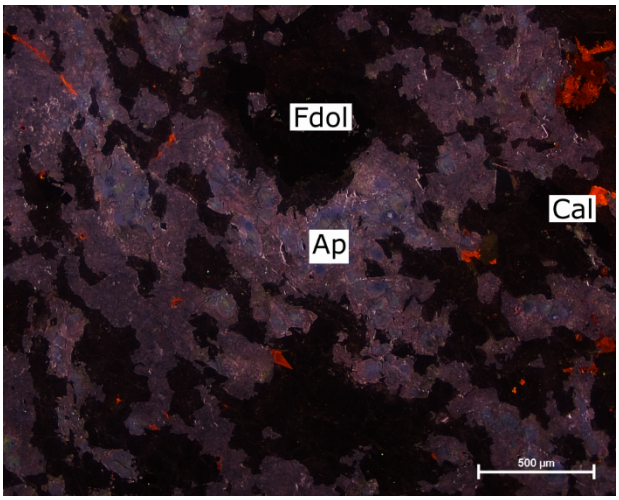

DDH-04-666

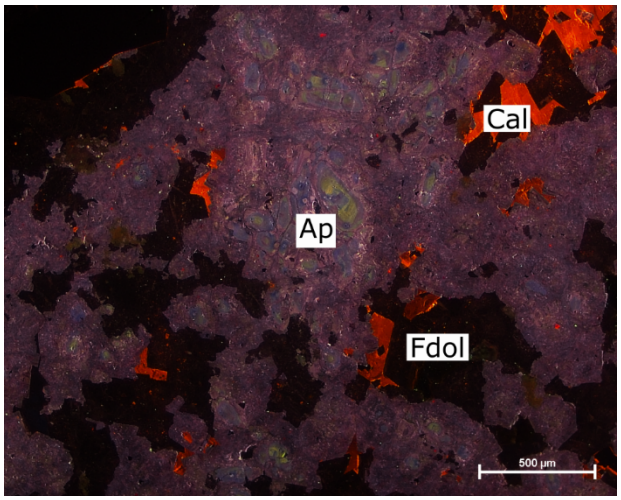

DDH-04-666

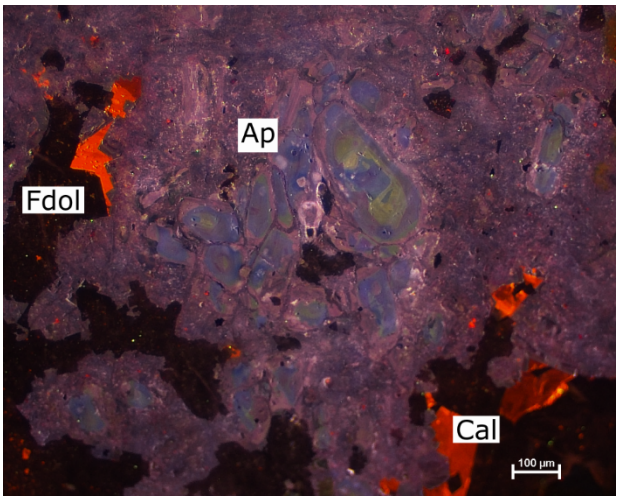

DDH-04-666

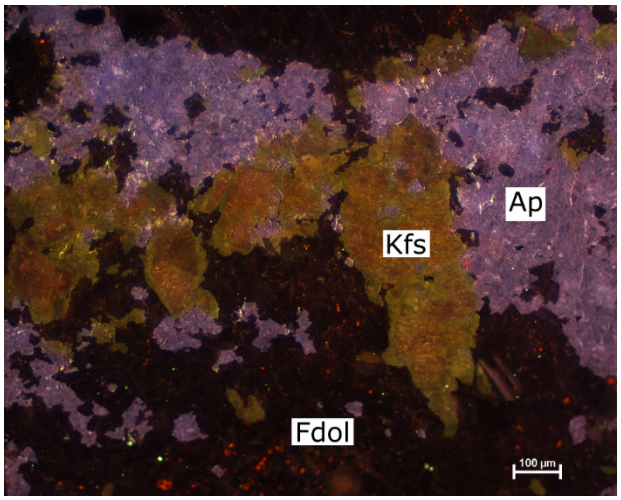

DDH-04-666

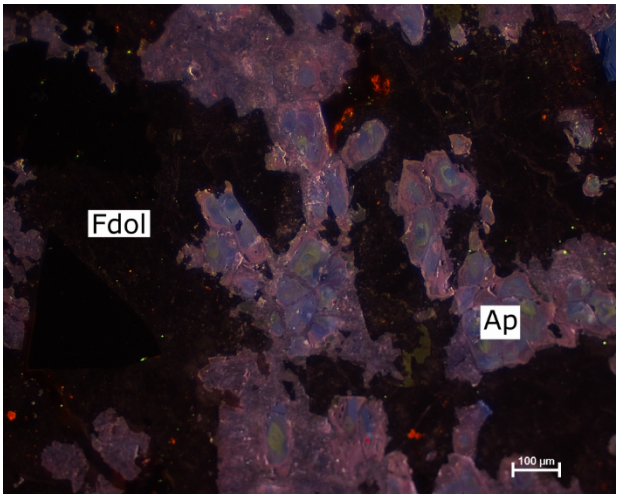

DDH-04-666

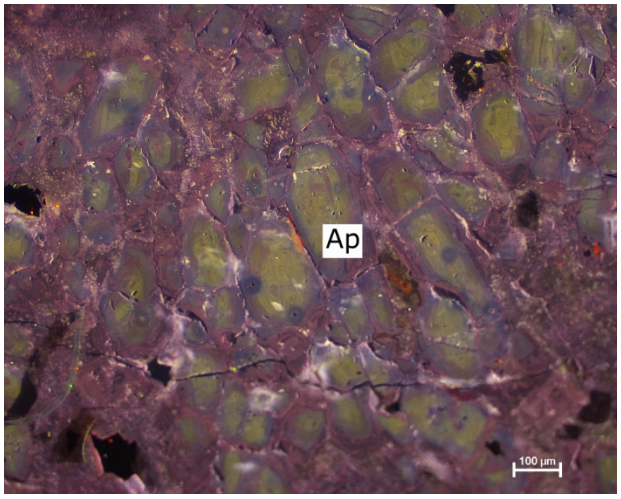

DDH-07-179

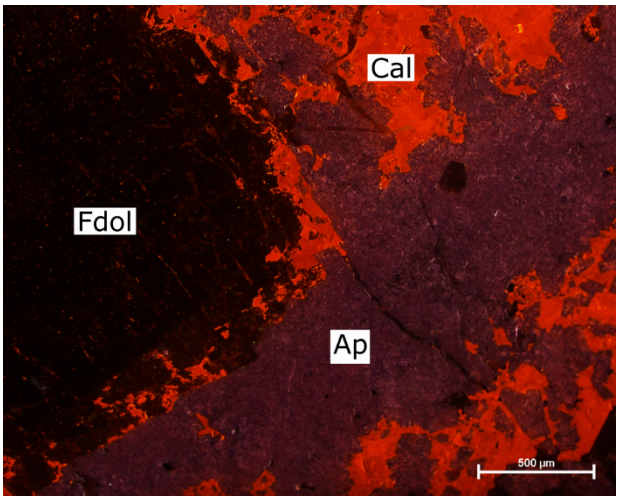

DDH-07-179

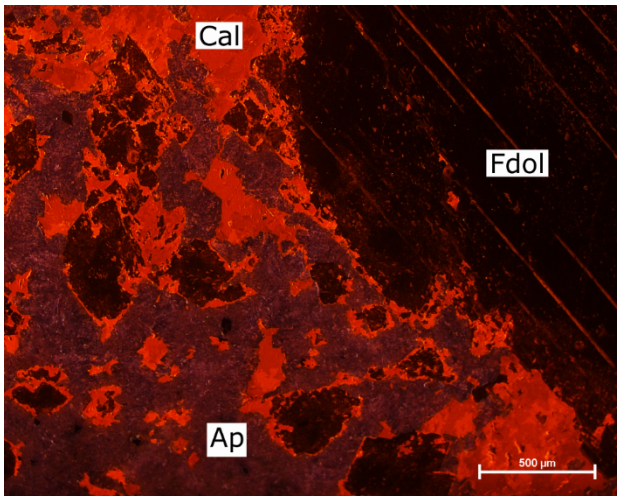

DDH-07-179

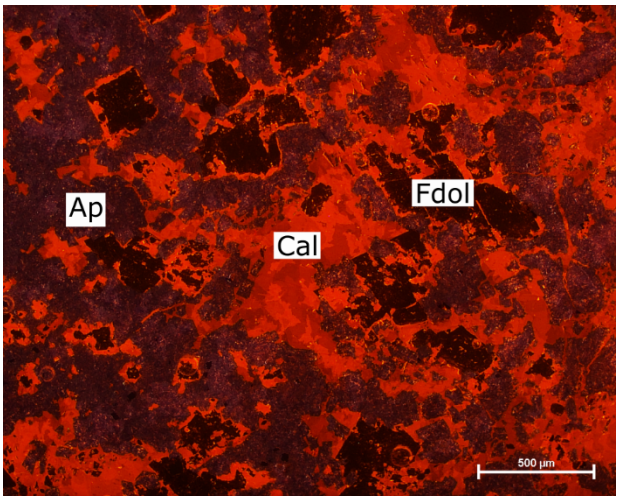

DDH-09-205

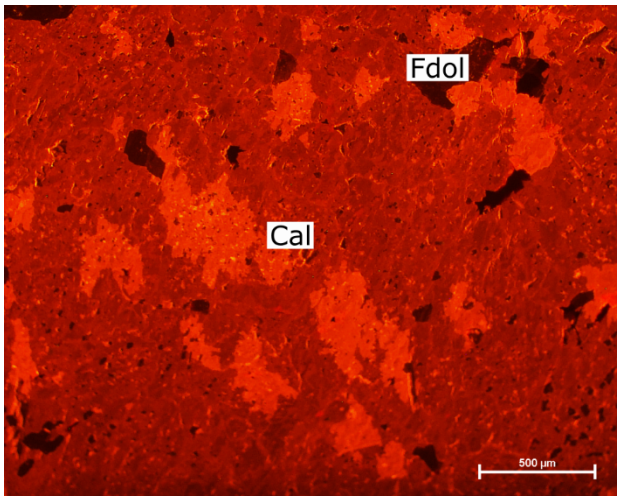

DDH-09-205

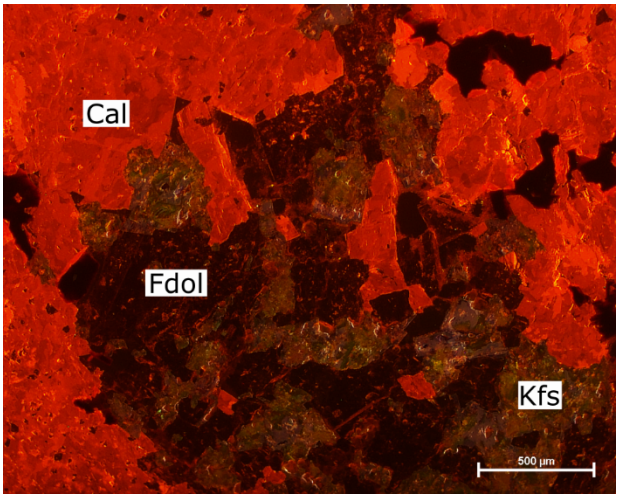

DDH-09-205

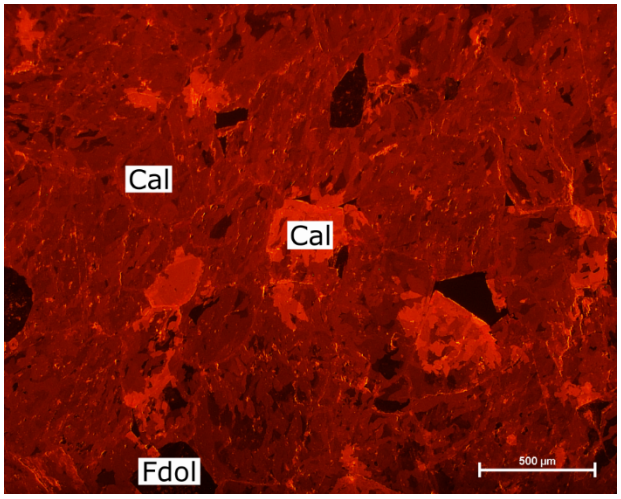

DDH-09-205

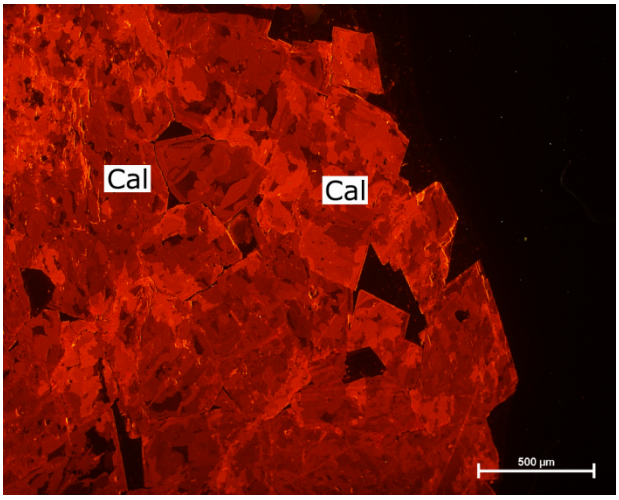

DDH-09-205

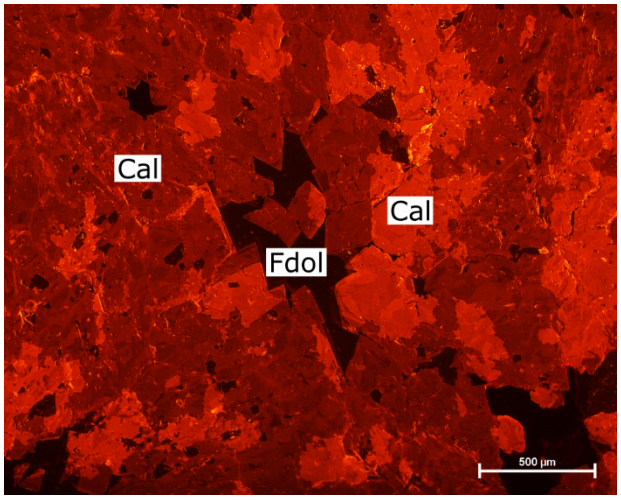

DDH-09-459

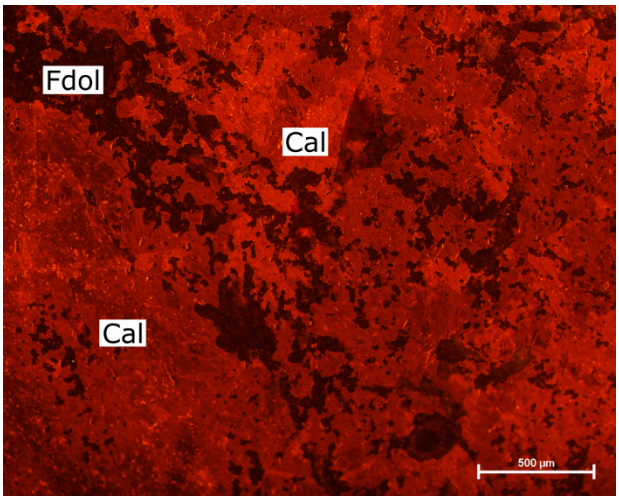

DDH-09-459

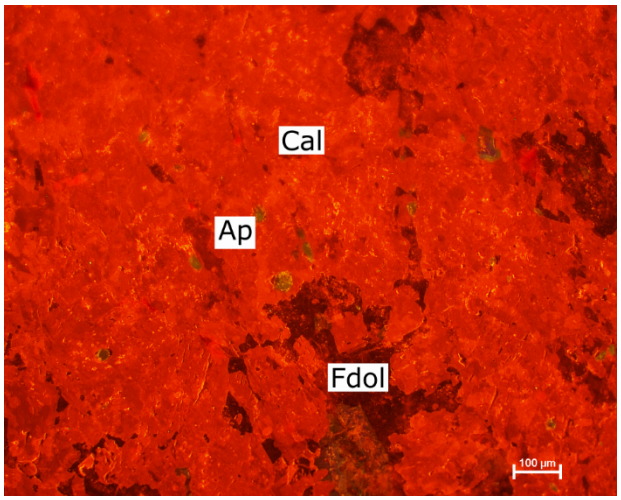

DDH-09-459

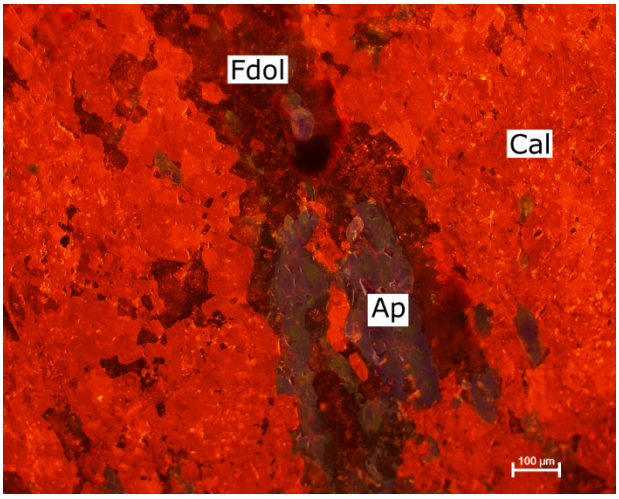

DDH-09-459

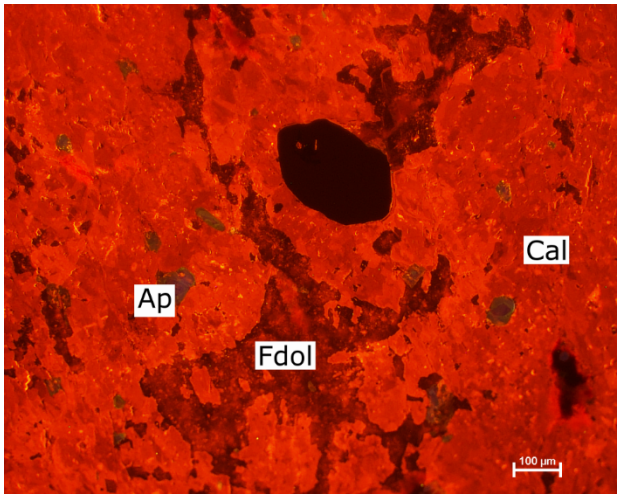

PGH-18-07-174

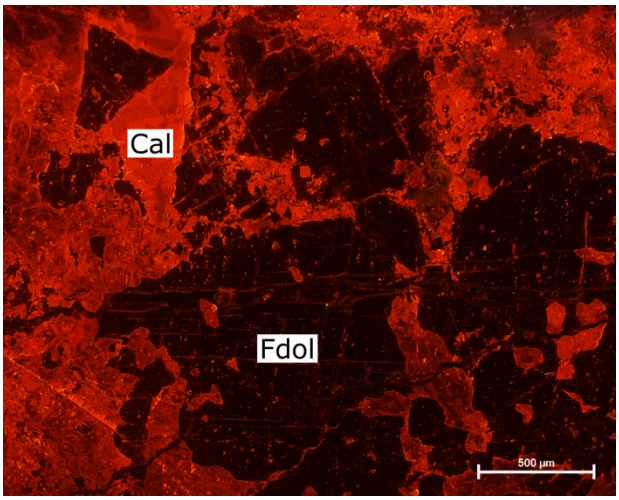

PGH-18-07-174

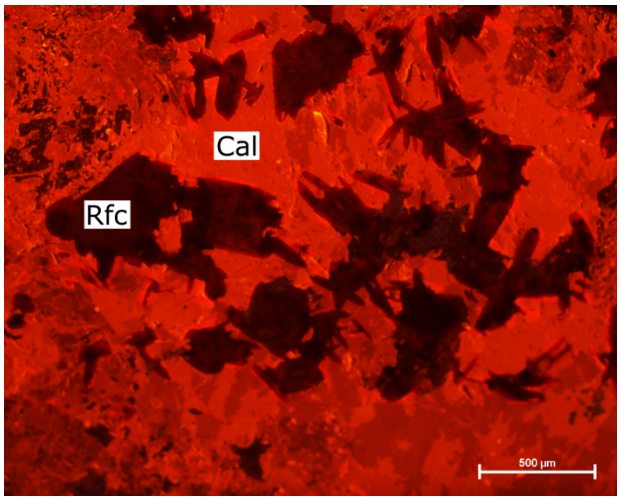

PGH-18-07-427

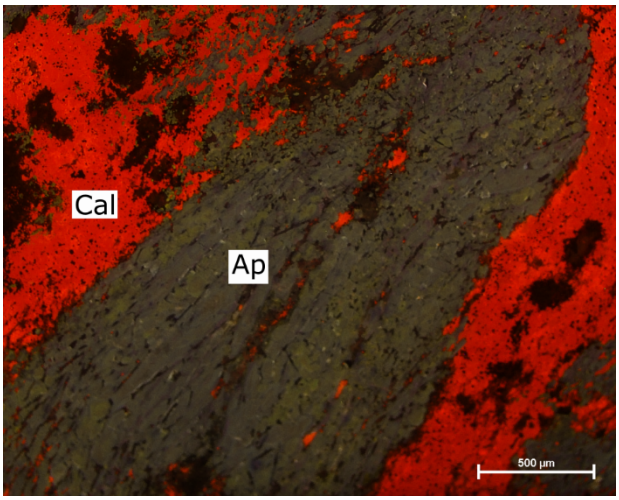

PGH-18-07-427

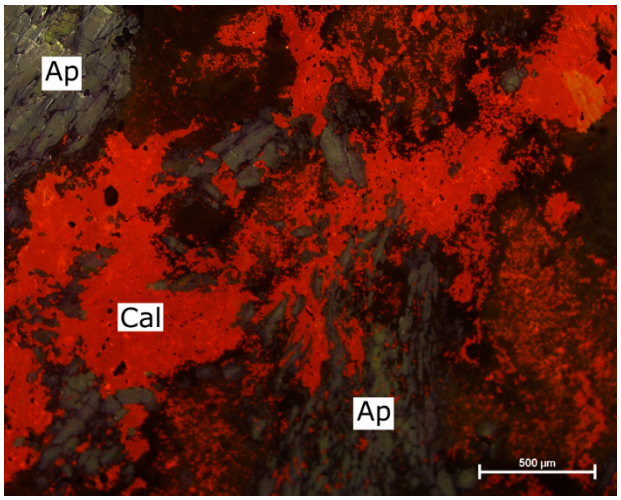

PGH-18-07-427

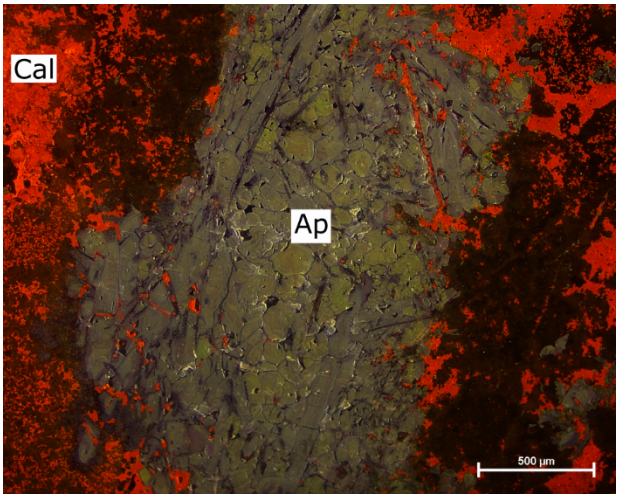

PGH-18-07-427

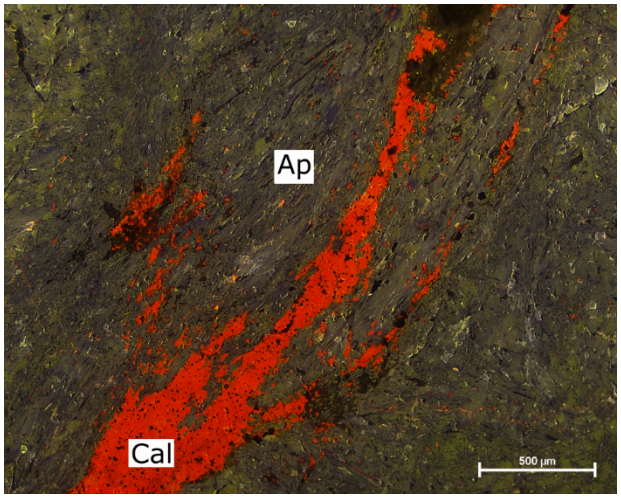

PGH-18-07-427

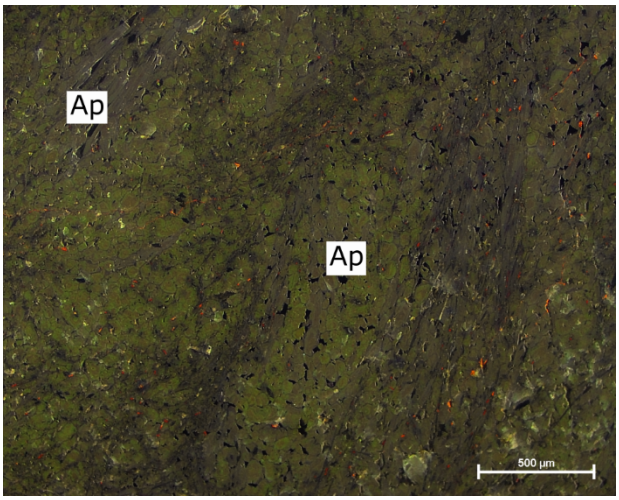

PGH-18-07-427

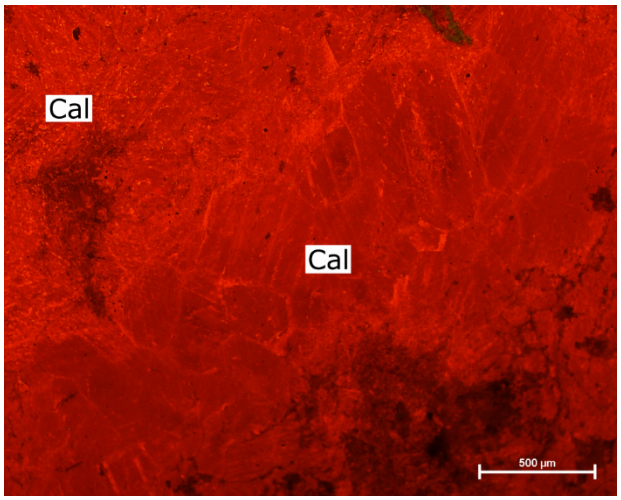

PGH-18-07-427

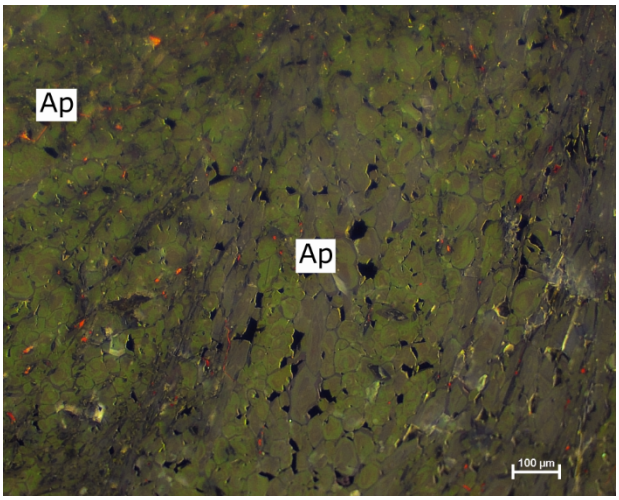

PGH-18-07-427

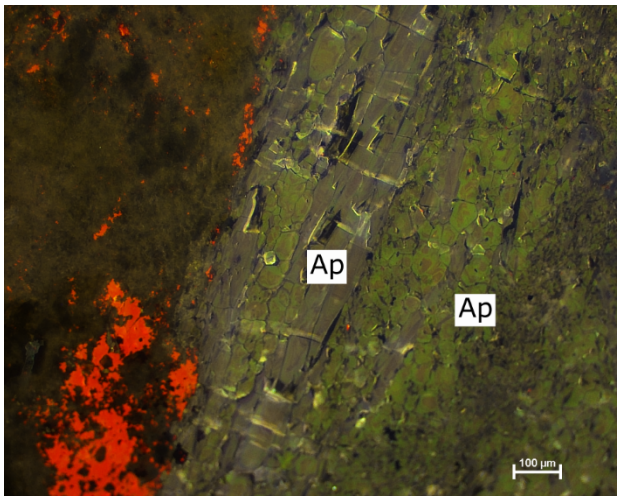

PGH-18-07-427

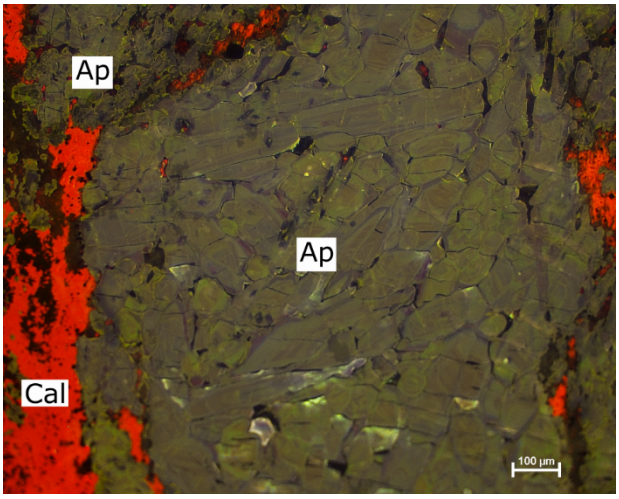

PGH-18-07-650

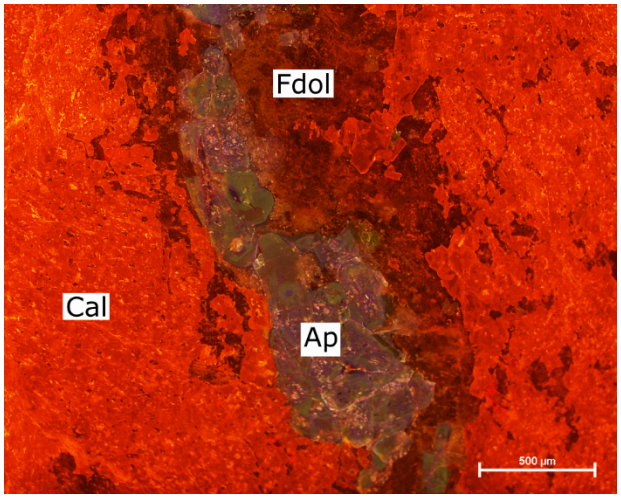

PGH-18-07-650

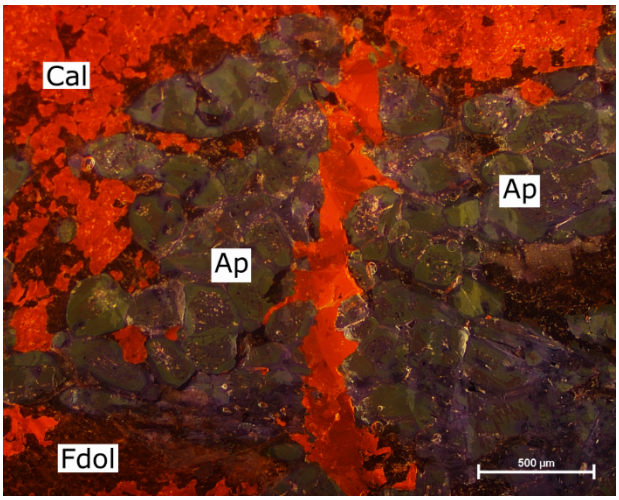

PGH-18-07-650

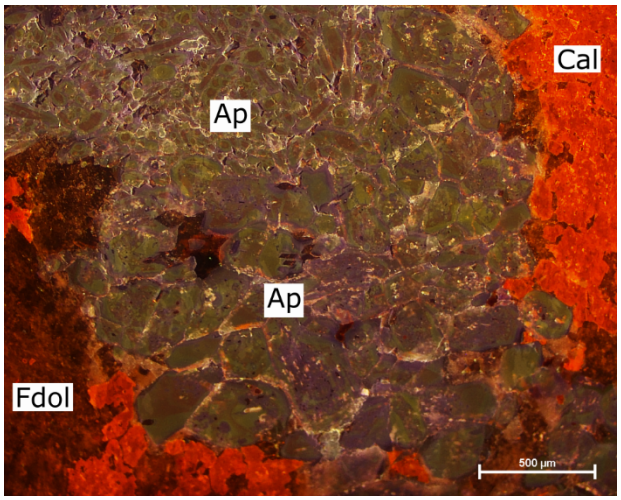

PGH-18-07-650

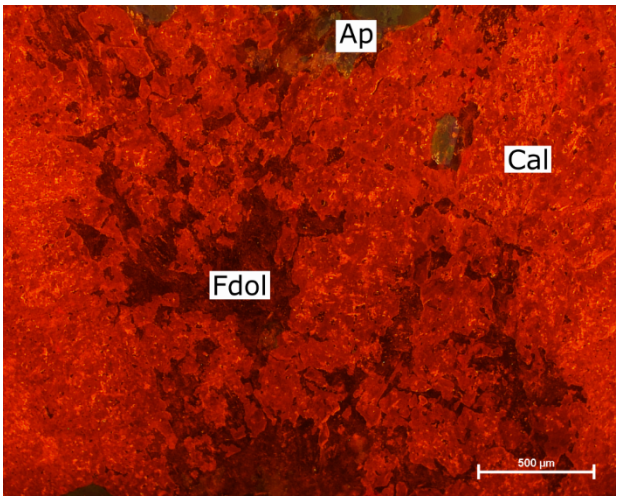

PGH-18-07-650

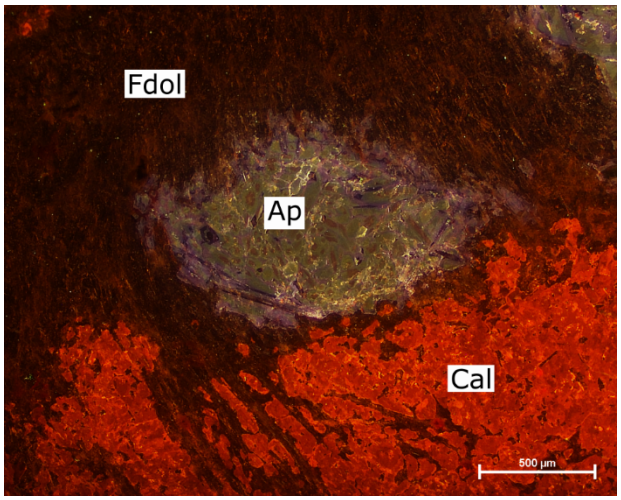

PGH-18-07-650

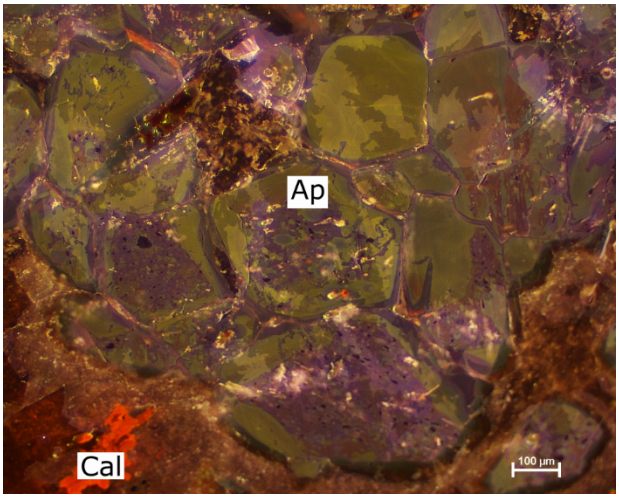

PGH-18-07-650

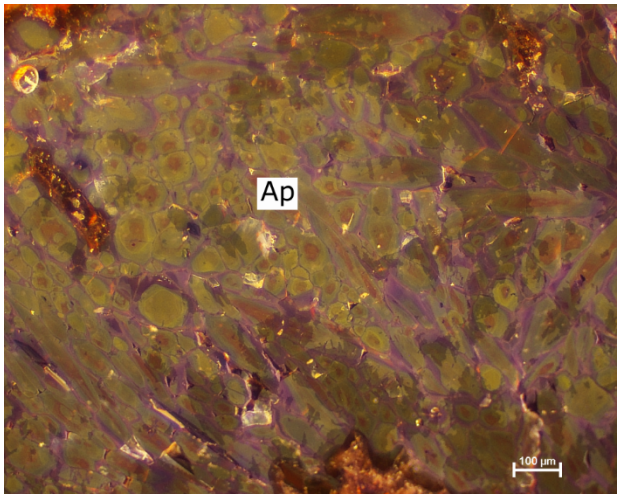

PGH-18-07-650

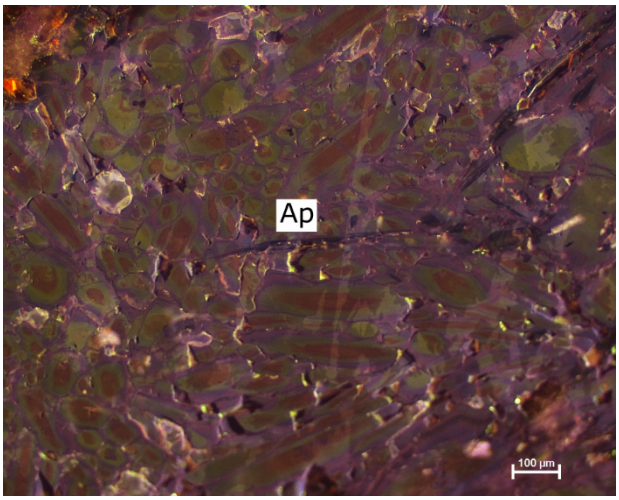

RHM-03

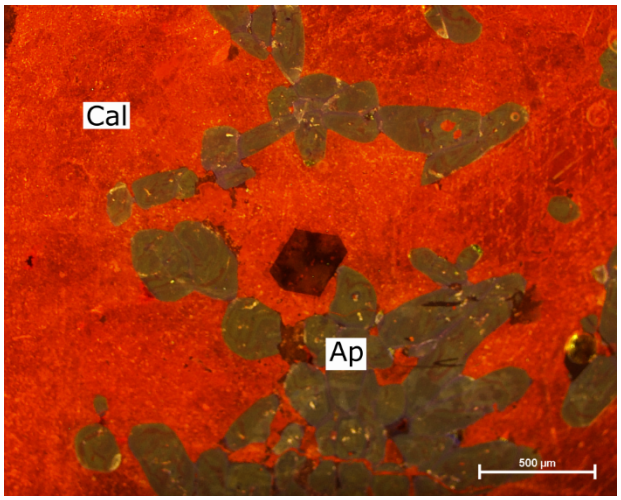

RHM-03

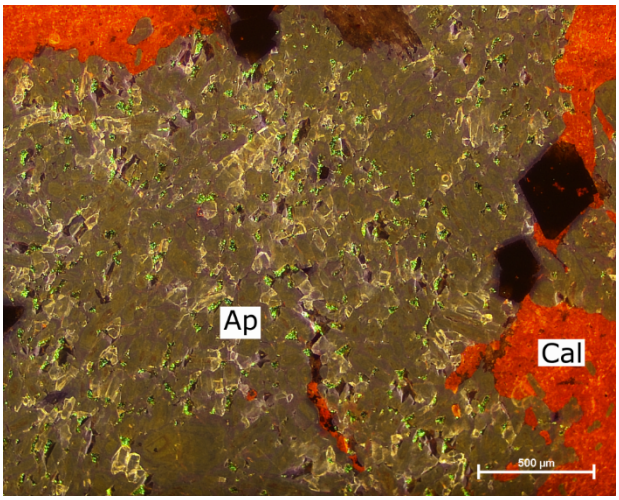

RHM-03

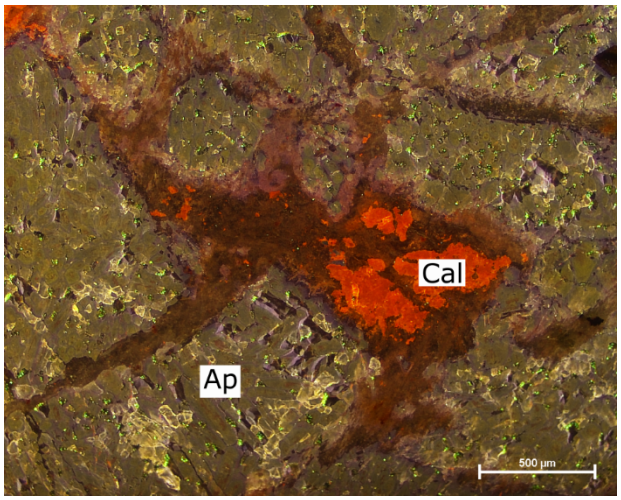

RHM-03

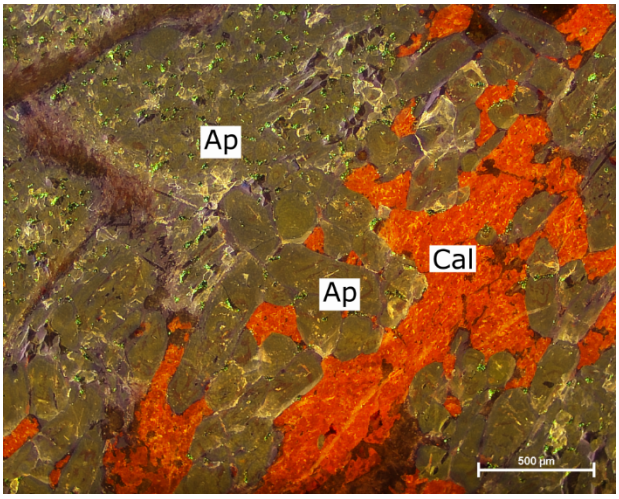

RHM-03

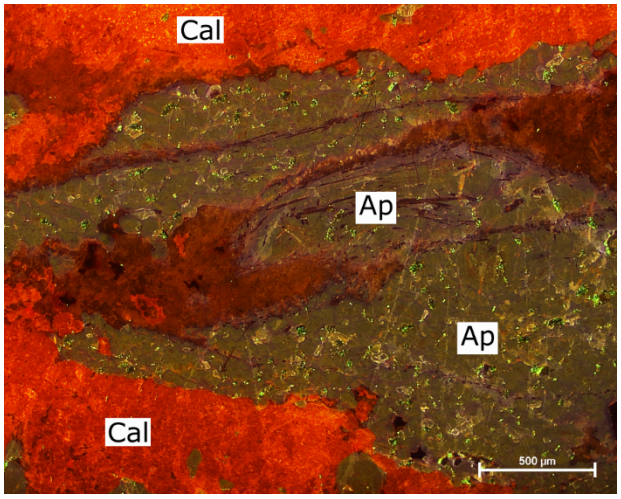

RHM-03

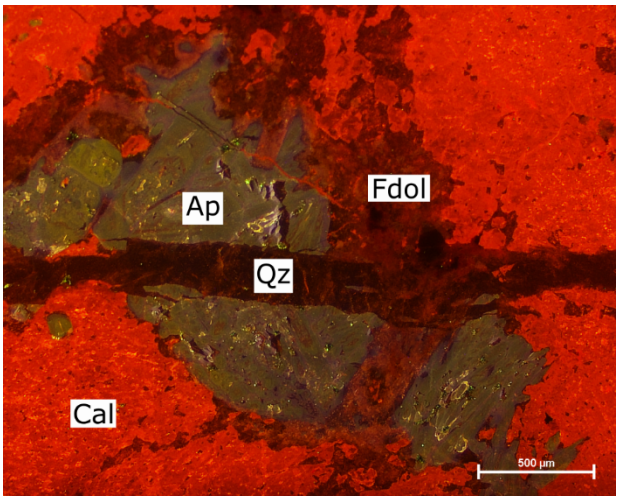

RHM-03

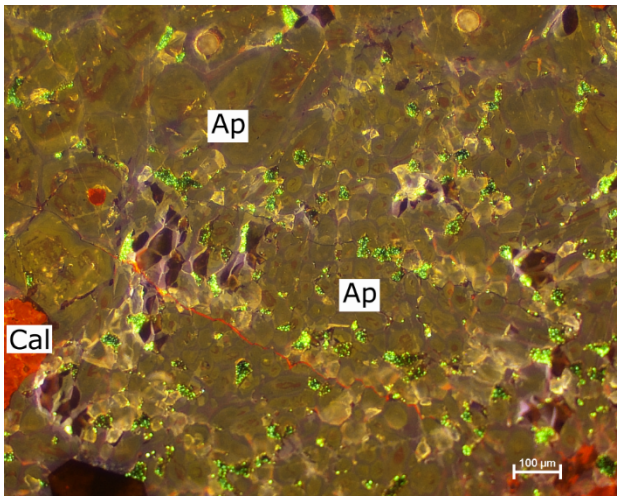

RHM-09

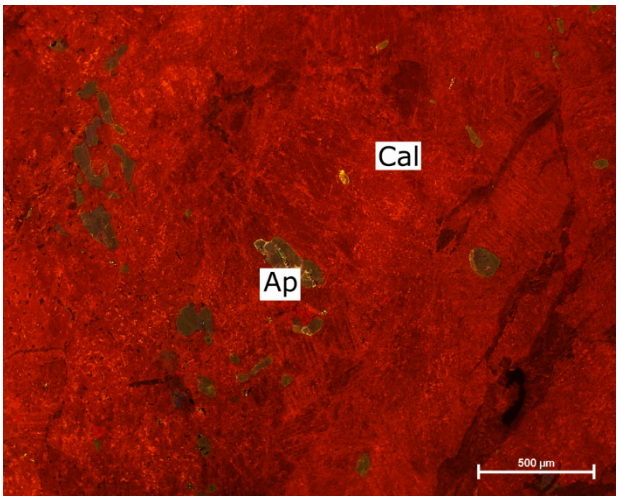

RHM-09

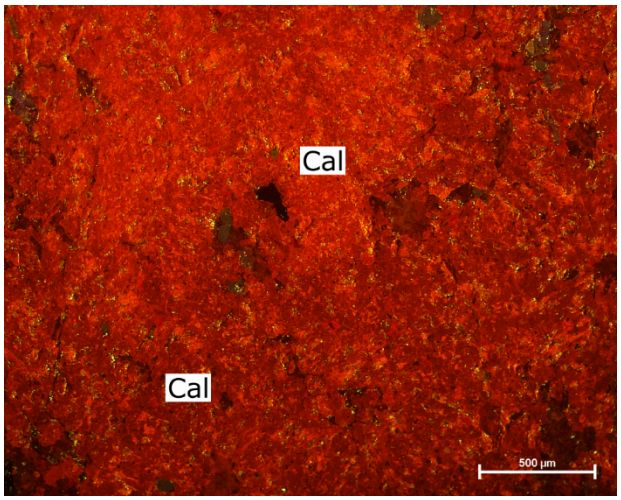

RHM-09

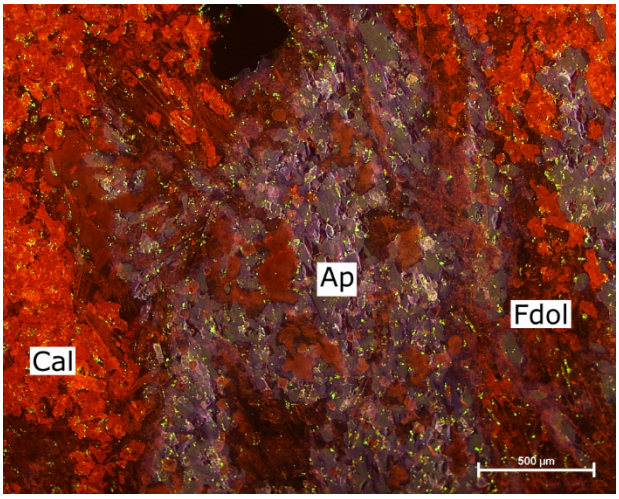

RHM-09

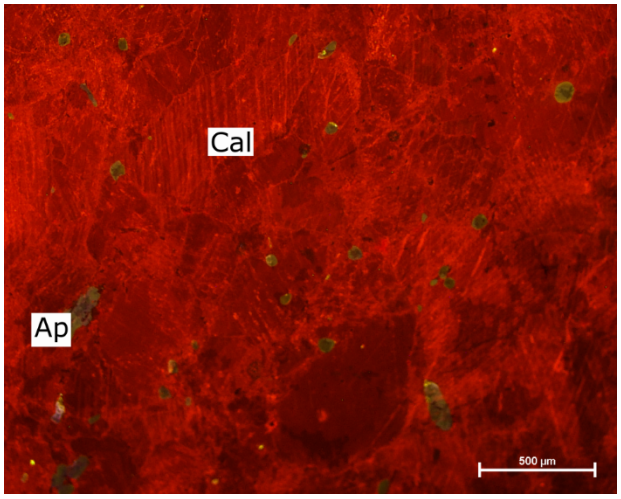

RHM-09

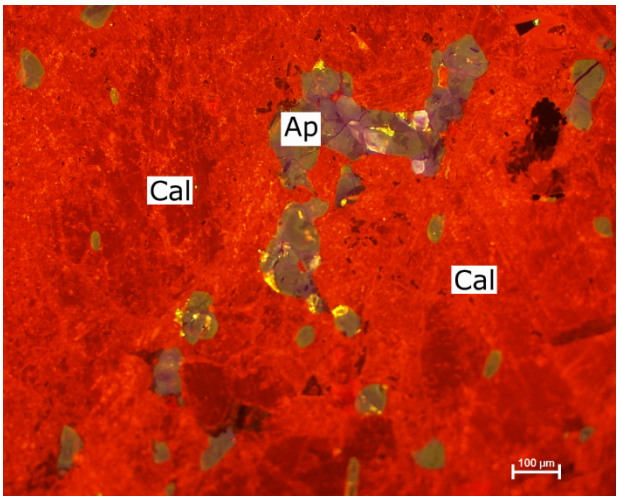

RHM-09

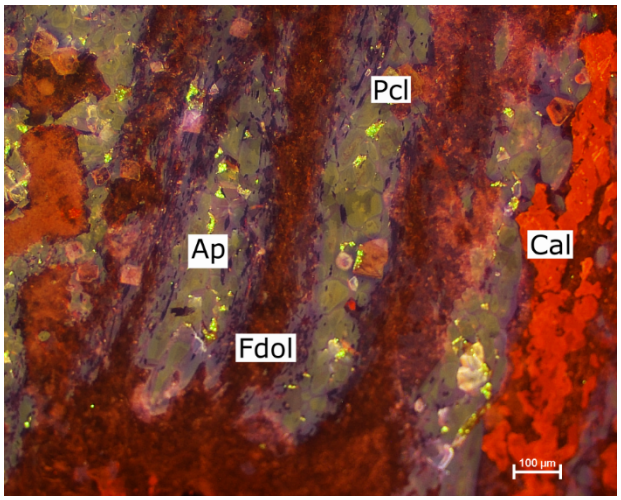

RHM-11

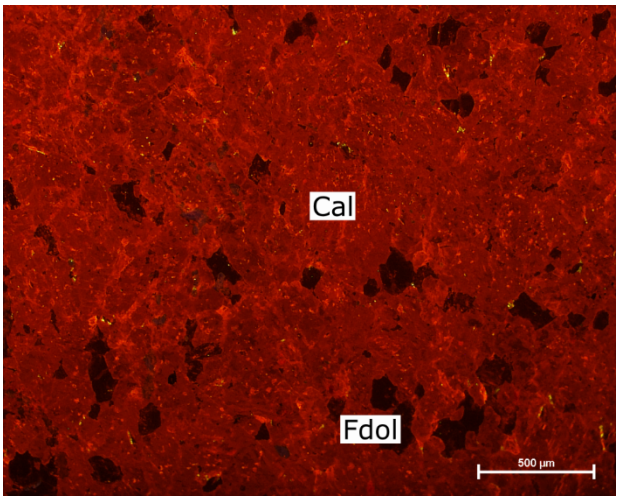

RHM-11

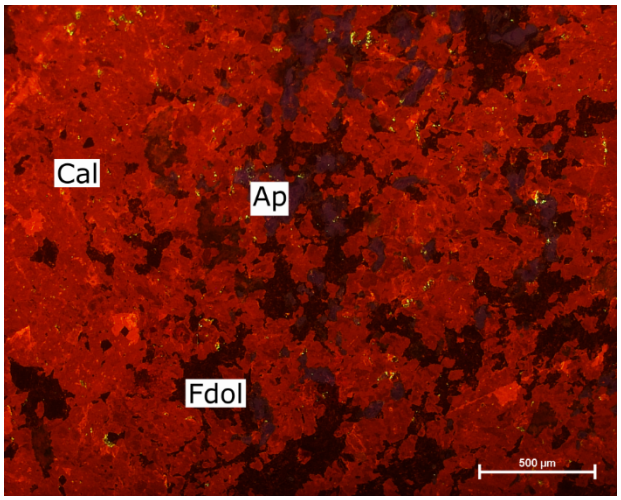

RHM-11

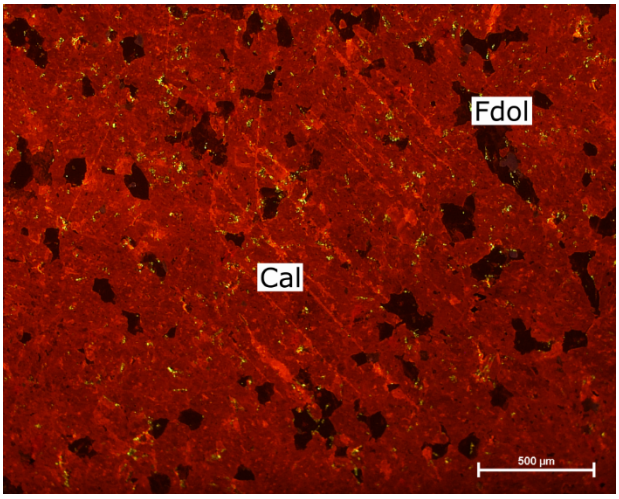

RHM-11

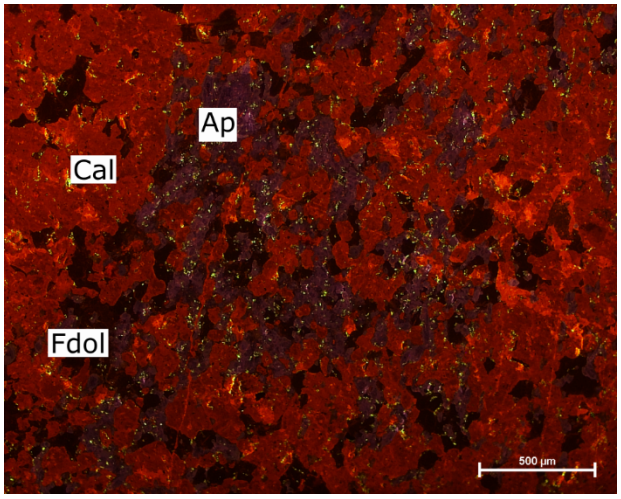

RHM-11

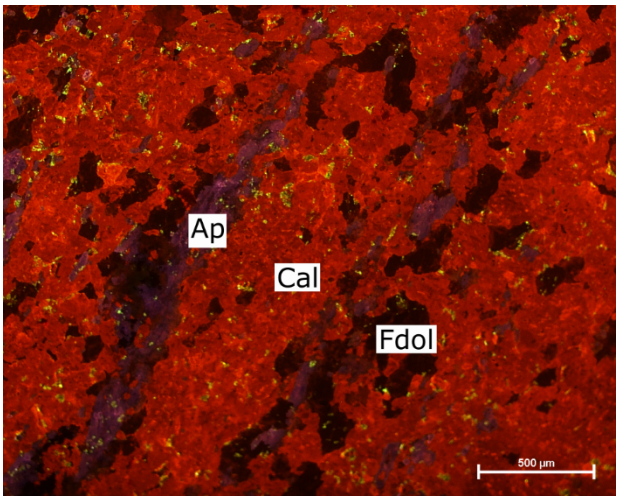

02-46

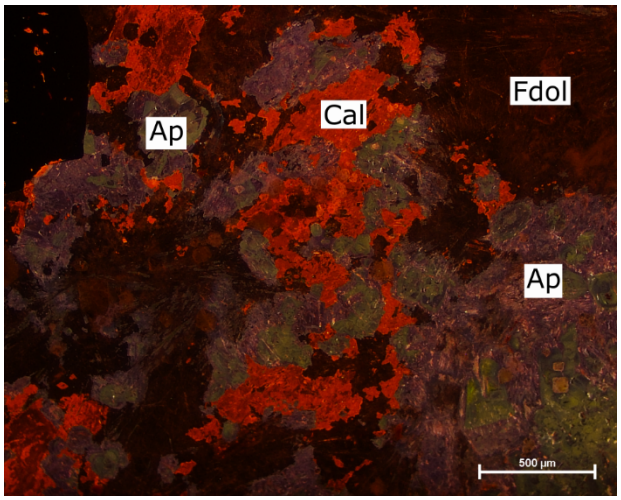

02-46

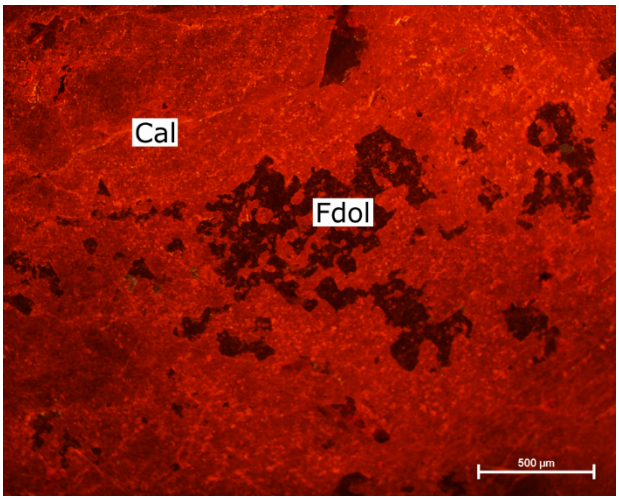

02-46

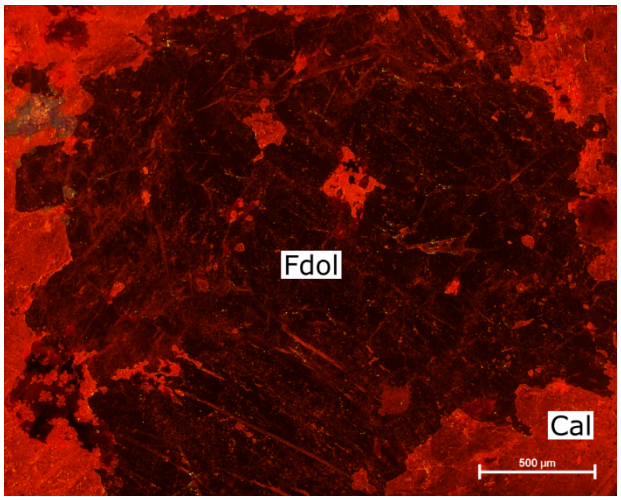

02-46

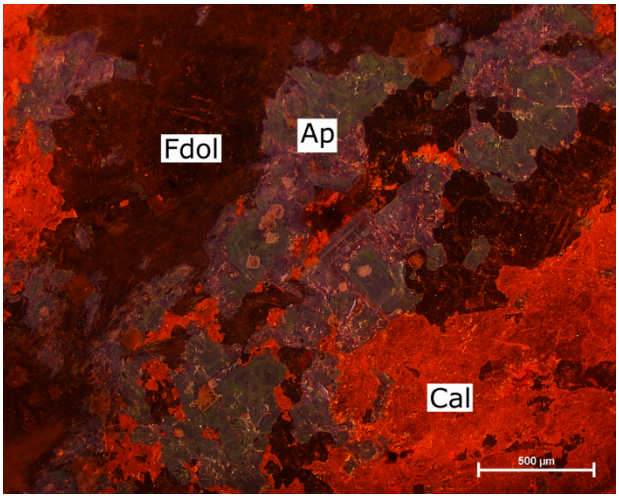

02-46

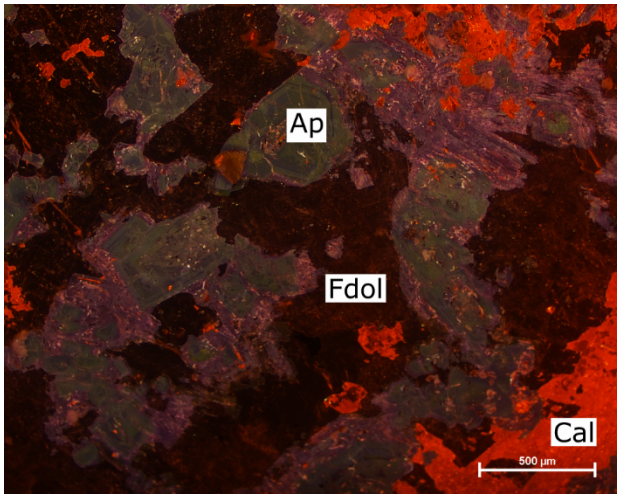

02-46

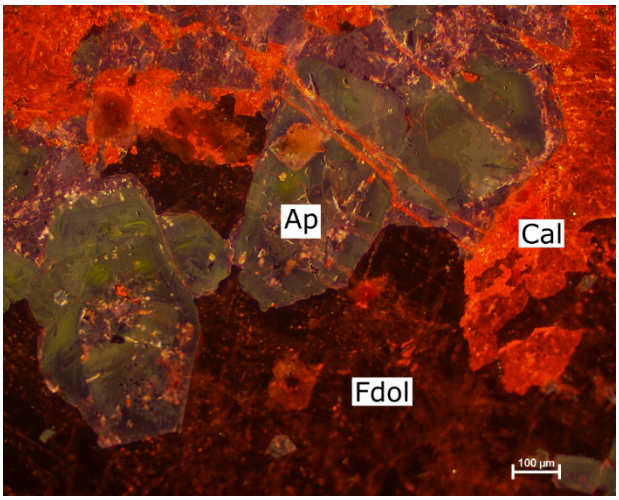

DDH-03-61

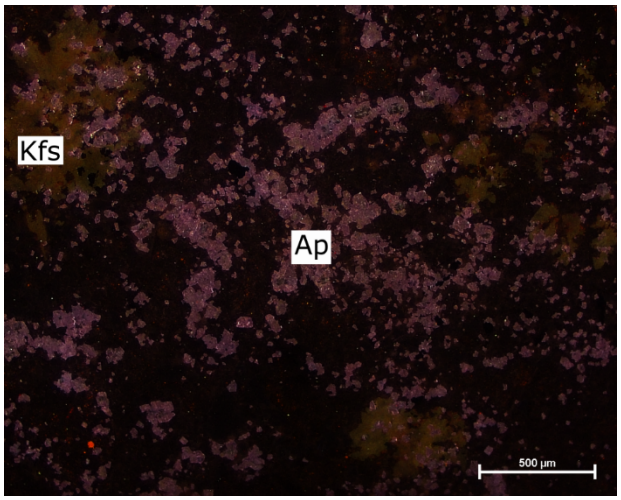

DDH-03-61

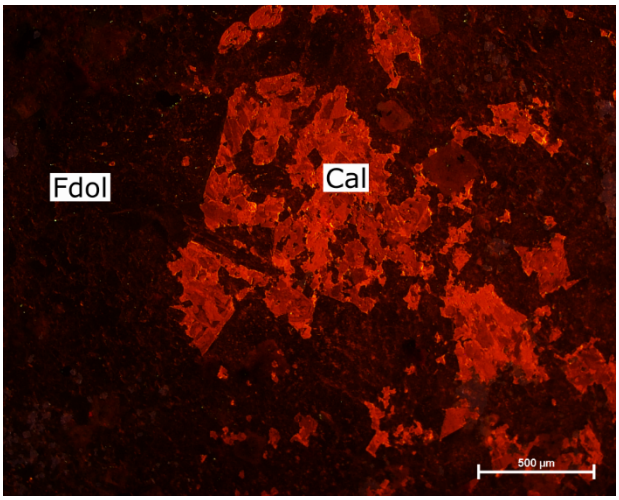

DDH-03-61

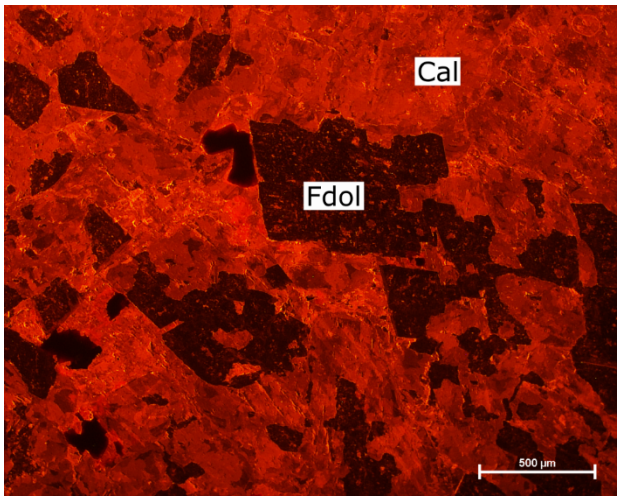

DDH-04-40

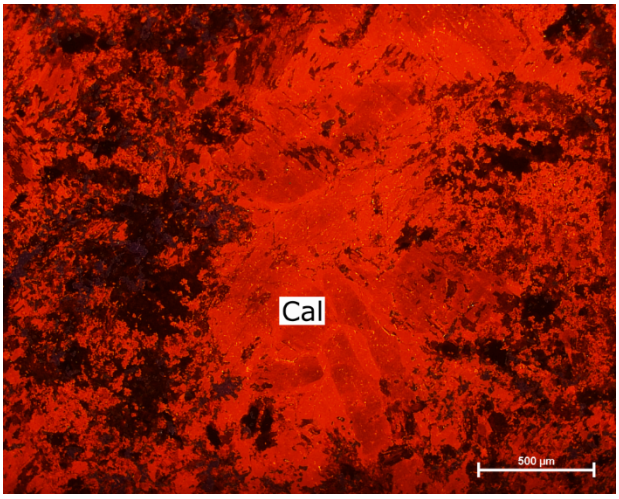

DDH-04-40

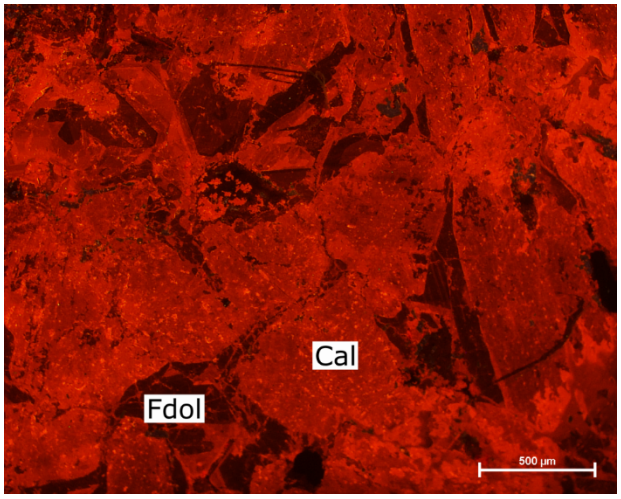

DDH-04-47A

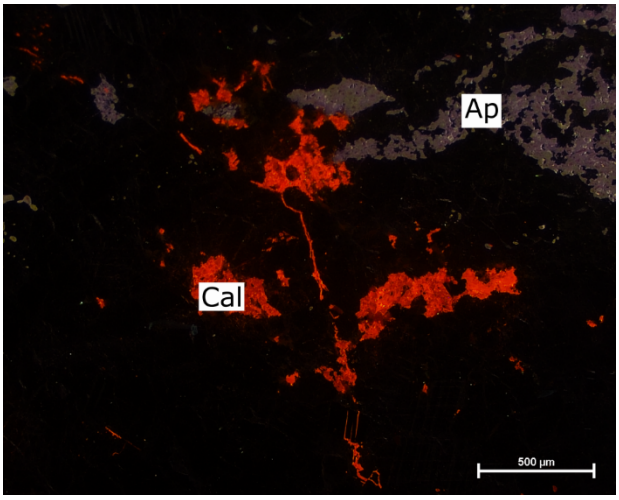

DDH-04-47A

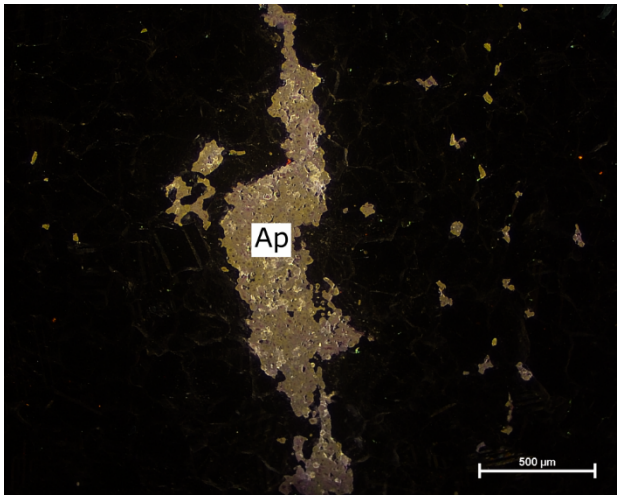

DDH-04-47A

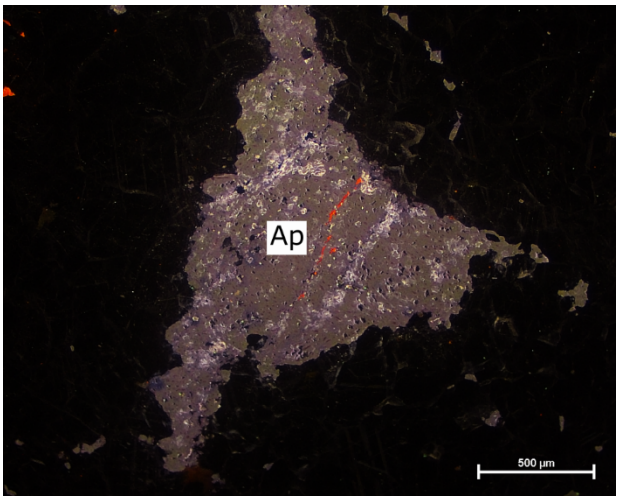

DDH-04-47A

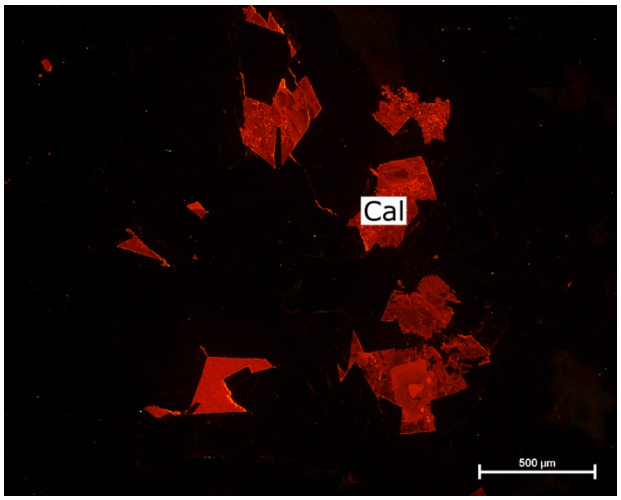

DDH-04-47A

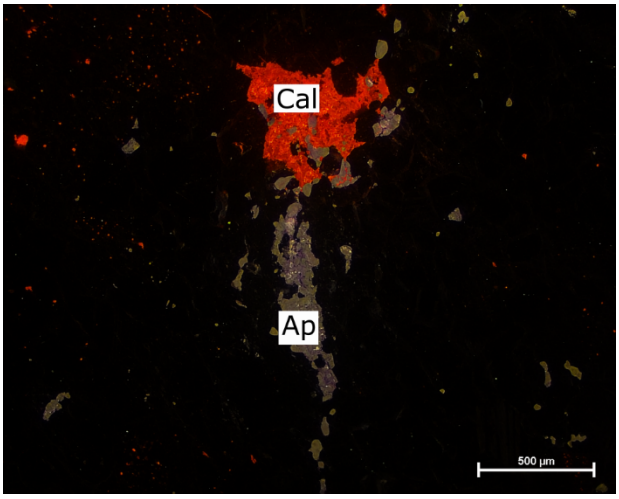

DDH-04-47A

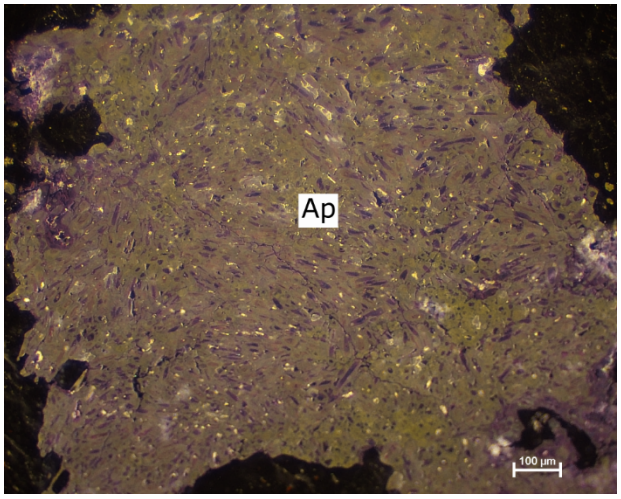

DDH-04-47A

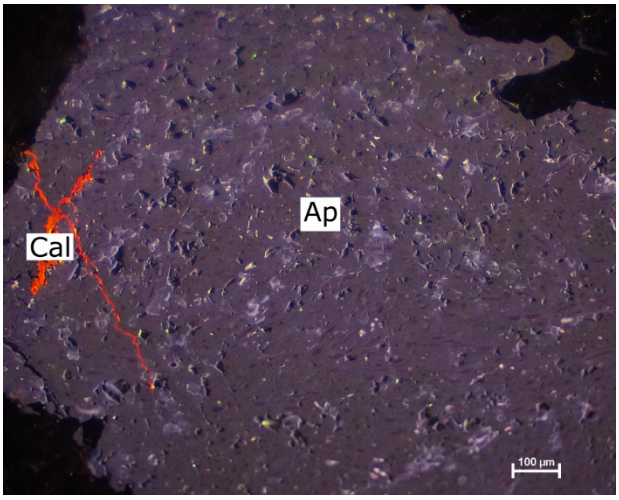

DDH-04-47A

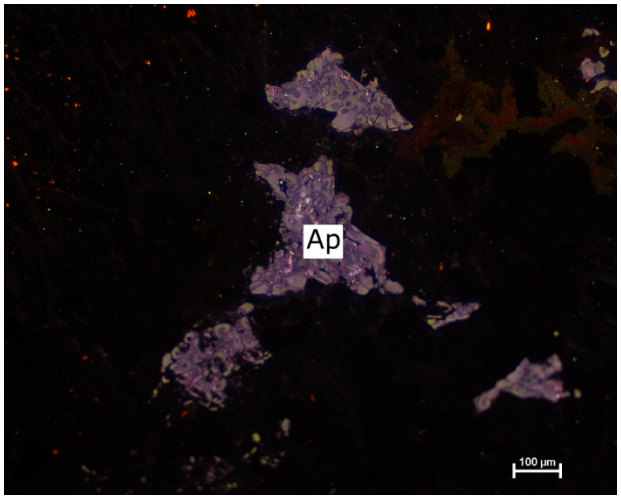

DDH-04-532

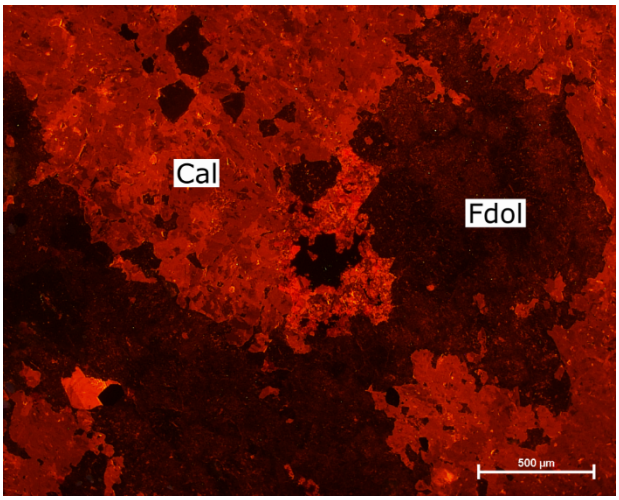

DDH-04-532

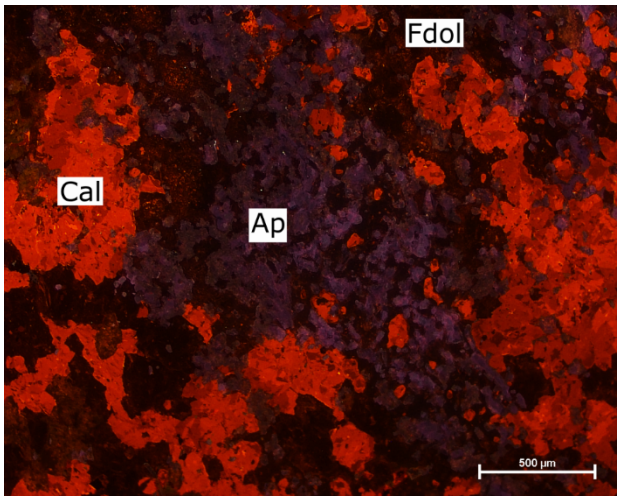

DDH-04-532

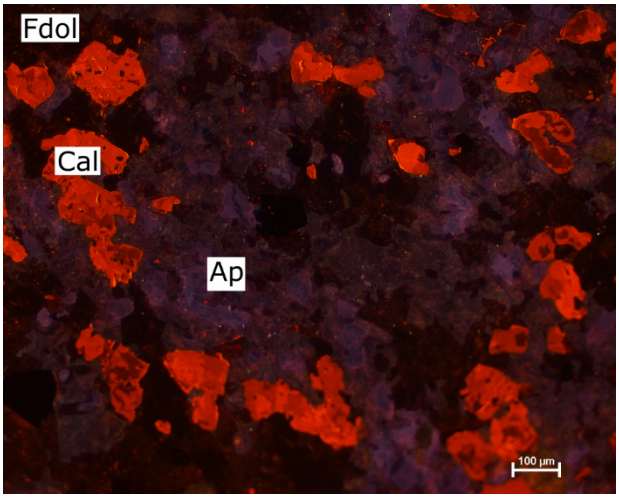

DDH-04-608

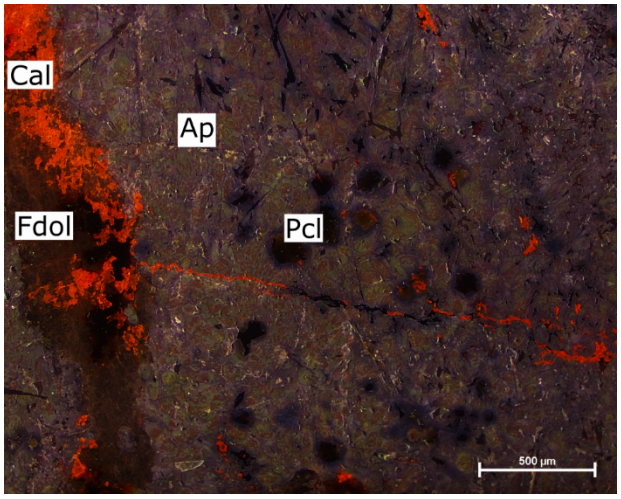

DDH-04-608

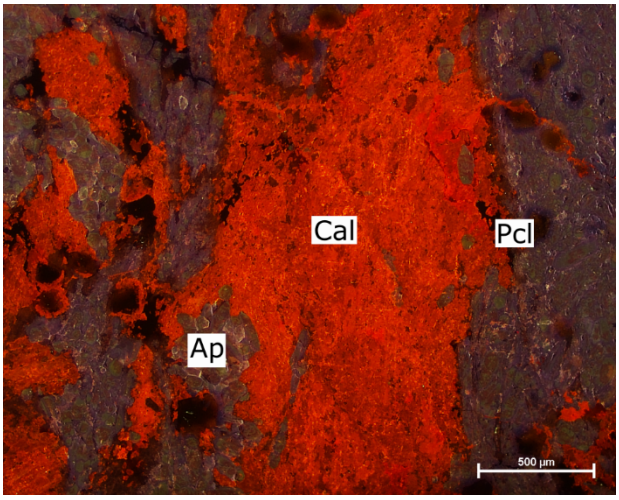

DDH-04-608

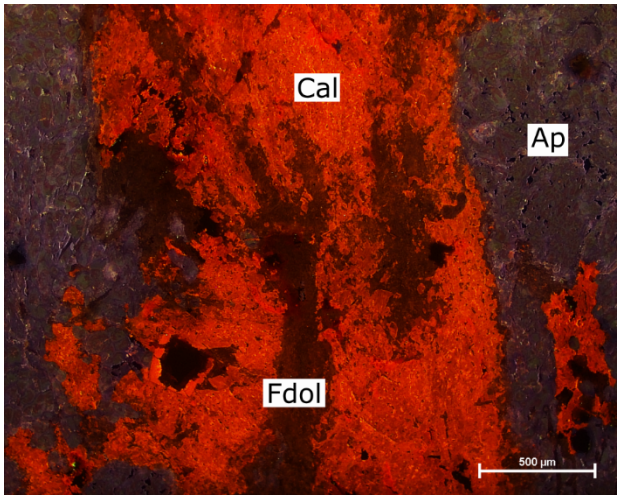

DDH-04-608

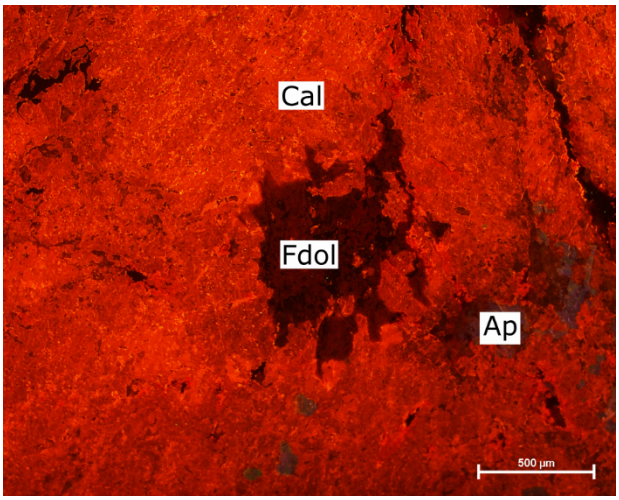

DDH-04-608

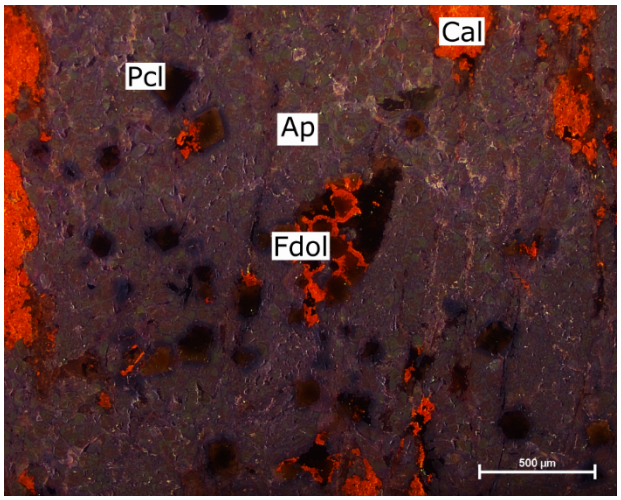

DDH-04-608

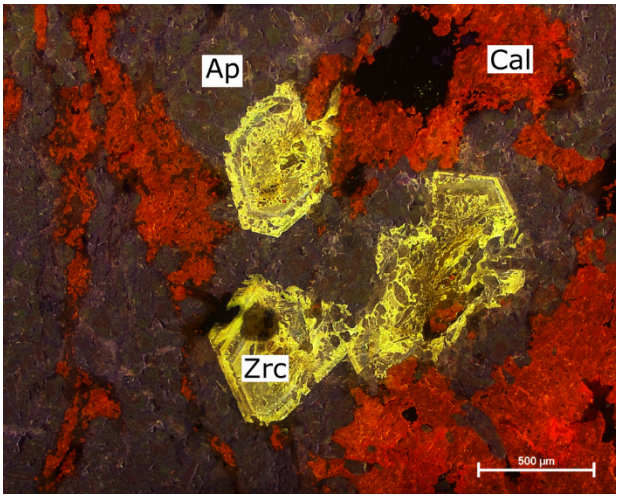

DDH-04-608

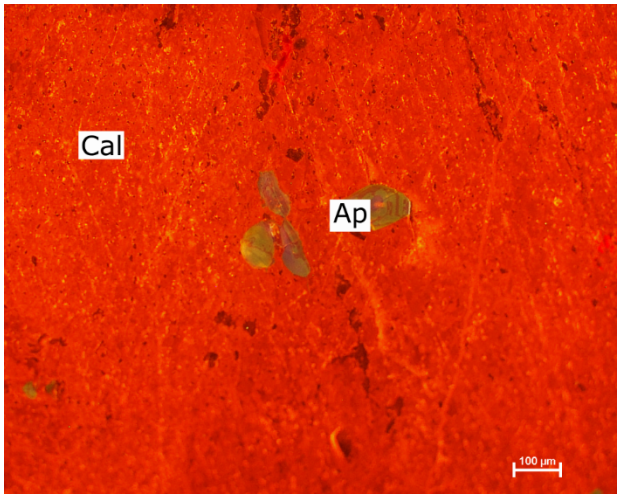

DDH-04-608

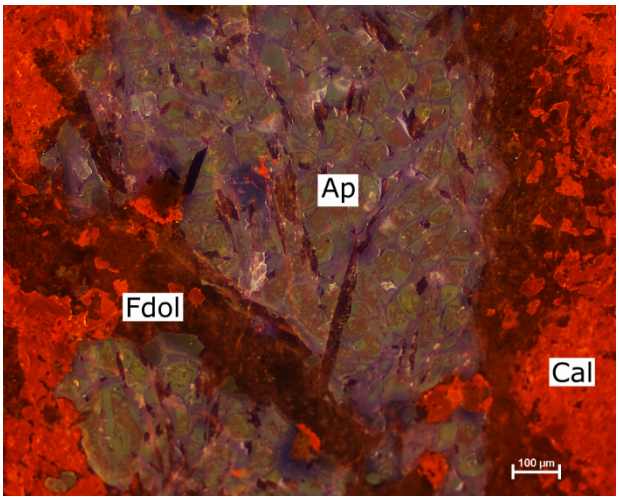

DDH-08-13

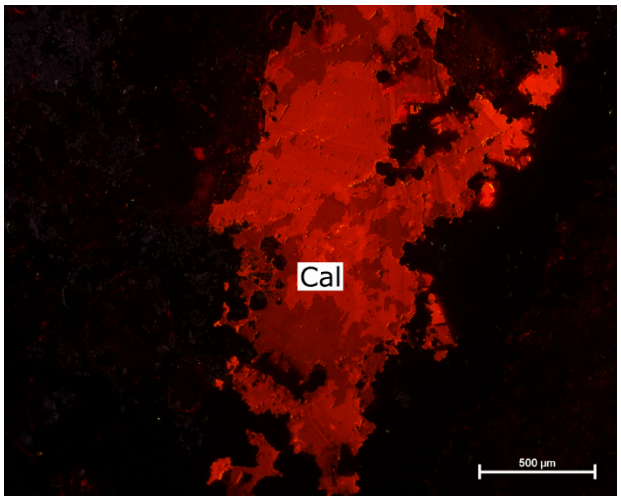

DDH-08-13

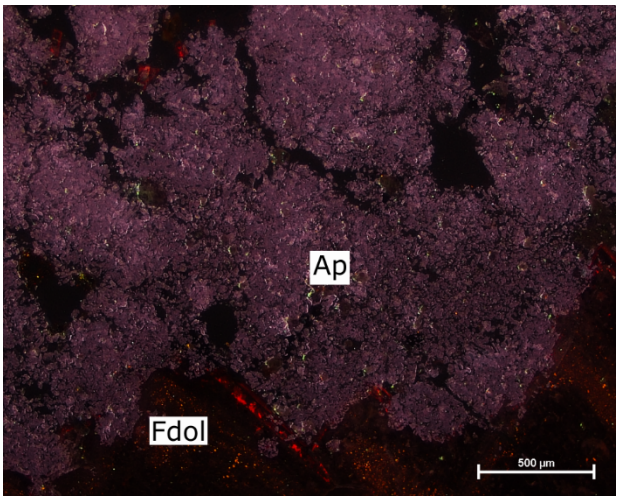

DDH-08-13

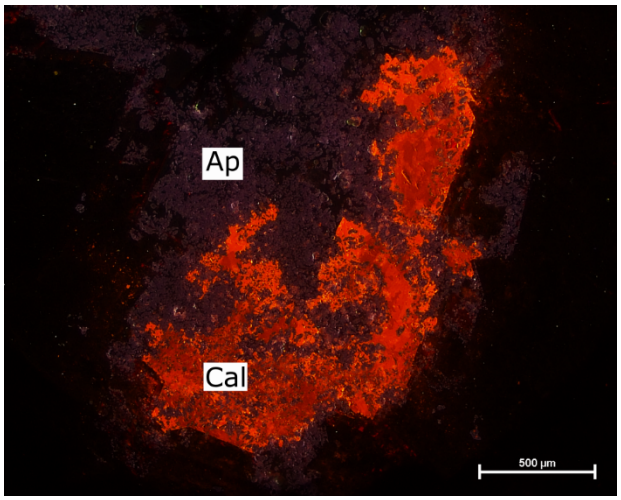

DDH-08-13

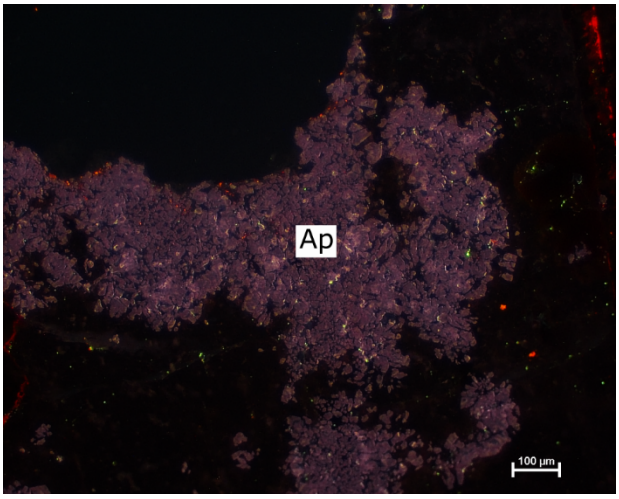

DDH-08-293

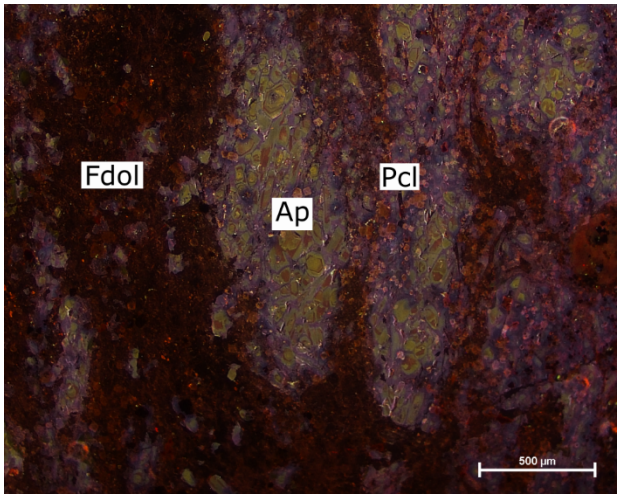

DDH-08-293

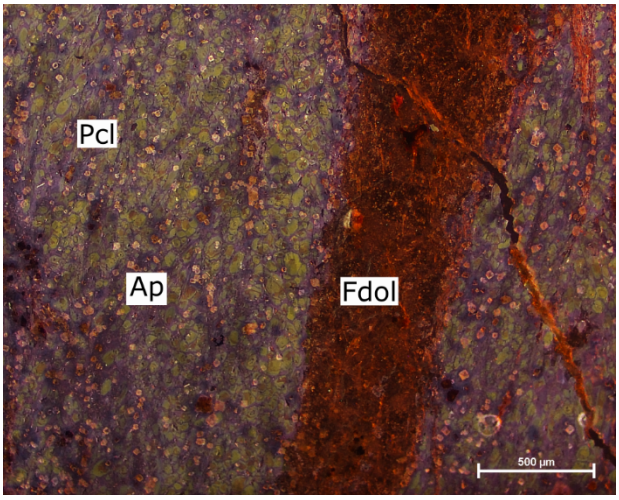

DDH-08-293

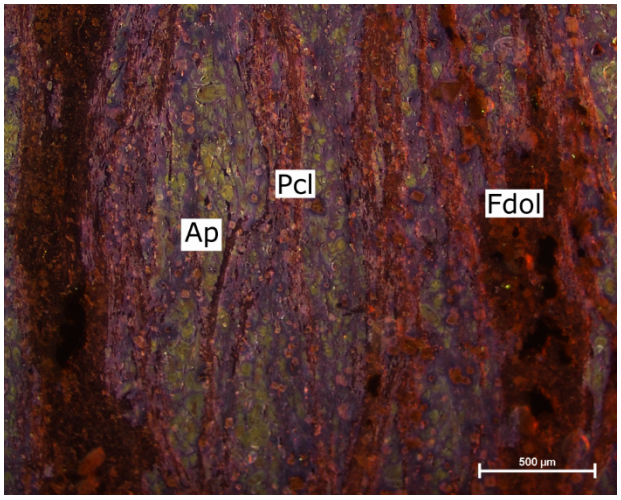

DDH-08-293

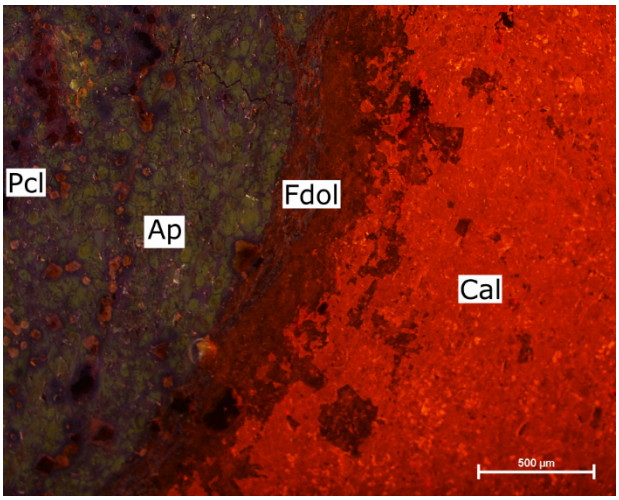

DDH-08-293

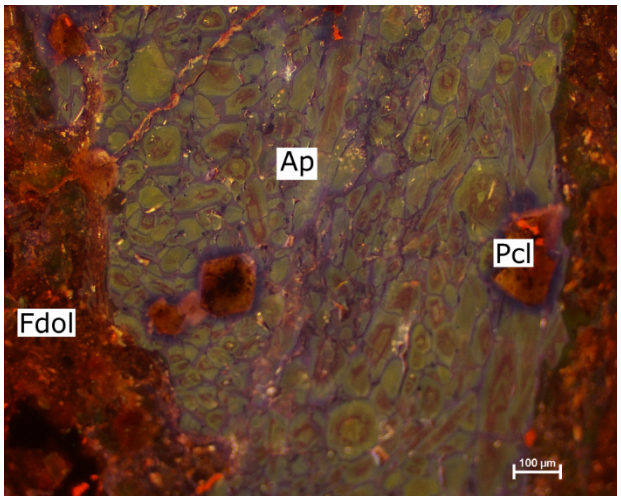

DDH-08-293

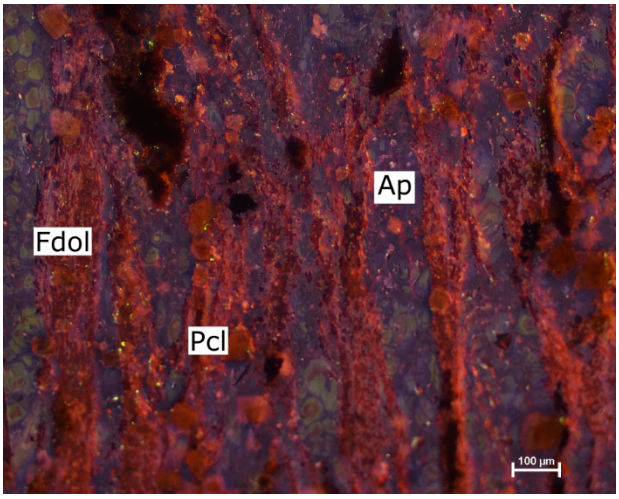

DDH-08-380

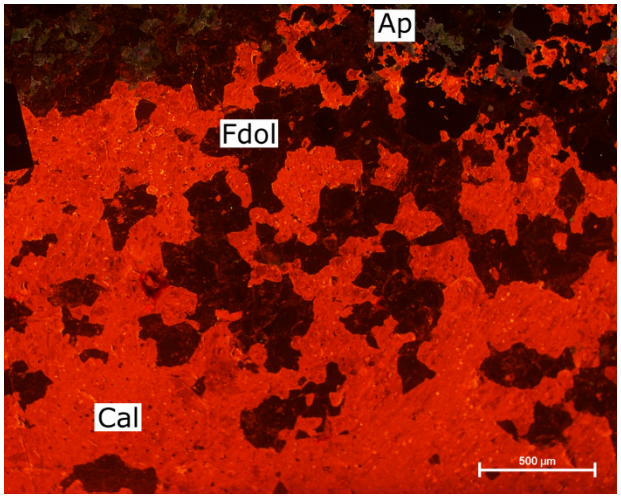

DDH-08-380

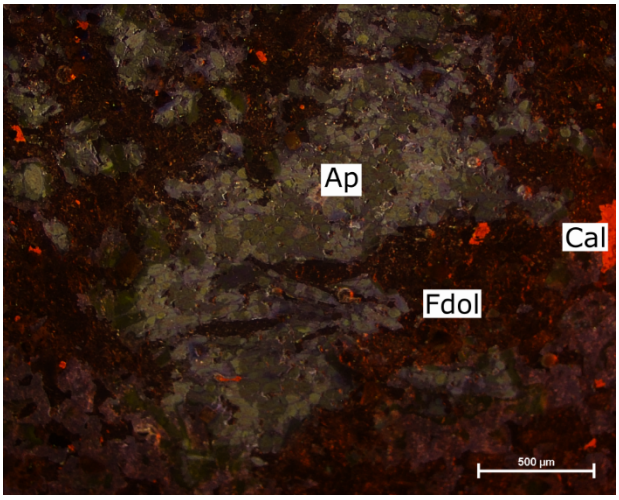

DDH-08-380

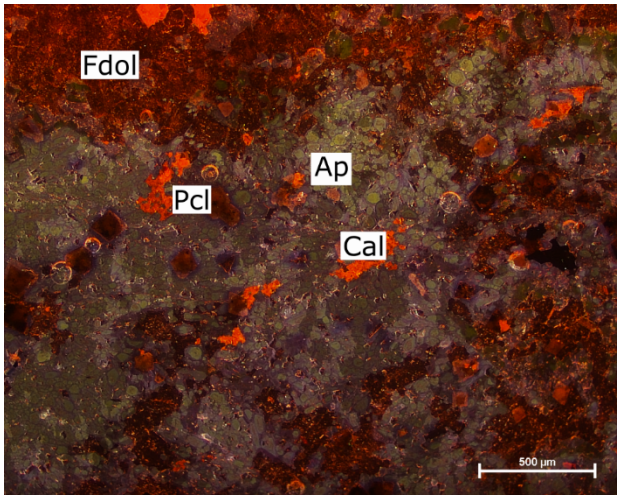

DDH-08-380

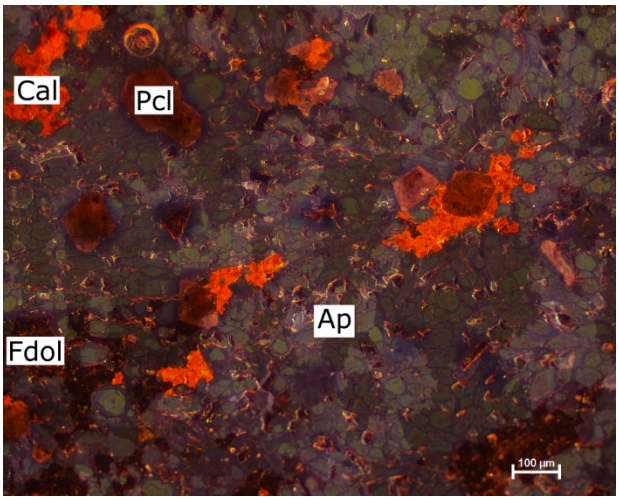

PGH-18-01-66

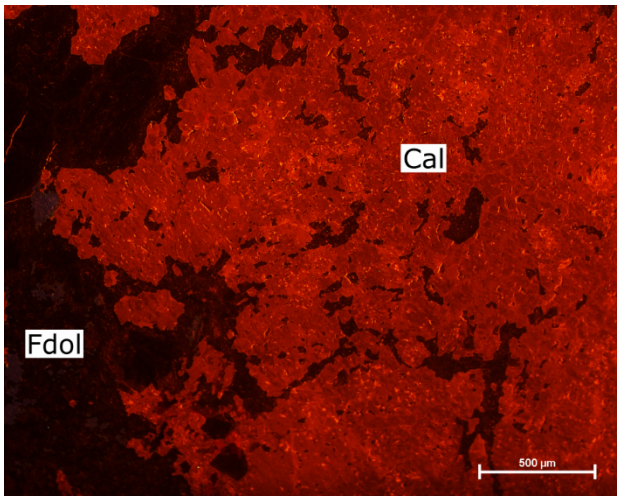

PGH-18-01-66

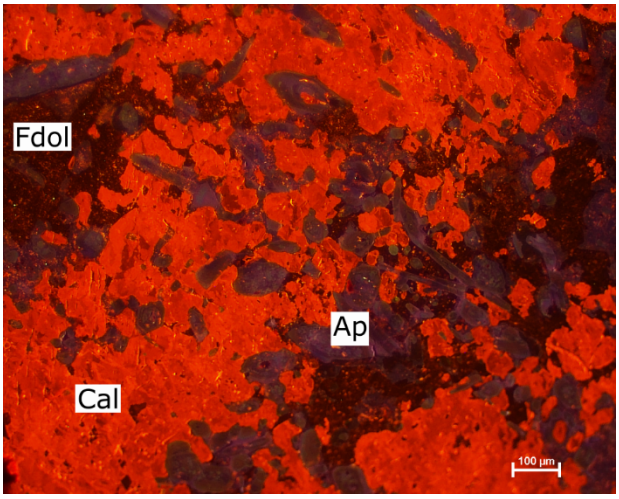

PGH-18-01-337

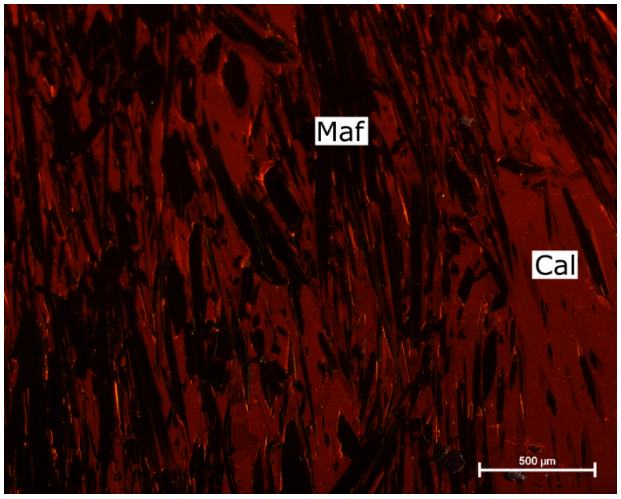

PGH-18-01-337

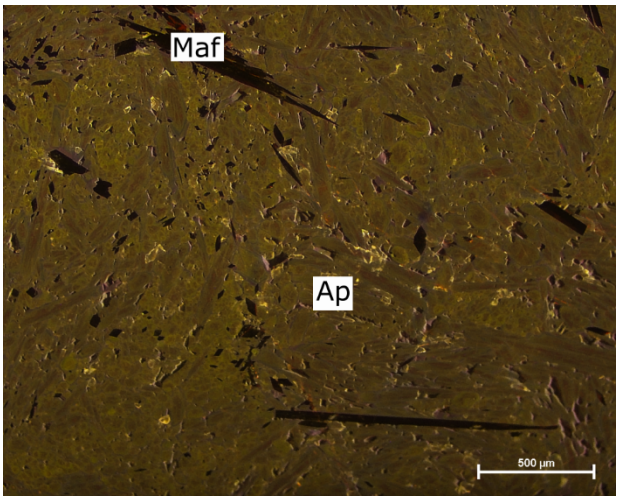

PGH-18-01-337

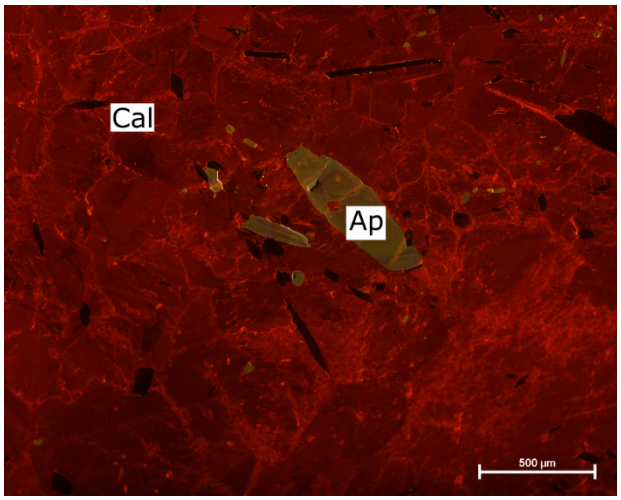

PGH-18-01-337

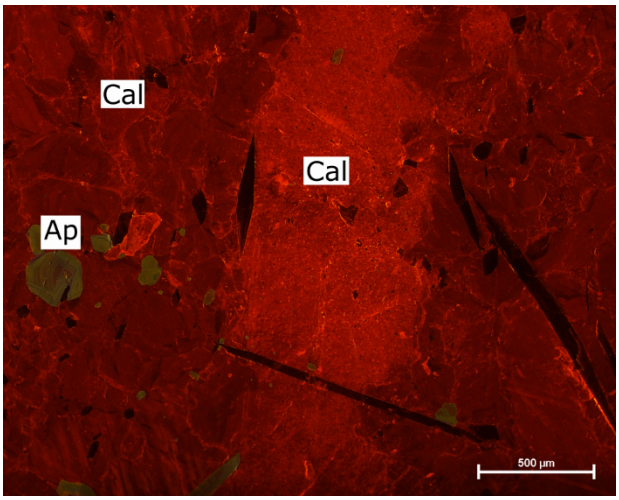

PGH-18-01-337

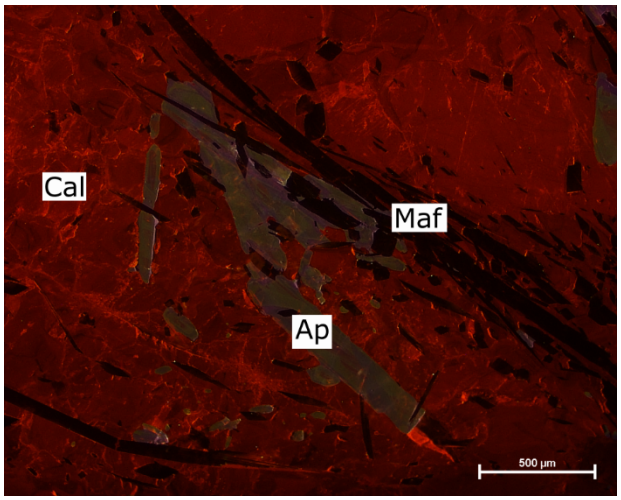

PGH-18-01-337

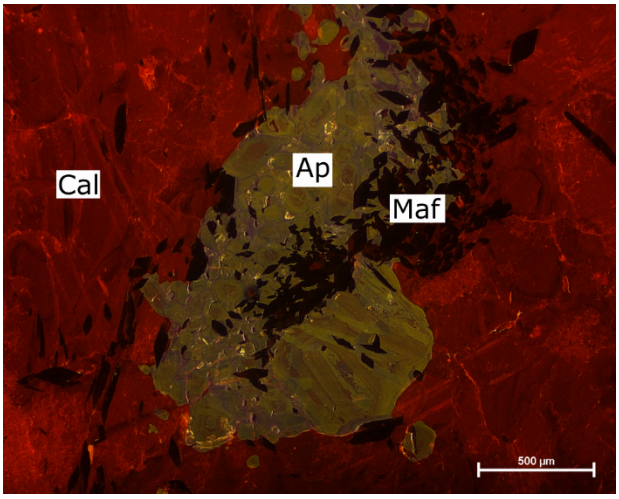

PGH-18-01-337

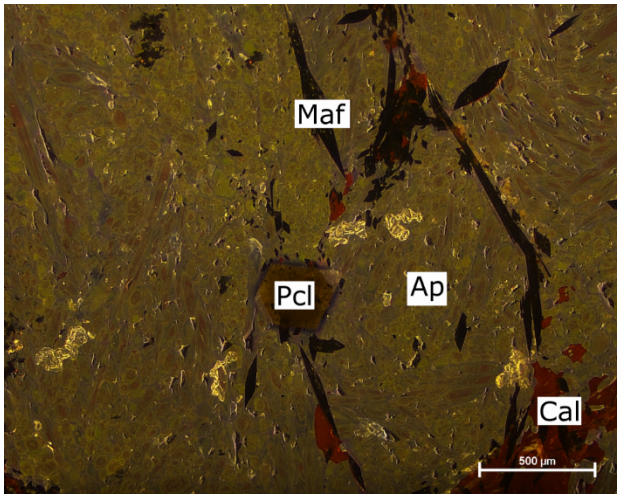

PGH-18-07-609

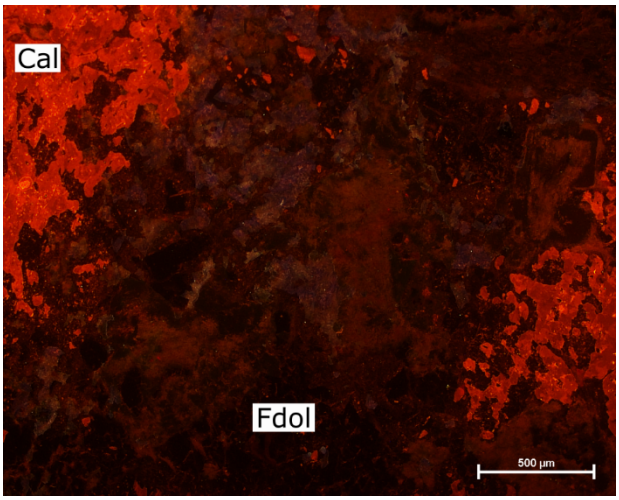

PGH-18-07-609

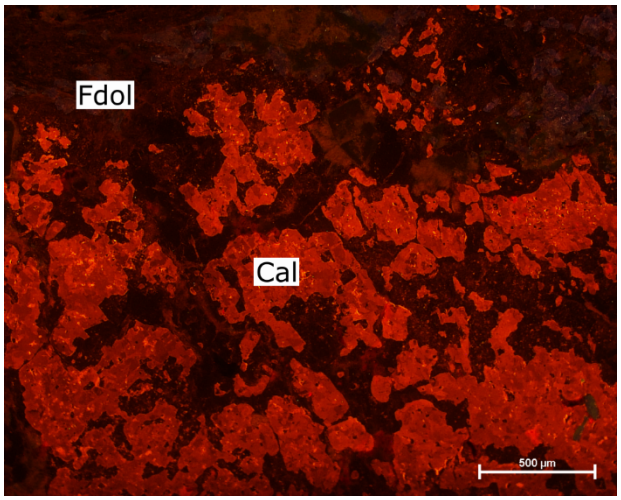

PGH-18-07-609

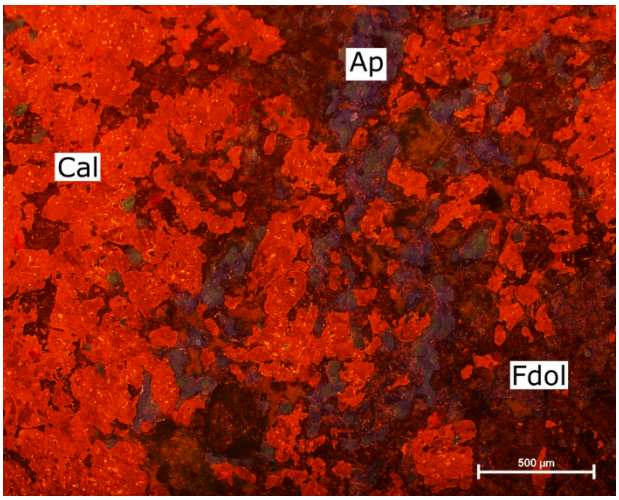

PGH-18-07-609

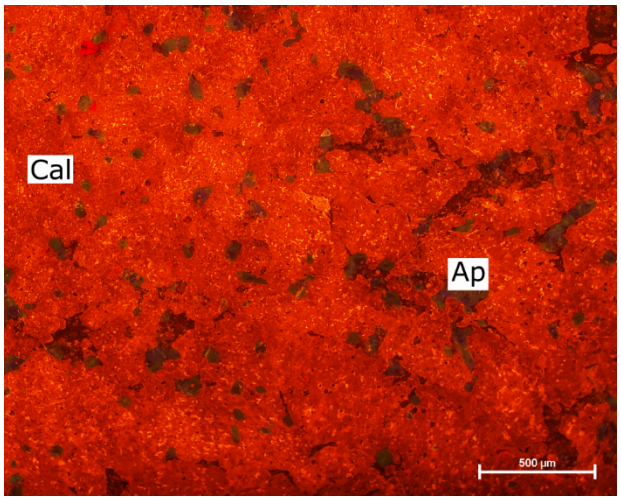

PGH-18-07-609

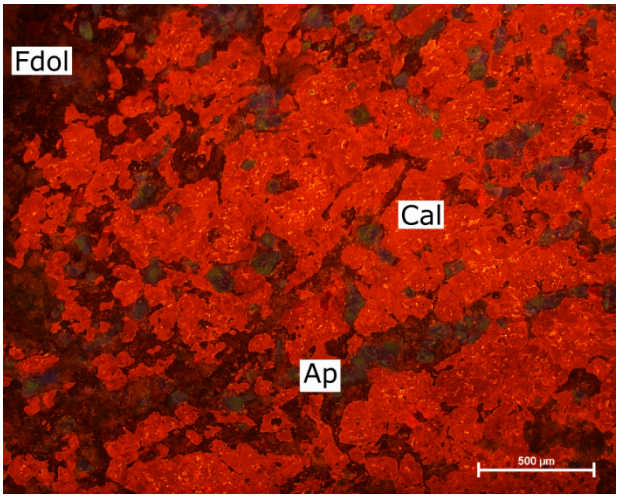

PGH-18-07-609

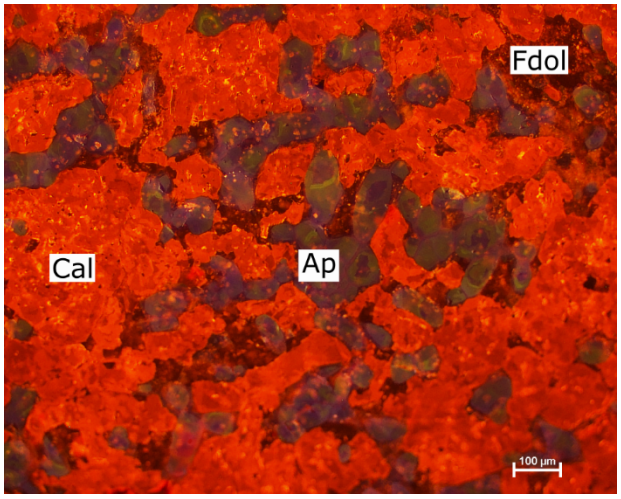

II-II Spectra (Queen's University)

02-46

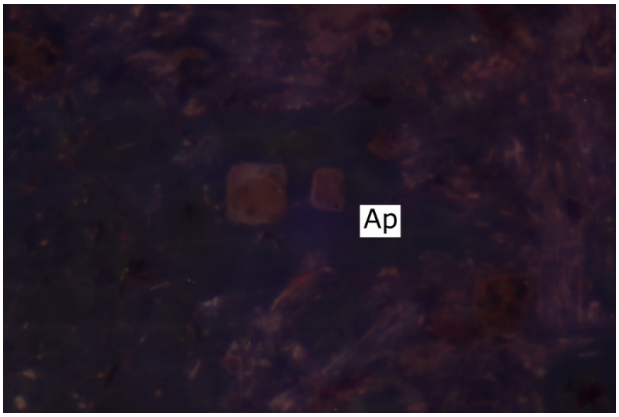

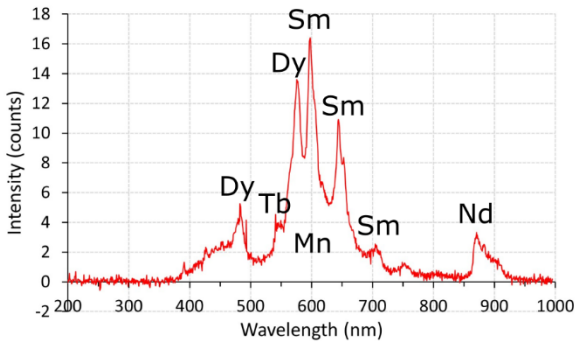

02-46

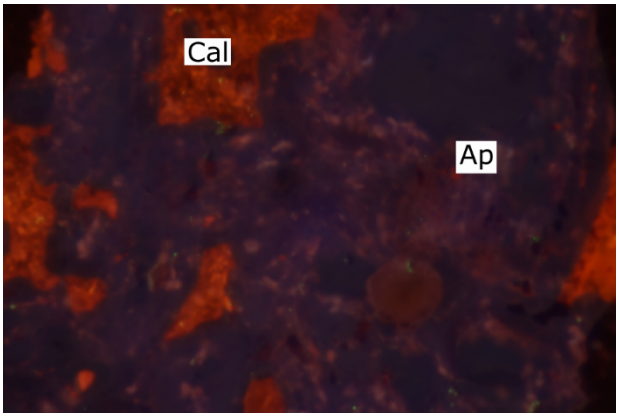

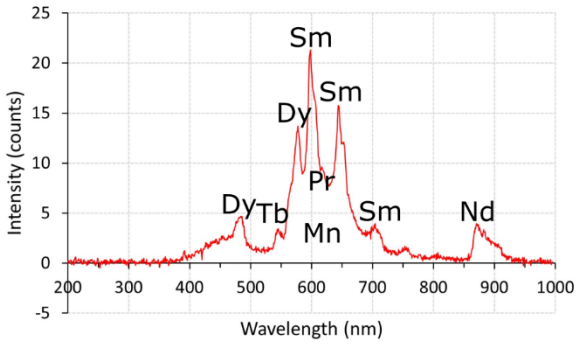

02-46

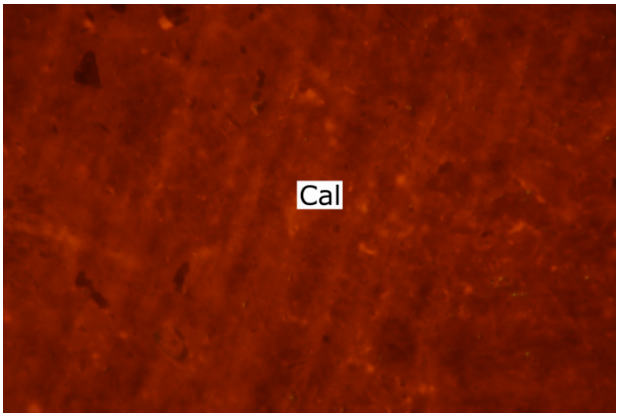

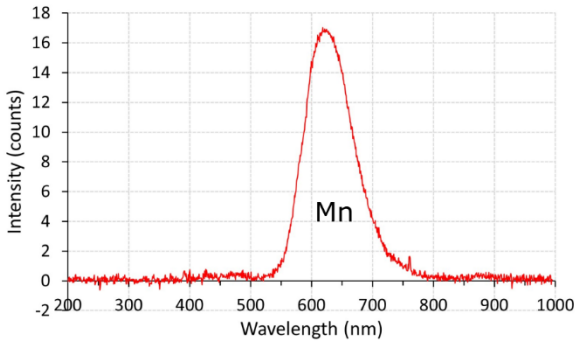

02-46

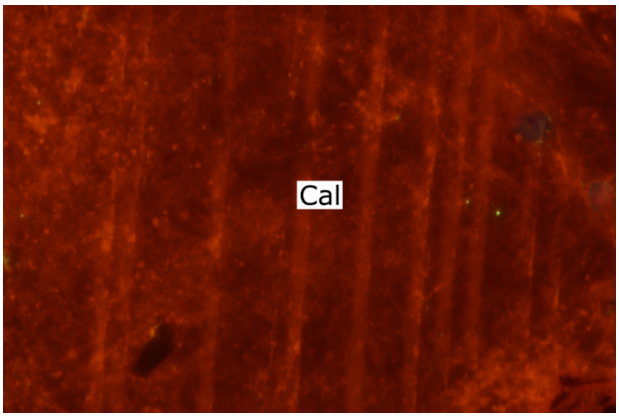

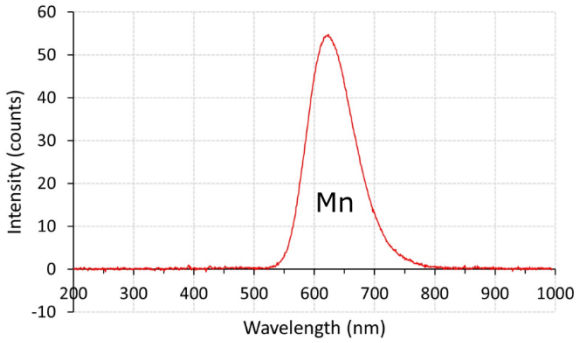

DDH-03-251

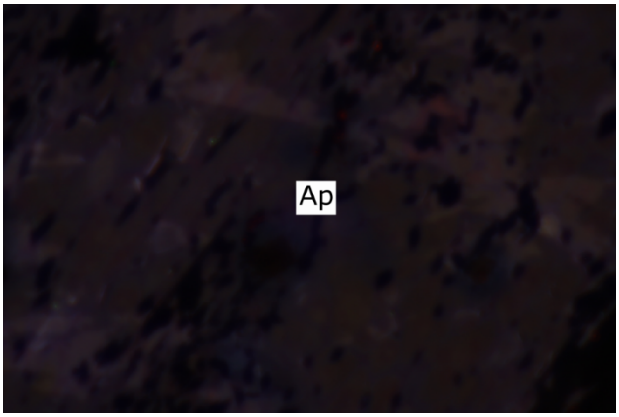

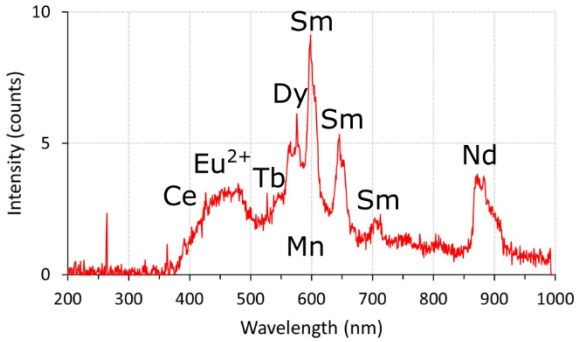

DDH-03-251

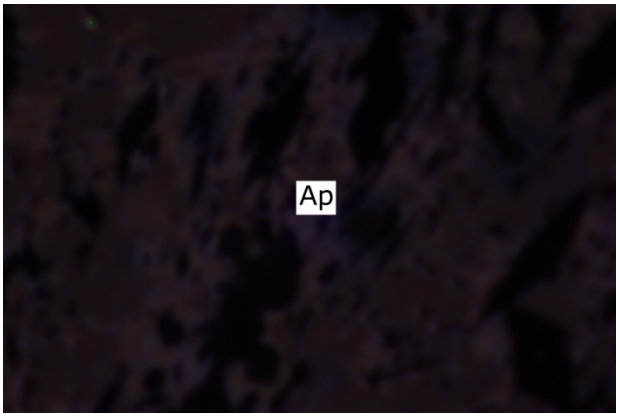

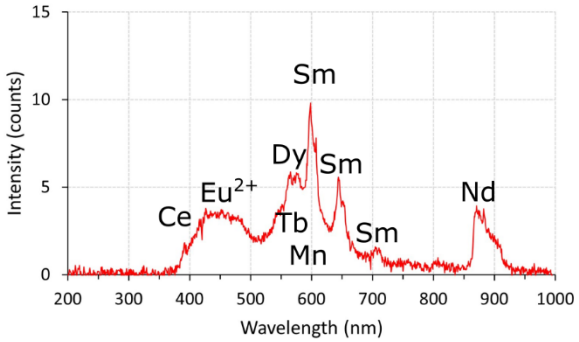

DDH-03-251

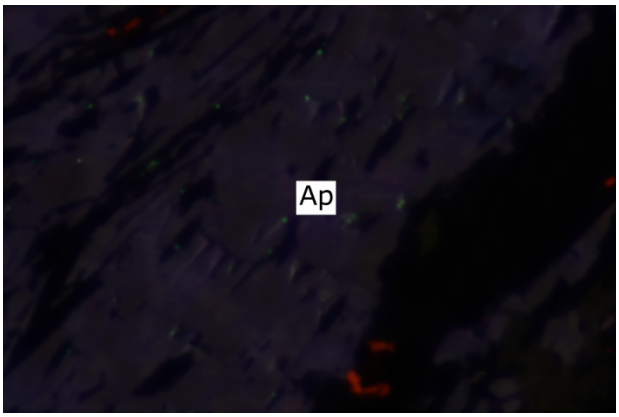

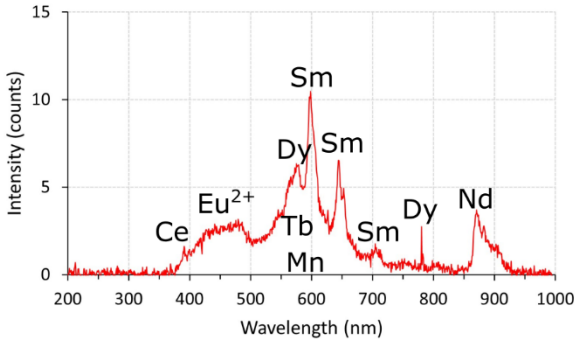

DDH-04-47A

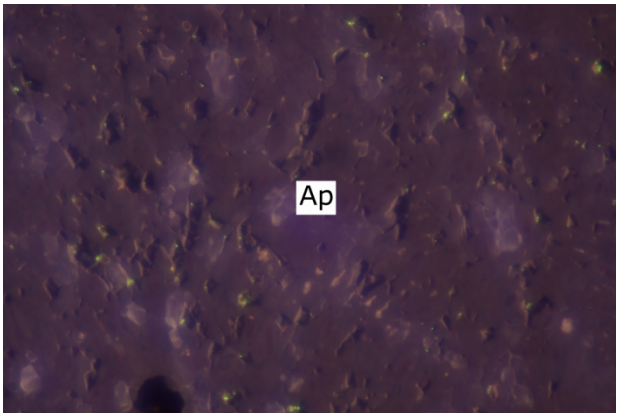

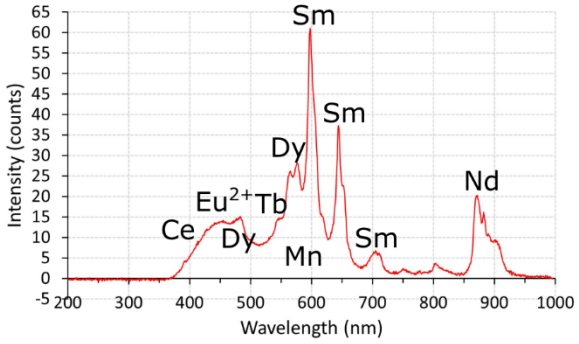

DDH-04-47A

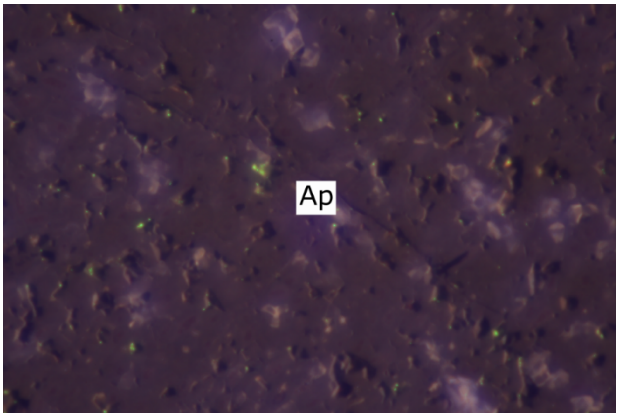

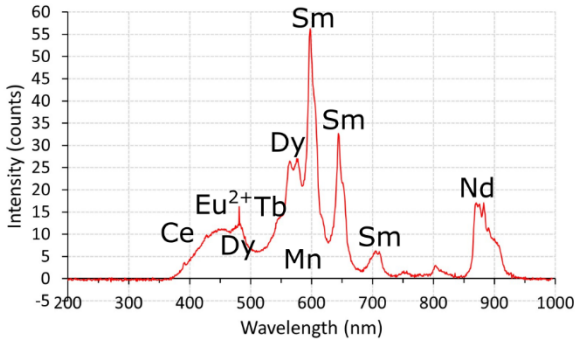

DDH-04-47A

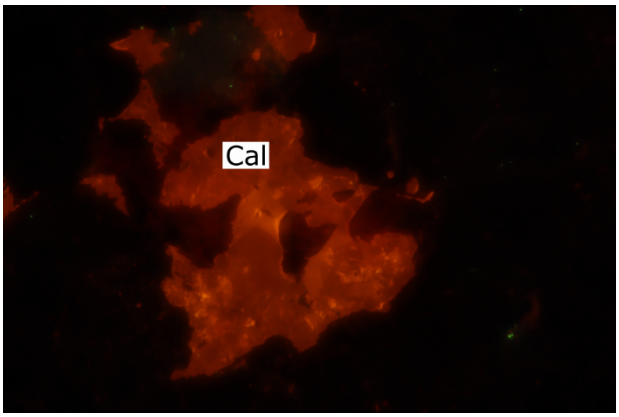

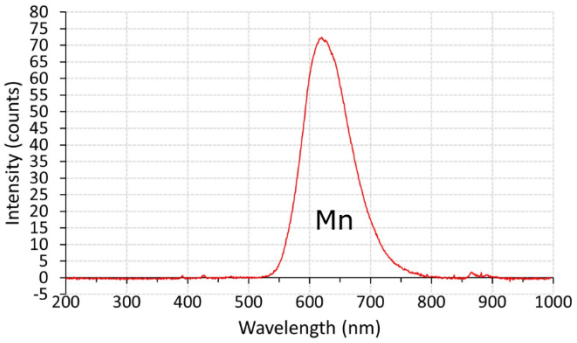

DDH-04-495

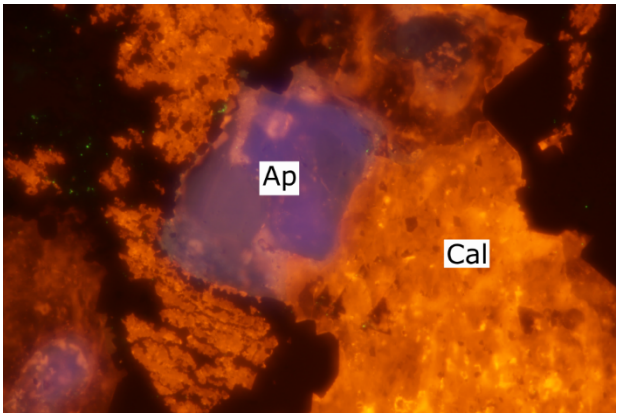

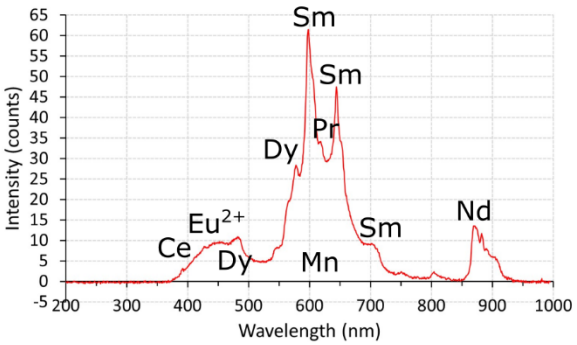

DDH-04-495

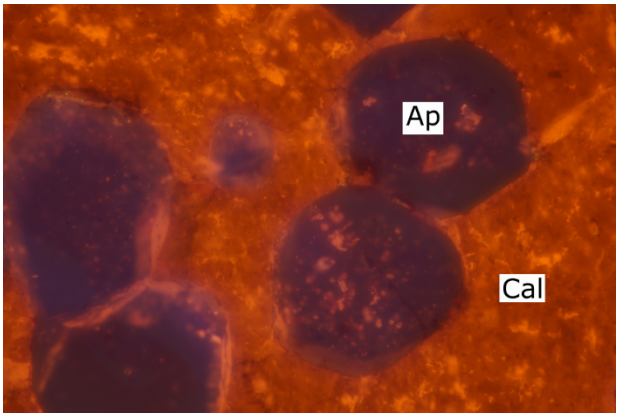

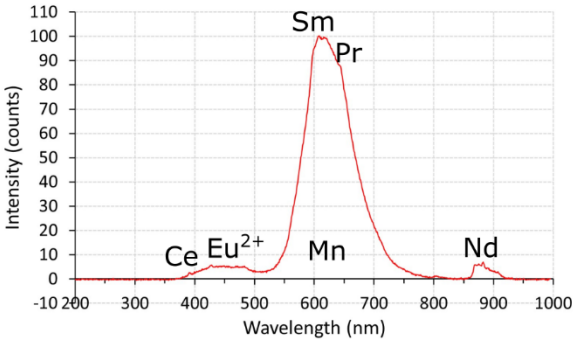

DDH-04-495

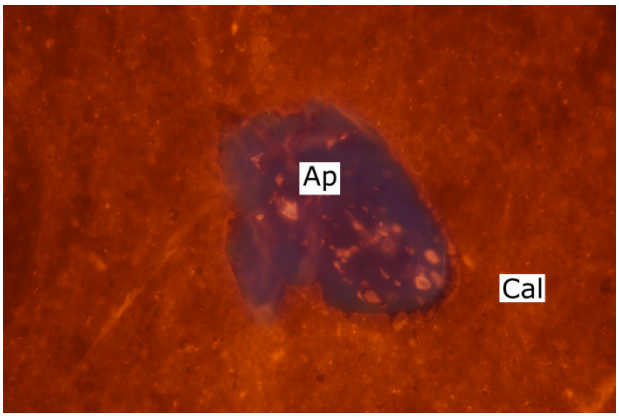

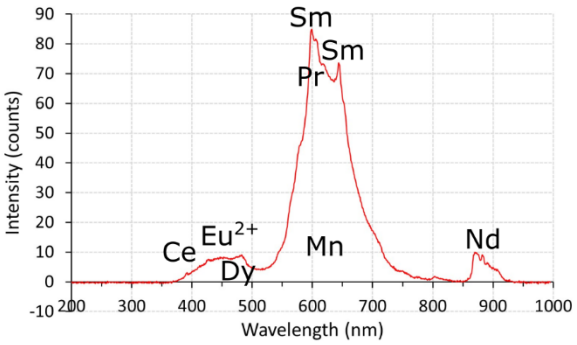

DDH-04-495

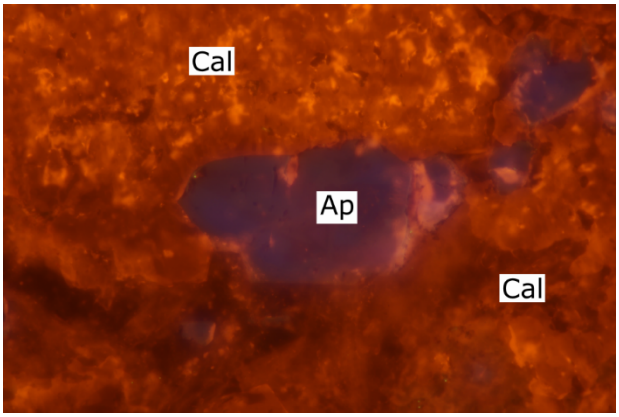

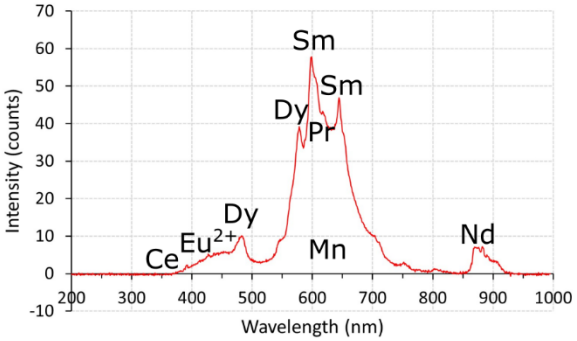

DDH-04-495

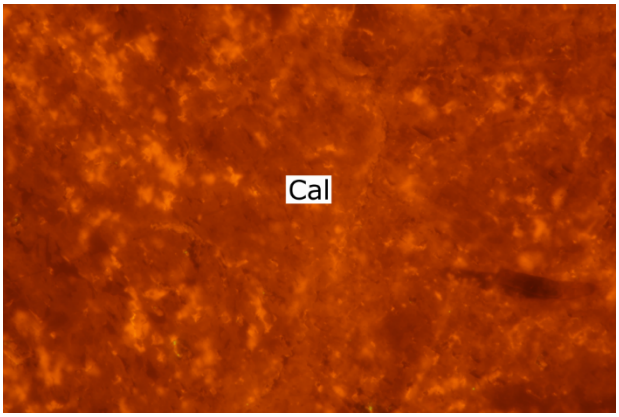

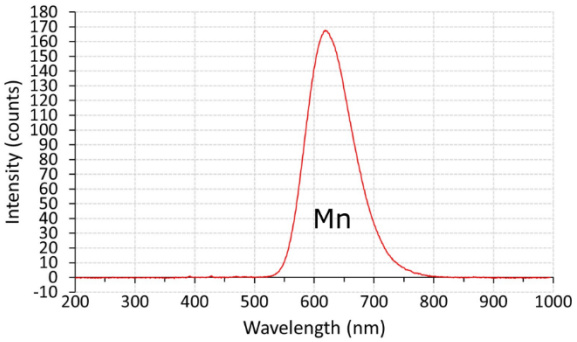

DDH-04-495

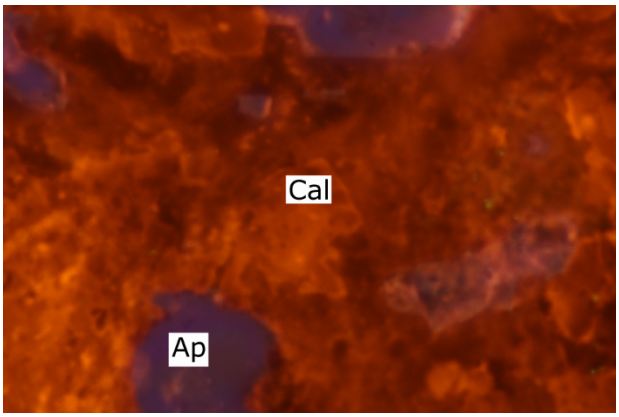

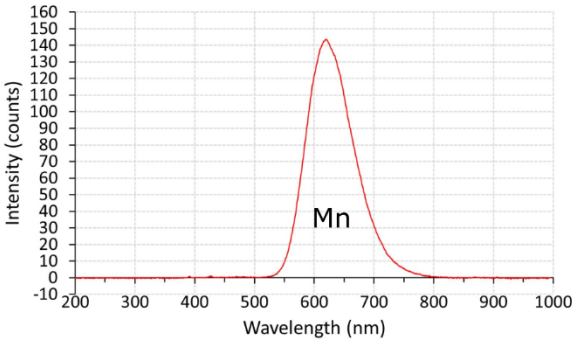

DDH-04-495

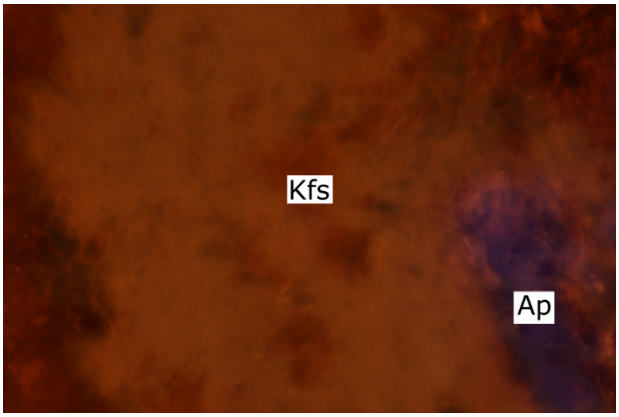

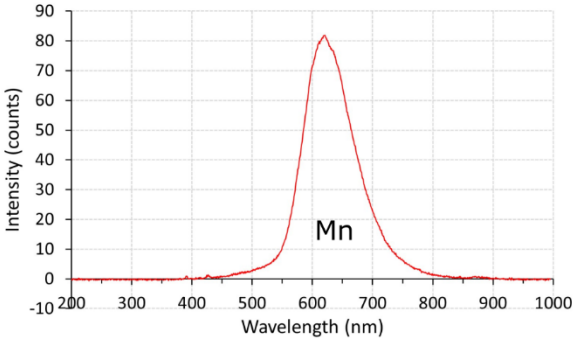

DDH-09-457B

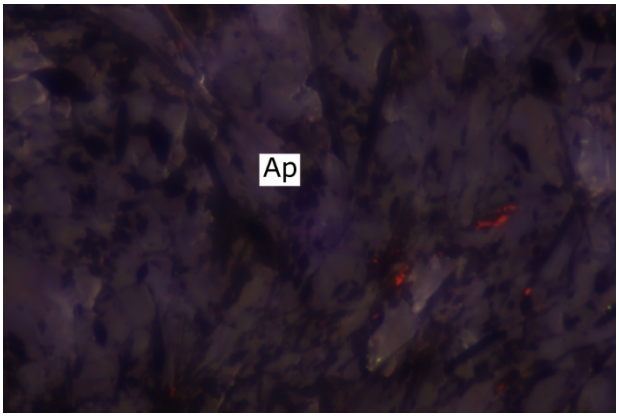

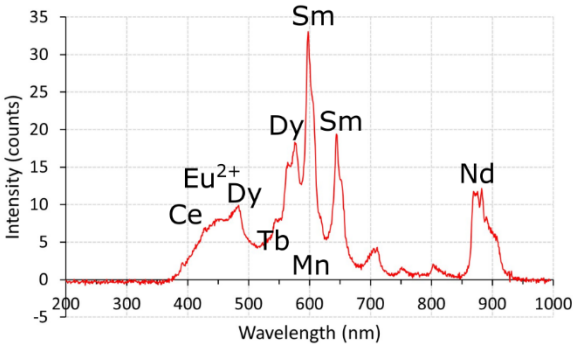

DDH-09-457B

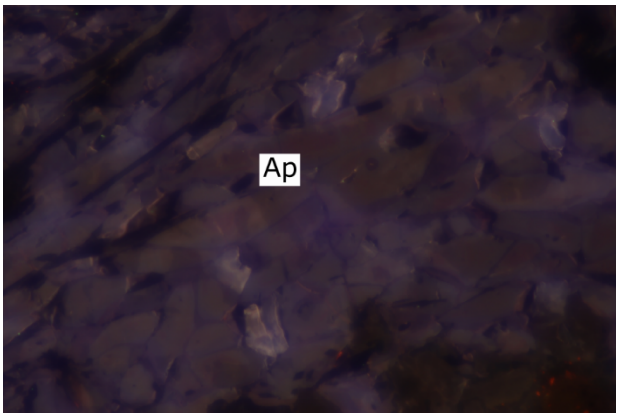

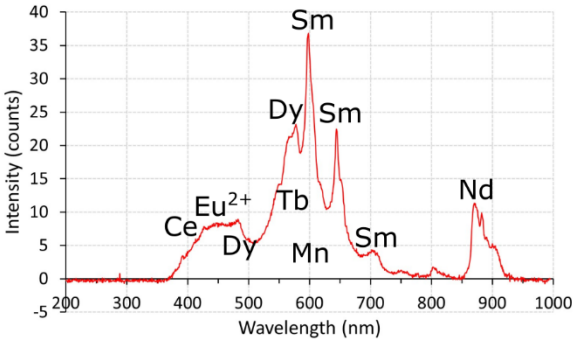

DDH-09-457B

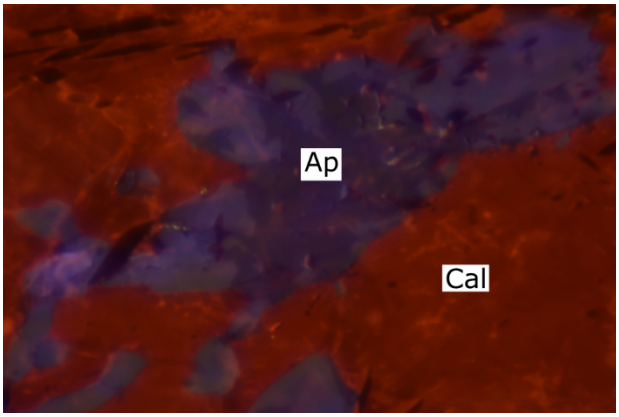

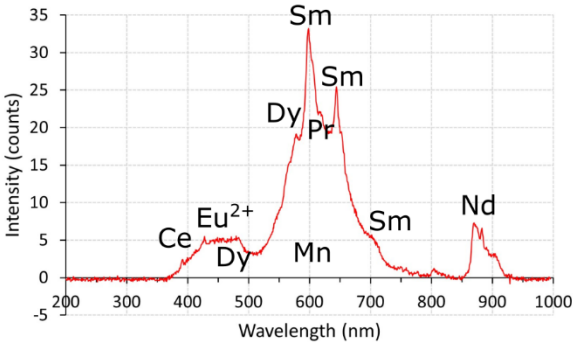

DDH-09-457B

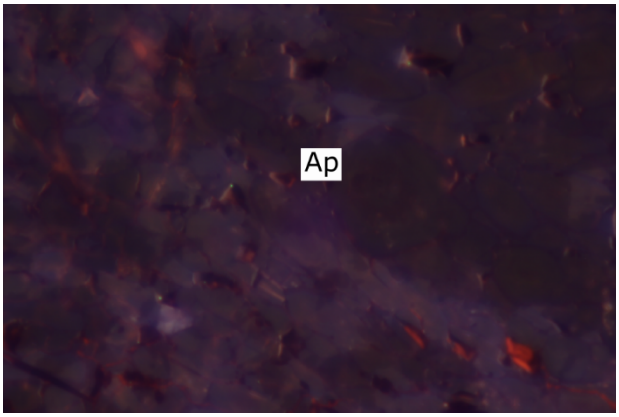

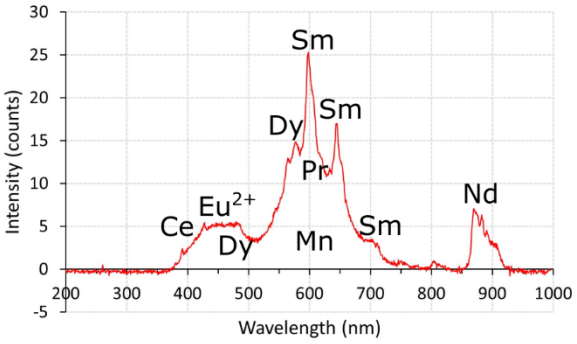

DDH-09-457B

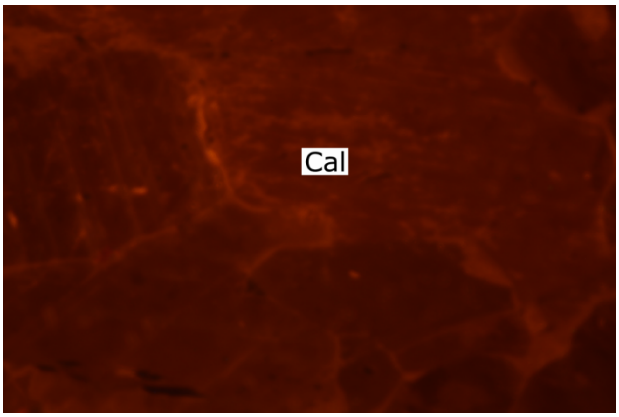

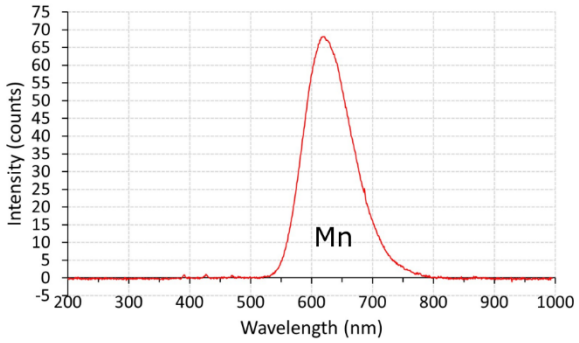

PGH-18-07-650

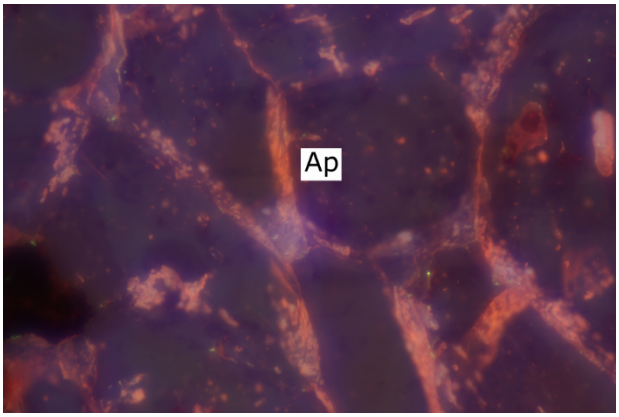

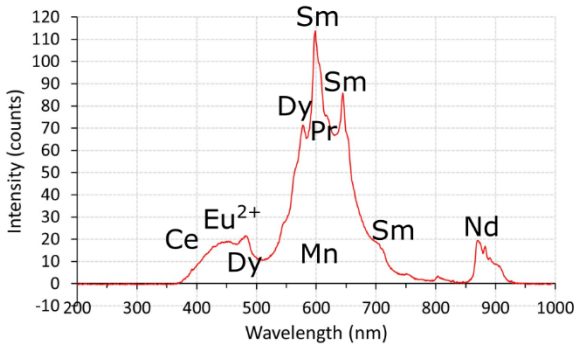

PGH-18-07-650

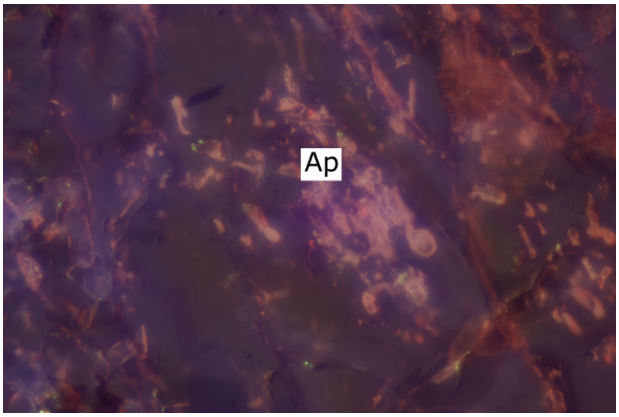

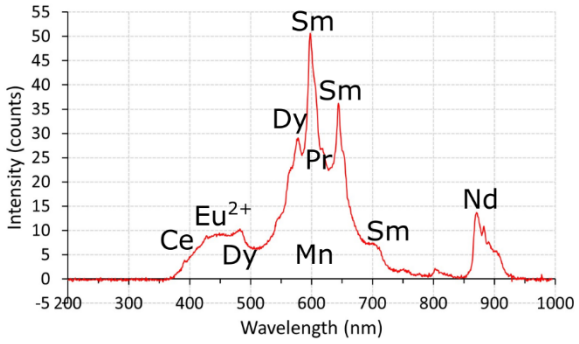

PGH-18-07-650

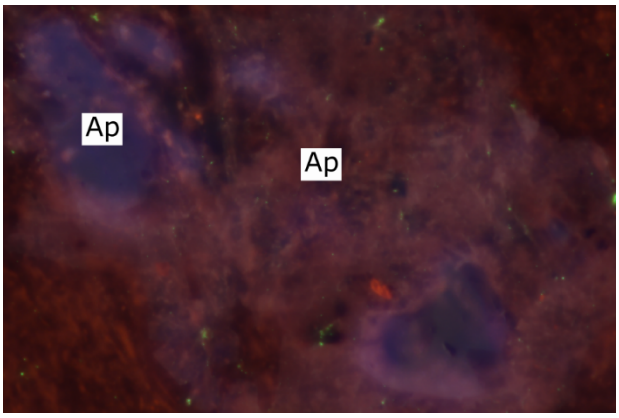

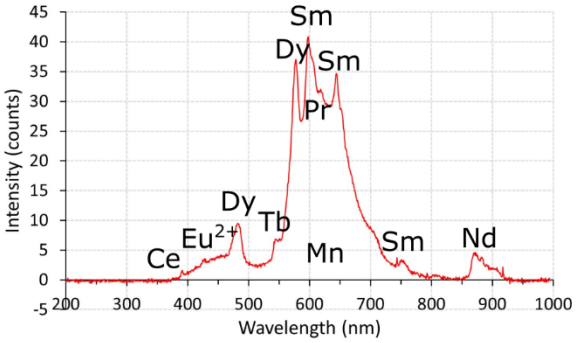

DDH-04-608

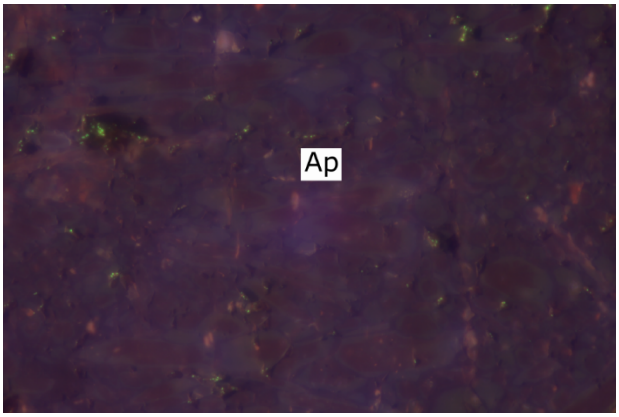

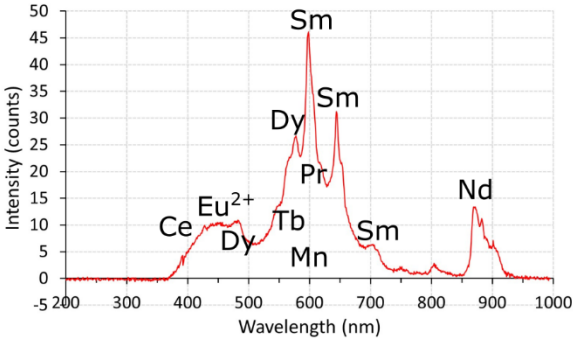

DDH-04-608

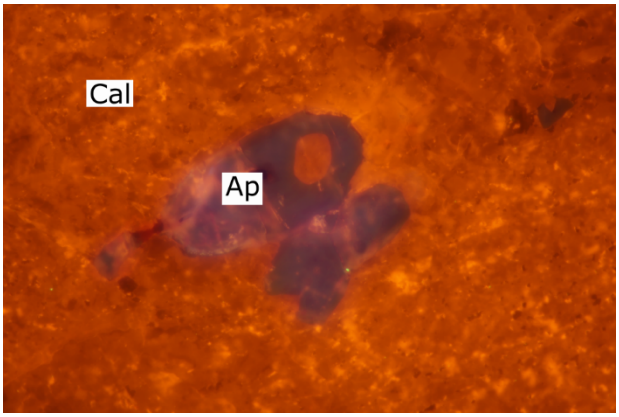

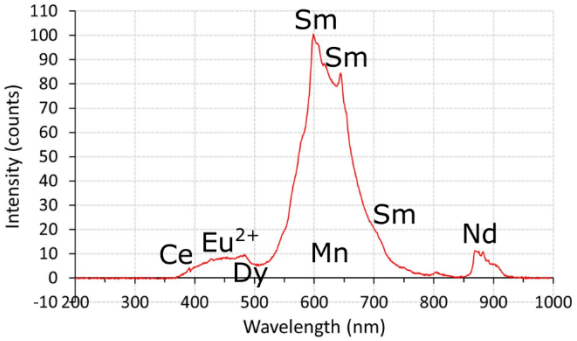

DDH-04-608

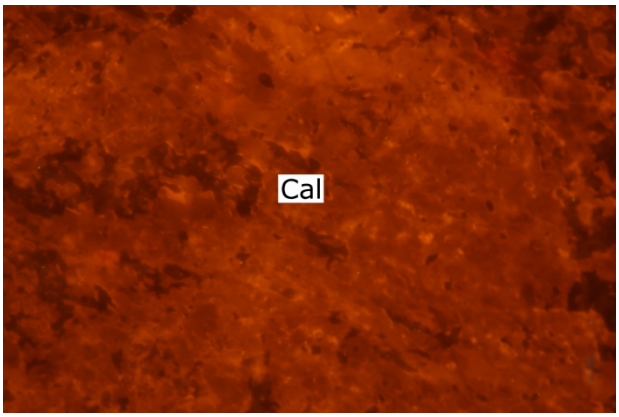

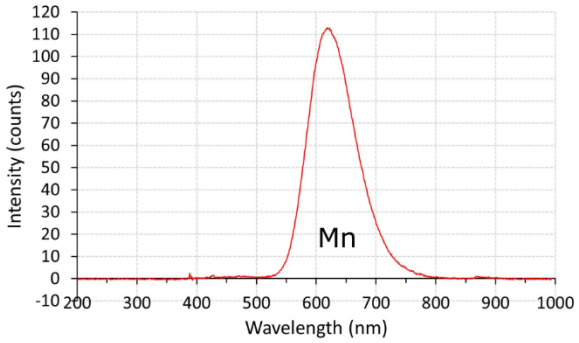

DDH-08-13

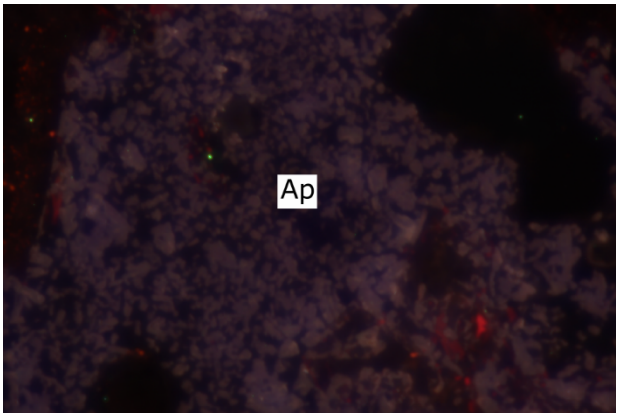

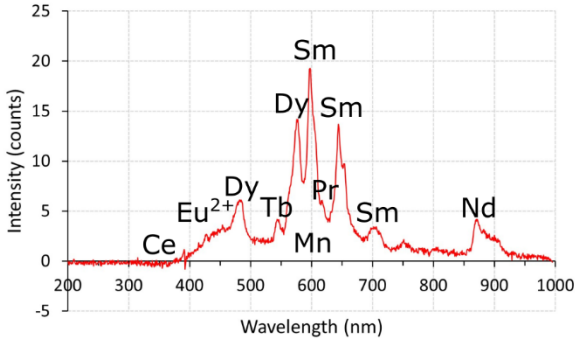

DDH-08-13

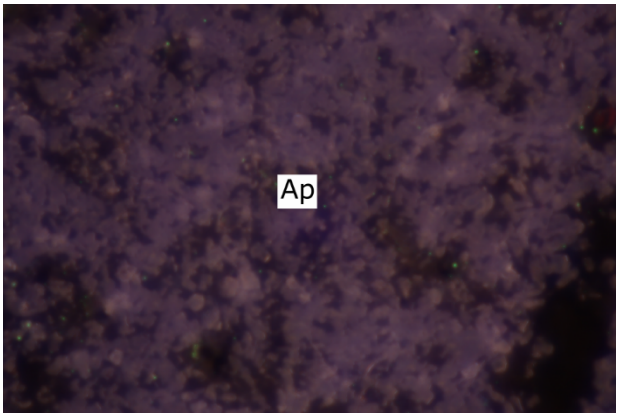

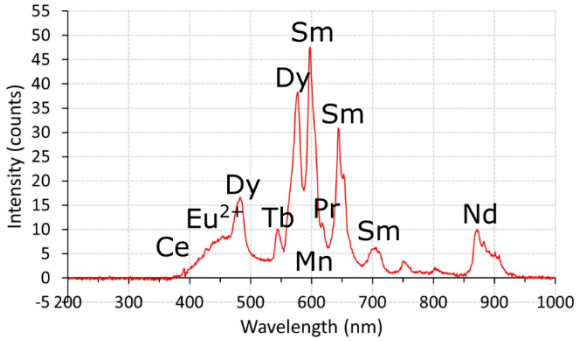

DDH-08-13

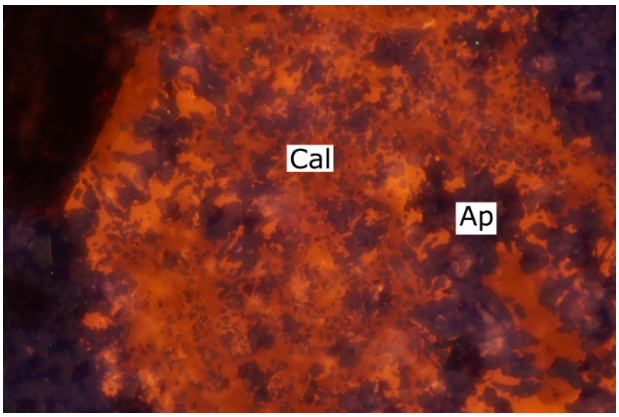

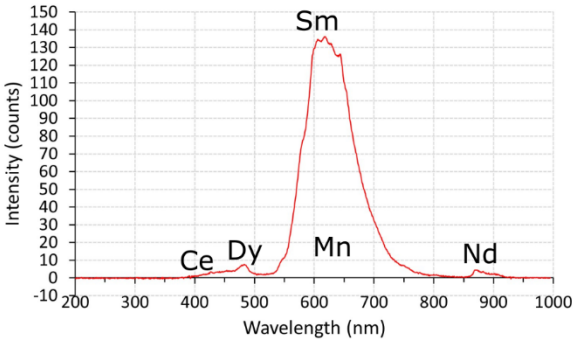

DDH-08-13

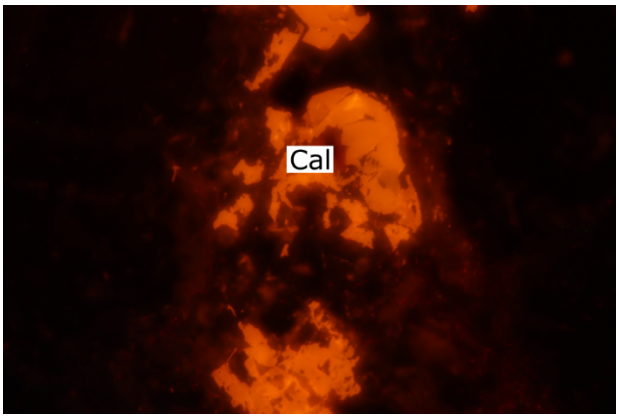

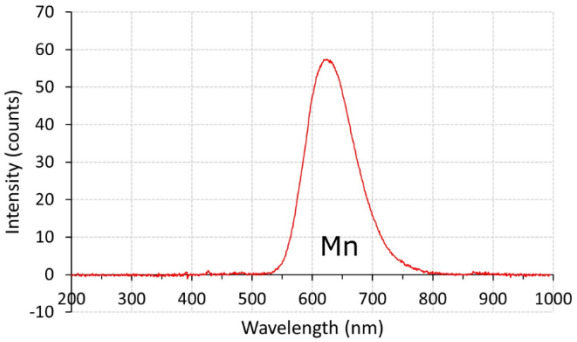

DDH-08-293

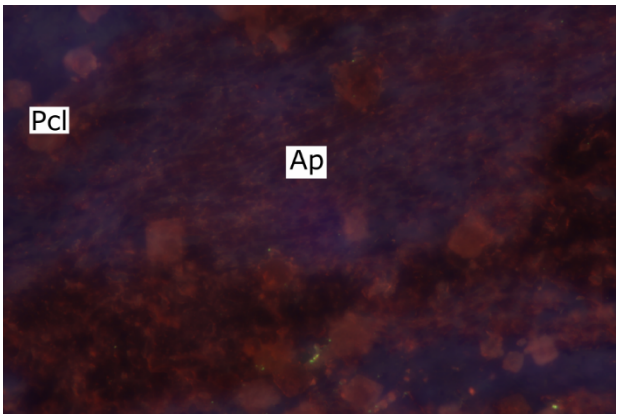

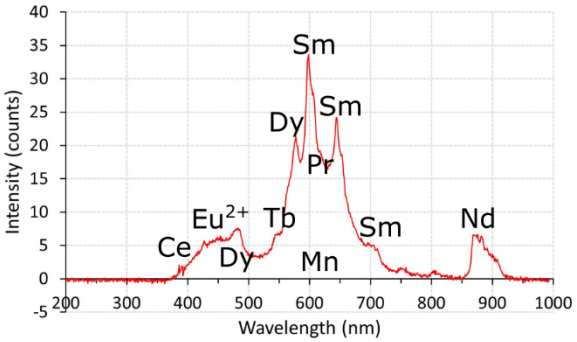

DDH-08-293

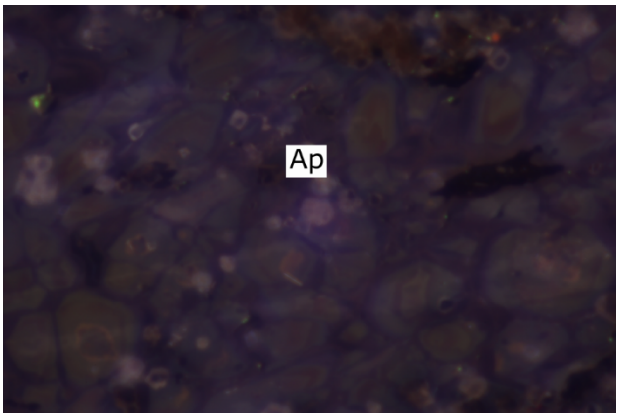

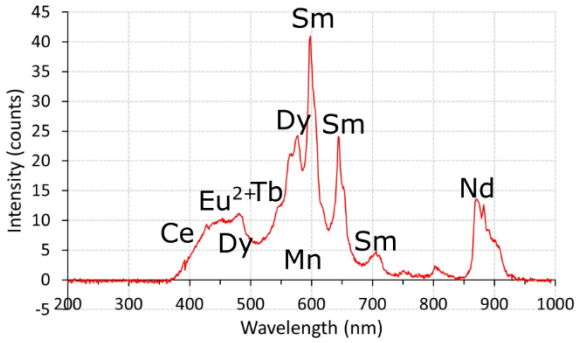

DDH-08-293

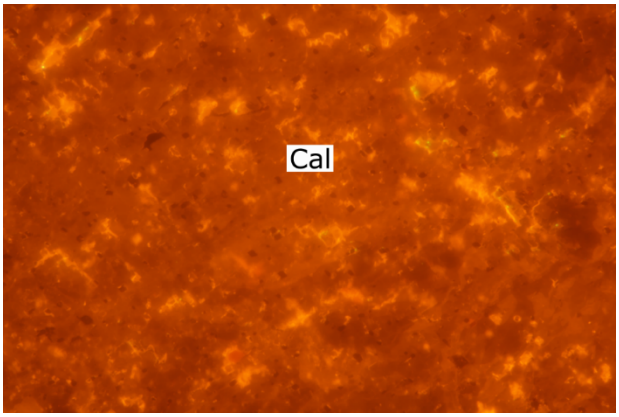

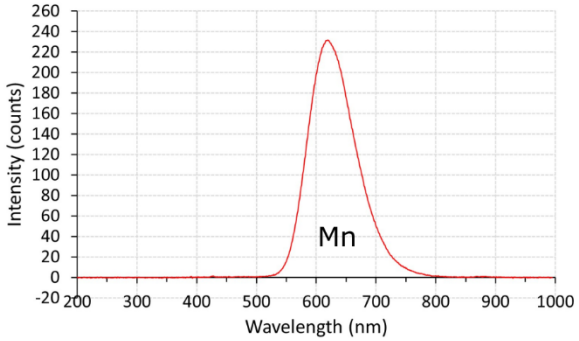

PGH-18-07-427

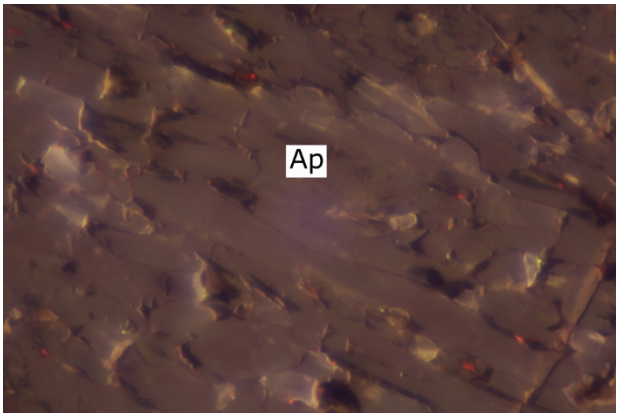

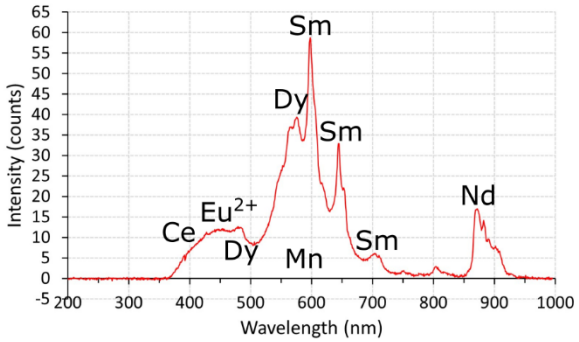

PGH-18-07-427

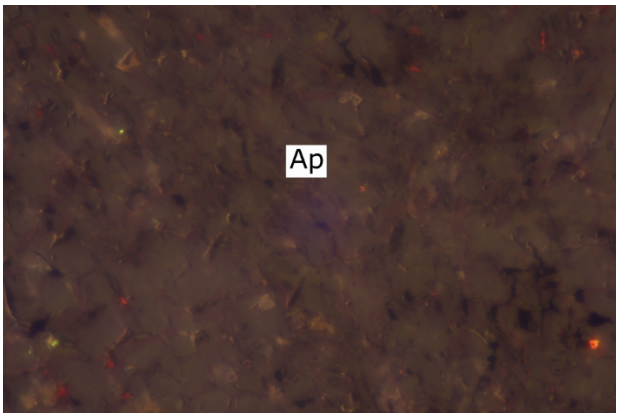

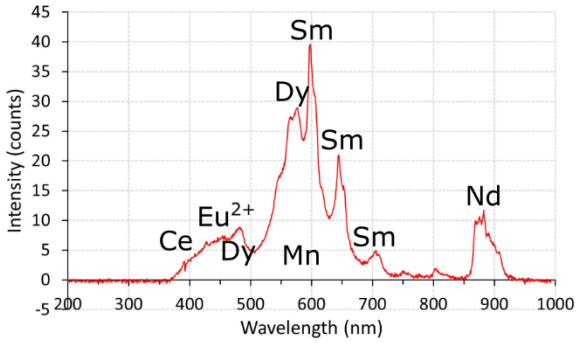

PGH-18-07-427

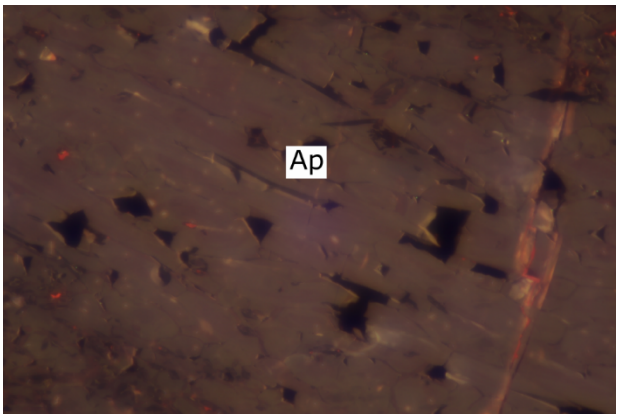

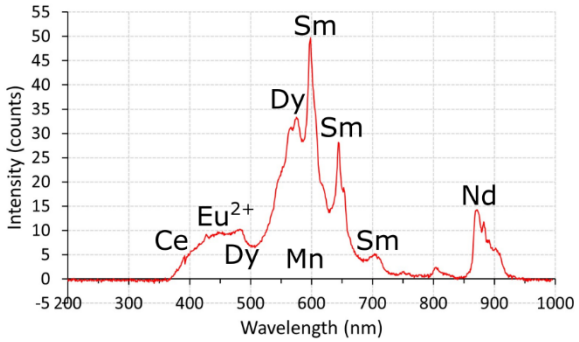

PGH-18-07-427

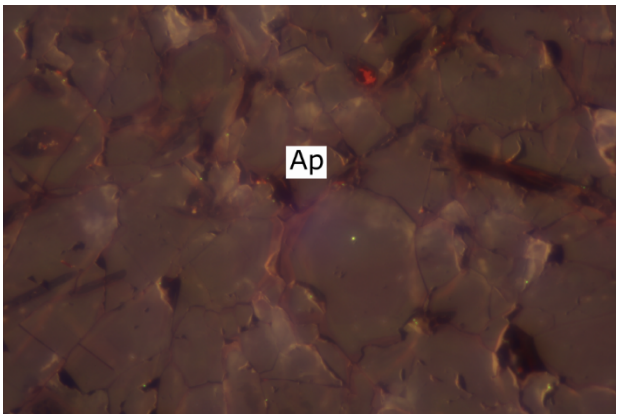

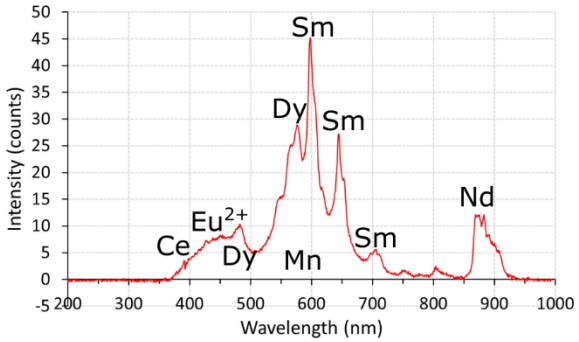

PGH-18-07-427

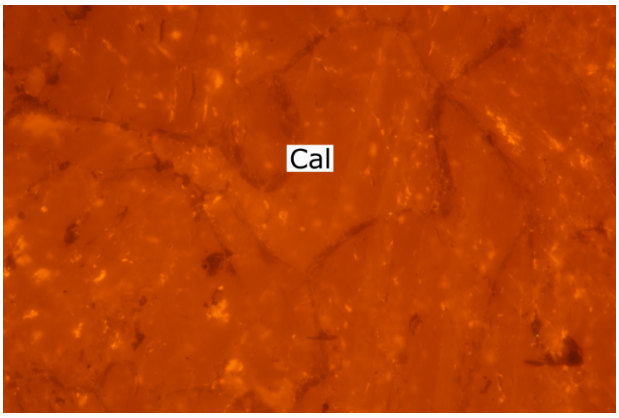

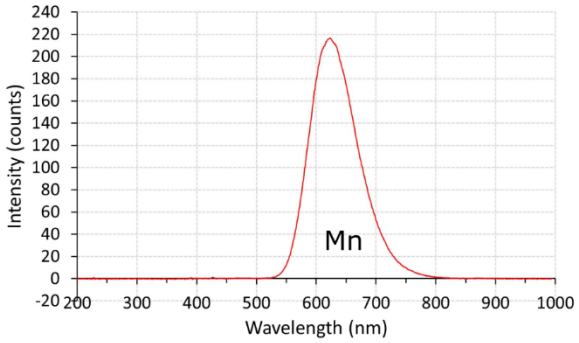

PGH-18-07-427

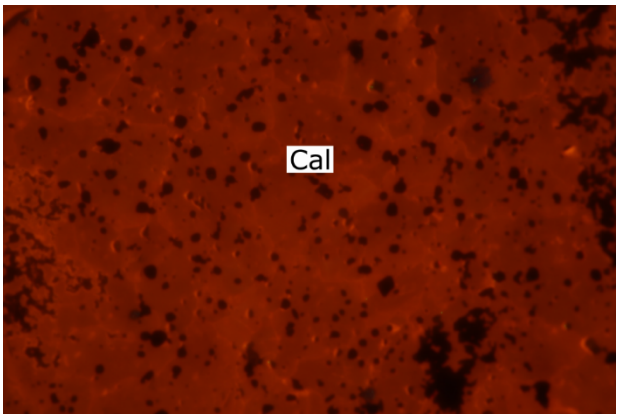

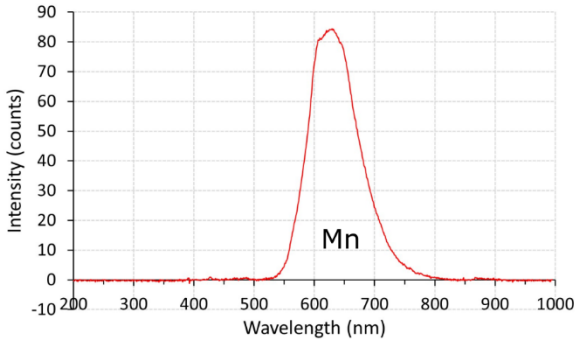

Appendix III Orbicular carbonatite Ti-magnetite – ilmenite geothermometry

III-I Magnetite Input

	Mgt-1	Mgt-2	Mgt-3	Mgt-4	Mgt-5	Mgt-6	Mgt-7	Mgt-8	Mgt-9	Mgt-10	Mgt-11
Wt. %											
SiO_2	-	-	-	-	-	-	-	-	-	-	-
TiO_2	0.37	0.56	0.51	0.49	0.57	0.66	1.11	0.63	0.30	0.73	1.13
Al_2O_3	-	-	-	-	-	-	-	-	-	-	-
V_2O_3	0.96	0.86	0.98	1.10	1.16	1.05	0.83	0.77	0.91	0.88	0.91
Cr_2O_3	-	-	-	-	-	-	-	-	-	-	-
Nb_2O_3	-	-	-	-	-	-	-	-	-	-	-
Fe_2O_3	-	-	-	-	-	-	-	-	-	-	-
FeO	93.37	93.97	93.36	94.49	93.36	94.39	92.85	92.71	92.88	92.58	92.40
MnO	-	-	-	-	-	-	-	-	-	-	-
NiO	-	-	-	-	-	-	-	-	-	-	-
ZnO	-	-	-	-	-	-	-	-	-	-	-
MgO	-	-	-	-	-	-	-	-	-	-	-
CaO	-	-	-	-	-	-	-	-	-	-	-
Na_2O	-	-	-	-	-	-	-	-	-	-	-
K_2O	-	-	-	-	-	-	-	-	-	-	-
BaO	-	-	-	-	-	-	-	-	-	-	-
Total	**94.70**	**95.39**	**94.85**	**96.08**	**95.09**	**96.10**	**94.79**	**94.11**	**94.09**	**94.19**	**94.44**
Fe_2O_3 (calc.)	68.34	68.57	68.14	68.96	68.00	68.68	67.02	67.57	68.09	67.30	66.63
FeO (calc.)	31.87	32.27	32.04	32.44	32.17	32.59	32.55	31.91	31.61	32.02	32.45

III-II Ilmenite Input

	Ilm-1	Ilm-2	Ilm-3	Ilm-4	Ilm-5	Ilm-6	Ilm-7	Ilm-8	Ilm-9	Ilm-10	Ilm-11
Wt. %											
SiO_2	-	-	-	-	-	-	-	-	-	-	-
TiO_2	48.98	48.90	49.35	48.15	48.40	48.25	48.09	48.57	48.42	48.38	48.21
Al_2O_3	-	-	-	-	-	-	-	-	-	-	-
V_2O_3	-	-	-	-	-	-	-	-	-	-	-
Cr_2O_3	-	-	-	-	-	-	-	-	-	-	-
Nb_2O_3	0.94	0.98	0.76	0.77	0.30	0.39	0.85	1.03	0.79	0.82	0.66
Fe_2O_3	-	-	-	-	-	-	-	-	-	-	-
FeO	50.80	51.08	50.62	49.68	49.99	49.97	49.85	50.12	50.17	50.47	49.86
MnO	0.70	0.66	0.55	0.74	0.52	0.61	0.50	0.58	0.57	0.64	0.47
NiO	-	-	-	-	-	-	-	-	-	-	-
ZnO	-	-	-	-	-	-	-	-	-	-	-
MgO	-	-	-	-	-	-	-	-	-	-	-
CaO	-	-	-	-	-	-	-	-	-	-	-
Na_2O	-	-	-	-	-	-	-	-	-	-	-
K_2O	-	-	-	-	-	-	-	-	-	-	-
BaO	-	-	-	-	-	-	-	-	-	-	-
Total	**101.42**	**101.62**	**101.28**	**99.34**	**99.21**	**99.22**	**99.29**	**100.30**	**99.95**	**100.31**	**99.20**
Fe_2O_3 (calc.)	8.28	8.62	7.54	7.91	7.75	7.98	7.89	7.80	7.99	8.44	7.74
FeO (calc.)	43.35	43.32	43.84	42.56	43.01	42.79	42.75	43.10	42.98	42.87	42.89

III-III Output

	Pair-1	Pair-2	Pair-3	Pair-4	Pair-5	Pair-6	Pair-7	Pair-8	Pair-9	Pair-10	Pair-11
Mol. %											
[Usp	1.06	1.59	1.45	1.38	1.62	1.86	3.17	1.81	0.86	2.09	3.23
Mgt]	98.94	98.41	98.55	98.62	98.38	98.14	96.83	98.19	99.14	97.91	96.77
[Ilm	91.65	91.32	92.45	91.95	92.40	92.12	91.91	91.95	91.90	91.49	92.16
Hem]	8.35	8.68	7.55	8.05	7.60	7.88	8.09	8.05	8.10	8.51	7.84
[Usp	1.07	1.60	1.47	1.39	1.64	1.88	3.19	1.82	0.87	2.11	3.26
Ilm]	92.09	91.78	92.82	92.29	92.50	92.26	92.34	92.47	92.28	91.86	92.49
[Usp	1.07	1.60	1.47	1.39	1.64	1.88	3.19	1.82	0.87	2.11	3.26
Ilm]	92.09	91.78	92.82	92.29	92.50	92.26	92.34	92.47	92.28	91.86	92.49
[Usp	1.07	1.61	1.47	1.40	1.65	1.89	3.21	1.83	0.87	2.12	3.28
Ilm]	92.15	91.84	92.86	92.35	92.54	92.31	92.38	92.52	92.33	91.92	92.53
$[X_{Usp}$	0.01	0.02	0.01	0.01	0.02	0.02	0.03	0.02	0.01	0.02	0.03
$X_{Mgt}]$	0.99	0.98	0.99	0.99	0.98	0.98	0.97	0.98	0.99	0.98	0.97
$[X_{Ilm}$	0.92	0.92	0.93	0.92	0.93	0.92	0.92	0.93	0.92	0.92	0.93
$X_{Hem}]$	0.08	0.08	0.07	0.08	0.07	0.08	0.08	0.07	0.08	0.08	0.07
$[X'_{Usp}$	0.01	0.02	0.01	0.01	0.02	0.02	0.03	0.02	0.01	0.02	0.03
X'_{Mgt}	0.99	0.98	0.99	0.99	0.98	0.98	0.97	0.98	0.99	0.98	0.97
X'_{Ilm}	0.92	0.92	0.93	0.92	0.92	0.92	0.92	0.92	0.92	0.92	0.92
$X'_{Hem}]$	0.08	0.08	0.07	0.08	0.08	0.08	0.08	0.08	0.08	0.08	0.08

III-IV Temperature

	Pair-1	Pair-2	Pair-3	Pair-4	Pair-5	Pair-6	Pair-7	Pair-8	Pair-9	Pair-10	Pair-11
°C											
PP77, C67	434.33	463.43	447.74	448.80	455.32	467.05	507.94	466.85	419.99	481.29	506.97
PP77, A68	431.36	460.08	444.96	446.52	455.19	466.53	504.17	462.52	417.49	478.51	504.30
PP77, LS82	431.36	460.08	444.96	446.52	455.19	466.53	504.17	462.52	417.49	478.51	504.30
PP77, S83	431.17	459.87	444.88	446.32	455.19	466.41	504.06	462.34	417.38	478.31	504.25
SL81, C67	565.69	586.13	571.41	574.23	576.53	585.22	610.94	585.83	554.97	596.80	609.10
SL81, A68	562.05	582.22	567.90	571.33	576.01	584.30	606.59	580.77	551.81	593.51	605.86
SL81, LS82	562.05	582.22	567.90	571.33	576.01	584.30	606.59	580.77	551.81	593.51	605.86
SL81, S83	561.69	581.85	567.65	570.94	575.81	583.99	606.31	580.43	551.54	593.15	605.62
AL85, C67	572.93	595.77	579.70	582.65	585.47	595.18	624.26	595.78	560.98	607.91	622.39
AL85, A68	568.98	591.59	575.89	579.53	584.93	594.21	619.68	590.33	557.53	604.42	618.97
AL85, LS82	568.98	591.59	575.89	579.53	584.93	594.21	619.68	590.33	557.53	604.42	618.97
AL85, S83	568.60	591.21	575.62	579.11	584.73	593.89	619.39	589.97	557.24	604.05	618.73
S08	567.73	569.85	562.65	566.36	564.90	566.58	566.01	565.06	566.40	569.29	564.97
GE08	556.32	558.65	550.75	554.82	553.22	555.06	554.44	553.39	554.87	558.04	553.29
Average	**527.37**	**548.18**	**534.13**	**537.00**	**541.67**	**550.25**	**575.30**	**547.63**	**516.93**	**560.12**	**574.54**

*PP77: Powell and Powell (1977)
SL81: Spencer and Lindsley (1981)
AL85: Anderson and Lindsley (1985)
S08: Sauerzaph et al. (2008)
GE08: Ghiorso and Evans (2008)
C67: Carmichael (1967)
A68: Anderson (1968)
LS82: Lindsley and Spencer (1982)
S83: Stormer (1983)

III-V Oxygen Fugacity

	Pair-1	Pair-2	Pair-3	Pair-4	Pair-5	Pair-6	Pair-7	Pair-8	Pair-9	Pair-10	Pair-11
-log fO_2											
PP77, C67	-31.44	-29.15	-29.57	-29.90	-28.96	-28.20	-25.20	-28.36	-32.58	-27.56	-25.06
PP77, A68	-31.35	-29.07	-29.49	-29.82	-28.88	-28.14	-25.12	-28.28	-32.50	-27.49	-24.99
PP77, LS82	-31.35	-29.07	-29.49	-29.82	-28.88	-28.14	-25.12	-28.28	-32.50	-27.49	-24.99
PP77, S83	-31.32	-29.04	-29.46	-29.78	-28.85	-28.10	-25.10	-28.26	-32.47	-27.46	-24.96
SL81, C67	-18.16	-17.66	-18.47	-18.16	-18.35	-18.06	-17.52	-17.96	-18.47	-17.55	-17.68
SL81, A68	-18.44	-17.94	-18.74	-18.38	-18.41	-18.14	-17.81	-18.32	-18.73	-17.79	-17.90
SL81, LS82	-18.44	-17.94	-18.74	-18.38	-18.41	-18.14	-17.81	-18.32	-18.73	-17.79	-17.90
SL81, S83	-18.48	-17.97	-18.76	-18.42	-18.44	-18.17	-17.83	-18.35	-18.76	-17.82	-17.92
AL85, C67	-17.87	-17.36	-18.16	-17.85	-18.04	-17.74	-17.19	-17.65	-18.19	-17.24	-17.34
AL85, A68	-18.15	-17.63	-18.42	-18.07	-18.10	-17.82	-17.46	-18.00	-18.44	-17.47	-17.55
AL85, LS82	-18.15	-17.63	-18.42	-18.07	-18.10	-17.82	-17.46	-18.00	-18.44	-17.47	-17.55
AL85, S83	-18.18	-17.66	-18.45	-18.11	-18.12	-17.85	-17.49	-18.03	-18.47	-17.50	-17.57
S08	-16.26	-16.28	-16.51	-16.37	-16.46	-16.44	-16.67	-16.48	-16.28	-16.38	-16.72
Average	**-22.12**	**-21.11**	**-21.74**	**-21.63**	**-21.38**	**-20.98**	**-19.83**	**-21.10**	**-22.66**	**-20.54**	**-19.86**

*PP77: Powell and Powell (1977)
SL81: Spencer and Lindsley (1981)
AL85: Anderson and Lindsley (1985)
S08: Sauerzaph et al. (2008)
C67: Carmichael (1967)
A68: Anderson (1968)
LS82: Lindsley and Spencer (1982)
S83: Stormer (1983)